Volume 7 No 3 Year 2024

IECO

■ Volume 7

■ No 3

■ Year 2024

IECO

International Journal Of
Industrial Electronics Control and Optimization

University of
Sistan and Baluchestan

Iranian Association of
Electrical and Electronics Engineers

International Journal Of

Industrial Electronics Control and Optimization

In This Issue:

Research Artivles:

About Journal

The University of Sistan and Baluchestan entered into strategic partnership with Iranian Association of Electrical and Electronic Engineers (IAEEE) to publish the **International Journal of Industrial Electronics Control and Optimization (IECO)**. The IECO is a refereed international journal which presents to the international scientific community important results of work in these fields, whether in the form of modeling simulation, analysis, fundamental research, development, application, design or real-time implementation. The scope of IECO is broad, encompassing all aspects of Industrial Electronics, Control and Optimization.

Note: International Journal of Industrial Electronics, Control and Optimization (IECO) has qualified to **ACADEMIC RESEARCH JOURNAL (ELMI-PAJOHESHI)** status certified by the ministry of Science, Research and Technology of Iran (No. 231566/3/18 dated 1396/10/09), and is published by the University of Sistan and Baluchestan through a formal partnership (No. 952/2/1500 dated 1395/11/04) with Iranian Association of Electrical and electronic Engineers (IAEEE) in order to develop scientific and research cooperation.

Aims and Scope

International Journal of Industrial Electronics, Control and Optimization (IECO) is a Peer reviewed journal of advanced and state-of-the-art in the science and engineering of Industrial Electronics, Control and Optimization. Its Scope encompasses the applications of Industrial Electronics, power systems, control, optimization and computational intelligence for the enhancement of industrial and manufacturing system and processes. The scope of the journal include the following:

I. Industrial Electronics

- Low and high-power converters
- Renewable energy
- Drive control techniques
- Techniques for advanced power semiconductor devices
- Power quality and utility applications
- Communications
- Flexible AC Transmission Systems (FACTS)
- Control in power electronics
- Electromagnetic and thermal performance of electronic power converters
- Motion control, robotics, sensors and actuators
- Fault detection and diagnosis
- Power systems
- Factory automation, communication, and computer networks

II. Control

- Adaptive control
- Control of process systems
- Control theory
- Data processing
- Design of control systems
- Hybrid systems
- Identification and observation
- Intelligent systems
- Model-predictive control
- Optimal control
- Robust control
- Fractional order systems

III. Optimization

- Ant Colony
- Chaos Theory
- Evolutionary Computing
- Fuzzy Computing
- Hybrid Methods
- Immunological Computing
- Neuro Computing

- Particle Swarm
- Probabilistic Computing
- Rough Sets
- Wavelet

Director-in-Charge:
Dr. S. Masoud Barakati

Editor-in-Chief
Dr. Gevork B. Gharehpetian

Editorial Board
Dr. S. Masoud Barakati- University of Sistan and Baluchestan
Dr. Gevork B. Gharehpetian- University of Technology (Tehran Polytechnic)
Dr. Ebrahim Babaei-University of Tabriz & Near East University
Dr. Seyyed Hossein Hosseini-University of Tabriz
Dr. Hasan Bevrani-University of Kordestan
Dr. Amirnaser Yazdani-Toronto Metropolitan University
Dr. Mehrdad Kazerani-Ryerson University
Dr. Hossein Askarian-Abyaneh-Amirkabir University of Technology (Tehran Polytechnic)
Dr. Hasan Monsef-University of Tehran
Dr. Massoud Rashidi Nejad-University of Shahid Bahonar Kerman
Dr. Mohammad Monfared- Ferdowsi University of Mashhad
Dr. Saeed Tavakoli-University of Sistan and Baluchestan
Dr. Mahmood Joorabian-Shahid Chamran University of Ahvaz
Dr. Mehri Mehrjoo-University of Sistan and Baluchestan
Dr. Mohammad Reza Aghaebrahimi- University of Birjand
Dr. Reza Ghazi-Ferdowsi University of Mashhad
Dr. Bin Wu- Toronto Metropolitan University
Dr. Tahere Fanaei Sheikhosleslami-University of Sistan and Baluchestan
Dr. Mahmoud Okati Sadegh-University of Sistan and Baluchestan

Assistant Editors
Dr. Ahmad khajeh-University of Sistan and Baluchestan
Dr. Hamde Torabi-University of Sistan and Baluchestan
Dr. Mojgan MollahassaniPour-University of Sistan and Baluchestan
Dr. Poria Jafari-University of Sistan and Baluchestan
Dr. Abbas-Ali Zamani-Technical and vocational University
Dr. Samaneh Sadat Sajjadi-Hakim Sabzevari University
Dr. Alireza HosseinPur-University of Zabol
Dr. Majid Ghadrdan-University of Sistan and Baluchestan
Dr. Saeed Yousefi-Darmian-University of Sistan and Baluchestan
Dr. Samaned Soradi-zeid-Industry and Mining (Khash)
Dr. Mohammad Ali Azghandi-University of Sistan and Baluchistan
Dr. Mahdi Kazeminia- Velayat University
Dr. Sobhan Dorahaki- Qatar University
Dr. Ali Hassannia -University of Sistan and Baluchistan

Executive Manager
Kazem Piran

Page Designer
Dr. Ali Hassannia

IECO International Journal Of Industrial Electronics Control and Optimization
Print ISSN: 3517-2645
Online ISSN: 3568-2645
Homepage: https://ieco.usb.ac.ir/

The Performance and Robustness of One-Parameter Fractional Linear Prediction

Seyed Mostafa Alaviyan Shahri[1] | Hamid Reza Abutalebi[2]

Department of Electrical Engineering, Yazd University, Yazd, Iran.[1,2]
Corresponding author's email: habutalebi@yazd.ac.ir

Article Info

Article type:
Research Article

Article history:
Received: 12-January-2024
Received in revised form: 18-March-2024
Accepted: 21-Apri- 2024
Published online: 22-sep-2024

Keywords:
Fractional Calculus,
Sampling Frequency,
Noise,
Reverberation,
Fractional Linear Prediction.

ABSTRACT

This paper deals with the problem of signal modeling using fractional-order linear prediction. In this research, we obtain the closed-form expression of the optimum sampling frequency of the One-Parameter Fractional-order Linear Prediction (OPFLP) and examine the performance when the fractional order (α) is in $0 \le \alpha \le 2$. Our investigation focuses on determining optimum α within the individual ranges of $0 \le \alpha \le 1$ and $1 < \alpha \le 2$ while considering various influential parameters, such as sampling frequency and environmental interferences. We initiate our study by examining the impact of the sampling frequency, a critical parameter that demands meticulous selection, on the optimal value of α. Simulation results demonstrate that if the sampling rate falls within five to six times the maximum frequency of the signal under scrutiny, the optimal range for α resides within $1 < \alpha \le 2$ .Conversely, when the sampling frequency exceeds six times the maximum signal frequency, the optimal α shifts to $0 \le \alpha \le 1$ .This observation underscores the crucial relationship between sampling frequency and the appropriate selection of the fractional order α for effective OPFLP performance. In the next step, we assess the robustness of OPFLP in handling challenging signal processing tasks, particularly in hands-free speech acquisition applications. We evaluate the model's performance and robustness against environmental interferences in three scenarios: noisy environments, reverberant environments, and noisy-reverberant settings. Simulation outcomes highlight OPFLP's superior robustness compared to second-order LP in handling environmental interferences. Furthermore, our investigations elucidate that noise exerts a more detrimental impact on OPFLP performance than reverberation, emphasizing the nuanced effects of these interferences on the model's efficacy.

I. Introduction

In various scientific and engineering domains, significant attention has been directed towards fractional calculus and its applications over recent decades [1]–[6]. Models incorporating fractional derivatives and integrals are referred to as fractional order systems, aiming to introduce memory into signal and system modeling [1], [4]. The fractional order (α) typically falls within the range $0 \le \alpha \le 2$. However, it is crucial to note that the system behavior, concerning stability and robustness, differs considerably between the ranges $0 \le \alpha \le 1$ and $1 < \alpha \le 2$ [7],[8].

Linear prediction (LP) is widely employed in the processing of various signals, including audio and speech [9], image [10], and biomedical signals. In the context of speech processing, LP has been applied in synthesis, coding, and compression [9].

Frequency-domain linear prediction (FDLP) has been a valuable tool for modeling and analyzing signals in the frequency domain, particularly for Automatic Speech

Publisher: University of Sistan and Baluchestan

Recognition (ASR) applications [11]. It leverages the concept of linear prediction, where the current sample is predicted using past samples in a linear combination. In the context of FDLP, this prediction is performed in the frequency domain, focusing on the spectral characteristics of the signal.

Recently, a noteworthy advancement was presented in [12] with the introduction of Complex Frequency-Domain Linear Prediction (CFDLP). CFDLP offers a significant improvement over conventional FDLP by enabling straightforward interpretation of the complex cepstrum as temporal modulations within an all-pole model approximation of the speech signal's power spectrum.

Furthermore, CFDLP boasts a remarkable advantage in terms of computational efficiency. Compared to conventional FDLP, CFDLP achieves the same level of approximation with significantly faster processing speeds. This is a crucial advantage for real-time speech processing applications where computational efficiency is paramount. [13].

Recently, fractional-order linear prediction (FLP) has emerged in signal processing, termed as a generalized version of LP. However, its exploration in this field has been limited to a few notable papers [14]–[18].

In [14], the authors introduced One-Parameter FLP (OPFLP) within the range $0 \le \alpha \le 1$ and determined the optimal coefficients for the corresponding model. Their approach involved expanding the fractional Taylor series and truncating it to a single term to obtain the optimal OPFLP coefficients. Subsequently, they compared the performance of OPFLP against the first- and second-order LPs using standard sinusoidal waves and real signals, such as clean speech and Electrocardiogram (ECG) signals. In another study [15], the authors examined the performance of OPFLP ($0 \le \alpha \le 1$) by applying it to clean musical signals, such as piano and Western music. In [16], standard sinusoidal and damped sinusoidal waves were tackled to derive a closed-form solution for the optimal derivative order. Additionally, the authors proved that the optimal derivative order for OPFLP is inversely related to the number of memory samples utilized in the model.

The authors of [17] proposed a novel approach for bearing fault diagnosis in induction motors using OPFLP as a noise elimination technique. The presence of noise in the stator current, unrelated to bearing faults, can hinder accurate fault detection and lead to false alarms. This work proposes FLP as a method to address this challenge. FLP leverages the principles of linear prediction theory to identify and remove predictable noise components, leaving behind the unpredictable fault signature. A key advantage of this approach lies in its computational efficiency. The paper employs a limited memory FLP model, requiring optimization of only the fractional derivative order parameter after determining the optimal number of memory samples. This significantly reduces the computational complexity compared to other methods.

Navish et al. [18] delve into the challenge of noise contamination in biomedical signals acquired from various devices. These signals, often crucial for diagnoses, can be impacted by external factors like the environment, device functionality, and even clinician activity. To address this, the study investigates the effectiveness of two denoising techniques: stationary wavelet transform (SWT) and OPFLP, specifically applied to electromyography (EMG) signals. The primary objective is to compare the performance of these two methods in removing noise from EMG signals and ultimately improve the accuracy of diagnosis. The research employs five different methods to calculate the fractal dimension of the denoised signals: Higuchi, Katz, rescaled-range analysis, relative dispersion, and power spectral density. Based on the analysis, the study concludes that FLP outperforms SWT in terms of achieving a more reliable denoised signal, as evidenced by the fractal dimension analysis.

In the aforementioned studies, it has been assumed that the fractional derivative order is in the range of $0 \le \alpha \le 1$. While this assumption is satisfied in some cases, the optimum α can differ as the sampling frequency of the signal changes. According to the Nyquist theorem, the sampling frequency must exceed at least twice the maximum signal frequency. We demonstrate that if the sampling frequency equals two, three, or four times the maximum frequency, the optimal derivative order converges to $\alpha = 0$. However, as the sampling frequency reaches five or six times the maximum signal frequency, the optimal α shifts to $1 < \alpha \le 2$. Beyond six times the maximum frequency, the optimal derivative order resides within $0 \le \alpha \le 1$.

Another assumption when applying OPFLP to speech signals in the aforementioned research often relies on a single frame of voiced speech, leading to results that may not adequately represent practical situations such as hands-free speech signal acquisition. In practical situations, the processed speech signal contains voiced, unvoiced, and silent segments, commonly contaminated by noise and reverberation as two major environmental interferences. These environmental factors exert a substantial impact on speech signals, as extensively discussed in existing literature [19]–[23]. Reverberation occurs in enclosed spaces, manifesting as multiple delayed and attenuated speech reflections from enclosing walls and objects [23]. Meanwhile, diverse noise types, notably diffuse noise, pervade most environments [23].

Motivated by previous researches, our primary objective is to determine the optimal derivative order of OPFLP, assuming $0 \le \alpha \le 2$. Subsequently, we evaluate the performance of OPFLP in hands-free speech signal acquisition, assessing how noise and reverberation influence its efficacy. Additionally, we examine the robustness of the OPFLP model under three scenarios: 1) the presence of reverberation, 2) the presence of noise, and 3) the simultaneous presence of noise and reverberation. To assess comparative performance, we consider the first- and second-order LPs as baseline methods, given their acceptable performance in various signal processing applications.

In summary, although [14] provides a closed-form expression for the optimal coefficient in $0 \le \alpha \le 1$, it is very conservative to investigate only one parameter, lacking theoretical justification. Furthermore, while acknowledging the critical role of sampling frequency in model performance, [14] does not offer a framework to determine its optimal value. Additionally, the [14] assumes the usage of a single frame of voiced speech for analysis might not be suitable for real-world situations that speech signal typically consists of diverse segments like voiced, unvoiced, and silent, and are often further contaminated by environmental noise. In this research, we overcome these limitations by deriving a closed-form expression for the optimal sampling frequency and determining the optimal derivative order in $0 \le \alpha \le 2$. Also the OPFLP performance and robustness are evaluated against environmental interferences.

This paper is organized as follows: Section II explains the fundamentals of the first- and second-order LPs alongside OPFLP. Section III details performance metrics employed for robustness and performance assessment and presents evaluation outcomes. Finally, Section IV concludes this research.

II. Preliminaries And Backgrounds

In this section, we briefly explain the first- and second-order LP as the baseline methods. Then, after presenting the basics of the fractional linear prediction, the OPFLP will be obtained.

Considering stationary signal $y(n)$, the linear prediction model estimates the current signal sample as a linear combination of *q* previous samples, i.e. [14]–[16]:

$$\hat{y}(n) = \sum_{i=1}^{q} a_i y(n-i) \tag{1}$$

where $\hat{y}(n)$ is the estimated signal sample and q is called the prediction order. $q = 1$ and $q = 2$ results in the first- and the second-order LPs, respectively, as follows [14]–[16]:

$$q = 1, \quad \hat{y}(n) = a.y(n-1) \tag{2}$$

and

$$q = 2, \hat{y}(n) = a_1.y(n-1) + a_2.y(n-2)a \tag{3}$$

The MMSE framework can be used to obtain the optimum coefficient(s) in each case. In this regard, the error function is introduced as [14]–[16]:

$$e(n) = \hat{y}(n) - y(n) \tag{4}$$

Then, the optimal coefficient(s) is(are) obtained as the solution of the following optimization problems:

$$\begin{aligned} a_{opt} &= \arg\min_{a} \;\; J = E\left[e^2(n)\right] \\ &= \frac{R_y(1)}{R_y(0)} \;, \qquad (q=1) \end{aligned} \tag{5}$$

and

$$\begin{aligned} a_{1_{opt}}, a_{2_{opt}} &= \arg\min_{a_1, a_2} \;\; J = \mathrm{E}\left[e^2(n)\right] \\ &= \begin{cases} a_{1_{opt}} = \dfrac{R_y(1)R_y(0) - R_y(2)}{R_y^2(0) - R_y^2(1)} \\ a_{2_{opt}} = \dfrac{R_y(2)R_y(0) - R_y(1)}{R_y^2(0) - R_y^2(1)} \end{cases} ,(q=2) \end{aligned} \tag{6}$$

where $R_y(k)$ denotes the autocorrelation function of y at lag k.

In the Fractional-order Linear Prediction (FLP) model, the current signal sample is estimated by the linear combination of q fractional-order terms [14]:

$$\hat{y}(t) = \sum_{i=1}^{q} a_i D_t^{\alpha_i} y(t) \tag{7}$$

where $\hat{y}(n)$ is the estimated signal, $a_i \; (i = 1, ..., q)$ are the FLP coefficients, D^{α} is the fractional-order derivative operator, and $\alpha_i \; (i = 1, ..., q)$ are the derivative orders.

The fractional derivative can be expanded using the Grundwall-Letnikov (G-L) definition. G-L is one of the basic definitions widely used in the numerical calculation of the fractional derivative of a function, and is expressed as [12], [13]:

$$D_t^{\alpha_i} y(t) = \lim_{h \to \infty} \frac{1}{h^{\alpha}} \sum_{j=0}^{K} (-1)^j \binom{\alpha}{j} y(t - jh) \tag{8}$$

where K is the integer part of the fraction $\dfrac{(t-b)}{h}$, t and b are lower and upper limits of differentiation, respectively. h is sampling period ($h = 1/F_S$, F_S : sampling frequency) and $\alpha \in R$ is the arbitrary real order of the fractional derivative. By substituting $t = nh$ into (7) and (8), the discretized version of the equations are obtained as [14], [16]:

$$D^{\alpha} y(n) = \lim_{h \to \infty} \frac{1}{h^{\alpha}} \sum_{j=0}^{K} (-1)^j \binom{\alpha}{j} y(n - j) \tag{9}$$

and

$$\hat{y}(n) = \sum_{i=1}^{q} a_i D_y^{\alpha_i} y(n) \tag{10}$$

In (10), the system is known as “commensurate order” if the order of differentiation is integer multiple of a single base order $\alpha_i = i\alpha$. In this case, (10) is re-written as [14], [16]:

$$\hat{y}(n) = \sum_{i=1}^{q} a_i D_y^{i\alpha} y(n) \qquad (11)$$

By considering only the first term of (11), the first-order fractional linear prediction model is obtained as:

$$\hat{y}(n) = a.D^{\alpha} y(n-1) \qquad (12)$$

where a and α are determined via the minimization of a cost function (e.g., mean squared error). In this regard, considering $m \in N$ as the upper limit of the summation in (9), we have:

$$D^{\alpha} y(n-1) = \frac{1}{h^{\alpha}} \sum_{j=0}^{m} (-1)^j \binom{\alpha}{j} y(n-1-j) \qquad (13)$$

If $m = 1, 2,$ or 3, the following three cases are respectively obtained from (12) and (13):

1. First-order OPFLP model with two samples memory:

$$\hat{y}(n) = \frac{a}{h^{\alpha}} \big(y(n-1) - \alpha y(n-2) \big) a \qquad (14)$$

By defining the prediction error as $e(n) = \hat{y}(n) - y(n)$ and minimizing the mean squared error criteria, the optimal coefficient (a_{opt}) is obtained as follows:

$$a_{opt} = \arg\min_{a} \ \mathrm{J{=}E}\left[e^2(n)\right]$$

$$a_{opt} = \mathrm{h}^{\alpha} \frac{R_y(1) - \alpha R_y(2)}{R_y(0) - 2\alpha R_y(1) + \alpha^2 R_y(0)} \qquad (15)$$

It is called OPFLP-2 hereafter.

2. First-order OPFLP model with three samples memory:

$$\hat{y}(n) = a.h^{\alpha}.y(n-1) - a.h^{\alpha}.\left(\alpha y(n-2) + \frac{\alpha(1-\alpha)}{2} y(n-3) \right) \qquad (16)$$

In this case, the optimal coefficient a_{opt} is determined by minimizing the mean squared prediction error:

$$a_{opt} = \arg\min_{a} \ \mathrm{J{=}E}\left[e^2(n)\right]$$

$$a_{opt} = h^{\alpha} \frac{\left(R_y(1) - \alpha R_y(2) - \frac{\alpha(1-\alpha)}{2} R_y(3) \right)}{R_y(0) - 2\alpha \left(\frac{1-\alpha}{2} R_y(2) \right) + \alpha^2 (I)} \qquad (17)$$

$$I = R_y(0) - (\alpha - 1) R_y(1) + \frac{(\alpha-1)^2}{4} R_y(0),$$

The obtained model is called OPFLP-3 hereafter.

3. First-order OPFLP model with four samples memory:

$$\hat{y}(n) = a.h^{\alpha} y(n-1) - \alpha y(n-2) - \frac{a.h^{\alpha}.\alpha(1-\alpha)}{2} \left(y(n-3) + \frac{2-\alpha}{3} y(n-4) \right) \qquad (18)$$

By minimizing the mean squared of the prediction error, the optimal coefficient is obtained as follows:

$$a_{opt} = \arg\min_{a} \ J = E\left[e^2(n)\right] = h^{\alpha}.\frac{\left(R_y(1) - \alpha R_y(2) - \frac{\alpha(1-\alpha)}{2}(A) \right)}{\left(B + \frac{\alpha^2(\alpha-1)^2}{4} C + D \right)}$$

$$A = R_y(3) - \frac{\alpha-2}{3} R_y(4) \qquad (19)$$

$$B = R_y(0) - 2\alpha R_y(1) + \alpha^2 R_y(0)$$

$$C = R_y(0) - \frac{(2\alpha-4)}{3} R_y(1) + \frac{(\alpha-2)^2}{9} R_y(0)$$

$$D = \alpha(\alpha-1) R_y(2) - \alpha R_y(1) - (\alpha-1)$$

$$\times\alpha\big((\alpha-2) R_y(3) + \alpha(\alpha-2) R_y(4)\big)/3$$

It is called OPFLP-4 hereafter.

Considering (18), (20) and (22), if the fractional derivative order α tends to zero, in all three cases the coefficient a_{opt} becomes: $a_{opt} = \frac{R_y(1)}{R_y(0)}$ [14], [15], [16].

Therefore, it can be concluded that the OPFLP is the generalization of the classical first-order LP. In other words, the first-order LP is a special case of the first-order OPFLP model when the fractional derivative tends to zero [14], [15], [16].

III. Proposed Methods

In this section, we derive closed-form expressions for the optimal sampling frequency (F_{s-opt}) parameter across three OPFLP models $(m = 1, 2, 3)$. This provides valuable and comprehensive insights into the theoretical foundations of these models. Additionally, to delve into the practical implications, we introduce a signal model to investigate how real-world environmental interferences such as noise and reverberation influence the performance and robustness of OPFLP systems, offering insights into enhancing the robustness and efficacy of OPFLP techniques amidst real-world challenges.

While the work presented in [14] offers a valuable closed-form expression for the optimal coefficient, its approach to determining the differential order (α_{opt}) relies on a trial-and-error only in $0 \le \alpha \le 1$. This method, while effective, can be inefficient and lacks theoretical justification. Additionally, the authors rightfully acknowledge the significant impact of sampling frequency on model performance, but [14] does not provide a framework to determine a closed-form solution for the optimal sampling frequency.

Also [14] relies on a single frame of voiced speech, when applying OPFLP to speech. This leads to the results that may not adequately represent practical situations. In practical situations, the processed speech signal contains voiced, unvoiced, and silent segments, commonly contaminated by environmental interferences

In our work, we address these limitations by:

1- Deriving a closed-form expression for the optimal sampling frequency: This eliminates the need for arbitrary choices and provides a data-driven approach to setting this crucial parameter.
2- Determining the optimal derivative order in $0 \le \alpha \le 2$: It is crucial to note that the system behavior, concerning stability and robustness, differs considerably between the cases $0 \le \alpha \le 1$ and $1 < \alpha \le 2$.
3- Evaluating the model's performance and robustness against environmental interferences in diverse scenarios: We analyze the model's performance in noisy, reverberant, and combined noisy-reverberant environments.

By addressing these limitations, our approach offers a more robust and theoretically grounded framework for model development compared to the work presented in [14].

A. Optimal Sampling Frequency

By considering $h = 1/F_s$, the following three cases are respectively obtained from (14), (16) and (18):

1. First-order OPFLP model with two samples memory:

$$\hat{y}(n) = a.F_s^{\alpha}\left(y(n-1) - \alpha y(n-2)\right) \tag{20}$$

To obtain the optimal sampling frequency (F_{s-opt}), defining the prediction error as $e(n) = \hat{y}(n) - y(n)$ and minimizing the mean squared error criteria, we have:

$$F_{s-opt} = \underset{F_s}{\arg\min} \quad \text{J=E}\left[e^2(n)\right]$$

$$F_{s-opt} = e^{\frac{\ln\left(\frac{R_y(2)\alpha + R_y(1)}{a\left(R_y(0) + 2\alpha R_y(1) + \alpha^2 R_y(0)\right)}\right)}{\alpha}} \tag{21}$$

2. First-order OPFLP model with three samples memory:

$$\hat{y}(n) = a.F_s^{\alpha} y(n-1) - a.F_s^{\alpha}\left(\alpha y(n-2) + \frac{\alpha(1-\alpha)}{2} y(n-3)\right) \tag{22}$$

In this case, F_{s-opt} is determined by minimizing the mean squared prediction error:

$$F_{s-opt} = \underset{F_s}{\arg\min} \quad \text{J=E}\left[e^2(n)\right]$$

$$F_{s-opt} = \mathrm{e}^{\frac{\ln\left(\frac{2\left(\alpha^2 R_y(3) - 2R_y(2)\alpha - \alpha R_y(3) + 2R_y(1)\right)}{a(A+B)}\right)}{\alpha}}$$

$$A = R_y(0)\alpha^4 - 2R_y(0)\alpha^3 - 4R_y(1)\alpha^3 + 5R_y(0)\alpha^2 \tag{23}$$

$$B = 4R_y(1)\alpha^2 + 4R_y(2)\alpha^2 - 8R_y(1)\alpha - 4R_y(2)\alpha + 4R_y(0)$$

3. First-order OPFLP model with four samples memory:

$$\hat{y}(n) = a.F_s^{\alpha} y(n-1) - \alpha y(n-2) - \frac{a.F_s^{\alpha}.\alpha(1-\alpha)}{2}\left(y(n-3) + \frac{2-\alpha}{3} y(n-4)\right) \tag{24}$$

By minimizing the mean squared of the prediction error, the F_{s-opt} is obtained:

$$F_{s-opt} = \underset{F_s}{\arg\min} \quad \text{J=E}\left[e^2(n)\right]$$

$$F_{s-opt} = e^{\frac{\ln\left(\frac{6(A+B)}{a(C+D)}\right)}{\alpha}}$$

$$A = -\alpha^3 R_y(4) + 3\alpha^2 R_y(3) + 3\alpha^2 R_y(4)$$

$$B = -6\alpha R_y(2) - 3\alpha R_y(3) - 2\alpha R_y(4) + 6R_y(1)$$

$$\begin{aligned} C = {} & R_y(0)\alpha^6 - 6R_y(0)\alpha^5 - 6R_y(2)\alpha^5 \\ & +22R_y(0)\alpha^4 + 24R_y(1)\alpha^4 + 12R_y(2)\alpha^4 \\ & -30R_y(0)\alpha^3 - 66R_y(1)\alpha^3 - 36R_y(2)\alpha^3 \\ & -12R_y(3)\alpha^3 \end{aligned} \tag{25}$$

$$\begin{aligned} D = {} & 49R_y(0)\alpha^2 + 48R_y(1)\alpha^2 + 60R_y(2)\alpha^2 \\ & +36R_y(3)\alpha^2 - 72R_y(1)\alpha - 36R_y(2)\alpha \\ & -24R_y(3)\alpha + 36R_y(0) \end{aligned}$$

B. Signal model

In this study, it is assumed that the microphone receives the speech signal contaminated by noise and reverberation. So, the received microphone signal, $y(n)$, is expressed as follows:

$$y(n) = s(n) * h(n) + v(n) = x(n) + v(n) \tag{26}$$

where $h(n)$ is the impulse response between an unknown speech source and the microphone, $v(n)$ is an additive noise signal, and $*$ stands for linear convolution. The statistical characteristics of $x(n)$ and $v(n)$ are assumed to be real, broadband, and zero mean. The two signals are also considered to be statistically uncorrelated. Fig.1. shows an arbitrary room where we record the speech signal.

IV. Evaluations And Simulation Results

Our primary objective is to determine the optimal derivative order (α) for OPFLP considering variations in sampling frequency. Then, our investigation extends to the evaluation of OPFLP's effectiveness in hands-free speech signal acquisition.

In this regard, we introduce three performance measures, delving into their relevance to our study in subsection IV.A. Subsection IV.B focuses on the effect of sampling frequency on the optimal derivative order (α). We further explore the impact of environmental interferences, e.g. noise and reverberation, on OPFLP's robustness in subsection IV.C under three distinct scenarios: 1) reverberant environment, 2) Noisy environment, and 3) noisy and reverberant environment. To establish a comparative framework, we leverage the first- and second-order LPs [9] and CFDLP [12] as baseline methods, considering their established performance across diverse signal processing applications.

CFDLP is a novel approach built upon the conventional FDLP model, offering two key advantages: 1- Enhanced Interpretability by simplifying the interpretation of the complex cepstrum. It facilitates understanding complex cepstral components as temporal modulations within an all-pole model approximation of the signal's power spectrum. 2- Enhancing computational efficiency compared to conventional FDLP. This translates to faster processing times.

A. Performance Measures

Within signal prediction, the evaluation of prediction performance is fundamental, serving as a crucial measure of efficacy. One fundamental metric in this arena is Prediction Gain (PG), extensively utilized for analyzing prediction performance, particularly in relation to alterations in sampling frequency.

PG, measured in decibels (dB), quantifies the ratio between the variance of the input signal and the variance of the error [14], [15], [16]; i.e.:

$$PG[dB] = 10\log_{10}\left(\frac{\sigma_y^2}{\sigma_e^2}\right) \tag{27}$$

where σ_y^2 and σ_e^2 are the input signal variance and the error variance, respectively. Furthermore, our secondary focus lies in the comprehensive assessment of OPFLP performance within hands-free speech acquisition. Specifically, our scrutiny centers on the received speech quality, a key aspect of analysis.

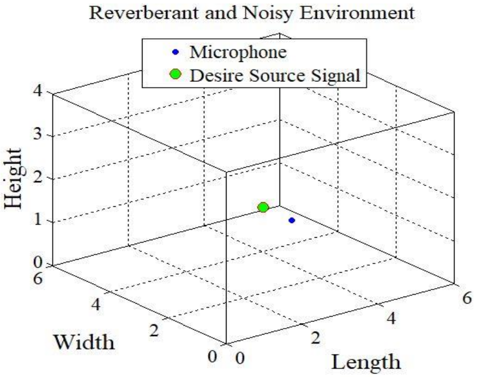

Fig.1: Simulated Environment

To gauge and quantify this aspect, we employ the Perceptual Evaluation of Speech Quality (PESQ), an esteemed measure parameter widely acknowledged within the field for its reliability and relevance in evaluating speech quality [24], and Signal To Noise power Ratio (SNR).

B. The Effect of Sampling Frequency

The influence of sampling frequency on linear prediction is fundamental in determining the accuracy and effectiveness of the signal prediction model. Sampling frequency directly affects the resolution and accuracy with which the signal is represented in the digital domain. Higher sampling frequencies capture more details of the original analog signal, allowing for better representation and potentially improving the accuracy of linear prediction models. However, excessively high sampling frequencies can lead to redundant information and increased computational complexity without significant gains in prediction accuracy. Conversely, lower sampling frequencies might result in a loss of crucial signal details, leading to reduced accuracy in prediction models. As per the Nyquist theorem, the sampling frequency must be at least twice the maximum frequency to avoid aliasing. However, beyond merely meeting this criterion, the specific relationship between the sampling frequency and the optimal α becomes critical in fractional linear prediction models. To comprehensively examine the impact of sampling frequency on OPFLP performance, we employ a sinusoidal signal $x(t) = A\sin(2\pi ft)$ characterized by frequency $f = 1Hz$ and amplitude $A = 1$. The sampling frequency is systematically varied from 2 to 70 times the maximum signal frequency to examine its influence on the optimum fractional derivative order. Notably, within the range of α spanning 0 to 2, the α value yielding the maximum PG is selected as the optimal parameter.

Fig. 2 shows the results obtained for the optimal α values.

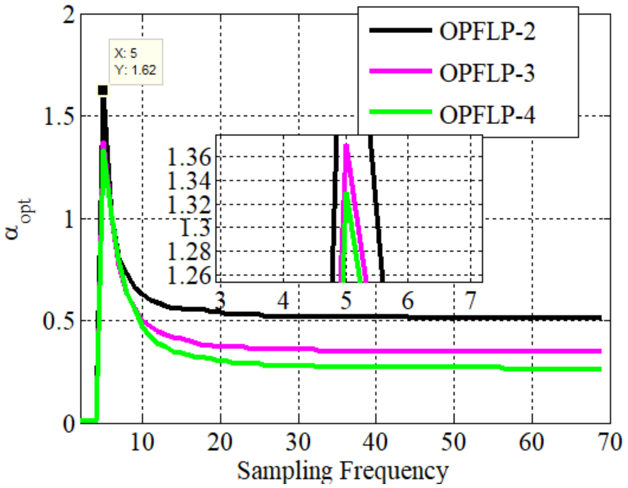

Fig. 2. the optimum derivative order of OPFLP in terms of sampling frequency changes

Remarkably, across all three scenarios, employing OPFLP with memory settings of 2, 3, and 4 at sampling frequencies of 2, 3, and 4 times the maximum signal frequency consistently yields $\alpha_{opt} = 0$. However, when the sampling frequency escalates to 5 and 6 times the maximum signal frequency, the α_{opt} resides within $1 < \alpha \le 2$. Intriguingly, as the sampling frequency surpasses 7 times the maximum signal frequency, the α_{opt} shifts within the $0 \le \alpha \le 1$. Figs. 3 and 4 further elucidate the dynamics, showcasing the impact of α variations on PG at sampling frequencies 5 and 40 times greater than the maximum signal frequency, respectively.

Further analysis reveals important insights. For instance, at a memory setting of 2, α_{opt} at 5 times the frequency settles at 1.6, while at 40 times, it reduces to 0.51. These findings, spanning Figs. 2 to 4, unequivocally highlight the substantial influence of sampling frequency on the performance dynamics of OPFLP.

This sensitivity to sampling frequency highlights the intricate relationship between the sampling rate and the selection of the fractional derivative order, emphasizing the need for meticulous consideration and adjustment of sampling parameters to optimize the performance of fractional linear prediction techniques.

C. Performance and Robustness in Challenging Environmental Conditions

Here, we evaluate and compare the performance and robustness of the OPFLP with the first-, second-order LP, and CFDLP in a simulated noisy and reverberant environment of size $6m \times 6m \times 4m$ (length × width × height). The source-microphone distance is $1m$.

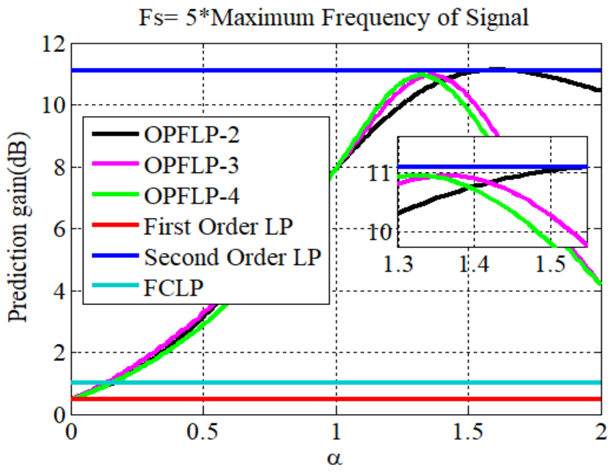

Fig. 3. PG in term of α changes and $F_s = 5\times$ maximum frequency

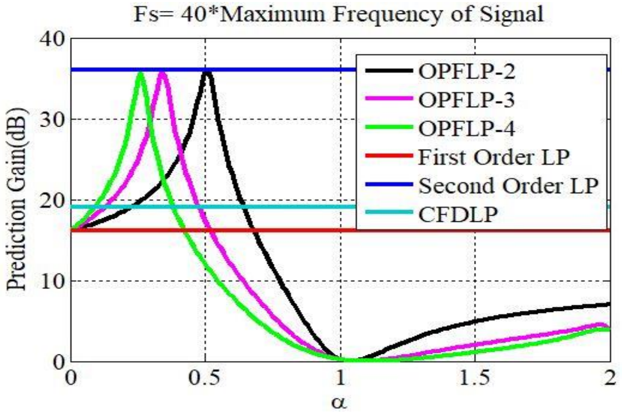

Fig. 4. PG in term of α changes and $F_s = 40\times$ maximum frequency

The room impulse response is computed using an effective implementation of the Image method [25]. At the sampling frequency of 16 kHz, the length of room impulse response is set to 4096 samples.

The performance and robustness of the OPFLP are examined in the following three scenarios of the presence of noise and reverberation:

Scenario 1: Reverberant environment

Scenario 2: Noisy environment

Scenario 3: Noisy and reverberant environment

The additive noise contains a mixture of spatially white noise and spherically isotropic (diffuse) noise generated using the method explained in [26]. Experiments are performed on speech signals from the TIMIT dataset [27] including 700 sentences uttered by 26 female and 44 male speakers in 8 different dialects of the American English language. The processing was performed at $16kHz$ sampling frequency on $30ms$ frames of the speech signal. These conditions are called Common Conditions (CC) in the rest of this paper.

Scenario 1:

To evaluate the performance in the presence of reverberation, the OPFLP models are compared to the first-, second-order LPs, and CFDLP at CC at three reverberation times $RT_{60} = 150ms$ (low reverberation), $RT_{60} = 350ms$ (moderate reverberation), and $RT_{60} = 700ms$ (high reverberation). The results of this experiment are presented in Tables 1 and 2 in terms of PG and PESQ, respectively.

Table 1 shows the PG for different models. Comparing the performance of the OPFLP at different reverberation times, it is observed that the prediction performance decreases as the reverberation time increases. For example, the OPFLP-2 can obtain $PG = 9.74dB$ in $RT_{60} = 150ms$ and when the reverberation is increased ($RT_{60} = 700ms$) in the environment, its performance decreases to $PG = 7.12dB$. Therefore $\Delta PG = 9.74 - 7.12 = 2.62dB$ which shows the influence of the reverberation on the performance.

On the other hand, the performance of the OPFLP-2 is better than the OPFLP-3 and OPFLP-4; however, the rate of performance decay of the OPFLP-4 is less than OPFLP-2 and OPFLP-3. Thus, the robustness of OPFLP-4 is higher than the other fractional models. The last column of Table 1 shows the difference in prediction gain (ΔPG) between the cases of low and high reverberation times as the PG loss. Comparing the PG loss of each model, it can be seen that the PG loss of OPFLPs is higher than the first-order LP and CFDLP models, but lower than the second-order LP. In other words, it can be argued that in the presence of the reverberation, the robustness of the OPFLP is lower than the first-order LP and CFDLP, but it is higher than the second-order LP.

Table 2 presents the quality of the estimated speech by the OPFLP and the baseline methods. Comparing the first three columns of Table 2, it is observed that speech quality decreases when reverberation time increases. As can be seen in the fourth column, the robustness of the OPFLP-4 is higher than those with two and three memories. Although the yield loss of the OPFLP is higher than first-order LP and CFDLP, it has been less affected than second-order LP by the reverberation.

The results in this table are verified the result of Table 1. Thus, we can conclude that the robustness of OPFLP is higher than the second LP model in reverberant environments.

Scenario 2:

In this scenario, the performance of the OPFLP is evaluated in a noisy environment. We consider the CC along with three simulated noisy environments at signal-to-noise ratios (SNRs) $5dB$, $15dB$, and $30dB$. These SNR values represent high, medium, and low levels of noise in the environment, respectively. According to the results shown in Tables 3 and 4, similar to the previous scenario, the performance of OPFLP decreases by reducing SNR. In other words, the higher the noise level in the environment, the lower the performance.

According to the ΔPG , the OPFLP is more robust to noise than the second-order LP, although its robustness is less than the first-order LP and CFDLP. Comparing the results obtained in the first and second scenarios, it can be concluded that the effect of the noise on the OPFLP performance is more severe than the reverberation.

TABLE 1
PG IN REVERBERANT ENVIRONMENT

Reverberation time / **model**	$RT_{60} =$ 150ms	$RT_{60} =$ 350ms	$RT_{60} =$ 700ms	ΔPG
First Order LP	7.36	6.72	5.63	**1.73**
Second Order LP	10.34	9.40	7.71	**2.63**
CFDLP [12]	8.06	7.34	6.07	**1.99**
OPFLP-2	9.74	8.86	7.12	**2.62**
OPFLP-3	9.54	8.64	6.94	**2.60**
OPFLP-4	9.52	8.59	6.94	**2.58**

TABLE 2
PESQ IN REVERBERANT ENVIRONMENT

Reverberation time / **model**	$RT_{60} =$ 150ms	$RT_{60} =$ 350ms	$RT_{60} =$ 700ms	$\Delta PESQ$
First Order LP	3.33	2.29	1.80	**1.53**
Second Order LP	3.70	2.26	1.81	**1.89**
CFDLP [12]	3.41	2.26	1.78	**1.63**
OPFLP-2	3.48	2.19	1.78	**1.7**
OPFLP-3	3.43	2.20	1.76	**1.67**
OPFLP-4	3.40	2.20	1.75	**1.65**

Scenario 3:

Finally, the simulation conditions are considered similar to real-life environments, where the noise and the reverberation exist simultaneously. The results of this experiment are shown in Tables 5 and 6 in terms of the PG and the PESQ, respectively. These results show that the first-order LP and CFDLP are more robust to the environmental interferences rather than the OPFLP; but the OPFLP shows higher robustness compared to the second-order LP. For example, the proposed OPFLP methods (OPFLP-2, OPFLP-3, and OPFLP-4) exhibit a pronounced sensitivity to noise and reverberation. Their performance degradation, ranging from 1.68 to 1.74 units, is significantly lower in low noise and reverberation situations compared to high noisy and reverberant ones.

TABLE 3
PG IN NOISY ENVIRONMENT

Signal-to-Noise Ratio **model**	$SNR = 30dB$	$SNR = 15dB$	$SNR = 5dB$	ΔPG
First Order LP	6.78	6.72	1.88	**4.90**
Second Order LP	9.17	9.40	2.09	**7.08**
CFDLP [12]	8.15	7.47	1.47	**6.68**
OPFLP-2	8.22	8.86	1.20	**7.02**
OPFLP-3	8.38	8.64	1.39	**6.99**
OPFLP-4	8.44	8.59	1.54	**6.90**

TABLE 4
PESQ IN NOISY ENVIRONMENT

Signal-to-Noise Ratio **model**	$SNR = 30dB$	$SNR = 15dB$	$SNR = 5dB$	$\Delta PESQ$
First Order LP	3.16	2.44	1.66	**1.50**
Second Order LP	3.48	2.66	1.78	**1.70**
CFDLP [12]	3.19	2.41	1.66	**1.53**
OPFLP-2	3.25	2.43	1.72	**1.53**
OPFLP-3	3.21	2.41	1.66	**1.55**
OPFLP-4	3.19	2.40	1.63	**1.56**

TABLE 5
PG IN A NOISY AND REVERBERANT ENVIRONMENT

Signal to Noise Ratio, Reverberation time **model**	$SNR = 30dB$ $RT_{60} = 150ms$	$SNR = 15dB,$ $RT_{60} = 350ms$	$SNR = 5dB,$ $RT_{60} = 700ms$	ΔPG
First Order LP	6.74	4.44	1.65	**5.09**
Second Order LP	6.11	5.02	1.83	**4.28**
CFDLP [12]	6.59	4.80	1.56	**5.03**
OPFLP-2	8.35	3.99	1.07	**7.28**
OPFLP-3	8.33	4.29	1.23	**7.10**
OPFLP-4	8.39	4.51	1.37	**7.02**

TABLE 6
PESQ IN NOISY AND REVERBERANT ENVIRONMENT

Signal to Noise Ratio, Reverberation time **model**	$SNR = 30dB,$ $RT_{60} = 150ms$	$SNR = 15dB,$ $RT_{60} = 350ms$	$SNR = 5dB,$ $RT_{60} = 700ms$	$\Delta PESQ$
First Order LP	3.16	2.08	1.49	**1.67**
Second Order LP	3.52	2.13	1.51	**2.01**
CFDLP [12]	3.21	2.09	1.51	**1.70**
OPFLP-2	3.22	2.03	1.48	**1.74**
OPFLP-3	3.18	2.01	1.47	**1.71**
OPFLP-4	3.16	2.01	1.48	**1.68**

In contrast, the second-order LP method suffers from a more substantial performance drop of approximately 2.01 units, highlighting the potential advantage of the OPFLP methods in terms of noise and reverberation robustness. The results of this scenario confirm the outcomes of the previous ones which indicate that if the environmental interferences increase, the OPFLP performance is reduced. Finally, it should be noted that although the second-order LP outperforms the OPFLP, it is less robust to environmental interferences.

Furthermore, the OPFLP requires one parameter to estimate the signal which is very attractive speech coding applications, while the second-order LP requires two parameters.

V. Conclusions

In this paper, the closed-form of optimum sampling frequency was obtained for the One Parameter Fractional Order Linear Prediction (OPFLP). Then, the performance and robustness of the predictor were investigated in the range of $0 \le \alpha \le 2$. Our investigation meticulously probes the optimal α within $0 \le \alpha \le 1$ and $1 < \alpha \le 2$, considering fundamental parameters like sampling frequency and environmental interferences.

Simulation results underscore the intrinsic relationship between sampling frequency and the choice of α for optimal OPFLP performance. Notably, when the sampling rate aligns within five to six times the maximum signal frequency, the optimal α range settles within $1 < \alpha \le 2$. Conversely, exceeding a sixfold sampling frequency compared to the signal's maximum frequency shifts the optimal α to $0 \le \alpha \le 1$. Furthermore, in exploring OPFLP's resilience in challenging signal processing tasks, particularly in hands-free speech acquisition applications, our investigations highlight its superior robustness compared to second-order LP in handling environmental interferences. Notably, noise exerts a more pronounced detrimental impact on OPFLP performance than reverberation, illuminating the nuanced effects of these interferences on the model's efficacy. These observations underscore the criticality of considering sampling frequency and environmental interferences in optimizing OPFLP performance. Additionally, the discernment between the impacts of noise and reverberation on OPFLP performance is essential for enhancing its efficacy in practical applications.

REFERENCES

[1] D. Baleanu and A. M. Lopes, *Handbook of Fractional Calculus with Applications*. De Gruyter, 2019.

[2] D. Baleanu, Z. B. Güvenç, J. A. T. Machado, and others, *New trends in nanotechnology and fractional calculus applications*. Springer, 2010.

[3] S. Das and I. Pan, *Fractional order signal processing: introductory concepts and applications*. Springer Science & Business Media, 2011.

[4] H. Sheng, Y. Chen, and T. Qiu, *Fractional processes and fractional-order signal processing: techniques and applications.* Springer Science & Business Media, 2011.

[5] E. Abbaszadeh-Soorami and M. Haddad-Zarif, “Fractional-Order Variable Structure Equations In Robust Control,” Authorea Prepr., 2023.

[6] M. Ghamgosar, S. M. Mirhosseini-Alizamini, and M. Dadkhah, “Design of optimal sliding mode control based on linear matrix inequality for fractional time-varying delay systems,” Int. J. Ind. Electron. Control Optim., vol. 5, no. 4, pp. 317–325, 2022.

[7] Y.-N. Li, H.-R. Sun, and Z. Feng, “Fractional abstract Cauchy problem with order α in (1, 2),” Dyn. Partial Differ. Equations, vol. 13, no. 2, pp. 155–177, 2016.

[8] C. Li and M. Li, “Hölder regularity for abstract fractional Cauchy problems with order in (0, 1),” J. Appl. Math. Phys, vol. 6, pp. 310–319, 2018.

[9] J. D. Markel and A. H. J. Gray, *Linear prediction of speech*, vol. 12. Springer Science & Business Media, 2013.

[10] H. Yang, Y. Ye, D. Wang, and B. Jiang, “A novel fractional-order signal processing based edge detection method,” in 11th International Conference on Control Automation Robotics & Vision, 2010, pp. 1122–1127.

[11] M. Athineos and D. P. W. Ellis, “Frequency-domain linear prediction for temporal features,” in IEEE Workshop on Automatic Speech Recognition and Understanding (IEEE Cat. No. 03EX721), 2003, pp. 261–266.

[12] S. Sadhu and H. Hermansky, “Complex Frequency Domain Linear Prediction: A Tool to Compute Modulation Spectrum of Speech,” arXiv Prepr. arXiv2203.13216, 2022.

[13] B. Jo and S. Beack, “Representations of the complex-valued frequency-domain LPC for audio coding,” IEEE Signal Process. Lett., 2024.

[14] V. Despotovic, T. Skovranek, and Z. Peric, “One-parameter fractional linear prediction,” Comput. & Electr. Eng., vol. 69, pp. 158–170, 2018.

[15] T. Skovranek and V. Despotovic, “Audio signal processing using fractional linear prediction,” Mathematics, vol. 7, no. 7, p. 580, 2019.

[16] T. Skovranek, V. Despotovic, and Z. Peric, “Optimal fractional linear prediction with restricted memory,” IEEE Signal Process. Lett., vol. 26, no. 5, pp. 760–764, 2019.

[17] K. Xu and X. Song, “A Current Noise Cancellation Method Based on Fractional Linear Prediction for Bearing Fault Detection,” Sensors, vol. 24, no. 1, p. 52, 2023.

[18] A. A. Navish, M. Priya, and R. Uthayakumar, “A comparative study on estimation of fractal dimension of EMG signal using SWT and FLP,” Comput. Methods Biomech. Biomed. Eng. Imaging ¥& Vis., vol. 11, no. 3, pp. 586–597, 2023.

[19] E. A. P. Habets and J. Benesty, “A two-stage beamforming approach for noise reduction and dereverberation,” IEEE Trans. Audio. Speech. Lang. Process, vol. 21, no. 5, pp. 945–958, 2013.

[20] V. W. Neo, C. Evers, and P. A. Naylor, “Enhancement of noisy reverberant speech using polynomial matrix eigenvalue decomposition,” IEEE/ACM Trans. Audio, Speech, Lang. Process., vol. 29, pp. 3255–3266, 2021.

[21] N. Yazdi and K. Todros, “Measure-transformed MVDR beamforming,” IEEE Signal Process. Lett., vol. 27, pp. 1959–1963, 2020.

[22] S. Zhang and X. Li, “Microphone array generalization for multichannel narrowband deep speech enhancement,” arXiv Prepr. arXiv2107.12601, 2021.

[23] J. Benesty, J. Chen, and E. A. P. Habets, *Speech enhancement in the STFT domain.* Springer Science & Business Media, 2011.

[24] A. W. Rix, J. G. Beerends, M. P. Hollier, and A. P. Hekstra, “Perceptual evaluation of speech quality (PESQ)-a new method for speech quality assessment of telephone networks and codecs,” in Proc. IEEE Int. Conf. Acoust., Speech Signal Process. (ICASSP),, 200, vol. 2, pp. 749–752, May 2001.

[25] J. B. Allen and D. A. Berkley, “Image method for efficiently simulating small-room acoustics,” J. Acoust. Soc. Am., vol. 65, no. 4, pp. 943–950, 1979.

[26] E. A. P. Habets, I. Cohen, and S. Gannot, “Generating nonstationary multisensor signals under a spatial coherence constraint,” J. Acoust. Soc. Am., vol. 124, no. 5, pp. 2911–2917, 2008.

[27] J. S. Garofolo, L. F. Lamel, W. M. Fisher, J. G. Fiscus, D. S. Pallet, and N. L. Dahlgren, “TIMIT Acoustic Phonetic Continuous Speech Corpus,” Linguist. Data Consortium, 1993, Accessed: May 24, 2019. [Online].Available:http://ci.nii.ac.jp/naid/20000921365/en/.

Seyed Mostafa Alaviyan Shahri received the B.Sc. degree in Telecommunication Engineering from Birjand University and the M.Sc. degree in Communication System Engineering from Yazd University, Yazd, Iran, in 2012 and 2015, respectively. He is currently Ph.D candidate at Yazd University, Yazd, Iran. His research interests include speech processing, fractional calculus, and Artificial intelligence. Email: mostafa.alavian@yahoo.com.

Hamid Reza Abutalebi received the B.Sc. and M.Sc. degrees from Sharif University of Technology, Tehran, Iran in 1996 and 1998, respectively, and the Ph.D. degree from Amirkabir University of Technology, Tehran, Iran in 2003, all in electrical engineering (signal processing). Also, he was with University of Waterloo, Ontario, Canada as a visiting scholar during Mar. 2002 to Feb. 2003. Since 2003, Dr. Abutalebi has been with Electrical Engineering Department of Yazd University, Yazd, Iran, where he is now a full professor. During fall 2010 to summer 2011, he was on sabbatical at Idiap Research Institute, Martigny, Switzerland. His research interests are microphone arrays, speech enhancement, sound source localization, and time-frequency analysis.

IECO International Journal Of Industrial Electronics Control and Optimization
Print ISSN: 3517-2645
Online ISSN: 3568-2645
Homepage: https://ieco.usb.ac.ir/

Improving the MPC Performance of the Model in Order to Improve the Frequency Stability of the Two-Area Microgrid

Farhad Amiri[1] | Mohammad Hassan Moradi[2]

Department of Electrical Engineering, Faculty of Engineering, Bu-Ali Sina University.[1, 2]
Corresponding author's email: mhmoradi@basu.ac.ir

Article Info

Article type:
Research Article

Article history:
Received: 11-December-2023
Received in revised form:
12-March-2024
Accepted: 23-April-2024
Published online: 22-Sep-2024

Keywords
Less complexity,
Social Spider Optimization,
Model Predictive Control,
Craziness-based Particle Swarm Optimization.

ABSTRACT

In the context of frequency stability in a two-area microgrid, it is crucial to address the fluctuations in frequency caused by load disturbances. To achieve this, an effective load-frequency control (LFC) system, which serves as the secondary control, must be implemented. However, the presence of renewable energy sources such as wind turbines and photovoltaic systems adds complexity to the operation of the LFC system due to their inherent uncertainty. To enhance the performance of the LFC system in the two-area microgrid, this paper proposes a reduction in the number of controllers employed, aiming for a less complex structure. Specifically, Model Predictive Control (MPC) is utilized for LFC, and the weight parameters of the MPC controller are determined using Craziness-based Particle Swarm Optimization (CRPSO). The proposed method is compared with alternative approaches, including PID controller optimized with Social Spider Optimization (SSO), Fractional Order Fuzzy PI (FOFPI), and conventional MPC. The effectiveness of the proposed method is evaluated in various scenarios, considering load variations and the presence of distributed microgrid generation resources. The results demonstrate that the proposed method outperforms the other controllers in terms of speed of response, reduction of overshoot and undershoot, and overall complexity. Importantly, the proposed method significantly improves the frequency stability of the two-area microgrid. The simulation and analysis are conducted using MATLAB software, providing a comprehensive understanding of the system dynamics and the performance of the proposed controller.

I. Introduction

The increasing adoption of renewable energy sources in the electricity industry has led to a rise in the deployment of microgrids, which are small power networks operating at medium voltage levels. These microgrids incorporate a combination of renewable energy sources, traditional energy sources, energy storage systems, and localized loads [1]. Microgrids can operate in either grid-connected or islanded mode, providing flexibility and resilience to the power system. Additionally, interconnections between microgrids in a geographical area enable the formation of multi-area microgrids, such as the two-area microgrid configuration. One of the challenges associated with integrating renewable energy sources into microgrids is their inherent variability due to the unpredictable nature of wind and solar radiation. Fluctuations in the power output of renewable sources, coupled with changes in load demand, can lead to imbalances and significant deviations in the microgrid frequency when operating in islanded mode [2]. To address this issue, Load-Frequency Control (LFC) strategies are employed to mitigate power and frequency fluctuations, restore the frequency to its nominal value, and maintain power exchange between interconnected microgrids [1-3].

Publisher: University of Sistan and Baluchestan

Wind turbines and photovoltaic systems are significant contributors to distributed production within microgrids. While these renewable energy sources offer numerous advantages, they also present challenges for microgrid control [4]. The variable nature of power production from wind turbines and photovoltaic systems introduces fluctuations in the microgrid's overall power supply. These fluctuations, combined with load disturbances, can disrupt the balance within the islanded microgrid, resulting in substantial frequency deviations [2].

To address these challenges, Load-Frequency Control (LFC) strategies are utilized. These strategies aim to mitigate power and frequency fluctuations, restore the frequency to its nominal value, and maintain power flow across communication lines within the microgrid [1-3]. The frequency control strategy in an islanded microgrid typically employs two control loops: the primary control loop and the secondary control loop. The primary control loop plays a crucial role in limiting frequency deviations following a disturbance. However, it is unable to restore the frequency to its nominal value. Hence, a secondary control loop, known as secondary frequency control, is employed to restore the frequency to its desired set point [4-6]. While the primary control loop is typically implemented on the diesel generator, the secondary control loop requires different controllers to manage the LFC system. The performance of the controllers used within the secondary control loop is of utmost importance to ensure effective frequency control in the microgrid [4-6]. These controllers are responsible for regulating power generation or consumption within the microgrid, enabling the restoration of frequency to its nominal value. The selection and design of appropriate controllers are critical factors in achieving accurate and efficient frequency regulation.

Extensive research has been done in connection with LFC in microgrids. LFC methods in microgrids can be divided into two general categories. 1) Islanded microgrid [7-27]. Two-area microgrid [28-30].

Several controllers such as conventional PI [7, 8], conventional PID [9], PID based on coefficient determination by Ziegler-Nichols method [10], PID based on GA [11], PI based on PSO [12] PID based on BIO [13], PI/PID based on QOH [14], PID based on fractional order [15], fuzzy-PID based on fractional order [16], PI based on type 2-fuzzy logic in combination with improved HSA [17, 18], fuzzy-PID based on PSO [19], PID based on HBEL [20] for LFC Presented in microgrids. PID controller is a common controller in LFC systems related to microgrids. However, this controller also has problems, such as that it does not perform well against the disturbances on the microgrid, and it does not have the ability to weaken these disturbances, and it also does not perform well against the uncertainty of the parameters related to the islanded microgrid.

The robust controller based on the H_∞ has been used to control the LFC related to the microgrid [21-23]. One of the main problems of the robust controller (H_∞) in the LFC system is that it requires accurate information about the disturbances and uncertainty of the system parameters, which greatly increases the complexity of the design of this controller.

In [24], the self-adjusting order fuzzy controller has been used to control the load frequency related to the islanded microgrid. In [25], coordinated control of electric vehicles and renewable energy sources is used for frequency control in microgrids. In [26, 27], a robust control method has been presented to improve frequency stability in the power system with the presence of a wind turbine. The presence of the wind turbine causes more uncertainty and disturbance in the power system and ultimately complicates the load-frequency control problem.

The issue of LFC in a two-area microgrid is of significant importance. The LFC system not only focuses on regulating the frequency within each microgrid but also plays a crucial role in controlling the power fluctuations between the interconnected microgrids [28-30].

In [28], the effect of time delay of telecommunication systems on the stability of LFC in a system consisting of a two-area microgrid has been investigated. The presence of time delay will cause problems in the LFC function and endanger the frequency stability of the two-area microgrid. In [29], a tertiary monitoring control strategy for LFC in a two-area microgrid is presented. In [30], the LFC in a two-area microgrid with the PID method optimized with SSO is presented.

In the existing methods [7-30], energy storage sources are often treated as uncontrollable sources, or separate controllers are employed to manage energy storage devices such as batteries, flywheels, and superconducting storage systems. These approaches introduce additional complexity by increasing the number of microgrid controllers. Moreover, when it comes to Load-Frequency Control (LFC) in a two-area microgrid, these methods exhibit limitations in effectively addressing system disturbances and uncertainties in system parameters. Consequently, there is a pressing need for a suitable control method that can robustly handle such issues. MPC is a widely utilized controller in the industry that offers promising solutions. Unlike conventional methods, MPC demonstrates resilience in the face of system disturbances and uncertainties in parameters. This control methodology incorporates the ability to predict future events, enabling proactive decision-making and response. By leveraging predictive capabilities, MPC can anticipate changes in power generation, load demand, and other system dynamics, thereby facilitating effective frequency regulation and power balance in the microgrid.

One of the most important factors related to the MPC of the model is the weight parameters, whose optimal setting makes the MPC play an effective role against the disturbances and uncertainty of the two-area microgrid parameters.

Therefore, in this paper, the CRPSO has been used to adjust the weight parameters of the MPC in the two-area microgrid. CRPSO has many advantages over other optimization algorithms, including [31-34]:

The (CRPSO) algorithm offers several advantages over other optimization algorithms:

- Enhanced Exploration: CRPSO introduces a higher level of randomness and exploration compared to other algorithms. This allows CRPSO to effectively explore a larger search space, potentially discovering better solutions that may be missed by other algorithms that rely on more deterministic search strategies.
- Population-Based Approach: CRPSO operates on a population of particles that communicate and cooperate with each other. This population-based approach enables information sharing and collective intelligence, leading to faster convergence and improved global search capabilities.
- Flexibility and Adaptability: CRPSO is highly flexible and adaptable to different problem domains. It can handle both continuous and discrete optimization problems, making it applicable to a wide range of real-world scenarios. Additionally, CRPSO can easily incorporate problem-specific constraints and objectives, making it a versatile algorithm for various optimization tasks.
- Efficient Convergence: CRPSO tends to converge to optimal or near-optimal solutions relatively quickly. The collective learning and sharing of information among particles allow the algorithm to exploit promising regions of the search space efficiently, leading to faster convergence and better overall performance.
- Easy Implementation and Parameter Tuning: CRPSO is relatively easy to implement and does not require
- complex operators or encoding schemes. It has a small number of intuitive parameters that can be tuned to adapt to specific problem characteristics, making it accessible to both researchers and practitioners.

It's important to note that the effectiveness of CRPSO, like any optimization algorithm, can vary depending on the problem being addressed. Therefore, it is essential to carefully analyze the problem requirements and consider the specific characteristics and limitations of CRPSO before applying it. In general, the innovations of this paper include the following sections:

1) Reduction of controllers used for energy storage systems such as batteries, flywheels and SMES (less complexity).

2) LFC in two-area microgrid based on MPC.

3) Improving the performance and adjusting the weight parameters related to the MPC against disturbances and uncertainty related to the two-area microgrid parameters using the CRPSO.

4) Testing the performance of the proposed algorithm compared to GA and PSO algorithms in optimizing the weight parameters of the MPC considering the ITAE objective function.

5) Performance testing of the proposed controller (MPC(CRPSO)) in order to improve the performance of LFC against disturbances and uncertainty of the parameters related to the two-area microgrid.

The paper consists of several sections. In the second part, the model and components of the studied two-area microgrids have been discussed, in the third part, the state space equations of the two-area microgrid have been discussed, in the fourth part, the design of the proposed controller for the two-area microgrid has been discussed, and in the fifth part, the simulation has been described. And the results.

II. The model and components of the studied two-area microgrid:

A. Two-area microgrid model

Fig. 1 illustrates the block diagram of a two-area microgrid, where the microgrid of the first area is connected to the microgrid of the second area through a communication line. The microgrid of the first area comprises a WTG, a DEG_1, and SMES system. On the other hand, the microgrid of the second area consists of a DEG_2, PV panels, and BESS. The primary source of power supply in the microgrid is the wind turbines, which are operated at their MPPT to maximize energy extraction. However, due to the variable nature of wind power output, the DEG_1 serves as a backup power source to meet load demand during periods of low wind power generation. The DEG1 dynamically adjusts its power output to respond to changes in load requirements [28-30].

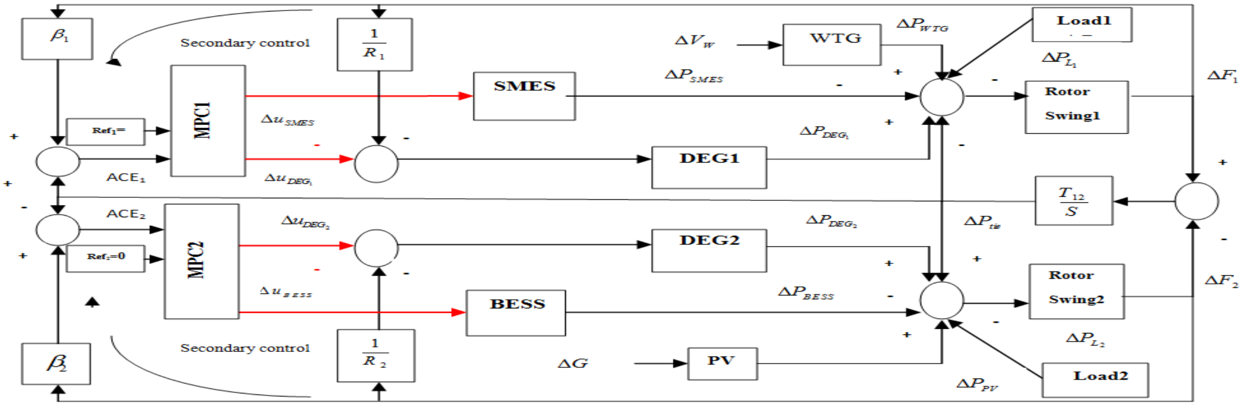

Fig. 1. The block diagram of the two-area microgrid [25, 27]

III. The state-space equations of the two-area microgrid

A. *The state space equations related to the microgrid of the first region*

Due to the fact that the components of the microgrid are different in each region, therefore, each MPC has different state-space equations in each region. Therefore, the state-space equation of the microgrid of the first region are according to Equation (1).

$$\begin{bmatrix} \dot{\Delta F_1} \\ \dot{\Delta P_{DEG1}} \\ \dot{\Delta X_{g1}} \\ \dot{\Delta P_{SMES}} \\ \dot{\Delta P_{tie}} \end{bmatrix} = \begin{bmatrix} \frac{-1}{T_{P1}} & \frac{k_{P1}}{T_{P1}} & 0 & -\frac{k_{P1}}{T_{P1}} & -\frac{k_{P1}}{T_{P1}} \\ 0 & \frac{-1}{T_{E1}} & \frac{k_{E1}}{T_{E1}} & 0 & 0 \\ \frac{-1}{R_1 T_{V1}} & 0 & \frac{-1}{T_{V1}} & 0 & 0 \\ 0 & 0 & 0 & \frac{-1}{T_L} & 0 \\ T_{12} & 0 & 0 & 0 & 0 \end{bmatrix} \begin{bmatrix} \Delta F_1 \\ \Delta P_{DEG1} \\ \Delta X_{g1} \\ \Delta P_{SMES} \\ \Delta P_{tie} \end{bmatrix} + \begin{bmatrix} 0 & 0 \\ 0 & 0 \\ \frac{-1}{T_{V1}} & 0 \\ 0 & \frac{k_L}{T_L} \\ 0 & 0 \end{bmatrix} \begin{bmatrix} \Delta u_{DEG1} \\ \Delta u_{SMES} \end{bmatrix} + \begin{bmatrix} -\frac{k_{P1}}{T_{P1}} & \frac{k_{P1}}{T_{P1}} & 0 \\ 0 & 0 & 0 \\ 0 & 0 & 0 \\ 0 & 0 & 0 \\ 0 & 0 & -T_{12} \end{bmatrix} \begin{bmatrix} \Delta P_{L1} \\ \Delta P_{WTG} \\ \Delta F_2 \end{bmatrix} \quad (1)$$

$$y = ACE_1 = \begin{bmatrix} B_1 & 0 & 0 & 0 & 1 \end{bmatrix} \begin{bmatrix} \Delta F_1 \\ \Delta P_{deg1} \\ \Delta X_{g1} \\ \Delta P_{SMES} \\ \Delta P_{tie} \end{bmatrix}$$

B. *The state space equations related to the microgrid of the second region*

Based on Fig. 1, the state-space equation related to the microgrid of the second region have been obtained according to Equation (2).

$$\begin{bmatrix} \dot{\Delta F_2} \\ \dot{\Delta P_{DEG2}} \\ \dot{\Delta X_{g2}} \\ \dot{\Delta P_{BESS}} \\ \dot{\Delta P_{tie}} \end{bmatrix} = \begin{bmatrix} \frac{-1}{T_{P2}} & \frac{k_{P2}}{T_{P2}} & 0 & -\frac{k_{P2}}{T_{P2}} & \frac{k_{P2}}{T_{P2}} \\ 0 & \frac{-1}{T_{E2}} & \frac{k_{E2}}{T_{E2}} & 0 & 0 \\ \frac{-1}{R_2 T_{V2}} & 0 & \frac{-1}{T_{V2}} & 0 & 0 \\ 0 & 0 & 0 & \frac{-1}{T_B} & 0 \\ -T_{12} & 0 & 0 & 0 & 0 \end{bmatrix} \begin{bmatrix} \Delta F_2 \\ \Delta P_{DEG2} \\ \Delta X_{g2} \\ \Delta P_{BESS} \\ \Delta P_{tie} \end{bmatrix} + \begin{bmatrix} 0 & 0 \\ 0 & 0 \\ \frac{-1}{T_{V2}} & 0 \\ 0 & \frac{k_{BESS}}{T_{BESS}} \\ 0 & 0 \end{bmatrix} \begin{bmatrix} \Delta u_{DEG2} \\ \Delta u_{BESS} \end{bmatrix} + \begin{bmatrix} -\frac{k_{P2}}{T_{P2}} & \frac{k_{P2}}{T_{P2}} & 0 \\ 0 & 0 & 0 \\ 0 & 0 & 0 \\ 0 & 0 & 0 \\ 0 & 0 & -T_{12} \end{bmatrix} \begin{bmatrix} \Delta P_{L2} \\ \Delta P_{PV} \\ \Delta F_1 \end{bmatrix} \quad (2)$$

$$y = \begin{bmatrix} B_2 & 0 & 0 & 0 & -1 \end{bmatrix} \begin{bmatrix} \Delta F_2 \\ \Delta P_{deg2} \\ \Delta X_{g2} \\ \Delta P_{BESS} \\ \Delta P_{tie} \end{bmatrix}$$

IV. Designing a proposed controller for a two-area microgrid:

A. *MPC*

The utilization of MPC has been observed across a wide range of industries, including the chemical processes, oil sector, and electromechanical systems. Fig. 2 illustrates the overall configuration of the MPC controller. As per the diagram, the MPC controller makes use of a system model to forecast and regulate its forthcoming behavior. Within this controller, the generation of a control signal is achieved by minimizing a cost function. The horizon's control signal values are determined to ensure that the system's future output aligns with the specified reference path. To accomplish this objective, the cost function is minimized, typically by considering the squared difference between the controlled variables and their desired values, along with the sum of the squared control signals.

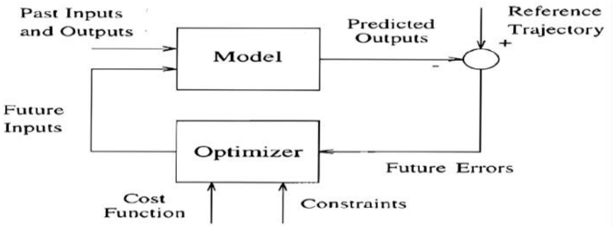

Fig. 2. Overall structure of the MPC

The cost function, represented by Equation (3), along with the constraints on the control signals (Equation (4)) and output signals (Equation (5)) are presented to manage and regulate the system.

$$J(N_1, N_2, N_u) = \min \sum_{j=N_1}^{N_2} ([y(k+j) - r(k+j)]^T W_y [y(k+j) - r(k+j)]) + \sum_{0}^{N_u} ([u(k) - u(k-1)]^T W_u [u(k) - u(k-1)]) \tag{3}$$

$$u_{\min} \le u(k) \le u_{\max} \tag{4}$$

$$y_{\min} \le y(k) \le y_{\max} \tag{5}$$

In Equations (3) and (4), J(N_1, N_2,Nu) is the cost function which is to be minimized, N_1 is the lower prediction horizon, N_2 is the upper prediction horizon, Nu is the control horizon, y(k+j) is the output signal at k+j, r(k+j) is reference output in control horizon at k+j, u(k-1) is the calculated control signal at k-1, and W_y, W_u are respectively the input weight matrix and the output weight matrix. The information depicted in Fig. 3 illustrates the sequential process of determining control signals and the corresponding calculations involved.

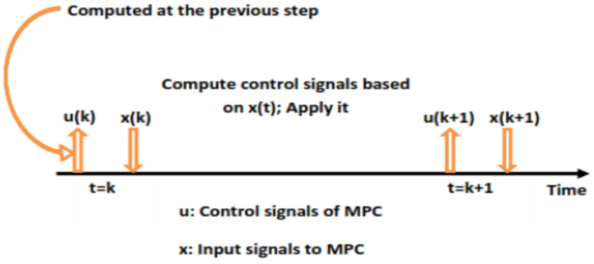

Fig. 3. The sequential process of determining control signals and the corresponding calculations

Variation in the generated power of the sources and load in each microgrid results in the variation of frequency and power of the connection line of the two microgrids. The power sources of a microgrid are categorized into two sections: controllable sources including DEG, BESS, and SMES; and b, uncontrollable sources including WTG and PV. When designing the MPC, variations of uncontrollable power sources are considered as predictable turbulence and load variation is considered as unpredictable turbulence. State-space equations for both controllers are formulated in Equation (6):

$$\dot{X}_i = A_i X_i + B_i U_i + D_i W_i \qquad i = 1,2$$
$$Y_i = C_i X_i \tag{6}$$

In Equation (6), X_i=1,2 is the vector of state variables for the first and second MPC, B_i=1,2 is factor matrix of the first and the second MPC, Ui=1,2 is the output control vector of the first and the second MPC, W_i=1,2 is the turbulence vector (uncontrollable input) of the first and the second MPC, and D is turbulence factor matrix for the first and the second MPC. Equations (7) and (8) are respectively complementary control errors of the first and second microgrid. With help of Equations (1) and (2) respectively, state-space equations for the MPC of the first and the second microgrid are written.

$$ACE_1 = \beta_1 \Delta F_1 + \Delta P_{tie} \tag{7}$$

$$ACE_2 = \beta_2 \Delta F_2 - \Delta P_{tie} \tag{8}$$

In Equations (7) and (8), ACE_1 is the complementary control error of the first area, ACE_2 is the complementary control error of the second area, β_1, β_2 are respectively bias frequency of the first and the second regions, and ΔP_{tie} is power variations of the connection line. Based on the information provided in Fig. 4 of the proposed controller, the initial phase involves assessing and measuring variations in load, power resources, and microgrid frequency. Subsequently, the system's output (ACE) is predicted, and the appropriate controller signals are applied using a prescribed rule.

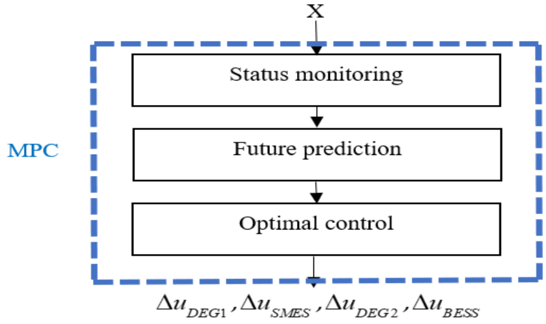

Fig. 4. The MPC controller

The behavior of the controller is governed by a set of equations, specifically Equation (9) to (14), which are explained in detail.

$$\min J = \sum_{j=N_1}^{N_2} W_{y_i} (ACE_n(k+j))^2 + \sum_{i=1}^{N_u} W_{ui} (\Delta u(k+j) - \Delta u(k+j-1))^2 \tag{9}$$

$$\Delta u(k) = \Delta u(k-1) + \sum_{i=0}^{N_t} \delta_i ACE_n(k-i) \tag{10}$$

$$W_{yi,\min} \le W_{yi} \le W_{yi,\max}$$
$$W_{ui,\min} \le W_{ui} \le W_{ui,\max} \tag{11}$$

$$\Delta u = \{\Delta u(k), \Delta u(k+1), \ldots, \Delta u(k+N_u)\}$$
$$\Delta u = [\Delta u_{DEG1}, \Delta u_{SMES}, \Delta u_{DEG2}, \Delta u_{BESS}] \tag{12}$$

$$X(k+1) = AX(k) + Bu(k) + DW(k)$$
$$Y(k) = CX(k) \tag{13}$$

$$P_{index}=\int_{0}^{T}\mathrm{t}(|ACE_1|\,dt+\int_{0}^{T}|ACE_2|)dt \tag{14}$$

Equation (9) represents an objective function that has been designed to be quadratic. By minimizing this function, a set of control signals (described in Equation (12)) can be derived. Equation (10) describes how to calculate the Δu signal at each time step. The variable "δi" corresponds to the numerical coefficients that are determined through the solution of the optimization problem, specifically the minimization of the objective function "J". Equation (11) provides the specified ranges for the coefficients employed in the objective function. Equation (13) demonstrates the procedure for computing the state variables at any given time step. Equation (14) is derived during the calculations as an index, which serves as a comparative measure for evaluating different control methods in the simulation section.

B. Optimizing weight parameters related to MPC controller using CRPSO algorithm

The PSO algorithm is a computational model and stochastic search technique inspired by swarm intelligence. It updates the position and velocity of each particle using Equations (15) and (16).

$$v_i^{k+1}=v_i^k+c_1r_1(P_{best}-x_i^k)+c_2r_2(g_{best}-x_i^k) \tag{15}$$

$$x_i^{k+1}=x_i^k+v_i^{k+1} \tag{16}$$

Equation (17) is utilized to update the velocity equations within the PSO algorithm, enhancing its overall search capability. Additionally, by incorporating a concept known as "craziness" into the algorithm, the position of the particle is updated using Equation (18), which is referred to as the CRPSO technique [31-34].

$$\begin{aligned}&v_i^{k+1}=r_2sign(r_3)v_i^k+(1-r_2)c_1r_1(P_{best}-x_i^k)\\&+(1-r_2)c_2(1-r_1)(g_{best}-x_i^k)\\&sign(r_3)=\begin{cases}-1 & r_3\le 0.05\\ 1 & r_3>0.05\end{cases}\end{aligned} \tag{17}$$

$$\left\{\begin{aligned}&x_i^{k+1}=P_r(r_4)sign(r_4)v_i^{craziness}+v_i^{k+1}\\&P_r(r_4)=\begin{cases}1 & r_4\le P_{craz}\\ 0 & r_4>P_{craz}\end{cases}\\&sign(r_4)=\begin{cases}1 & r_4\le 0.05\\ -1 & r_4>0.05\end{cases}\end{aligned}\right\} \tag{18}$$

In this paper, the weight parameters of the MPC controller are considered to be the most influential adjustable parameter, significantly affecting the system response. As a result, the CRPSO algorithm is employed to optimize these weight parameters. The selection of the CRPSO algorithm is based on its demonstrated effectiveness and efficiency in achieving optimal solutions quickly, surpassing the performance of other algorithms. Equation (19) represents the objective function used to fine-tune the weight parameters associated with the microgrid's LFC system in the MPC controller. The constraints for this optimization process are defined by Equation (11).

$$P_{index}=\min\int_{0}^{T}\mathrm{t}(|ACE_1|\,dt+\int_{0}^{T}|ACE_2|)dt \tag{19}$$

The goal of optimization is to minimize the ITAE by adjusting the weight matrices W_{yi} and W_{ui}, which serve as input and output matrices, respectively. The following steps outline the process of optimizing the weight parameter of the MPC controller.

1. The optimization process begins with an initialization step where various parameters are set. This includes selecting a particle population size of 100 and specifying the maximum number of iterations as 100. Additionally, the values of c_1 and c_2 are set to 1.8 and 2.2, respectively, while the exploration rate (P_r) is set to 0.28. Typically, the P_r value falls within the range of 0.4 to 0.9. Optimization algorithms involve two fundamental concepts: exploration and exploitation. Exploration refers to the generation of new solutions through random search, while exploitation involves refining and improving current solutions through local search. By increasing P_r, c_1, and c_2, the emphasis is placed on exploration, whereas decreasing these values favors exploitation. Optimization algorithms are designed to initially have a high exploration rate and a low exploitation rate. As the process progresses, the exploration rate decreases while the exploitation rate increases. Therefore, it is crucial to consider this aspect during implementation, and the initial values of P_r, c_1, and c_2 are selected to be high and gradually decreased. These initial values are chosen to initiate the algorithm effectively.

2. Generate an initial population of particles randomly according to the $\{W_{yi}, W_{ui}\} \in [0\ 1]$.

3. For every particle in the optimization process, the objective function is evaluated using Equation (19). This evaluation determines the fitness or performance of each particle. Based on the evaluation, P_{best} is determined for each particle, representing the best solution found by that particle so far. Additionally, g_{best} is determined for the entire group of particles, representing the best solution found among all particles in the population.

4. The velocity of the particles is calculated using Equations (17), and based on this velocity, the new positions of the particles are determined using Equation (18). In other words, the particles' movements are determined by their velocities, and their positions are updated accordingly.

5. Repeat steps (3) and (4) until the maximum number of iterations is reached.

6. Identify the particle that achieves the optimal solution.

In the MPC control method being proposed, the optimization problem described in Equation (19) needs to be solved at the start of each cycle, specifically at moment k, in order to calculate the X vector. The X vector are defined in Equations (1) and (2). In this method, the variables' vectors are updated only once, along with the forecast horizon N, which helps to significantly reduce the computational workload. These updated vectors are then optimized using the CRPSO.

The PSO algorithm involves defining the position and velocity variables for each particle. In this paper, both the position and velocity vectors are linear and have the same dimension as the decision variables in the X vector. These particles navigate the problem space with the aim of discovering the optimal solution. In the initial step, the position of a particle, denoted as variable X, is initialized along with the predicted values serving as model inputs. The timer counter k is set to zero to indicate the beginning of the optimization process. In the second step, the time step is incremented by k++. In the third step, the value of P_{index} (ACE_1+ACE_2) is calculated. If P_{index} (ACE_1+ACE_2) is not equal to zero, the process proceeds to the next step. In the fourth step, the particles and MPC control variables are updated. In the sixth step, if the number of time steps k reaches N, the process is terminated, and the objective function is evaluated using Equation (19) [31-33].

V. Simulation

A. Optimization of the problem

The weight parameters of MPC controllers have been optimized using three different algorithms: CRPSO, PSO, and GA. Initially, a change in the microgrid load of the first area was introduced, as shown in TABLE 1, with $\Delta P_{L1}(pu)=0.05pu$ at t=0. The optimization process, as depicted in Fig. 5, consisted of 100 iterations for each algorithm. Among the three algorithms, CRPSO exhibited favorable results. It converged in the 23rd iteration, achieving an impressive objective function (ITAE) value of 0.0019. Comparatively, PSO reached convergence in the 82nd iteration with an objective function value of 0.0028, while GA converged in the 58th iteration, yielding an objective function value of 0.0029. Given its faster convergence and lower objective function value, CRPSO was selected to optimize the weight parameters associated with the MPC. The weight parameters obtained through CRPSO for the MPC are as follows: $W_{y1}=0.5519$, $W_{u2}=0.0461$, $W_{y2}=0.5175$, and $W_{u1}=0.0772$. These values were determined to enhance the performance of the MPC system.

B. Different scenarios

The simulation was conducted under four distinct scenarios. In scenario (1), the focus was solely on load variations within the microgrid of the first area. Scenario (2) expanded the scope to include changes in both the load and the power output of the WTG associated with the first area's microgrid. Moving further, scenario (3) involved simultaneous load fluctuations in the first microgrid and power variations in the distributed generation sources of the second microgrid. Notably, this scenario also accounted for the uncertainty in microgrid inertia within the first area.

Scenario (1):

In this scenario, the changes in the power of distributed production sources in both microgrids are not considered, and only the load changes in the first microgrid are considered. Based on Fig. 1 have been simulated. Changes in the load of the first microgrid as much as $\Delta P_{L1}(pu)=0.05pu$ have occurred at the moment t=0. Figs 6, 7 and 8 respectively show the frequency changes of the first microgrid, the frequency changes of the second microgrid and the power changes of the communication line based on different controllers. The proposed controller (MPC(CRPSO)) was able to reduce the frequency deviations of the microgrid First, to minimize microgrid frequency deviations and power fluctuations of the communication line. The maximum frequency deviation of microgrid in area 1, the maximum frequency deviation of area 2 microgrid and the maximum deviation of power fluctuations between two microgrids have been improved by 20%, 25% and 42% by the proposed method. The settling time related to frequency deviation of microgrid in area 1 has been improved by 9% using the proposed controller. The settling time related to frequency deviation of area 2 microgrid has been improved by 13% using the proposed controller. Also, the settling time related to power power fluctuations between two microgrids has been improved by 7% using the proposed controller.

TABLE 1
THE PARAMETERS OF THE COMBINED ALGORITHM AND MPC

parameter	value	parameter	value
$N_2(mpc_1)$	5	$T(mpc_{1,2})$	0.1
$N_u(mpc_{1,2})$	3	$N_2(mpc_2)$	5

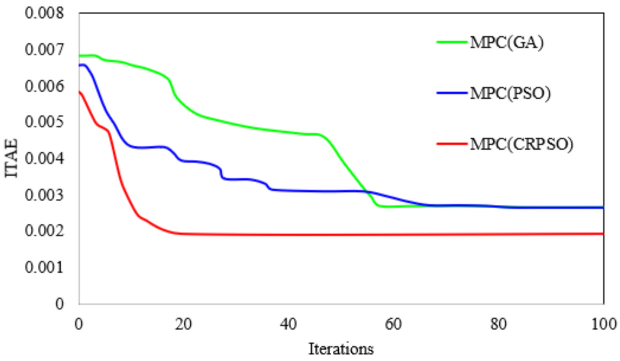

Fig. 5. The convergence of the different algorithms to solve the problem

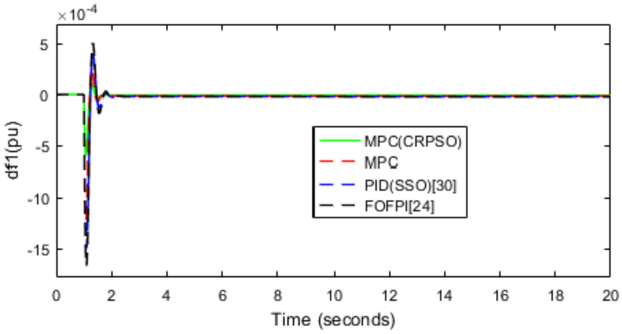

Fig. 6. The frequency changes of the first microgrid, scenario 1

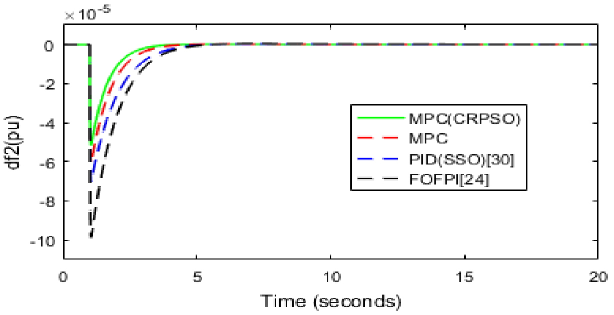

Fig. 7. The frequency changes of the second microgrid, scenario 1

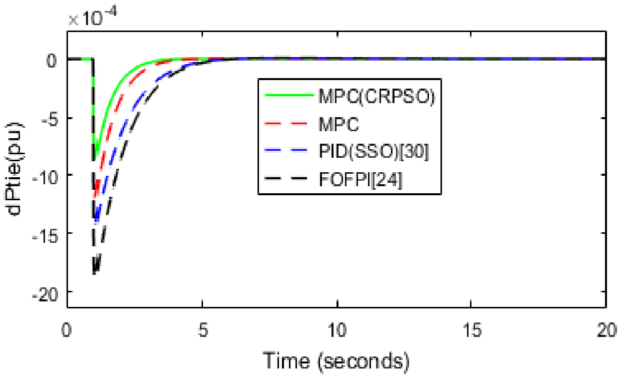

Fig. 8. The power changes of the communication line based on different controllers, scenario 1

Scenario (2):

In this scenario, the changes in the WTG and the load in the microgrid of the first area have happened. At t=0s, the load changes by the amount of ΔP_{L1}(pu)=0.05pu, and at t=10s, the change in the speed of the WTG by the amount of ΔV_{W1}=2(m/s), and at t=15s, the change in the speed of the WTG by the amount of ΔV_{W1}=-2(m/s) has occurred [30]. Figs 9, 10 and 11 respectively, the frequency changes of the first microgrid, the frequency changes of the second microgrid and the power changes of the communication line (system response to load changes) are shown based on different controllers. The proposed controller (MPC(CRPSO)) was able to reduce the microgrid frequency deviations First, to minimize microgrid frequency deviations and power fluctuations of the communication line. The maximum frequency deviation of microgrid in area 1, the maximum frequency deviation of area 2 microgrid and the maximum deviation of power fluctuations between two microgrids have been improved by 66%, 19% and 51% by the proposed method. The settling time related to frequency deviation of microgrid in area 1 has been improved by 19% using the proposed controller. The settling time related to frequency deviation of area 2 microgrid has been improved by 15% using the proposed controller. Also, the settling time related to power power fluctuations between two microgrids has been improved by 20% using the proposed controller.

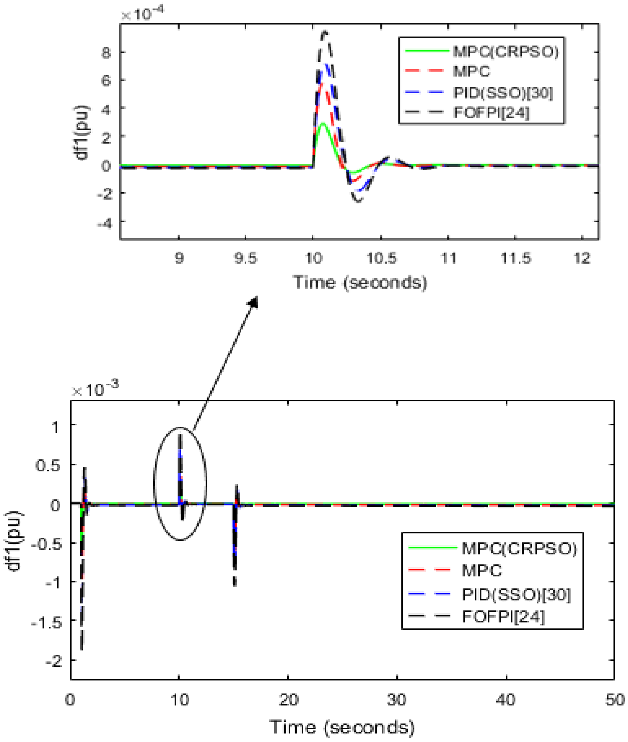

Fig. 9. The frequency changes of the first microgrid, scenario 2

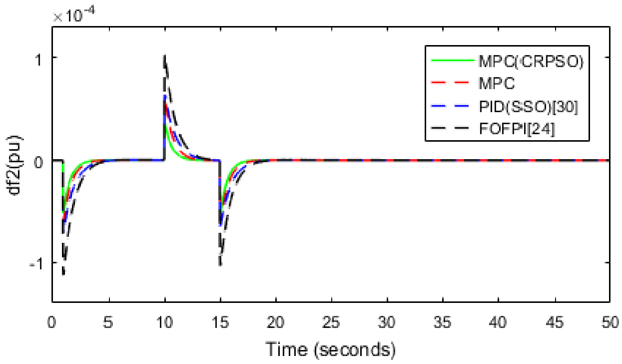

Fig. 10. The frequency variations for second microgrid, scenario 2

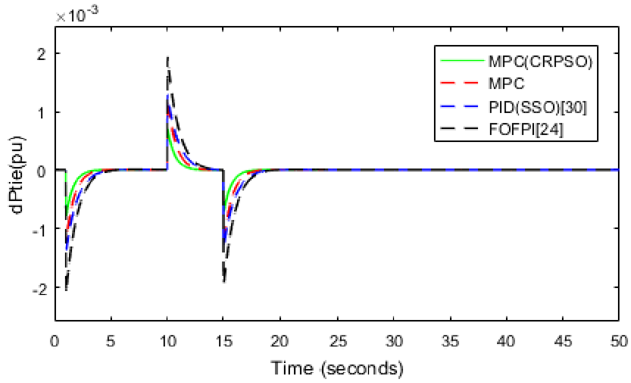

Fig. 11. The power changes of the communication line based on different controllers, scenario 2

Scenario (3):

In this scenario, changes in PV power (second area) and load changes in the microgrid of the first area have occurred. Also, the uncertainty in the inertia parameter of the first microgrid (H=-10%) is considered. At t=0s, the load changes by the amount of ΔP_{L1}(pu)=0.05pu, and at t=10s, the change in PV radiation by the amount of ΔG_2=400(w/m^2), and at t=15s, the change in PV radiation by the amount of ΔG_2=-400(w/m^2), Figs 12, 13 and 14 show the frequency changes of the first microgrid, the frequency changes of the second microgrid and the power changes of the communication line (system response to load changes) respectively. The proposed controller (MPC(CRPSO)) was able to reduce the microgrid frequency deviations First, it minimizes the frequency deviations of the second microgrid and the fluctuations of the power of the communication line, and it is also resistant to the uncertainty related to the parameters of the two-area microgrid. The maximum frequency deviation of microgrid in area 1, the maximum frequency deviation of area 2 microgrid and the maximum deviation of power fluctuations between two microgrids have been improved by 59%, 24% and 42% by the proposed method. The settling time related to frequency deviation of microgrid in area 1 has been improved by 22% using the proposed controller. The settling time related to frequency deviation of area 2 microgrid has been improved by 8% using the proposed controller. Also, the settling time related to power power fluctuations between two microgrids has been improved by 9% using the proposed controller.

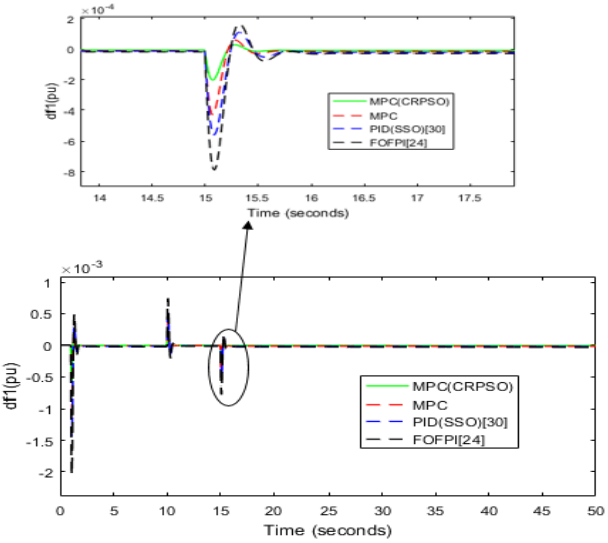

Fig. 12. The frequency changes of the first microgrid, scenario 3

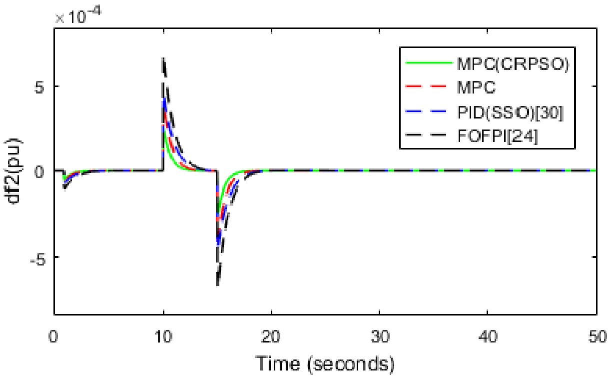

Fig. 13. The frequency variations for second microgrid, scenario 3

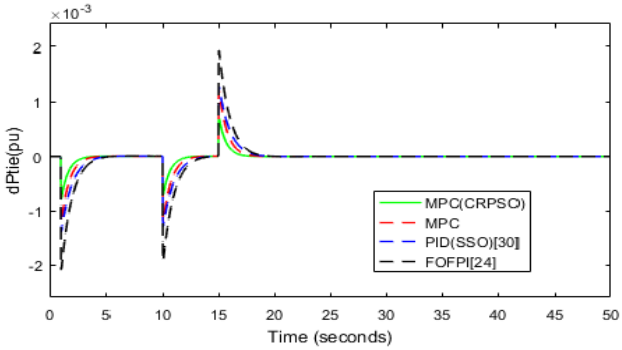

Fig. 14. The power changes of the communication line based on different controllers, scenario 3

VI. Conclusion

In this paper, the MPC whose weight parameters are used using the CRPSO is used for LFC in the two-area microgrid, as well as the number of controllers used for energy storage sources in the microgrid using the controller method. The proposal is reduced (less complexity). According to the results of the proposed controller and its comparison with different controllers, the effectiveness of the proposed method in reducing the use of fewer controllers (less complexity) has been shown, as well as the optimal performance of the proposed controller in terms of response speed and reducing overshoot and overshoot. It has been shown. The proposed method has also been able to be resistant to disturbances and uncertainty related to two-area microgrid parameters.

REFERENCES

[1] M. Jami, "Virtual Inertia Control and Small-Signal Stability Analysis of Electric Vehicle," International Journal of Industrial Electronics Control and Optimization, 2023.

[2] M. Safdari, M. R. Alizadeh Pahlavani, A. Dehestani Kolagar, "Model Predictive Voltage Balance Control of Single-Phase Half-Bridge Active Front End Rectifier," International Journal of Industrial Electronics Control and Optimization, 2023.

[3] F. Amiri, M. H. Moradi, "Improvement of Frequency stability in the power system considering wind turbine and time delay," Journal of Renewable Energy and Environment, Vol. 10. No. 1, pp. 9-18, 2023.

[4] M. Shahbazi, F. Amiri, (2019, December). Designing a Neuro-Fuzzy controller with CRPSO and RLSE algorithms to control voltage and frequency in an isolated microgrid. In *2019 International Power System Conference (PSC)* (pp. 588-594). IEEE.

[5] F. Amiri, A. Hatami, "A model predictive control method for load-frequency control in islanded microgrids," Computational Intelligence in Electrical Engineering, Vol. 8, No. 1, pp. 9-24, 2017.

[6] F. Amiri, M. Moradi, "Designing a new robust control for virtual inertia control in the microgrid with regard to virtual damping," Journal of Electrical and Computer Engineering Innovations (JECEI), Vol. 8, No. 1, pp. 53-70, 2019.

[7] H. Gu, T. Banki, A. Soleymani," Robust Frequency Control of Additive Manufacturing Based Microgrid Considering Delayed Fuel Cell Dynamics," Journal of New Materials for Electrochemical Systems, Vol. 26, No. 4, 2023.

[8] F. Amiri, A. Hatami, "Load Frequency Control Via Adaptive Fuzzy PID Controller In An Isolated Microgrid", In 32nd international power system conference, 2017.

[9] F. Amiri, M. Eskandari, M. H. Moradi, "Improved Load Frequency Control in Power Systems Hosting Wind Turbines by an Augmented Fractional Order PID Controller Optimized by the Powerful Owl Search Algorithm," Algorithms, Vol. 16, No. 12, pp. 539., 2023.

[10] D. Murugesan, K. Jagatheesan, P. Shah, R. Sekhar, " Fractional order PIλDμ controller for microgrid power system using cohort intelligence optimization," Results in Control and Optimization, Vol. 11, pp. 100218, 2023.

[11] K. Singh, M. Dahiya, A. Grover, R. Adlakha, M. Amir, "An effective cascade control strategy for frequency regulation of renewable energy based hybrid power system with energy storage system," Journal of Energy Storage, Vol. 68, pp. 107804, 2023.

[12] H. A. Muqeet, R. Liaqat, M. Jamil, A. A. Khan, "A State-of-the-Art Review of Smart Energy Systems and Their Management in a Smart Grid Environment," Energies, Vol. 16, No. 1, pp. 472, 2023.

[13] R. H. Kumar, S. Ushakumari, "Biogeography based tuning of PID controllers for Load Frequency Control in microgrid," In 2014 International Conference on Circuits, Power and Computing Technologies [ICCPCT-2014] (pp. 797-802). IEEE, 2014.

[14] G. Shankar, V. Mukherjee, "Load frequency control of an autonomous hybrid power system by quasi-oppositional harmony search algorithm," International Journal of Electrical Power & Energy Systems, Vol. 78, 715-734, 2016.

[15] R.Mandal, K. Chatterjee,"Application and optimization of a robust fractional-order FOPI-FOPID automatic generation controller for a multiarea interconnected hybrid power system," In Fractional Order Systems and Applications in Engineering (pp. 175-197). Academic Press, 2023.

[16] I. Pan, S. Das, "Fractional order fuzzy control of hybrid power system with renewable generation using chaotic PSO," ISA transactions, Vol. 62, pp. 19-29, 2016.

[17] H. Shayeghi, I. F. Davoudkhani, N. Bizon, "Robust self-adaptive fuzzy controller for load-frequency control of islanded airport microgrids considering electric aircraft energy storage and demand response," IET Renewable Power Generation, 2024.

[18] H. B. CH, C. Dhanamjayulu, I. Kamwa, S. M. Muyeen, "A novel on intelligent energy control strategy for micro grids with renewables and EVs," Energy Strategy Reviews, Vol. 52, pp. 101306, 2024.

[19] H. Bevrani, F. Habibi, P. Babahajyani, M. Watanabe, Mitani, Y., "Intelligent frequency control in an AC microgrid: Online PSO-based fuzzy tuning appCRPSOch," IEEE transactions on smart grid, Vol. 3, No. 4, pp. 1935-1944, 2012.

[20] M. R. Khalghani, M. H. Khooban, E. Mahboubi-Moghaddam, N. Vafamand, M. Goodarzi," A self-tuning load frequency control strategy for microgrids: Human brain emotional learning," International Journal of Electrical Power & Energy Systems, Vol. 75, pp. 311-319, 2016.

[21] S. K. Tripathi, V. P. Singh, Pandey, "Robust load frequency control of interconnected power system in smart grid," IETE Journal of Research", Vol. 69, No. 8, pp. 5351-5363, 2023.

[22] H. Bevrani, M. R. Feizi, S. Ataee, "Robust Frequency Control in an Islanded Microgrid: ${H} _ {\infty} $ and $\mu $-Synthesis AppCRPSOches," IEEE transactions on smart grid, Vol. 7, No. 2, pp. 706-717, 2015.

[23] F. Amiri, A. Hatami, "Load frequency control for two-area hybrid microgrids using model predictive control optimized by grey wolf-pattern search algorithm," Soft Computing, pp. 1-17, 2023.

[24] C. Mu, A. Naderipour, Z. Abdul-Malek, I. F. Davoodkhani, H. Kamyab, R. R. Ali, "Load-frequency control in an islanded microgrid PV/WT/FC/ESS using an optimal self-tuning fractional-order fuzzy controller," Environmental Science and Pollution Research, Vol. 30, No. 28, pp. 71677-71688, 2023.

[25] P. Jampeethong, S. Khomfoi, "Coordinated Control of Electric Vehicles and Renewable Energy Sources for Frequency Regulation in Microgrids," IEEE Access, Vol. 8, pp. 141967-141976, 2020.

[26] F. Amiri, M. H. Moradi, "Coordinated Control of LFC and SMES in the Power System Using a New Robust Controller," Iranian Journal of Electrical and Electronic Engineering, pp. 1912-1912, 2021.

[27] F. Amiri, M. H. Moradi, "Designing a Fractional Order PID Controller for a Two-Area Micro-Grid under Uncertainty of Parameters," Iranian journal of energy, Vol. 20, No. 4, pp. 49-78, 2018.

[28] V. P. Singh, N. Kishor, P. Samuel, "Communication time delay estimation for load frequency control in two-area

power system," Ad Hoc Networks, Vol. 41, pp. 69-85, 2016.

[29] F. Tedesco, A. Casavola, "Fault-tolerant distributed load/frequency coordination strategies for multi-area power microgrids," IFAC-PapersOnLine, Vol. 48, No. 21, pp. 54-59, 2015.

[30] A. A. El-Fergany, M. A. El-Hameed, "Efficient frequency controllers for autonomous two-area two-area microgrid system using social-spider optimiser," IET Generation, Transmission & Distribution, Vol. 11, No. 3, pp. 637-648, 2017.

[31] A. R. Moazzeni, E. Khamehchi, "Craziness based Particle Swarm Optimization (CRPSO): A new metaheuristic method for drilling optimization solutions," Journal of Petroleum Science and Engineering, Vol. 195, pp. 107512, 2020.

[32] I. V. Pustokhina, D. A. Pustokhin, P. T. Nguyen, M. Elhoseny, K. Shankar, "Multi-objective Craziness based Particle Swarm Optimization with WELM model for customer churn prediction in telecommunication sector," Complex & Intelligent Systems, pp. 1-13, 2021.

[33] S. Kumar, R. P. Mahapatra, "Design of multi-warehouse inventory model for an optimal replenishment policy using a Craziness based Particle Swarm Optimization," *Knowledge-Based Systems*, Vol. 231, 107406, 2021.

[34] F. Amiri, M. H. Moradi, "A new control strategy for controlling isolated microgrid," Engineering and Energy Management, Vol. 10, No. 4, pp. 60-73, 2023.

Particle Swarm Optimization (PSO)
Biogeography-based(BIO)
Quasi-oppositional harmony (QOH)
Fractional order(FO)
Human brain emotional learning(HBEL)
Social-spider optimizer (SSO)
Wind Turbine Generator (WTG)
Diesel Engine Generator1 (DEG1)
Super Magnetic Energy Storage(SMES)
Diesel Engine Generator2 (DEG2)
Photo voltaic (PV)
Battery Energy Storage System(BESS)
Maximum Power Point Tracker(MPPT)
Model Predictive Controller(MPC)
Harmony search algorithm (HSA)

Farhad Amiri was born in Ilam. He received his MSc and PhD degrees in electrical engineering in 2017 and 2022, respectively, from Bu-Ali Sina University. He also received his post-doctoral (Electrical engineering) in 2024 from the National Elites Foundation of Iran. His research interests include dynamic and transient performance of power system, control, Microgrid and renewable energy.

Mohammad Hassan Moradi was born in Nowshahr, Mazandaran, Iran. He obtained his B.Sc., M.Sc. and PhD from Sharif University of Technology, Tarbiat Modares University and Strathclyde University in Glasgow, Scotland in 1991 1993 and 2002 respectively. His research interests include New and Green Energy, Microgrid Modeling and Control, DG Location and Sizing in Power System, photovoltaic systems and power electronics, Combined Heat and Power Plant, Power Quality, Supervisory Control, Fuzzy Control.

IECO

This page intentionally left blank.

IECO
International Journal Of
Industrial Electronics Control and Optimization
Print ISSN: 3517-2645
Online ISSN: 3568-2645
Homepage: https://ieco.usb.ac.ir/

Evaluating the Robust Economic Operation Capabilities of Stationary and Mobile storage and Sources Management in the Smart Distribution network

Sasan Pirouzi[1] | Mahmoud Zadehbagheri[2] | Rohollah Rashidi[3]

Department of Engineering, Semmirom Branch, Islamic Azad University, Semmirom, Iran.[1,3]
Department of Engineering, Yasuj Branch, Islamic Azad University, Yasuj, Iran.[2]
Corresponding author's email: Ma.zadehbagheri@iau.ac.ir

Article Info

Article type:
Research Article

Article history:
Received: 24-February-2024
Received in revised form:
20-April-2024
Accepted: 13-May-2024
Published online: 22-Sep-2024

Keywords:
Distributed generation,
Electric vehicles,
Energy storage system,
Robust optimization,
Linear programming.

ABSTRACT

In this article, the robust scheduling of the distribution network is presented considering electric vehicles, distributed generation, and energy storage, in which the energy management of the mentioned elements is considered, and also only one scenario is needed. The proposed deterministic problem is an optimization problem whose objective function is equal to minimizing energy cost. Also, the limitations of the problem are equal to the power flow equations of the network, the limitations of the technical indicators of the network such as the voltage of the buses and the passing power of the lines, the operation equations of electric vehicles, energy storages, and distributed generation. It is worth mentioning that the mentioned problem is non-linear. In the following, to achieve the global optimal point with a high solution speed, the linear model of the mentioned problem is presented with a very low calculation error. In this research, the uncertainty parameters of the problem are equal to active and reactive loads, energy prices, parameters of electric vehicles, and renewable productions. Finally, to simplify the decision-making of the distribution network operator, a robust model of the mentioned problem was presented. Finally, the proposed problem is applied to the IEEE standard 33-bus radial distribution network using GAMS optimization software, and then the capabilities of the proposed design are evaluated.

Nomenclature

E^u	Uncertainty variable for energy consumption of electric vehicles (EVs) in per-unit (p.u.)
P^u, Q^u	Uncertainty variable for active and reactive load (p.u.)
PB	Active power of EVs battery (p.u.)
PB^u, SE^u	Uncertainty variable for charge rate of EVs battery and capacity of EVs charger (p.u.)
PE, QE	Active and reactive power of EVs (p.u.)
PG, QG	Active and reactive power of distribution station (p.u.)
PL, QL	Active and reactive power of distribution line (p.u.)
PLC, QLC	Active and reactive power losses of EVs chargers (p.u.)
PDG, PS	Active power of distributed generation (DG) and storage
QC	Reactive power of EVs charger (p.u.)
QDG, QS	Reactive power of distributed generation (DG) and storage (p.u.)

ES	Stored energy in storage (p.u.)
V	Voltage magnitude (p.u.)
ΔV, θ	Voltage deviation (p.u.) and voltage angle (rad)
	Dual variables
ρ^{up}	Uncertainty variable for energy price ($/MWh)
PD, QD	Active and reactive load (p.u.)
BC, SOC	(%) Battery capacity (kWh) and state of charge
PF^{min}	Minimum power factor
SE^{max}	Capacity of EVs charger (p.u.)
SG^{max}	Station capacity (p.u.)
SL^{max}	Distribution line capacity (p.u.)
SDG^{max}	DG capacity (p.u.)
SS^{max}	Storage capacity (p.u.)
TPF	Tangent value for minimum power factor
T_{step}, $\Delta\alpha$	Time step (hour) and angle deviation (rad)
V^{max}	Maximum value of voltage magnitude (p.u.)
V^{min}	Minimum value of voltage magnitude (p.u.)

Publisher: University of Sistan and Baluchestan

I. Introduction

Due to the pollution caused by the uncontrolled consumption of fossil fuels as well as the depletion of this fuel in recent years, organizations and governments have decided to use new technologies such as electric vehicles (EVs), distributed generations (DGs), and energy storage systems (ESSs) that has very low environmental pollution [1]. Therefore, according to various researches, it is predicted that the use of EVs, DGs, and ESSs will grow significantly in the next few years. In other words, it should be noted that to reduce environmental concerns, one way is to replace EVs instead of cars with fossil fuel consumption. Therefore, it is predicted that the number of EVs will increase worldwide [2]. Since EVs perform this process by connecting to the electrical network, especially the distribution network, to supply energy to their batteries, it is expected that the amount of energy demand in the distribution network will noticeably increase [3]. In addition, to reduce pollution, another solution is to use renewable energy sources (RESs). Therefore, these types of sources will grow significantly in the coming years, as they are generally connected to the distribution network. To establish flexibility in the distribution network, ESSs will have a high number in the distribution network in the coming years [4]. Since these elements are placed in the distribution network, increasing their number will cover a large volume of the distribution network. It is worth mentioning that the increase of the mentioned elements in the distribution network and their lack of energy management will cause challenges in the distribution network. In other words, the voltage profile goes out of the uniform and smooth state, and also network losses increase, and other cases will occur [5]. In addition to this, the behavior of EVs depends on the decision-making of their owners, and the output of RESs also depends on natural phenomena. Since the decisions of EV owners and natural phenomena are not certain, therefore the number of uncertainty parameters in the network has increased and therefore the decision-making of the distribution network operator will be very complicated. Therefore, there is a need to plan the schedule of the distribution network by considering EVs, DGs, and ESSs including the uncertainty model.

Various researches have been done in the field of distribution network operation. In [6], a Stackelberg game approach is proposed for the energy sharing management of a microgrid including prosumers and plug-in electric vehicle (PEV) charging stations (CSs), and a proper billing scheme is designed to increase the robustness of the approach on real-time applications. In the hereby game-theoretic approach, the energy demands of PEV CSs are determined as variable demands considering the operational characteristics of CSs. The purpose of [7] is to assess the impact of emergencies on smart grids through a novel optimization algorithm. The algorithm comprises an optimizer, which maximizes the autonomy of the smart grid, prioritizing its Renewable Energy Sources (RES), and Artificial Neural Networks (ANN), which provide forecasts related to the intermittent RES production. Ref. [8] presents an optimal and simultaneous allocation of the photovoltaic panel (PV) and wind turbine (WT) with the reconfiguration of radial distribution networks to reduce power losses and improve reliability. Determining the optimal optimization variables is very important to obtain the maximum benefits of renewable resource allocation and network reconfiguration, i.e. achieving the lowest losses and reliability cost. In [9], it investigates the optimal operation of a multi-carrier virtual energy storage system (VESS), including batteries, thermal energy storage (TES) systems, power to hydrogen (P2H), and hydrogen to power (H2P) technologies in hydrogen storage systems (HSS), and EVs in dynamic energy storage system (ESS). Further, the demand response program (DRP) for electrical and thermal loads has been considered as a tool of VESS due to the similar behavior of physical ESS. Changes in the climate, environmental pollution, and lack of classical energy sources forced many countries to address renewables. In [10], the smart distribution network reconfiguration is considered to minimize power losses and economic costs. Also, capacitor switching (placement of shunt capacitors) and the presence of distribution generation are always incorporated in modern networks. Further, the On Load Tap Changer in the supplying substation has to be used. Simulated Annealing and Minimum spanning tree algorithms work separately to find the best appropriate solution. The main goals of [10] are minimization of power losses and costs. A distributed operation optimization model incorporating peer-to-peer (P2P) electricity trading in a blockchain environment is proposed in [11], where network usage fees considering electrical distance are specially addressed. Meanwhile, the private information security of prosumers is ensured by the Proof-of-Authority (PoA) consensus blockchain during P2P electricity trading. The trading information of adjustable prosumers should be sent to the proxy entity authorized by the distribution network using the blockchain platform. The contribution of [12] includes the presentation of a model for managing the coordinated and uncoordinated charging system of grid-connected EVs with wind power and photovoltaic power units as dispersed generation sources and dividing the EVs into 4 classes by considering the share of each in the grid and considering a random number of vehicles per class using the normal distribution function and implementing the incoordination in wind speed and solar irradiation. In [13], a probability-solving model for a three-phase unbalanced modern power electronic distribution network with distributed generation (DG) integration is developed, and the probability model is solved using Point Estimation Method (PEM) combined with Gram–Charlier expansion and Monte Carlo Simulation (MCS). Besides, this paper presents a detailed analysis comparing the results of PEM and MCS solutions from the perspective of voltage and line loss. Based on the deep learning and mechanism models, a novel probabilistic power flow (PPF) method is proposed in [14] for multi-microgrid distribution systems considering incomplete network information. Firstly, accessible power exchange data as well as public and independent information are utilized to realize equivalent modeling for microgrid areas with incomplete parameters, based on a novel Kriging surrogate enhanced Gate Recurrent Unit-Temporal Convolutional Network (GRU-TCN). Ref. [15] presents a new management methodology to find the optimum operation of a grid-connected MG, which is modeled as an optimization approach and aims to minimize total cost. The uncertainties in renewable energy-based DG units, including WT and PV, are also considered in this study. The balance between total electricity generation and required demand in the system is determined based on the power interchange between the MG and the distribution system. Ref. [16] presents the optimal scheduling model of the active distribution network (ADN) containing RESs and flexible sources (FSs) such as non-RESs (NRESs) and EVs parking lot based on adaptive robust optimization (ARO). In the deterministic programming, a two-objective optimization model is expressed. It minimizes the difference between the network and NRES operation cost and the revenue of the RES, NRES, and FS due to the sale of active and reactive power in the first objective function, and the second objective function considers the minimizing of the voltage deviation. Ref. [17] develops a robust bundled active and reactive power management of EV-integrated smart distribution networks. To model the problem, at first, the deterministic formulation of the problem is expressed as a non-linear programing (NLP), which minimizes the difference between the energy cost and the revenue of EVs' (parking lot's) reactive power exchange with the network as the objective function, subject to the AC power flow equations, system operation limits and EVs' characteristics as the problem constraints. Ref. [18] presents a two-level optimization model for the optimal scheduling of an active distribution system in day-ahead and real-time market horizons. The distribution system operator transacts energy and ancillary services with the electricity market, plug-in hybrid electric vehicle parking lot aggregators, and demand response aggregators. Ref. [19] presents a two-level optimization problem for optimal day-ahead scheduling of an active distribution system that utilizes renewable energy sources, distributed generation units, electric vehicles, and energy storage units and sells its surplus electricity to the upward electricity market. Ref. [20] proposes an optimal scheduling of the distribution network considering the uncertainty of wind and solar output. This scheme takes the minimum expected value of electricity purchase cost from the main network as the objective function in several scenarios and uses the improved whale algorithm to solve the problem. As the influence of time-varying temperature and driving speed on electric vehicle charging load is not considered in the process of distribution network scheduling, a multi-objective optimal scheduling model for distribution networks, which considers electric vehicle charging load, is proposed in [21]. In [22], stochastic scheduling of a hybrid system (HS) composed of a photovoltaic (PV) array and wind turbines incorporated with a battery storage (HPV/WT/Batt) system in the distribution network was proposed to minimize energy losses, the voltage profile, and the HS cost, and to improve reliability in shape of the energy-not-supplied (ENS) index, considering energy-source generation and network demand uncertainties through the unscented transformation (UT). To improve the operating dependability of a generalized power active distribution network, a multi-objective optimal scheduling approach based on game theory is proposed in [23]. The active distribution network's multistakeholder coordinated and optimal dispatching mode is then established, and the game interaction between various stakeholders in the generalized power active distribution network is evaluated. Finally, a summary of the works is presented in Table 1.

TABLE 1
TAXONOMY OF RECENT ACADEMIC PUBLICATIONS

Ref.	**Reactive power management by**			**Uncertainty model**	**Optimal power flow (OPF) model**
	DG	**EV**	**ESS**		
[6]	×	×	×	Stochastic optimization	Non-linear OPF
[7]	×	×	×		
[8]	×	×	×		
[9]	×	×	×		
[10]	✓	×	×		
[11]	×	×	×		
[12]	×	×	×	-	
[13]	×	×	×	Probabilistic optimization	
[14]	×	×	×	Stochastic optimization	
[15]	×	×	×		
[16]	✓	✓	×	ARO	Linearized OPF
[17]	×	✓	×	ARO	
[18-23]	×	×	×	Stochastic optimization	Non-linear OPF
Current paper	✓	✓	✓	**ARO**	**Linearized OPF**

Based on the research background and Table 1, there are major research gaps in the field of distribution network exploitation. As a research gap, in most researches, only the control and management of the active power of resources and storage devices has been considered. However, it should be noted that some of the technical and economic indicators of the network are improved by reactive power management. Like the voltage profile, the control of the reactive power leads to the regulation of the voltage. Even reactive power control can be effective in reducing energy losses and network power factors, which can play a significant role in reducing the cost of network operation. However, this issue has been considered in less research. Of course, in various researches such as [10], reactive power control with capacitors has been considered. However, it should be said that to reduce environmental pollution, the use of renewable resources and storage devices in the distribution network increases. These elements generally have electronic power converters, which can play a role in reactive power control. This issue has been considered in less researches such as [16-17]. As another research gap, it should be noted that network energy management is a power system operation problem. In these problems, the implementation step is low, so that in some applications it is less than 1 hour. Therefore, low computing time is of particular importance in these problems. To access this topic, it is necessary that the volume of the problem is low and the equations are simplified. However, it should be noted that in most researches such as [6-15], stochastic optimization has been used to model uncertainties. This method extracts a significant number of scenarios to reach a reliable solution, which leads to an increase in the volume of the problem. To compensate for this issue, methods with a low number of scenarios are needed. This issue is accessible in robust optimization, but it has been included in less researches such as [16-17]. In most researches, the nonlinear optimal power flow (OPF) model has been used. The solution to this problem is based on methods according to repetition. Therefore, this method leads to an increase in computing time. To compensate for this issue, linearization of the equations is effective, but it is included in less researches such as [16-17].

In this article, to compensate for the research gaps, the simultaneous management of active and reactive power in the smart distribution network using DGs, EVs, and ESSs is used. The proposed plan minimizes the cost of purchasing energy from the distribution network from the upstream network. It is bound to the equations of AC optimal power low and the operation model of resources and storage devices. The proposed design has a non-linear model, where a linear approximation model for OPF is used to compensate for the last research gap. This plan has uncertainties regarding load, renewable power, energy price, and parameters of EVs. In this article, to reach the optimal solution resistant to the prediction error of uncertainties in low computing time, adaptive robust optimization (ARO) is used to model the aforementioned uncertainties. This method has only one scenario which has the worst case of uncertainties. Finally, the innovations of this article are as follows:

- Simultaneous management of active and reactive power of the distribution network using electric vehicles, distributed generations, and stationary storage devices.
- Simultaneous improvement of the economic and operational indicators of the distribution network with the addition of the ability to control reactive power to sources and storage devices.
- Access to a suitable linear approximation model with low calculation error for the AC optimal power distribution problem, and
- Simultaneous modeling of uncertainties of load, parameters of electric vehicles, energy price, and renewable power using adaptive robust optimization.

Next, the power management modeling of the distribution network is presented in the second section, and then the uncertainty modeling based on ARO is described in the third section. Numerical results obtained from different study cases are reported in the fourth section. Finally, the conclusions are presented in the fifth section.

II. Optimal scheduling of distribution network

2.1. Original model

This section outlines the non-linear deterministic model proposed for the design. This technique minimizes energy costs to satisfy network, resource, and storage device requirements [16]. Therefore, the problem model is as follows:

A. Objective function:

The objective function of the proposed plan is stated in Equation (1), which represents the minimization of the cost of energy received from the upstream network [17].

$$min_{PG}\ \sum_{t\varepsilon\varphi_t}\sum_{b\varepsilon\varphi_b} T_{stop}F_b^{sub}\rho_{b,t}^{p}PG_{b,t} \qquad (1)$$

B. Power flow equations:

Constraints (2) to (6) express the power distribution equations, which are equal to active power balance, reactive power balance, active power passing through the lines, reactive power passing through the lines, and the reference bus voltage angle, respectively. Slack) are It should be noted that in these equations, the terms PG and QG are non-zero only for slack bass, and they are equal to zero in other basses [16-17].

$$\begin{aligned} PG_{b,t} + PDG_{b,t} + PS_{b,t} - PE_{b,t} - \sum_{j\varepsilon\varphi_b} A_{b,j}PL_{b,j,t} \\ = PD_{b,t} \quad \forall b,t \end{aligned} \qquad (2)$$

$$\begin{aligned} QG_{b,t} + QDG_{b,t} + QS_{b,t} - QE_{b,t} - \sum_{j\varepsilon\varphi_b} A_{b,j}QL_{b,j,t} \\ = QD_{b,t} \quad \forall b,t \end{aligned} \qquad (3)$$

$$\begin{aligned} PL_{b,j,t} = g_{b,t}\left(V_{b,t}\right)^2 \\ - V_{b,t}V_{j,t}\{g_{b,j}cos\left(\theta_{b,t} - \theta_{j,t}\right) \\ + b_{b,j}sin\left(\theta_{b,t} - \theta_{j,t}\right)\} \quad \forall b,j,t \end{aligned} \qquad (4)$$

$$\begin{aligned} QL_{b,j,t} = -b_{b,t}\left(V_{b,t}\right)^2 \\ + V_{b,t}V_{j,t}\{b_{b,j}cos\left(\theta_{b,t} - \theta_{j,t}\right) \\ - g_{b,j}sin\left(\theta_{b,t} - \theta_{j,t}\right)\} \quad \forall b,j,t \end{aligned} \qquad (5)$$

$$\theta_{b,t} = 0 \quad \forall b = ref, t \tag{6}$$

C. Technical limitations of the distribution network

The voltage limitation of the buses, the capacity of the lines and the upstream network, and the power factor of the upstream network are shown in relations (7) to (10) respectively. It should be noted that in (10), the equivalent relationship with the power factor limit is presented, in which TPF is equal to tan(cos-1(PFmin)), and the minimum power factor is considered to be 0.9 [2-3, 17].

$$V^{{min_{b,t}}^{max}} \tag{7}$$

$$\left(PL_{b,j,t}\right)^2 + \left(QL_{b,j,t}\right)^2 \le \left(SL_{b,j}^{max}\right)^2 \quad \forall b, j, t \tag{8}$$

$$\left(PG_{b,t}\right)^2 + \left(QG_{b,t}\right)^2 \le F_b^{sub}(SG_b^{max})^2 \quad \forall b, t \tag{9}$$

$$\begin{aligned} -F_b^{sub}TPF \times PG_{b,t} \le QG_{b,t} \\ \le F_b^{sub}TPF \times PG_{b,t} \quad \forall b, t \end{aligned} \tag{10}$$

D. EV aggregation restrictions:

The constraints on electric vehicles (EVs) are demonstrated in relationships (11) to (17), which indicate the necessary energy consumption of EVs in the parking area, the power balance between the EV battery and the grid, the power balance between the EV charger and the grid, the losses from the EV charger, the charging rate for all EV batteries, and the limitation of EV chargers [2, 16].

$$PE_{b,t} = PB_{b,t} + PLC_{b,t} \quad \forall b, t \tag{11}$$

$$QE_{b,t} = QB_{b,t} + QLC_{b,t} \quad \forall b, t \tag{12}$$

$$PLC_{b,t} = a_r\left|PE_{b,t}\right| + a_{im}\left|QE_{b,t}\right| \quad \forall b, t \tag{13}$$

$$QLC_{b,t} = b_r\left|PE_{b,t}\right| + b_{im}\left|QE_{b,t}\right| \quad \forall b, t \tag{14}$$

$$0 \le PB_{b,t} \le PB_{b,j}^{max} \quad \forall b, t \tag{15}$$

$$\left(PE_{b,t}\right)^2 + \left(QE_{b,t}\right)^2 \le (SE_b^{max})^2 \quad \forall b, t \tag{16}$$

$$\sum_{t\varepsilon\varphi_t} T_{stop} PE_{b,t} = EC_b \quad \forall b \tag{17}$$

According to [3], EVs can work in the charging and discharging mode of their batteries, but the discharging mode will reduce the useful life of the battery, so the owners of EVs do not want to inject active power into the network. Also, based on [17], it is assumed in this article that EVs connect to the grid after their last trip during the day and night and receive the electrical energy they need from the grid. Therefore, in relation (17), the term EC is equal to the total energy consumption required by EVs in the parking lot. Also, the required energy consumption of an EV is calculated from the equation (1-SOC)*BC, where SOC is equal to the state of charge and BC is equal to the battery capacity of the EV. SOC is like the fuel gauge of gasoline cars that displays the amount of remaining fuel. In addition, SOC is also calculated from the relationship (1-L/AER) where L is equal to the distance traveled by EV in electric mode and AER is the total distance traveled by EV in electric mode proportional to the battery capacity [17].

E) *Operation model of DGs*: Condition (18) is related to distributed generation, which indicates their apparent power control capacity. This condition expresses the capability curve of DGs, and it includes the limitation of active power generation and the limitation of reactive power control of DGs. In addition, it should be noted that this relationship is also true for renewable DGs, with the difference that the term PDG is considered a parameter for them. But this expression is a variable in non-renewable DGs [3]

$$\left(PDG_{b,t}\right)^2 + \left(QDG_{b,t}\right)^2 \le (SDG_b^{max})^2 \quad \forall b, t \tag{18}$$

F) *The operation model of the stationary storage device*: the limitations of the energy storage device are stated in relations (19) to (21), which respectively indicate the limitation of the apparent power generation capacity of its charger, the calculation of the stored energy and the limitation of the stored energy. It is noteworthy that the difference between two efficiency of charging and discharging in storage devices has a low value [3], therefore the equation (21) can be written according to the hypothesis of equality of charging and discharging efficiency.

$$\left(PS_{b,t}\right)^2 + \left(QS_{b,t}\right)^2 \le (SS_b^{max})^2 \quad \forall b, t \tag{19}$$

$$ES_{b,t} = ES_{b,t-1} - \eta * PS_{b,t} \quad \forall b, t \tag{20}$$

$$E^{min} \le ES_{b,t} \le E^{max} \quad \forall b, t \tag{21}$$

This problem is for the distribution network. The model of the network is based on optimal power flow constraints, i.e. (2)-(10). Also, this paper considers the capabilities of ESS, DG, and EVs. Hence, the problem includes the formulation of ESS, DG, and EVs according to constraints (11)-(21).

2.2. Linear approximation model of the problem

In formulation (1)-(21), constraints (4), (5), (8), (9), (13), (14), (16), (18) and (19) have the format It is non-linear. Also, constraints (4) and (5) are non-convex. Therefore, the model (1)-(21) is non-convex in a non-linear way [16]. Algorithms for solving this problem are generally based on numerical methods based on repetition, so their computing time is expected to be high for solving complex engineering problems like model (1)-(21). Also, due to the non-convexity of the problem, different solvers do not extract a unique solution [16]. However one of the goals of this article, based on part 1, is to derive a stable model of uncertainties. This modeling requires the convexity of the basic problem. For this purpose, a linear approximation model is obtained in this section for the proposed design. One of the characteristics of the linear model is its convexity, its different solvers can extract a unique solution, and the computing time of the solvers of this problem is lower than the nonlinear model [17].

CPLEX solver is a strong algorithm to obtain the optimal solution. This solver is for linear problems, hence, the linear model of the scheme is obtained in this paper. Also, this paper needs robust optimization. The robust formulation is for linear programming. Hence, the linear model was obtained for the scheme.

According to [2], in a distribution network, generally, the voltage angle difference between two ends of a line is less than 6 degrees or 0.105 radians. Therefore, the terms sin(θ) and cos(θ) in relations (4) and (5) can be approximated to and 1, respectively. Bus voltage based on the piecewise linearization technique [17] can be expressed as$V^{min\sum_{l\varepsilon\phi_l}\Delta V_l}$. ΔV represents the voltage deviation and has a value much less than one per-unit. According to the piecewise linear method, the expressions V2 and VbVj are equal to and $\left(V^{min}()^{2^{min\sum_{l\varepsilon\phi_l}\Delta V_{b,l}}}{}^{min\sum_{l\varepsilon\phi_l}\Delta V_{j,l}}\right)$, respectively. m represents the slope of the line segments. The variables θ and ΔV have a low value, so their product and their power are very small and can be neglected. With these conditions, the linear approximation model of relations (3) and (4) is the same as relations (22) and (23) respectively:

$$PL_{b,j,t} = g_{b,j}\left(\sum_{l\varepsilon\varphi_l}(m_l - V^{min})\,\Delta V_{b,t,l} - V^{min}\Delta V_{b,t,l}\right) - (V^{min})^2 b_{b,j}\left(\theta_{b,t} - \theta_{j,t}\right) \;:\; \lambda^{pl}_{j,t} \quad \forall b,j,t \tag{22}$$

$$QL_{b,j,t} = -b_{b,j}\left(\sum_{l\varepsilon\varphi_l}(m_l - V^{min})\,\Delta V_{b,t,l} - V^{min}\Delta V_{j,t,l}\right) - (V^{min})^2 g_{b,j}\left(\theta_{b,t} - \theta_{j,t}\right) \;:\; \lambda^{ql}_{j,t} \quad \forall b,j,t \tag{23}$$

Since the voltage deviation variable is used in the linear approximation model of relations (4) and (5), therefore, since the voltage deviation variable is used in the linear approximation model of relations (4) and (5), therefore, the following limit replaces the limit The voltage (7) becomes: the following constraint replaces the voltage constraint (7):

$$0 \le \Delta V_{b,t,l} \le \Delta V^{max} \;:\; \bar{\mu}^{v}_{b,t,l} \quad \forall b,j,t \tag{24}$$

Constraints (8), (9), (16), (18) and (19) are circular inequalities that can be linearized using the regular polygon method. In this method, the circular plane, $(P)^2 + (Q)^2 \le (S)^2$, is approximated to a regular polygonal plane. The equation of each side (k) of this plane is linear, which can be expressed as (24):

$$\cos(k\Delta\alpha)\,P + \sin(k\Delta\alpha)\,Q = S \tag{25}$$

In this regard, Δα represents the angular deviation, and its value is equal to 360/nk. nk represents the number of regular polygon sides. The square plane resulting from the linear equation (25) is as (26):

$$\cos(k\Delta\alpha)\,P + \sin(k\Delta\alpha)\,Q \le S \tag{26}$$

Repetition of equation (26) for all values of k leads to extraction of the plane in the form of regular polygons. Therefore, constraints (8), (9), (16), (18) and (19) can be expressed as relations (27)-(31) respectively:

$$the\ \cos(\mathrm{k}\Delta\alpha)\,PL_{\mathrm{b,j,}t} + \sin(\mathrm{k}\Delta\alpha)\,QL_{\mathrm{b,j,}t} \le SL^{max}_{b,j} \;:\; \bar{\mu}^{sl}_{b,j,t,k} \quad \forall b,j,t,k \tag{27}$$

$$\cos(\mathrm{k}\Delta\alpha)\,PG_{b,t} + \sin(\mathrm{k}\Delta\alpha)\,QG_{b,t} \le F^{sub}_{b}SG^{max}_{b} \;:\; \bar{\mu}^{sg}_{b,t,k} \quad \forall b,t,k \tag{28}$$

$$\cos(\mathrm{k}\Delta\alpha)\,PE_{b,t} + \sin(\mathrm{k}\Delta\alpha)\,QE_{b,t} \le SE^{max}_{b,j} \;:\; \bar{\mu}^{se}_{b,t,k} \quad \forall b,t,k \tag{29}$$

$$\cos(\mathrm{k}\Delta\alpha)\,PDG_{b,t} + \sin(\mathrm{k}\Delta\alpha)\,QDG_{b,t} \le SDG^{max}_{b,j} \;:\; \bar{\mu}^{dg}_{b,t,k} \quad \forall b,t,k \tag{30}$$

$$\cos(\mathrm{k}\Delta\alpha)\,PS_{b,t} + \sin(\mathrm{k}\Delta\alpha)\,QS_{b,t} \le SS^{max}_{b,j} \;:\; \bar{\mu}^{ss}_{b,t,k} \quad \forall b,t,k \tag{31}$$

Based on relations (11) and (15), the variable PE always has a positive value, so the expression |PE| In relations (13) and (14), it can be written as PE. In addition, it should be noted that generally the consumers of the distribution network are ohmic-selfish. Therefore, reactive power control devices such as EVs will work in a capacitive mode to compensate for reactive power consumption. Therefore, the term QE will always have a negative value, following this, |QE| can be written as -QE. Therefore, relations (13) and (14) can be written as (32) and (33), respectively:

$$PLC_{b,t} = a_r PE_{b,t} - \; a_{im} QE_{b,t} \;:\; \lambda^{plc}_{b,t} \quad \forall b,t \tag{32}$$

$$QLC_{b,t} \;= b_r PE_{b,t} - \; b_{im} QE_{b,t} \;:\; \lambda^{qlc}_{b,t} \quad \forall b,t \tag{33}$$

Finally, the linear approximation model for the proposed design can be written as follows:

$$min_{PG} \sum_{t\varepsilon\varphi_t}\sum_{b\varepsilon\varphi_b} T_{stop}F^{sub}_{b}\rho^{p}_{b,t}PG_{b,t} \tag{34}$$

Subject to:

Constraints (2), (3), (6), (10)-(12), (15), (17), (20)-(21) with dual variables as $\lambda_{b,t}^{p}$, $\lambda_{b,t}^{q}$, λ_{t}^{θ} , $\mu_{b,t}^{pf}$ and $\bar{\mu}_{b,t}^{pf}$, $\lambda_{b,t}^{pc}$, $\lambda_{b,t}^{qc}$, $\bar{\mu}_{b,t}^{pb}$, λ_{b}^{cc} , λ_{b}^{es}, $\mu_{b,t}^{es}$ and $\bar{\mu}_{b,t}^{es}$ respectively. (35)

Constraints (22)-(24), (27)-(33) (36)

The expressions λ and μ in each relationship represent binary variables related to this relationship.

III. ROBUST OPTIMIZATION

A. Uncertainty parameters

The issue model includes characteristics with uncertainties such as active and reactive loads, PD and QD, energy price, , charging rate of EV battery aggregation (PB), EV charger aggregation capacity (SEmax), needed energy consumption of EV aggregation (EC), and active power Renewable DGs (PDGs). The matrix representing the uncertainty parameter is as follows:

$$\bar{u}=\left[PD_{b,t}QD_{b,t}PB_{b,t}^{max_{b,t}^{\;\;max_{b_{b,t_{b,t}}^{p}}}}\right] \tag{37}$$

The uncertainty parameter matrix has nb rows and (6nt + 1) columns. Nb represents the number of network buses and nt represents the operating hours. Uncertainty is a reliable indicator of the expected value of variables, as stated in reference [18]. Another way to define the uncertainty variable matrix is as follows:

$$u=\left[P_{b,t}^{u}Q_{b,t}^{u}PB_{b,t}^{u}SE_{b,t}^{u}E_{b}^{u}\rho_{b,t}^{up}PDG_{b,t}^{u}\right] \tag{38}$$

B. ARO formulation

This part uses the ARO formulation to represent the uncertainty in (38), making up for the remaining research gap in section 1. In ARO, a scenario that results in the worst possible circumstance for the issue in terms of the objective function is retrieved for the uncertainty variables [17]. We refer to this situation as the worst-case scenario. ARO finds both the worst-case situation and the ideal quantity of the problem's primary variables at the same time. As a result, the problem's objective function in ARO is given by the expression max min, where the term max is used to extract the number of uncertainty variables, u, in the worst scenario, and the term min (corresponding to relation (1)) is used to find the main problem's optimal variable value. It is the scenario's case. The same specific issue, (34)– (36), is included in the internal formulation of the ARO problem (min expression). The u matrix in relation (38) takes the place of the matrix in this issue. The collection of uncertainties yields the u matrix's range of changes, which may be expressed as the following relationship for row b of the u matrix [18]:

$$U^{b}(\bar{u}^{b},\tilde{u}^{b},\triangle^{b})=\left\{\begin{matrix}u^{b}\varepsilon R^{6n_t+1}:\frac{1}{6n_t+1}\sum_{i=1}^{6n_t+1}\frac{\left|u_i^b-\tilde{u}_i^b\right|}{\tilde{u}_i^b}\leq\triangle^{b},\\ \tilde{u}_i^b\varepsilon[\bar{u}_i^b-\tilde{u}_i^b,\bar{u}_i^b+\tilde{u}_i^b]\end{matrix}\right\} \tag{39}$$

In this regard, , and respectively show the i-th variable of uncertainty, the amount of deviation of uncertainty, and the normal value (prediction) of uncertainty in bus b. represents the uncertainty budget, which is between zero and one. If is equal to zero, the deterministic model is established, and if the uncertainty budget is greater than zero, the stable model is established. Moreover, the interval is equal to the interval of variation of the uncertainty variable. Then the uncertainty set is defined as [18]. In the following phase of ARO, the term max min must be modified to max or min so that the issue may be solved using traditional solvers. In these circumstances, the dual model of the internal issue (i.e. the problem involving the word min) is retrieved. In these circumstances, the term max max is retrieved for the ARO issue, which corresponds to an objective function problem with max. As a result, the ARO model for the proposed plan includes a dual objective function for problems (34)-(36). It has two constraints: issue (34)-(36) and constraint [18]. Thus, the suggested ARO model is as follows:

$$max_{u,\lambda,\mu}\sum_{b\in\varphi_b}\{E_b^u\lambda_b^{ec}+\sum_{t\in\varphi_t}\{P_{b,t}^u\lambda_{b,t}^p+Q_{b,t}^u\lambda_{b,t}^q+PB_{b,t}^u\bar{\mu}_{b,t}^{pb} \tag{40}$$

$$+\left(\sum_{l\in\varphi_l}^{\bar{\Sigma}_{b,t,l}^{v}}\Delta V_b^{max}\;()\right)$$

$$\sum_{\substack{k\in\varphi_k\\ b\text{withrenewableDG}}}\left\{cos(k\Delta\alpha)PDG_{b,t}^{u}\bar{\mu}_{b,t,k}^{se}\right\}+E$$

$$\Sigma\Sigma^{\Sigma}_{k\in\varphi_k}\left\{\begin{matrix}SDG_{b,t}\mu_{b,t,k}^{dg}+SS_{b,t}\mu_{b,t,k}^{ss}\\ +SE_{b,t}^{u}\bar{\mu}_{b,t,k}^{se}+F_b^{sub}SG_b^{ma\bar{x}_{b,t,k}^{sg}}\end{matrix}\right\}\}\}\}$$

$$ma\bar{x}_{b,t}^{es\;min_{b,t}^{es}}\sum_{j\in\varphi_b}\sum_{k\in\varphi_k}^{\Sigma}\left\{SL_{b,j}^{ma\bar{x}_{b,j,t,k}^{sl}}\{\}\right\}$$

Subject to:

$$\lambda_{b,t}^{p}+\sum_{k\in\varphi_k}cos(k\Delta\alpha)\overline{\mu}_{b,t,k}^{sg}+F_b^{sub}TPF(\mu_{b,t}^{pf}-\overline{\mu}_{b,t}^{pf}) \tag{41}$$
$$=T_{stop}F_b^{sub}\rho_{b,t}^{p}:PG_{b,t}\quad\forall b$$
$$=ref,t$$

$$\lambda_{b,t}^{q}+\mu_{b,t}^{pf}+\overline{\mu}_{b,t}^{pf}+\sum_{k\in\varphi_k}sin(k\Delta\alpha)\overline{\mu}_{b,t,k}^{sg} \tag{42}$$
$$=0:QG_{b,t}\quad\forall b=ref,t$$

$$-\lambda_{b,t}^{p}+\lambda_{b,t}^{pe}-a_r\lambda_{b,t}^{plc}-b_r\lambda_{b,t}^{qlc} \tag{43}$$
$$+\sum_{k\in\varphi_k}cos(k\triangle\alpha)\overline{\mu}_{b,t,k}^{se}\leq 0$$
$$:\;PE_{b,t}\;\forall b,t$$

$$-\lambda^{q}_{b,t} + \lambda^{qe}_{b,t} + \sum_{k\in\varphi_k} sin(\,k \triangle \alpha)\overline{\mu}^{se}_{b,t,k} \geq 0 \quad : \; QE_{b,t} \; \forall b,t \tag{44}$$

$$-\lambda^{pe}_{b,t} + T_{stop}\lambda^{ec}_{b} + \overline{\mu}^{pb}_{b,t} \leq 0 : \; PB_{b,t} \; \forall b,t \tag{45}$$

$$-\lambda^{qe}_{b,t} = 0 : \; QC_{b,t} \; \forall b,t \tag{46}$$

$$-\lambda^{pe}_{b,t} + \lambda^{plc}_{b,t} \leq 0 : \; PLC_{b,t} \; \forall b,t \tag{47}$$

$$-\lambda^{qe}_{b,t} + \lambda^{qlc}_{b,t} \leq 0 : \; QLC_{b,t} \; \forall b,t \tag{48}$$

$$-A_{b,j}\lambda^{p}_{b,t} + \lambda^{pl}_{b,j,t} + \sum_{k\in\varphi_k} cos(\,k \triangle \alpha)\overline{\mu}^{sl}_{b,j,t,k} = 0 \quad : \; PL_{b,j,t} \; \forall b,j,t \tag{49}$$

$$-A_{b,j}\lambda^{q}_{b,t} + \lambda^{ql}_{b,j,t} + \sum_{k\in\varphi_k} sin(\,k \triangle \alpha)\overline{\mu}^{sl}_{b,j,t,k} = 0 \quad : \; QL_{b,j,t} \; \forall b,j,t \tag{50}$$

$$\lambda^{p}_{b,t} + \sum_{k\in\varphi_k} cos(k\Delta\alpha)\, \mu^{dg}_{b,t,k} \leq 0 : PDG_{b,t} \; \forall b, tif \text{DGisnotrewnable} \tag{51}$$

$$\lambda^{q}_{b,t} + \sum_{k\in\varphi_k} sin(k\Delta\alpha)\, \mu^{dg}_{b,t,k} = 0 : QDG_{b,t} \; \forall b,t \tag{52}$$

$$\lambda^{p}_{b,t} + \eta\lambda^{es}_{b,t} + \sum_{k\in\varphi_k} cos(k\Delta\alpha)\, \mu^{ss}_{b,t,k} = 0 : PS_{b,t} \; \forall b,t \tag{53}$$

$$\lambda^{q}_{b,t} + \sum_{k\in\varphi_k} sin(k\Delta\alpha)\, \mu^{ss}_{b,t,k} = 0 : QS_{b,t} \; \forall b,t \tag{54}$$

$$\lambda^{es}_{b,t} - \lambda^{es}_{b,t+1} + \mu^{es}_{b,t} + \bar{\mu}^{es}_{b,t} \leq 0 : ES_{b,t} \; \forall b,t \tag{55}$$

$$\left(V^{min}()^2 \sum_{j\in\varphi_b} \Big(b_{b,j}(\lambda^{pl}_{b,j,t} - \lambda^{pl}_{j,b,t}) + g_{b,j}(\lambda^{ql}_{b,j,t} - \lambda^{ql}_{j,b,t})\Big)^{\theta}_{b_t \; b,t} \right) \quad \forall b,t \& z_b = 1 \; \forall b \; = \; ref \tag{56}$$

$$\bar{\mu}^{v}_{b,t,l} - \sum_{j\in\varphi_b} \Big\{ g_{b,j}\Big(\big(m_l - V^{\min}\big)\lambda^{pl}_{b,j,t} - V^{\min}\lambda^{pl}_{b,j,t} \Big) + b_{b,j}\Big(\big(m_l - V^{\min}\big)\lambda^{ql}_{b,j,t} - V^{\min}\lambda^{ql}_{b,j,t} \Big) \Big\} \leq 0 : \Delta V_{b,t,l} \quad \forall b,j,t,l \tag{57}$$

$$\lambda = free, \;\; \mu \leq 0, \; \bar{\mu} \geq 0 \tag{58}$$

$$u \in U \tag{59}$$

The relations (40)-(58) represent the duals of the problem (34)-(36), in case the variable u is parameterized instead $\bar{u}$. Constraint (59) represents the limitation of uncertainties or the worst-case scenario. In addition, it should be noted that relation (40) has non-linear expressions $E^{u}_{b}\lambda^{ec}_{b}$, $P^{u}_{b,t}\lambda^{p}_{b,t}$, $Q^{u}_{b,t}\lambda^{q}_{b,t}$, $PB^{u}_{b,t}\bar{\mu}^{pb}_{b,t}$, and $PDG^{u}_{b,t}\bar{\mu}^{se}_{b,t,k}$. But these expressions are in the objective function and the objective function is of the second degree. This type of problem is due to having convex linear constraints, and it can be solved by powerful solvers such as CPLEX in optimization software such as GAMS [25]. Finally, the flowchart of the scheme is shown in Fig. 1.

The scheme includes the mathematical formulation [26-29]. This formulation is based on the optimization model [30-31]. The optimization problem contains an objective function [32-34]. This function includes min or max term [35-36]. It is a single of multi-objective model [37]. There are different constraints in the optimization problem [38-39]. Constraint contains equality or inequality formulations [40]. To apply the optimization model on the network, the network needs smart devices [41-43]. The smart devices are based on Telecommunication tools and smart algorithms [44-46].

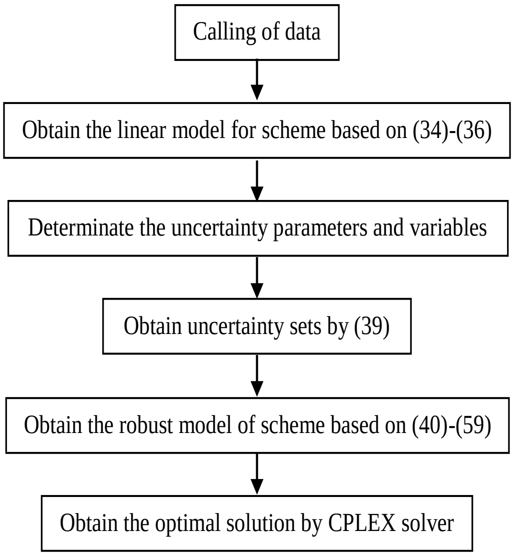

Fig. 1. Single-line Flowchart of scheme

IV. Numerical results

A. Case study

The proposed scheme in this section is implemented on the IEEE standard 33-bus radial distribution network, whose single-line circuit is shown in Figure (2) [47]. This network has a basic voltage and power of 12.66 kV and one megawatt, and its minimum and maximum allowed voltage range is equal to 0.9 to 1.05 per-unit [48-53]. The characteristics of distribution lines and substations are reported in [47]. Reference [47] also includes peak load data. The amount of load in other hours is calculated by multiplying the load of the peak hour and the load factor curve [54-59]. This curve is presented in [17]. The price of energy for hours 1:00-7:00 is equal to \$16/MWh, it is equal to \$30/MWh in hours 17:00-22:00. In other hours, the energy price is equal to \$24/MWh [17]. It has been assumed that there is parking for EVs in all buses except the slack bus. Their number in the parking lot is 21, 30 or 60. Buses whose active peak load is between zero and 0.1 (0.2-0.1) per-unit, the number of EVs in that bus is equal to 21 (30). But if the reactive peak load is more than 0.2, the number of EVs in that bus is equal to 60. Other characteristics of EVs such as battery capacity, SOC, charger capacity, and charging rate are stated in [16-17]. The loss coefficients , and are assumed to be the same for all EVs, which are assumed to be 0.09, 0.0475, 0.02, and 0.02, respectively. The number of EVs per hour is equal to the product of the total number of EVs in the park and the daily EV penetration rate curve. This curve is described in [17]. In the mentioned network, two wind system (WS) type DGs with 1.5 and 1.8 per-unit capacities were installed in 16 and 47 buses, respectively. In Bus 31 / 56, there is a photovoltaic (PV) / fuel cell (FC) DG with a capacity of 2.1/1. The active production power of WS and PV is equal to the product of their capacity and the daily curve of their production power rate. These curves are presented in [1]. In buses 18 and 57, two batteries with a capacity of 1 MWh and an efficiency of 92% have been installed, the charger capacity of which is equal to 0.3 per-unit. The minimum energy stored in each of the batteries is equal to 0.1 MWh. The time step is one hour and the starting time of the simulation is 10:00 am due to the continuous energy in terms of time or relation (17).

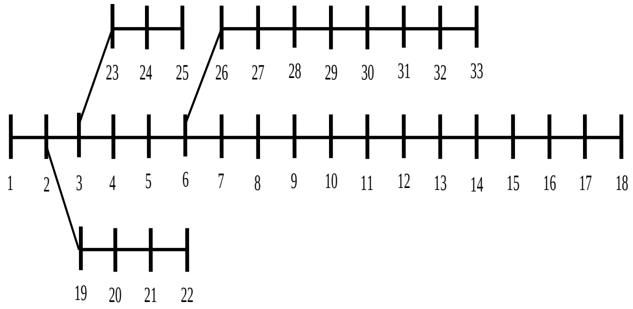

Fig. 2. Single-line circuit of IEEE standard 33 bus radial distribution network [47]

V. Simulation results

The proposed design is coded according to the data of sections 1-4 in the GAMS software environment [25]. 5 linear pieces are used for voltage linearization. A circular plate is rounded to a regular 90-sided plate. The uncertainty deviation, $\tilde{u}$, is equal to the product of the uncertainty budget, Δ, the radius of uncertainty, r, and $\bar{u}$is considered.

A. Comparison of different deterministic models for the proposed plan

The nonlinear model for the requested issue is shown in Table (2) inside the GAMS software [21]. The nonlinear model utilizes mathematical solvers CONOPT, COUENNE, IPOPT, MINOS, PATHNLP, and SNOPT, whilst the linear model employs solvers CPLEX, BDMLP, CBC, CONOPT, and GLPK. These answers rely on mathematical approaches detailed in reference [21]. This table shows that various solvers' solutions to the nonlinear problem model vary, and that their solution times are lengthy. Additionally, the state of the solution is identical to the local optimum for certain solvers. The problem is not with the convergence point. However, in exchange, other linear problem solvers have succeeded in reaching the ultimate optimum point, and their optimal solution yields an answer that is the same for every solver. The computation time and the quantity of problem-solving iterations are the sole distinctions between them. The suggested linear issue is best served by the CPLEX method, whereas the nonlinear problem is best served by the IPOPT algorithm. The CPLEX method is selected due to its very short calculation time, and the IPOPT algorithm is selected because it has been able to reach a low level of the objective function in comparison to other algorithms in the nonlinear problem.

TABLE 2

COMPARISON OF THE RESULTS OBTAINED FROM DIFFERENT SOLVERS AND ALGORITHMS

The deterministic non-linear model

Solver	Iteration	Calculation time (sec)	Objective function ($)	Model state
CONOPT	390	44	1432.6	**Locally optimal**
IPOPT	34	51.4	1007.3	
MINOS	400	546.5	1268.3	
COUENNE	Infeasible solution			
PATHNLP				
SNOPT				

The deterministic linear model

Solver	Iteration	Calculation time (sec)	Objective function ($)	Model state
CPLEX	7444	6.6	523.7	**Global optimal**
BDMLP	7787	139.3		
CBC	3788	10.4		
CONOPT	92	57.1		
GLPK	9395	182.2		

B. Checking the performance of resources and storage devices

In this section, two studies have been carried out, which are:

- The first study cases (I): evaluation of the results obtained from the deterministic linear model of the proposed problem
- Second study cases (II): evaluation of the results obtained from the robust linear model of the proposed problem with the assumption of an uncertainty budget equal to 1 and uncertainty radius equal to 0.1

The results of this section are shown in figures (3)-(7), which are equal to the daily curve of active and reactive power of total

EVs, the daily curve of active and reactive power of PVs, the daily curve of active and reactive power of WS, the daily curve of power Active and reactive are the sum of FCs and the daily curve of active and reactive power is the sum of batteries. Based on Figure (3-A), it can be seen that EVs charge during off-peak hours due to low energy prices. Also, their charging level is higher in the stable model than in the deterministic model. Based on Figure (3-b), EVs spend more hours injecting reactive power into the distribution network in the stable model than in the deterministic model.

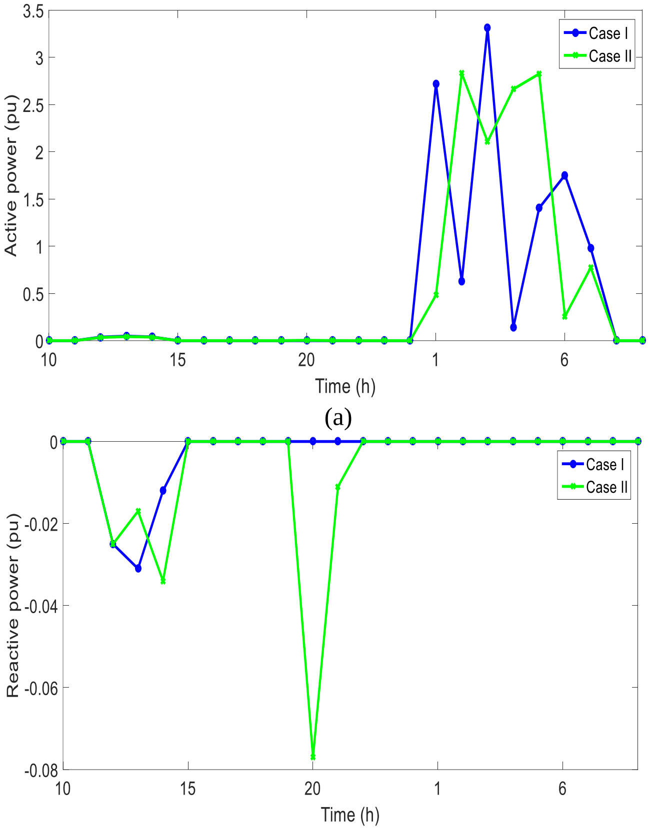

(a)

(b)

Fig. 3. Daily curve, (a) active power, (b) reactive power of total EVs

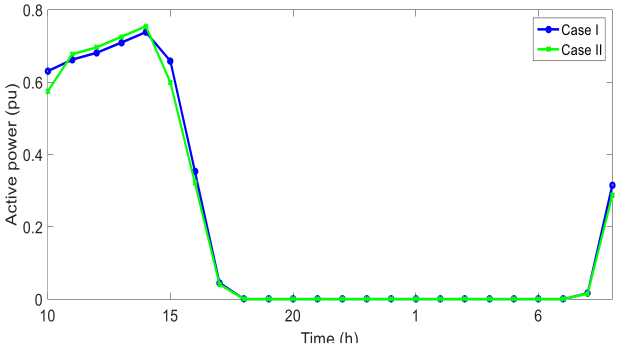

(a)

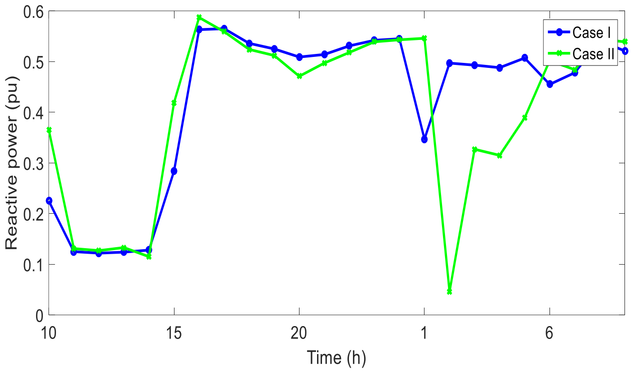

(b)

Fig. 4. Daily curve, (a) active power, (b) reactive power of total solar systems

Based on Figure (4-a) / (5-a), it can be seen that solar/wind systems inject active power into the distribution network when there is solar radiation/wind speed according to [1]. Also, in the stable model compared to the deterministic model, the active power level of renewable sources has decreased. Based on Figure (4-b)/(5-b), high reactive power is injected into the grid by solar and wind systems at most hours, and at most hours, the reactive power in the stable model is more than the reactive power in the deterministic model.

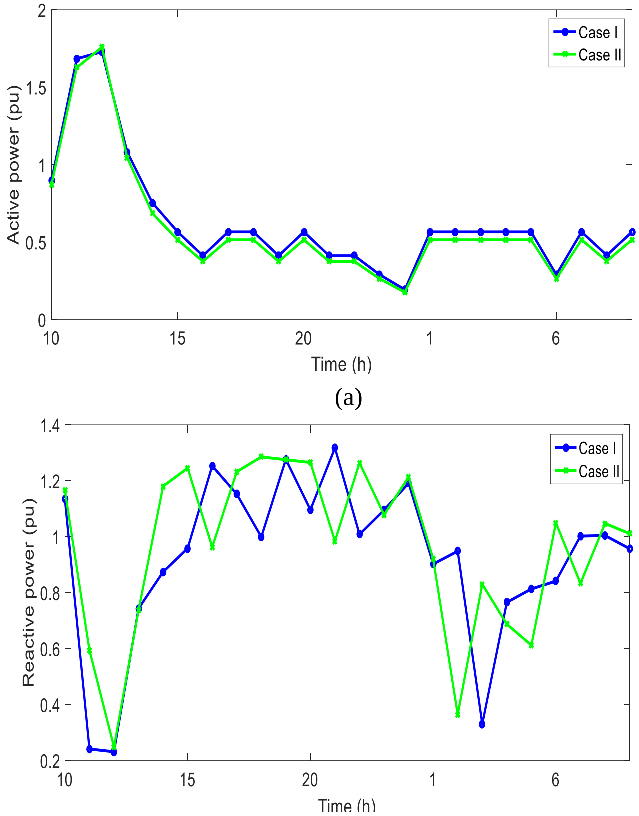

(a)

(b)

Fig. 5. Daily curve, (a) active power, (b) reactive power of total wind systems

Based on Figure (6-a), it can be seen that the fuel cell systems inject high active power into the network in all hours of the simulation compared to their capacity. Also, in the stable model and the deterministic model, the active power level of the fuel cell systems is the same. Based on Figure (6-b), low reactive power is injected into the network by fuel cell systems in most hours, and the reactive power of fuel cell systems is the same in two stable and deterministic models.

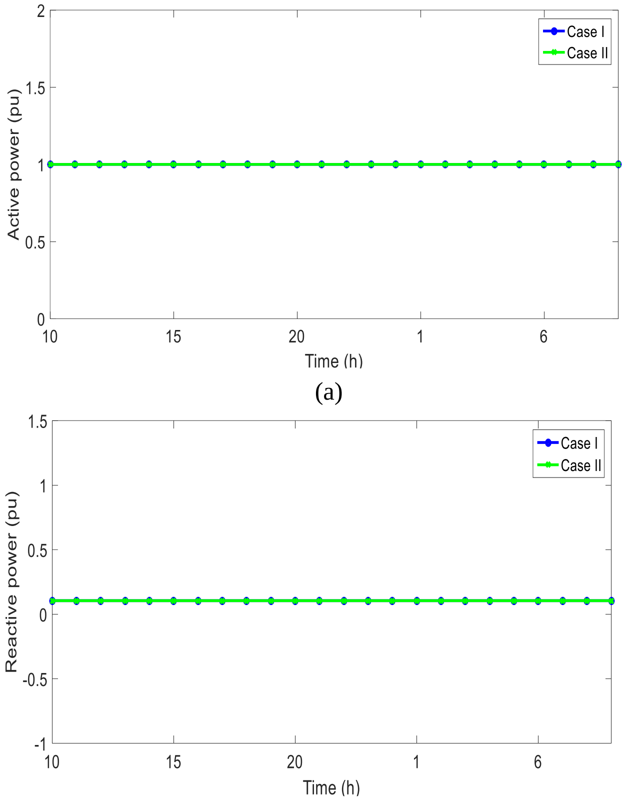

(a)

(b)

Fig. 6. Daily curve, (a) active power, (b) reactive power of total fuel cell systems

Based on Figure (7-A), it can be seen that energy storages perform charging operations during off-peak and mid-load hours due to the low price of energy and are discharged during other hours. It can also be said that in the stable model compared to the deterministic model, the power level of the storage generators has increased in most hours. In addition, based on Figure (7-b), it can be seen that the ripple of changes in the reactive power of energy storage is high both in the stable model and the deterministic model.

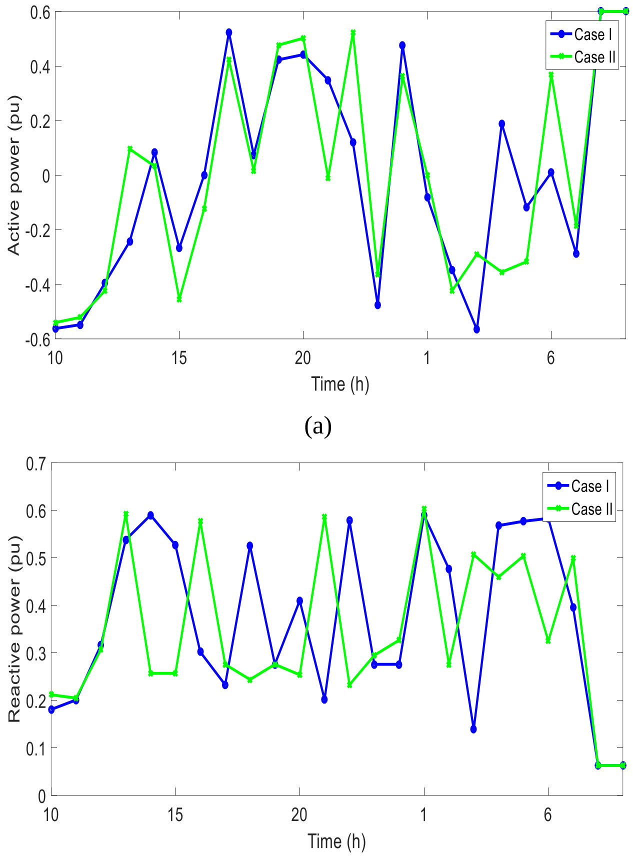

(a)

(b)

Fig. 7. Daily curve, (a) active power, (b) reactive power of total energy storage

C. *Check network indicators*

In this section, the network indicators, including the transmission power of the distribution post, voltage profile, and network losses due to the study cases of the previous section are evaluated. The results of this section are shown in figures (8) to (10). Based on Figure (8), it can be seen that in the stable model, the apparent power of the distribution substation located in the reference bus (bus 1) increases in most of the simulation hours compared to the deterministic model. This shows that in the worst-case scenario, the amount of active and reactive loads and the amount of demand for electric vehicles have increased compared to the scenario corresponding to the deterministic model. Also, the active power capacity of wind and solar systems and the reactive power capacity of wind and solar systems and electric vehicles have decreased. Therefore, the demand from the upstream network has increased in the stable model.

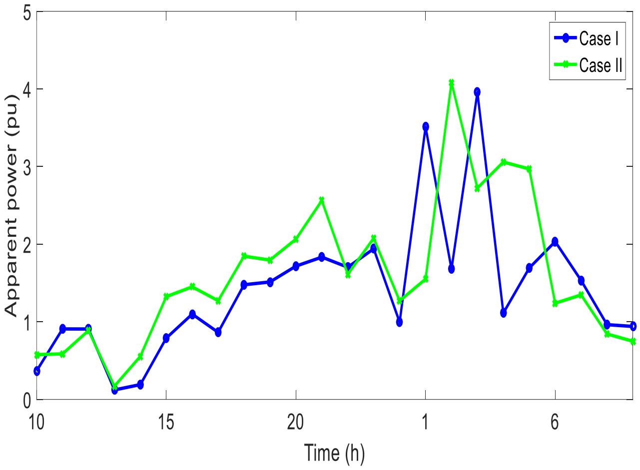

Fig. 8. The daily curve of the apparent power of the distribution substation (Bus 1)

It is worth noting that it can be seen that the voltage of all buses has decreased in the stable model compared to the deterministic model based on Figure (9). Therefore, the network voltage drop in the stable model is more than the voltage drop in the deterministic model. It can also be seen that following the mentioned topic, the active losses of the distribution network have increased in the stable model compared to the deterministic model. Therefore, it can be mentioned that in the stable model, the amount of power demand in the network has increased, but in return, the power generation capacity of scattered productions and electric vehicles has decreased.

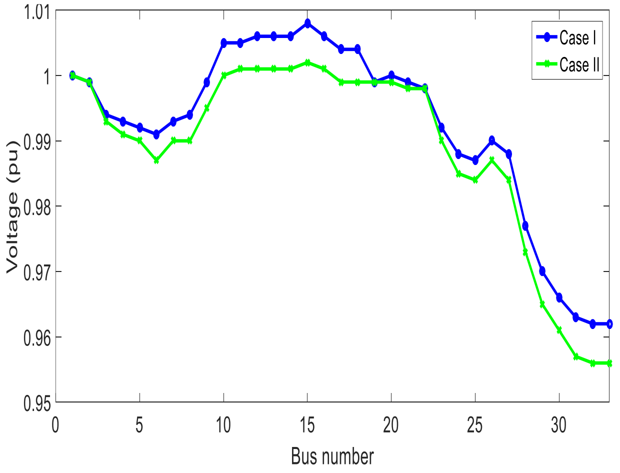

Fig. 9. Voltage profile at peak hour (20:00)

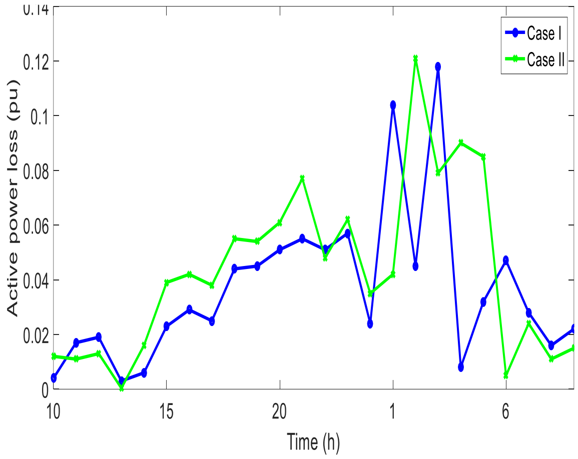

Fig. 10. Time curve of network losses

D. Evaluation of the robust model

Table (3) displays the results of this section, showing the energy cost (objective function), the uncertainty parameters of the robust model for different levels of uncertainty, and the uncertainty budget set at one. According to the statistics, in the worst-case scenario when the stable model is compared to the deterministic model (uncertainty level is zero), the active and reactive demand of network consumption, energy demand of electric vehicles, and energy price all increase. Now, these parameters rise along with these degrees of uncertainty. The level of reactive power production of all electric vehicles, the level of active power production of solar systems, the level of active power production of wind systems, and the charging rate of all electric vehicles in the worst-case scenario are all visible in this table. When comparing the stable model to the deterministic model, they are smaller (the amount of uncertainty is equivalent to zero). Now, these factors also drop as these degrees of uncertainty rise. These directives state that the price of energy will rise as the degree of uncertainty rises.

TABLE 3
THE AMOUNT OF ENERGY COST AND UNCERTAINTY PARAMETERS IN THE STABLE MODEL WITH AN UNCERTAINTY BUDGET EQUAL TO ONE AND VARIOUS LEVELS OF UNCERTAINTY

Parameter	**Unit**	**Uncertainty level**				
		0	**0.02**	**0.04**	**0.06**	**0.08**
Sum of P^u	p.u.	56.592	57.724	58.855	59.987	61.119
Sum of Q^u	p.u.	35.037	35.737	36.438	37.139	37.840
Sum of PW^u	p.u.	18.112	17.750	17.338	17.026	16.663
Sum of PPV^u	p.u.	7.654	7.501	7.348	7.195	7.042
Sum of PB^u	p.u.	48.825	47.849	46.872	45.895	44.919
Sum of S^u	p.u.	74.865	73.368	71.870	70.373	68.876
Sum of E^u	p.u.	241.416	246.244	251.073	255.901	260.729
Sum of ρ^{up}	$/MWh	556	567.12	578.24	589.36	600.48
Energy cost	$	523.751	571.458	621	672.380	725.305

VI. Conclusions

In this article, the operation of the intelligent distribution network in the presence of electric vehicles, stationary sources, and storage devices, taking into account the simultaneous management of their active and reactive power, was described. This plan was responsible for the minimization of the operating cost by taking into account the constraints of the optimal power distribution of the network and the operating model of the mentioned elements. This plan included load uncertainties, energy prices, renewable power, and parameters of electric vehicles, which adaptive robust optimization was used to model them. Also, this design used the linear approximation model of optimal power distribution. Further, based on the numerical results, it was observed that the linearized model of the proposed design can greatly reduce the calculation time compared to the non-linear model. It always has a unique solution. In the worst-case scenario, energy demand increases, while the ability of mobile resources and storage devices in energy production decreases. The performance of sources and storage is such that the apparent power passing through the distribution post is reduced, energy losses are reduced, and a smoother voltage profile is obtained. Effects of DG, EVs, and ESSs size and location not considered in this paper. Also, the simulation results under types of faults are not demonstrated. To cope with this issue, the reliability-based network operation considering the sitting and sizing model of sources and storage is investigated in future works.

REFERENCES

[1] F. Khalafian, and et al., “Capabilities of compressed air energy storage in the economic design of renewable off-grid system to supply electricity and heat costumers and smart charging-based electric vehicles,” Journal of Energy Storage, vol. 78, pp. 109888, 2024.

[2] H.R. Zafarani, S.A. Taher, M. Shahidehpour, “Robust operation of a multicarrier energy system considering EVs and CHP units,” Energy, vol. 192, pp. 116703, 2020.

[3] M.R. AkbariZadeh, T. Niknam, A. Kavousi-Fard, “Adaptive robust optimization for the energy management of the grid-connected energy hubs based on hybrid meta-heuristic algorithm,” Energy, vol. 235, pp. 121171, 2021.

[4] S.Pirouzi, “Network-constrained unit commitment-based virtual power plant model in the day-ahead market according to energy management strategy,” IET Generation, Transmission & Distribution, vol. 17, no. 22, pp. 4958-4974, 2023.

[5] R.C. Leou, C.L. Su, and C.N. Lu, “Stochastic analyses of electric vehicle charging impacts on distribution network,” IEEE Trans. Power Syst., vol. 29, no. 3, pp. 1055-1063, May 2014.

[6] O. Erol, Ü.B. Filik, “A Stackelberg game-based dynamic pricing and robust optimization strategy for microgrid operations,” International Journal of Electrical Power & Energy Systems, vol. 155, pp. 109574, 2024.

[7] M. Fotopoulou, D. Rakopoulos, S. Petridis, P. Drosatos, “Assessment of smart grid operation under emergency situations,” Energy, vol. 287, pp. 129661, 2024.

[8] R. Fathi, B. Tousi, S. Galvani, “Allocation of renewable resources with radial distribution network reconfiguration using improved salp swarm algorithm,” Applied Soft Computing, vol. 132, pp. 109828, 2023.

[9] F.H. Aghdam, M.W. Mudiyanselage, B. Mohammadi-Ivatloo, M. Marzband, “Optimal scheduling of multi-energy type virtual energy storage system in reconfigurable distribution networks for congestion management,” Applied Energy, vol. 333, pp. 120569, 2023.

[10] B. Stojanović, T. Rajić, D. Šošić, “Distribution network reconfiguration and reactive power compensation using a hybrid Simulated Annealing – Minimum spanning tree algorithm,” International Journal of Electrical Power & Energy Systems, vol. 147, pp. 108829, 2023.

[11] H. Ruan, H. Gao, H. Qiu, H.B. Gooi, J. Liu, “Distributed operation optimization of active distribution network with P2P electricity trading in blockchain environment,” Applied Energy, vol. 331, pp. 120405, 2023.

[12] Z. Yang, F. Yang, H. Min, H. Tian, W. Hu, J. Liu, N. Eghbalian, “Energy management programming to reduce distribution network operating costs in the presence of electric vehicles and renewable energy sources,” Energy, vol. 263, pp. 125-695, 2023.

[13] W. Li, Y. Han, Y. Feng, S. Zhou, P. Yang, C. Wang, A.S. Zalhaf, “Evaluation of probabilistic model solving methods for modern power electronic distribution networks with wind power integration,” Energy Reports, vol. 9, pp. 1159-1171, 2023.

[14] H. Xiao, W. Pei, L. Wu, L. Ma, T. Ma, W. Hua, “A novel deep learning based probabilistic power flow method for Multi-Microgrids distribution system with incomplete network information,” Applied Energy, vol. 335, pp. 120716, 2023.

[15] A.A. Dashtaki, S.M. Hakimi, A. Hasankhani, G. Derakhshani, B. Abdi, “Optimal management algorithm of microgrid connected to the distribution network considering renewable energy system uncertainties,” International Journal of Electrical Power & Energy Systems, vol. 145, pp. 108633, 2023.

[16] H. Kiani, K. Hesami, A.R. Azarhooshang, S. Pirouzi, S. Safaee, “Adaptive robust operation of the active distribution network including renewable and flexible sources,” Sustainable Energy, Grids and Networks, vol. 26, pp. 100476, 2021.

[17] S. Pirouzi, J. Aghaei, V. Vahidinasab, T. Niknam, A. Khodaei, “Robust linear architecture for active/reactive power scheduling of EV integrated smart distribution networks,” Electric Power Systems Research, vol. 155, pp. 8-20, 2018.

[18] H.Zakernezhad, H. Nazar, M.Shafie-khah, & J.Catalão, ”Optimal scheduling of an active distribution system considering distributed energy resources, demand response aggregators, and electrical energy storage”. Applied Energy, 314, 118865.2022.

[19]] A.Bostan, M. Nazar, M.Shafie-Khah & Catalão, J. P. “Optimal scheduling of distribution systems considering multiple downward energy hubs and demand response programs:. Energy, 190, 116349.2020

[20] Z.Liu, & H. Liang, H, November.” Optimal scheduling of distribution network based on improved whale algorithm’. In 2022 IEEE 5th International Conference on Automation,

Electronics and Electrical Engineering (AUTEEE) (pp. 987-990). IEEE.2022.

[21] N.Huang, L.Hu, R.Wang, Cai, G., Guo, Y., & Zhao, X, " Multi-Objective Optimal Scheduling of Distribution Network with Electric Vehicle Charging Load Considering Time-Varying Road Impedance", Journal of Electrical Engineering & Technology, 18(4), 2667-2681.2023

[22] H.Abdulwahid, A.Al-Razgan, M., Fakhruldeen, H. F., Churampi Arellano, M. T., Mrzljak, V., Arabi Nowdeh, S., & Moghaddam, M. J. H,"Stochastic multi-objective scheduling of a hybrid system in a distribution network using a mathematical optimization algorithm considering generation and demand uncertainties", Mathematics, 11(18), 3962.2023.

[23] X.Fan, " Multiobjective Optimal Dispatching Method of Generalized Power Active Distribution Network Based on Game Theory", Security and Communication Networks, PP, 1-10.2021.

[24] D. Bertsimas, E. Litvinov, X. A. Sun, J. Zhao, and T. Zheng, "Adaptive robust optimization for the security constrained unit commitment problem," IEEE Trans. Power Syst., vol. 28, no. 1, pp. 52-63, Feb. 2013.

[25] Generalized Algebraic Modeling Systems (GAMS), Available: http://www.gams.com, [Online].

[26] Z.Luo,H. Xu & Chen, F," Audio Sentiment Analysis by Heterogeneous Signal Features Learned from Utterance-Based Parallel Neural Network ",In AffCon@ AAAI , pp. 80-87.2019.

[27] F.Chen, Z.Luo, Y.Xu, & D.Ke, " Complementary fusion of multi-features and multi-modalities in sentiment analysis. arXiv preprint arXiv:1904.08138.2019

[28] Z.Luo, X.Zeng,Z. Bao, & Xu, M. , " Deep learning-based strategy for macromolecule classification with imbalanced data from cellular electron cryotomography, "IEEE International Joint Conference on Neural Networks (IJCNN) ,pp. 1-8, 2019.

[29] Z. Luo , " Knowledge guided Aspect based Summarization," IEEE International Conference on Communications, Computing and Artificial Intelligence (CCCAI) ,pp. 17-22, 2023.

[30] J. Mei, K.Li, A. Ouyang, K. Li,"A Profit Maximization Scheme with Guaranteed Quality of Service in Cloud Computing," IEEE Trans. Computers 64(11), pp.3064-3078 2015.

[31] K. Li, W. Yang, K. Li,"Performance Analysis and Optimization for SpMV on GPU Using Probabilistic Modeling,"IEEE Trans. Parallel Distributed Syst. 26(1),pp. 196-205 ,2015.

[32] Y. Xu, K.Li, L. He, L. Zhang, K. Li,"A Hybrid Chemical Reaction Optimization Scheme for Task Scheduling on Heterogeneous Computing Systems," IEEE Trans. Parallel Distributed Syst. 26(12),pp. 3208-3222 ,2015.

[33] X.Shi,K.Li, &L. Jia, "Improved Whale Optimization Algorithm via the Inertia Weight Method Based on the Cosine Function," Journal of Internet Technology, 23(7), PP.1623-1632.2022.

[34] J.Pan, Z.Fu, C. Hu, P. Tsai, & S.Chu, " Rafflesia optimization algorithm applied in the logistics distribution centers location problem," Journal of Internet Technology, 23(7), 1541-1555.2022.

[35] Q.Yang, S. Chu, C. Hu, J. Wu,& J.Pan, " Fish Migration Optimization with Dynamic Grouping Strategy for Solving Job-Shop Scheduling Problems," Journal of Internet Technology, 23(6), 1275-1286.2022.

[36] J.Pan,Q.Yang,C.Shieh, & S.Chu," Tumbleweed optimization algorithm and its application in vehicle path planning in smart city," Journal of Internet Technology, 23(5), 927-945.2022.

[37] C.Liu, K. Li & R.Buyya, R," A new service mechanism for profit optimizations of a cloud provider and its users," IEEE Transactions on Cloud Computing, 9(1),pp. 14-26.2017.

[38] J.Chen, K. Li, P. Yu & Z.Zeng,"Dynamic planning of bicycle stations in dockless public bicycle-sharing system using gated graph neural network," ACM Transactions on Intelligent Systems and Technology (TIST), 12(2), PP.1-22,2021.

[39] K.Li, X. Tang, & K.Li," Energy-efficient stochastic task scheduling on heterogeneous computing systems," IEEE Transactions on Parallel and Distributed Systems, 25(11), 2867-2876.2023

[40] X.Tang, K. Li, M. Qiu, & E.Sha, " A hierarchical reliability-driven scheduling algorithm in grid systems.," Journal of Parallel and Distributed Computing, 72(4), 525-535.2022.

[41] J.Wang, J.Caiyan , N. Xiong, Q. Tang, G.Srivastava," Intelligent Ubiquitous Network Accessibility for Wireless-Powered MEC in UAV-Assisted B5G," IEEE Transactions on Network Science and Engineering, vol.8, no.4, pp.2801-2813, 2021.

[42] D.Cao, K.Zeng, J.Wang, P. Kumar Sharma,M. Xiaomin, and L.Yonghe ,"BERT-based Deep Spatial-Temporal Network for Taxi Demand Prediction," IEEE Transactions on Intelligent Transportation Systems, vol.23, no.7, pp. 9442-9454, 2022.

[43] L.Zhuofan, P.Xiang ,J.Zhang,B.Xiong,J. Wang, "Blockchain on Security and Forensics Management in Edge Computing for IoT: A Comprehensive Survey," IEEE Transactions on Network and Service Management, vol.19, no.2, pp.1159-1175, 2022.

[44] L.Wenjun , Z. Chen, X. Gao, W.Liu, J. Wang, "Multimodel Framework for Indoor Localization Under Mobile Edge Computing Environment," IEEE Internet of Things Journal, vol.6, no.3, pp.4844-4853,2019.

[45] W.Li, H.Xu, H. Li, Y. Yang, "Complexity and Algorithms for Superposed Data Uploading Problem in Networks with Smart Devices, "IEEE Internet of Things Journal, vol.7, no.7, pp.5882-5891, July 2020.

[46] Z. Liao, J. Peng, J.Huang, J. Wang, J. Wang," Pradip Sharma, Uttam Ghosh, Distributed Probabilistic Offloading in Edge Computing for 6G-enabled Massive Internet of Things," IEEE Internet of Things Journal, vol.8, no.7, pp. 5298-5308, 2021.

[47] P. R. Babu, C. P. Rakesh, G. Srikanth, M. N. Kumar, and D. P. Reddy, "A novel approach for solving distribution networks," India Conference (INDICON), 2009Annual IEEE, pp. 1-5, Dec. 2009.

[48] A.Shahbazi, J.Aghaei, S.Pirouzi , T.Niknam,M. Shafie-khah, & J. Catalão, " Effects of resilience-oriented design on distribution networks operation planning," Electric Power Systems Research, 191, 106902.2021.

[49] A.Shahbazi, J.Aghaei, S.Pirouzi, T.Niknam, V.Vahidinasab, M.Shafie-khah," Holistic approach to resilient electrical energy distribution network planning," International Journal of Electrical Power & Energy Systems, 132, 107212, 2021.

[50] M.Norouzi,J. Aghaei, & S. Pirouzi, " Enhancing distribution network indices using electric spring under renewable generation permission," In 2019 International Conference

on Smart Energy Systems and Technologies (SEST) (pp. 1-6). IEEE.2019.

[51] S.Pirpoor, S. Rahimpour, M.Andi, N. Kanagaraj, S. Pirouzi, & A.Mohammed, " A novel and high-gain switched-capacitor and switched-inductor-based DC/DC boost converter with low input current ripple and mitigated voltage stresses," IEEE Access, 10, 32782-32802.2023.

[52] L.Bagherzadeh,H. Shayeghi, S.Pirouzi, M. Shafie-khah, M., & J.P.Catalão, "Coordinated flexible energy and self-healing management according to the multi-agent system-based restoration scheme in active distribution network," IET Renewable Power Generation, 15(8), 1765-1777,2021.

[53] S.Pirouzi,J. Aghaei, T.Niknam,H. Farahmand & M.Korpås, " Exploring prospective benefits of electric vehicles for optimal energy conditioning in distribution networks," Energy, 157, 679-689.2018.

[54] S.Pirouzi, & J.Aghaei, " Mathematical modeling of electric vehicles contributions in voltage security of smart distribution networks" Simulation, 95(5), 429-439.2019.

[55] M.Norouzi, J.Aghaei,S. Pirouzi, T. Niknam, M.Fotuhi-Firuzabad,&M.Shafie-khah, " Hybrid stochastic/robust flexible and reliable scheduling of secure networked microgrids with electric springs and electric vehicles. Applied Energy, 300, 117395.2021.

[56] S.Pirouzi and et al," Hybrid planning of distributed generation and distribution automation to improve reliability and operation indices," International Journal of Electrical Power & Energy Systems, 135, 107540,2022.

[57] S.Pirouzi, M. Latify, & G.Yousefi, " Investigation on reactive power support capability of PEVs in distribution network operation," 23rd Iranian Conference on Electrical Engineering, pp. 1591-1596, IEEE.2015.

[58] S.Pirouzi, J. Aghaei, T.Niknam, H. Farahmand, & M.Korpas, " Proactive operation of electric vehicles in harmonic polluted smart distribution networks," IET Generation, Transmission & Distribution, 12(4), 967-975,2018.

[59] M.Norouzi, J. Aghaei, S. Pirouzi, T. Niknam, & M. Lehtonen, " Flexible operation of grid-connected microgrid using ES," IET Generation, Transmission & Distribution, 14(2), 254-264,2020.

Sasan Pirouzi was born in Esfahan , Iran in 1981. He received a BSc degree in electrical engineering from the Technical and Vocational University, Mashhad, Iran, in 2012 and an MSc degree from the Isfahan University of Technology, Isfahan, Iran, in 2014, as well as a PhD from the Shiraz University of Technology (SUTECH), Shiraz, Iran, in 2017. He is an associate professor with the Department of Electrical Engineering, Islamic Azad University, Esfahan Branch. He authorizes one books, 77 ISI-ranked journal articles, and 40 conference papers. His research interests are power system operation and planning, electric vehicles, DERs and the application of optimization methods in power systems.

Mahmoud Zadehbagheri was born in Yasouj, Iran, in October 1979. He received a B.S degree in Electrical Engineering from Kashan University, in 2003, an M.S degree in Electrical Engineering from Islamic Azad University, Najafabad Branch, in 2008, and a joint Ph.D degree in Electrical Engineering from Universiti Teknologi Malaysia (UTM), Johor, Skudai, Malaysia, and Hakim Sabzvari University, Khorasan, Iran, in 2017. He is an associate professor with the Department of Electrical Engineering, Islamic Azad University, Yasouj Branch. He is a member of the IEEE Smart Grid Community and IEEE PES Technical Committee. Since 2018, he has been a co-supervisor and a consulting professor of more than 13 Ph.D and 50 M.Sc students. He authorizes two books, one published book chapter, 65 ISI-ranked journal articles, and 90 conference papers. He is currently collaborating as a reviewer and editorial board with the journals Applied Energy, Hydrogen Energy, IJRER, Micro Machines, sensors, Energy, EPCS, and IJPEDS. His research interests include power electronics, FACTS devices, optimization methods, renewable energy, energy hubs, and power quality.

Rohollah Rashidi was born in Semirom ,Iran in 1979 . He received his B.Sc. degree in software engineering from the Islamic Azad University of Najfabad, Najafabad, Iran, in 2003, and the M.Sc. degree in Software of Engineering from the Iran University of Science and Technology in 2005 and the Ph.D. degree in Computer Engineering - Software Systems from Isfahan Islamic Azad University, Iran. He is an assistant professor with the Department of Electrical Engineering, Islamic Azad University, Semirom Branch. His research interests are social network analysis, recommendation systems and optimization.

IECO

This page intentionally left blank.

IECO
International Journal Of
Industrial Electronics Control and Optimization
Print ISSN: 3517-2645
Online ISSN: 3568-2645
Homepage: https://ieco.usb.ac.ir/

Hardware Structure of an Efficient and Optimal Circuit for Induction Cap Sealing

Bahram Rashidi

Department of Electrical Engineering, Faculty of Engineering, Ayatollah Boroujerdi University, Boroujerd, Iran.
Corresponding author's email: b.rashidi@abru.ac.ir

Article Info

Article type:
Research Article

Article history:
Received: 09-March-2024
Received in revised form: 05-May-2024
Accepted: 15-May-2024
Published online: 22-Sep-2024

Keywords:
Container lid sealing,
Induction sealing,
Multivibrator,
Zero voltage switching,
Litz wire.

ABSTRACT

This paper presents the design and hardware implementation of an efficient and optimal induction heating circuit for induction sealing. The circuit has a low implementation cost, so the proposed system with a simple and efficient structure can cover the needs of this technology field. Here, the focus is on the implementation process and practical tips in this field. The proposed induction sealing circuit uses zero-voltage switching technology with parallel MOSFETs. In this structure, by using inductors and capacitors with appropriate tolerable current and voltage, it can provide the power and frequency of the output signal applied to the induction coil for various applications. The use of transistors with suitable current capability makes the circuit appropriate for applications that require stronger magnetic fields. In addition, the induction coil has an elliptical structure, which makes it efficient for sealing a wide range of bottles. It is constructed using Litz wire to reduce power loss in the coil. In the presented structure, the frequency of the output signal is equal to 31 kHz, which is suitable for creating an eddy current in the aluminum foil in the bottle caps. The circuit has been tested and investigated and has acceptable sealing for various industries.

I. Introduction

In the food, health, chemical, and pharmaceutical industries, induction sealing is a good method for sealing bottle caps and is very effective in the shelf life of products. Keeping products fresh and preventing contamination from entering the product during the handling and selling stages is one of the advantages of sealing products. Preventing contamination of pharmaceutical products, food (dairy products, beverages, etc.), cosmetics-hygiene, petroleum products, etc. is very important [1]. Induction sealing of products is one of the methods used for this purpose. The induction cap seal restricts the product from coming into contact with oxygen to prevent it from fermenting or spoiling. The method used by induction sealing equipment to heat metals is called induction heating. Induction heating is a process for heating metals. High-frequency sealing is a process of joining thermoplastic materials by induction heating [2]-[3]. Thermoplastics are materials that become soft and elastic when heated. During induction heating, when the metal absorbs current and a short circuit occurs, electrical losses occur in the metal. This electrical loss manifests itself as heat in the metal. Induction sealing is typically used for packaging food and pharmaceutical products. This process involves the controlled heating of a conductive metal such as aluminum foil by electromagnetic induction. Eddy currents are the reason for the generation of heat [4]-[5]. The most common application of induction sealing is the sealing bottle caps containing pharmaceutical or food substances. In this method, the cap is contactlessly attached to the lid of plastic or glass containers. This sealing process is done after filling and tightening the container lid. The lids are packed with a layer of aluminum foil that is already placed inside the bottle cap. Common induction seals are multi-layered. The top layer is paper that is usually attached to the cap in a dotted fashion. The next layer is wax, which functions to adhere the aluminum foil layer onto the paper. The bottom layer is a thin layer of polymer placed on the foil [6]. The lid is placed inside the door,

Publisher: University of Sistan and Baluchestan

then the lid is automatically or manually wound onto the container and the container passes under the induction coil. As the vessel passes under the induction coil, the eddy currents begin to heat the aluminum foil. The heat will melt the wax and release the foil from the cap. The thin polymer layer also heats up and flows to the edge of the container. After cooling, the polymer adheres to the container, resulting in a closed product [7]. The heat in this process does not affect the container or its contents. The foil can overheat and damage the sealing layer and the bottle cap. Therefore, proper induction sealing is necessary to produce a specific product.

In this paper, the design and implementation of a circuit for induction sealing based on an optimal and low-cost circuit is discussed. The proposed circuit has been tested and investigated. It has acceptable sealing for the various bottles. The most important features of the proposed structure are as follows:

- Here, the focus is on the implementation process of this circuit. The proposed circuit for induction sealing is very low cost.
- The induction sealing circuit is implemented based on zero voltage switching technology. This technology is simple and very efficient.
- The proposed circuit is based on paralleled Metal Oxide Silicon Field Effect Transistors (MOSFETs), for operating in a wide range of output powers. This feature reduces the heat of MOSFETs and their better cooling. Using transistors with high current capability for applications that require high power and stronger magnetic fields can be effective.
- In this structure, by changing the oscillator capacitors' capacity and the power supply's current, the frequency and strength of the applied signal to the induction coil can be controlled according to different applications.
- To reduce power loss significantly in the coil, it is constructed based on Litz wire. The induction coil has an elliptical structure that makes it suitable for sealing a wide range of bottles. This coil generates a uniform magnetic field along the length of the coil.

The rest of the paper is organized as follows. The related works are presented in Section 2. An introduction to the induction sealing method is presented in Section 3. In Section 4 the structure of the designed induction sealing circuit is discussed. The implementation considerations are presented in Section 5. The results of the circuit are described in Section 6. The conclusion of the work is presented in Section 7.

II. Related Works

In recent years, different works have discussed the design and implementation of induction heating circuits. For example, the work [2] summarizes the main milestones in the development of induction heating technology and analyzes the current state of induction heating technology in industrial, domestic, and medical applications. In [7] the authors investigate a method to show the allowable current density of various types of Litz wire-based coils used in induction heating applications. In [8], the heating of water using electromagnetic induction is demonstrated in the laboratory through an experimental approach. In [9], the second-order sliding mode control properties of the qualitative characteristics of an oscillator circuit in an air-cooled inductive seal were investigated. The paper [10] focuses on the role of inverter topology in the design of a 1.5kW, 50kHz induction heating system for induction sealing. In [11], an optimization method is proposed for the design of chokes on the PCB for use in domestic induction cookers. The cables of classic chokes are made of multi-strand round Litz wire for increased efficiency. A planar Litz structure in the PCB was used to achieve performance similar to traditional designs (in terms of maximum output power, inductive efficiency, and thermal behavior). In work [12], a three-phase, three-switch PWM rectifier with simple configuration and control is designed to achieve a high input power factor for industrial heating applications. A controlled multi-zone induction heating system was effectively implemented in [13] through a suitable spiral design. The coil is powered by a single-resonant converter. In [14], a low-frequency induction heating circuit for sealing plastic microfluidic systems is proposed. The work [15] presents the design and experimental analysis of a self-resonant inverter for induction heating of melting furnaces based on parallel IGBTs. An analytical calculation of the inductance of a flat air-core coil for induction heating applications is given in [16]. In [17], a study of design guidelines for flat induction heating systems whose coil is located significantly further from the load is discussed. In [18], the finite element method is used to perform an electromagnetic-thermal analysis for the proposed coil and to study its performance during the heating period. One of the important features of the proposed work is implementation based on a few numbers of elements, which are much less than the existing works. The use of two MOSFET transistors in parallel increases the current flow of the circuit and ultimately increases the output power. Another feature of the proposed circuit is using the Litz wires in an elliptical shape. In this case, we create a uniform magnetic field, which causes better sealing of the bottles. The proposed method has a simple structure, and all circuit parts (oscillator and capacitor bank) are implemented on a single board for a better and simpler assembly. This reduces the cost of circuit construction. In previous works, the authors used high hardware resources [10] and utilized more coils [13] and [19]. In the proposed work, the maximum diameter of the bottle that can be sealed is 13cm, while it is 12cm and 12.5cm in the works [10] and [13], respectively.

III. Induction sealing

Sealing the lid of containers using the induction method helps to create credibility for a product and its durability. Sealing methods can generally be divided into vacuum sealing, thermal sealing, thermoforming sealing, and induction sealing. The main difference between the induction method and other sealing methods is that the heat is delivered to the container through a magnetic field. Inductive cover lids (inductive wads) common for all kinds of containers such as polyethylene, polypropylene, PET, and glass are multi-layered. Fig. 1 shows the constructive layers of bottle caps in the food, health, and pharmaceutical industries. The upper layer is paper, which is usually attached to the cap. The next layer is wax, which is used to stick the aluminum foil layer to the paper. The bottom layer is a thin layer of polymer placed on the foil. When the inductive wads pass through the magnetic field which is created by the coil, the aluminum layer acts as a conductor of electric current. The electric current inside the aluminum foil causes the aluminum layer to be heated, and it is transferred to the polymer layer. When the polymer layer is heated, it is attached to the container lid and sealed.

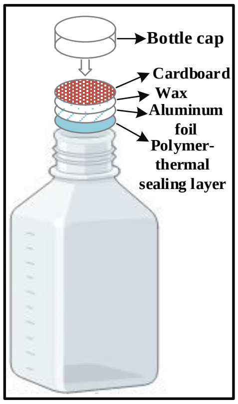

Fig. 1. Constructive layers bottle caps in the food, health, and pharmaceutical industries.

IV. The structure of induction sealing circuit

The implemented induction sealing circuit works based on zero-voltage switching technology. Each pair of MOSFETs is turned off as the opposite-phase pair of MOSFETs turns on, and this continues until the primary voltage reverses phase. This phase reverse happens when the primary voltage crosses zero, so switching occurs when there is zero voltage across the pair of MOSFETs. The MOSFETs in this technology are turned on when they have the minimum voltage and current to turn on. In this circuit, to create a magnetic field in the coil, we pass a large current through the coil with an oscillator. Fig. 2 shows the proposed circuit for the implementation of induction sealing. The induction heating circuit converts the DC input voltage, which must have a high current, into a high-frequency AC sinusoidal signal. This AC signal is generated in the coil. When current flows through the coil, a magnetic flux is created around it. This type of flux has the property of increasing heat in metals. One of the most important advantages of this process is that the heat is generated and induced in the metal itself instead of being provided through another external heat source. Therefore, metal can be heated much faster. When the bottle cap with aluminum foil is placed under the coil, the created magnetic field induces eddy currents in the foil. This process heats the polymer layer of the aluminum foil.

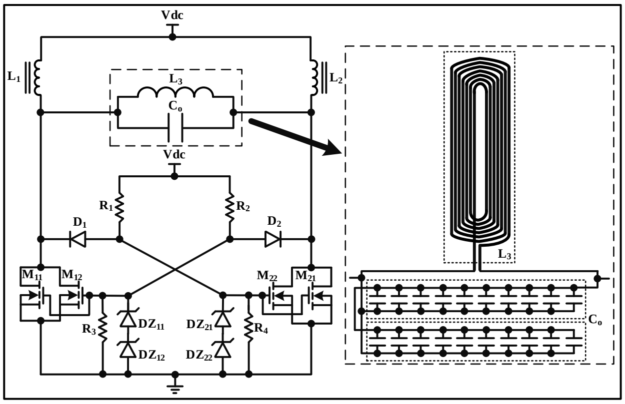

Fig. 2. The proposed circuit to implementation of the induction sealing.

In the circuit of Fig. 2 we use the four MOSFETs (M_{11}, M_{12}, M_{21}, M_{22}). In this circuit, the cathode of the Zener diode DZ_{11}, the anode of the diode D_2, the resistor R_3, and the resistor R_2 are connected to the gate pins of the MOSFETs M_{11} and M_{12}. For the MOSFETs M_{21} and M_{22} we have a similar case. Then the other pin of resistors (R_1 and L_2) and the pins of thyroid inductors (L_1 and L_2) are connected. On the other hand, the positive end of the power supply is connected to this node. The anode pin of the Zener diode DZ_{12}, the other end of the resistor R_3, the source pins MOSFETs (M_{11}, M_{12}), the anode pin of the Zener diode DZ_{22}, the resistor R_4, the source pins MOSFETs (M_{21}, M_{22}) are connected to each other. This node of the connections is connected to the negative pin (ground) of the power supply. In this circuit, 20 capacitors are connected in parallel to the drains of the MOSFETs. The cathode of the diode D_1 is connected to the drain pins of the MOSFETs M_{11}, M_{12} and the cathode of the diode D_2 is connected to the drain pins of the MOSFETs M_{21}, M_{22}. The main coil of the induction sealing circuit is connected to both ends of the capacitors.

The operation of the circuit can be presented as follows: At first, the supply voltage turns on the MOSFETs. But considering that no two MOSFETs can have the same conductivity characteristics, the four MOSFETs are not turned on together, but only one side ((M_{11}, M_{12}) or (M_{21}, M_{22})) of them is turned on. In other words, oscillation is kicked on by differences in the circuit components. Suppose M_{11} and M_{12} are turned on first. When this happens, due to the current flowing through these MOSFETs, the drain-source voltage drops to zero. In this case, diode D_1 is turned on, and the gate voltage of the MOSFETs M_{21} and M_{22} is reduced. However, the equivalent capacitor C_o, L_3 and inductor L_2 play an important role. The sudden conduction of M_{11} and M_{12} causes a sinusoidal pulse to be generated at the Drain pins M_{21} and M_{22}. When the amplitude of the sinusoidal pulse decreases, the gate voltage of M_{11} and M_{12} decrease and turn them off. This leads to an increase in the Drain voltage of M_{11} and M_{12} (in this case diode D_1 is turned off), which allows the gate voltage for M_{21} and M_{22} be increased (based on the voltage divider of the R_1 and R_4). Now, the MOSFETs M_{21} and M_{22} are turned on, and we have a similar process such as M_{11} and M_{12}.

Figure 3 shows the equivalent circuit of Fig. 2. Here, K_1 and K_2 keys are used instead of the MOSFETs. Suppose the MOSFETs M_{11} and M_{12} are turning on (in other words, the K_1 key is connected), in this case, the gate voltage at the MOSFETs M_{11} and M_{12} is almost zero. This voltage causes the diode D_1 to turn on. In this case, the gate-source voltage of MOSFETs M_{21} and M_{22} is reduced, and these transistors are turned off (in other words, the K_2 key is off). When these transistors are turned off, the drain current in them is practically zero. At this moment, the capacitors are charged through the inductor L_2. This process is shown in Fig. 4 (a). When the capacitors are charged, the drain voltage in the MOSFETs M_{11} and M_{12} increases and this causes the D_1 diode to turn off. Therefore, the gate-source voltage of the MOSFETs M_{21} and M_{22} is increased and these transistors are turned on (in other words, the K_2 key is connected). When these MOSFETs are turned on, the drain voltage in them becomes almost zero and the D_2 diode is turned on. In this case, the gate-source voltage of MOSFETs M_{11} and M_{12} decreases, and these transistors turn off (in other words, the K_1 key is turned off). When these transistors are turned off, the drain current in them becomes zero and the capacitors are charged through the inductor L_1 (Fig. 4 (b)). When the capacitors are charged, the drain voltage in the MOSFETs M_{21} and M_{22} increases and this causes the D_2 diode to turn off. Therefore, the gate-source voltage of the MOSFETs M_{11} and M_{12} is increased and these transistors are turned on (in other words, the K_1 key is connected). In this way, this cycle continues ((M_{11}, M_{12}) are on and (M_{21}, M_{22}) are off and (M_{11}, M_{12}) are off and (M_{21}, M_{22}) are on). Therefore, this cycle causes an oscillation and creates an AC voltage at the output. The oscillating happens when the drain voltage is close to zero. Therefore, it leads to the minimization of switching losses. This cycle continues and causes the circuit to oscillate at the resonant frequency of the L_3-C_o circuit.

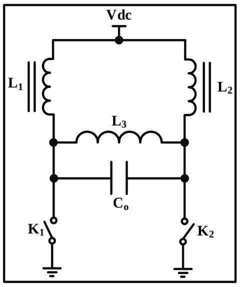

Fig. 3. Equivalent circuit of Fig.2.

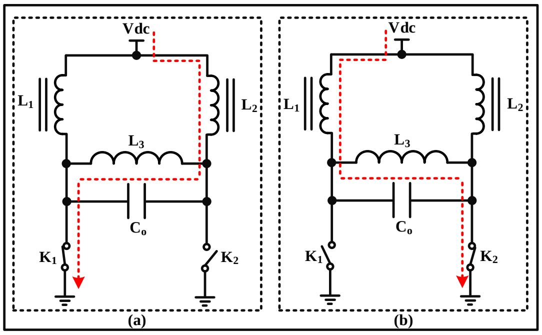

Fig. 4. The turning off and on process of the MOSFETs.

Figure 5 shows the waveforms of drain voltages and waveform across the main coil L_3. As seen from the figure, the waveforms of drain voltages have no overlap and the final output is a high-frequency sinusoidal waveform. Resonance is adjusted to an optimal point depending on the L_3-C_o values. The fast-switching ZVS has low dissipation and can normally be resolved with relatively small heatsinks. Due to this feature, the MOSFETs in ZVS self-amplification circuits need much smaller heatsinks. The frequency of the circuit depends directly on the inductance of the coil L_3 and the capacitor C_o. Oscillation frequency can be calculated using the following formula:

$$F = \frac{1}{2\pi\sqrt{L_3 C_o}}$$

The L_3 is the inductance of the main heating coil and C_o is the capacitor equivalent of all parallel capacitors. The total impedance of the parallel L_3-C_o is given by

$$Z = \frac{Z_{L_3} Z_{C_o}}{Z_{L_3} + Z_{C_o}}$$

after substitution of $Z_{L_3} = jwL_3$ and $Z_{C_o} = \frac{1}{jwC_o}$ and simplification, gives

$$Z(w) = -j\frac{wL_3}{w^2 L_3 C_o - 1}$$

Using $w_0 = \frac{1}{\sqrt{L_3 C_o}}$ it further simplifies to

$$Z(w) = -j(\frac{1}{C_o})(\frac{w}{w^2 - w_0^2}) = j\frac{1}{w_0 C_0(\frac{w_0}{w} - \frac{w}{w_0})}$$
$$= j\frac{w_0 L_3}{(\frac{w_0}{w} - \frac{w}{w_0})}$$

Note that $(\lim Z(w))_{w \to w_0} = \infty$ but for all other values of ω the impedance is finite. In the following, we analyze time domain solution of the circuit. By Kirchhoff's voltage law, the voltage V_{C_o} across the capacitor plus the voltage V_{L_3} across the inductor must equal zero:

$$V_{L_3} + V_{C_o} = 0$$

From the constitutive relations for the circuit elements, we also know that:

$$V_{L_3}(t) = L_3\frac{dI_{L_3}}{dt}, I_{C_o}(t) = C_o\frac{dV_{C_o}}{dt},$$

Rearranging and substituting gives the second order differential equation:

$$\frac{d^2}{dt^2}I(t) + \frac{1}{L_3 C_o}I(t) = 0,$$

Using the resonant angular frequency $w_0 = \frac{1}{\sqrt{L_3 C_o}}$ we can simplify the differential equation:

$$\frac{d^2}{dt^2}I(t) + w_0^2 I(t) = 0,$$

The associated Laplace transform is

$$s^2 + w_0^2 = 0,$$

Thus $s = \pm jw_0$, where j is the imaginary unit. The complete solution to the differential equation is

$$I(t) = Ae^{+jw_0 t} + Be^{-jw_0 t},$$

It can be solved for A and B by considering the initial conditions. Since the exponential is complex, the solution represents a sinusoidal alternating current. Since the electric current I is a physical quantity, it must be real-valued. As a result, it can be shown that the constants A and B must be complex conjugates $A = B^*$, Now let:

$$A = \frac{I_0}{2}e^{+j\phi}, B = \frac{I_0}{2}e^{-j\phi},$$

Next, we can use Euler's formula to obtain a real sinusoid with amplitude I_0, angular frequency $w_0 = \frac{1}{\sqrt{L_3 C_o}}$, and phase angle ϕ. Thus, the resulting solution becomes

$$I(t) = I_0 cos(w_0 t + \phi),$$

$$V_{L_3}(t) = L_3\frac{dI}{dt} = -w_0 L_3 I_0 sin(w_0 t + \phi),$$

The initial conditions that would satisfy this result are

$$I(0) = I_0 cos(\phi),$$

$$V_{L_3}(0) = -w_0 L_3 I_0 sin(\phi),$$

The higher the frequency of the induction heating circuit the heating operation of the circuit is increased. Also, the metal gets more heat. The output frequency of the induction heating circuit is usually between 20 kHz and 100 kHz [7]. In the output of the circuit, the capacitors are connected to the coil, and the coil creates an electromagnetic field. Fig. 6 shows how to create a magnetic field around the used coil in the circuit. This coil generates a uniform magnetic field along the length of the coil. The generated field covers around the coil for a wide range of cap sizes. Fig.7 shows the general structure of the induction sealing device and the bottle that is placed in the magnetic field around the coil. Using this device, containers can be sealed one after the other without stopping. This increases the speed of packaging. When the induction coil is placed next to or around the induction seal wads, the lines of the field are concentrated in the air gap between the coil and the induction seal wads. The magnetic field that surrounds the induction coil induces an equal and opposite current in the induction seal wad. The induction seal wad heats up due to the resistance to the induction current. The heating speed of the induction seal wad depends on the frequency of the induction current, the intensity of the induction current, the specific heat of the material, the magnetic permeability of the material, and the resistance of the material against the current. Induced currents have the highest intensity near the magnetic field. In this way, the aluminum foil in the bottle cap is heated and sticks to the container cap.

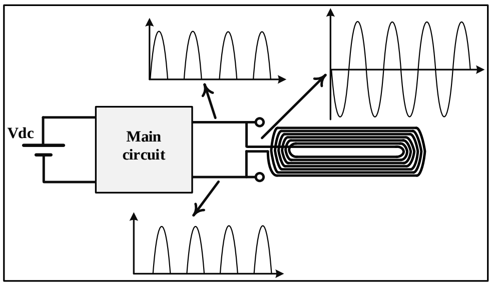

Fig. 5. The waveforms of drain voltages and across the main coils.

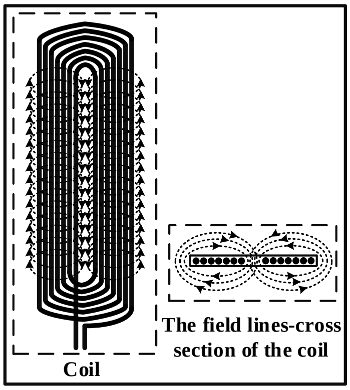

Fig. 6. Created unified magnetic field around the coil.

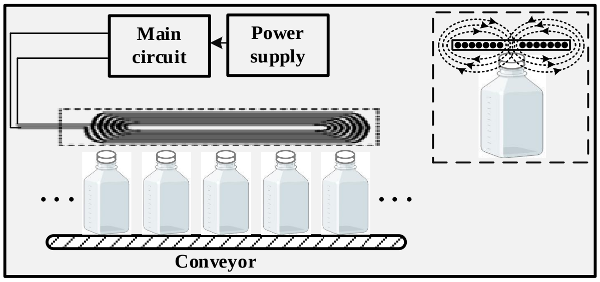

Fig. 7. The general structure of the induction sealing device and the bottle that is placed in the magnetic field around the coil.

In the following, the role of the components of the circuit is described. The role of Zener diodes in this circuit is to limit the gate voltage of the MOSFETs, which prevents the MOSFETs from being damaged. In case of high supply voltage, these diodes prevent gate voltage from going too high. Considering that to increase the power of the circuit, the number of parallel transistors is equal to 2, one of the parts that need to increase the power dissipation is the Zener diodes. For this purpose, we use two Zener diodes. The diodes are connected in series. Two fast recovery diodes $\mathrm{D_1}$ and $\mathrm{D_2}$ with resistors $\mathrm{R_1}$ - $\mathrm{R_2}$ provide gate drive. These fast diodes provide a fast turn-off of the MOSFET gates when they are driven toward the ground as the opposite-phase MOSFET saturates. When two MOSFETs $\mathrm{M_{11}}$ and $\mathrm{M_{12}}$are turned on, it pulls the gate of the opposite MOSFETs $\mathrm{M_{21}}$ and $\mathrm{M_{22}}$ down. Therefore, 4 MOSFETs can’t be on at the same moment. The inductors $\mathrm{L_1}$ and $\mathrm{L_2}$ provide almost constant current to the resonant circuit.

V. Implementation considerations

One of the most important parts of this paper is the implementation considerations. Because inappropriate elements and no consideration of the implementation points in the circuit lead to no desired answer in practice. In this circuit, we can use any N-channel MOSFET transistor with high power, voltage, and current in different ranges. It depends on the application and the expected power from the circuit. In addition, because of the resonant voltage rise in the drains about 2 times the power supply voltage. Therefore, the maximum drain-source voltage recommended is in the rating of 3 to 4 times the supply voltage. To receive high power, we can use MOSFETs that have a maximum drain-source voltage between 150v to 600v and a drain current between 20A to 100A. The heatsinks can be used to cool them. Here, in the circuit, we use four IRFP260N MOSFETs with the minimum $\mathrm{V}_{gs(th)}$ equal to 2v. The use of the Zener voltage higher than the minimum gate-to-source turn-on voltage ensures that the MOSFETs are conducting at a high level. On the other hand, the maximum V_{GS} is equal to 20V. Therefore, we use two series Zener diodes with a Zener voltage equal to 6v. Inductors $\mathrm{L_1}$ and $\mathrm{L_2}$ are a type of choke that helps eliminate any possible high-frequency content from the power supply and also limits the current to a safe level. These inductors have a ferrite core. The amount of these inductors should be much higher (about 10 times) compared to the induction coil. To prevent heating of the circuit, capacitors, and inductors $\mathrm{L_1}$ and $\mathrm{L_2}$ should be selected based on considerations. For this purpose, the inductors must have a high-tolerable current (more than 15 amps).

The inductors $\mathrm{L_1}$ and $\mathrm{L_2}$ must be able to handle the current drawn from the power supply and power losses in the core. Typically, the choke is wound on a powdered iron (Material 26 and Material 52). The relative permeability of these materials is equal to 75; the core will not saturate at the maximum power supply current. The wire used in the choke must be able to handle the maximum current demanded by the power supply without significant core losses. In this work, a 108 μH inductor with a current of about 40A is constructed and used in the circuit. The inductors $\mathrm{L_1}$ and $\mathrm{L_2}$ are made based on six 0.75mm lacquered wires twisted together. Fig. 8 shows the constructed inductor for $\mathrm{L_1}$ and $\mathrm{L_2}$. The core is based on material 52 with an inner diameter of 24mm, outer diameter of 47mm, and height of 18.2mm. Here, the two meters of 0.75mm Lacquered wire is used for the wiring of inductors. For the output capacitor, several capacitors should be used in parallel. The total capacity of parallel capacitors should be equal to the capacity of the equivalent capacitor (C_o). If the number of capacitors is low, for example, one or two capacitors equal to 20 capacitors are used the internal resistance increases and the possibility of their damage increases. By increasing the number of capacitors, the current value is increased and it is divided between parallel capacitors. In this case, the capacitors heat up less, and their useful life in the circuit increases. For example, if the output equivalent capacitor has a capacity of 3uF, it is better to use 20 capacitors of 150nF in parallel. The capacitors must have a high current and voltage. The best option for this work is MKT capacitors with a maximum voltage more than of 100V so that the circuit works better and does not heat up. In this work, we have used 20 capacitors of 150nF with a maximum voltage of 630V. If the equivalent capacity value of the capacitors decreases, the frequency of the circuit increases and the circuit becomes stronger, but capacitors with a lower capacity must be paralleled. So that the number of paralleled capacitors is not reduced. At the input of the induction sealing circuit, the electric current of the power supply has a higher priority. Because the higher the current provides, the higher the power of the induction sealing circuit. However, the higher input voltage affects the heating speed instead of the heating power. The voltage of the power supply can be between 5 to 48 volts, and the current from 5 to 50 amps, depending on the load. Fig.9

shows the used coil in the induction heating circuit. For the construction of the coil, we use Litz wire to increase the power transfer efficiency and reduce the heat losses. Because in many high-frequency heating applications, the induction coil is often based on Litz wire [7]. The coil is constructed based on a Litz wire with 24 strands of 0.5mm lacquered wires twisted together. As mentioned before, one of the characteristics of this coil is the creation of a uniform magnetic field. This feature is due to the winding of the wire in an elliptical shape. In the elliptical coils, due to their long length, it produces more field. So we have a field with a larger area. This kind of coil has a very good heating rate for this aluminum foil. When the bottles pass under it, there is enough time for sealing (due to the length of the coil). In this case, the sealing is done using only one coil and there is no need to use an additional coil. The creation of a uniform magnetic field along the length of the coil causes uniform heating of the aluminum foil on the bottle cap. By increasing the length of the wire, the coil can have larger dimensions and number of turns. In this case, it can seal a wide range of bottles with different sizes of lids. On the other hand, with the increase in dimensions and the number of turns of the coil, the power supply current must be increased. Also, cooling of the coil and the circuit should be considered. The amount of induced heat can be controlled based on changing the dimensions and number of turns of the coil, the diameter of the wire, and the current of the power supply. One of the points of implementation in this circuit is the cooling of the induction coil. In samples with powers more than 3kW, cooling is done by oil for easier cooling. On the other hand, in many cases, the cooling system is air-cooled, and cooling is done with fans that are placed on top of the induction coil. In the present work, a fan is used for cooling. One of the most important challenges of the circuit during the design process is to make a precise and symmetrical coil based on Litz wire. Because according to the output power of the circuit, the diameter of the wire and the number of turns should be considered. In addition, to have a uniform magnetic field, the symmetry of the coil (in terms of size and number of turns) is essential. Using high-voltage MKT capacitors is another limitation that should be considered in the design. Because of the working conditions (continuous work in industrial environments and increasing the temperature of the capacitors) and the high current of the circuit, the MKT capacitors must be used. Constructing the L_1 and L_2 inductors is another circuit challenge. These inductors must have a high current capability, in the process of designing them, the diameter of the wire and the size of the ferrite core must be considered.

Fig. 8. The constructed inductor for L_1 and L_2.

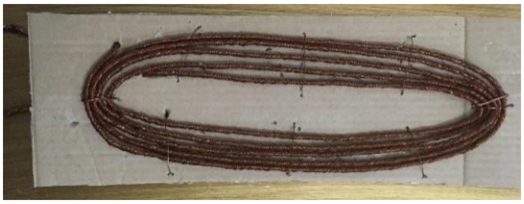

Fig. 9. The shape of the used coil in the induction heating circuit.

The printed circuit board (PCB) of the layer induction heating circuit is shown in Fig. 7. Interconnection traces on the PCB are wide and as short as possible. The dimensions of the board are $15\times30\text{cm}^2$. As can be seen from the figure, the paths with more current have a wider width (20mm). In addition, after making the printed circuit, the sensitive and high-current paths should be tin-plated. In order not to damage the MOSFETs, capacitors, and inductors, as well as heat them up, a suitable fan and heatsink must be used to prevent overheating during operation.

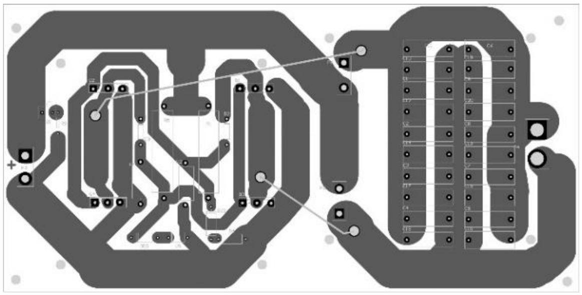

Fig. 10. One layer printed circuit board of the induction heating circuit.

VI. The Results of the Implementation

In this section, some results of the proposed circuit are presented. In the implementation of the circuit, we use a 24-volt switching power supply with a maximum current of 15 amps. The induction coil is wrapped by a Litz wire with an outer diameter of 12mm. The coil is constructed based on a Litz wire with a 24-strand of 0.5mm lacquered wires twisted together. The amount of the induction coil measured by the LCR meter is equal to 8.5uH. The desired oscillation frequency in the output is achieved by using the 20 capacitors 150nF-630v in parallel. The hardware parameters of the circuit are shown in Table 1. The components' tolerances and variability (variations in quality) impact the circuit's performance (efficiency and reliability). Therefore, we must consider some points in the design to reduce these effects as much as possible. For example, Litz wire reduces losses if there are many strands with a smaller diameter in the wire structure [7]. On the other hand, the MOSFETs must be of suitable quality and be connected to the heat sink to reduce electrical variations. The used capacitors in the output must be MKT type, which does not change their capacity due to temperature changes. The MKT capacitors are popular and normally used for large pulse handling such as dc-link for high-frequency inverters [20], etc.

TABLE 1: HARDWARE PARAMETERS OF THE CIRCUIT.

Elements	Specification
R_1-R_2	470Ω, 10W
R_3-R_4	10kΩ, 5W
D_1-D_2	Fast recovery diode UF4007
DZ_{11}-DZ_{22}	6V, 5W
M_{11}-M_{22}	IRFP260N
L_1-L_2	108uH, 40A
Coil L_3	8.5uH, 24-strand Litz wire
C_o	# 20 (150nF-600V)

Figure 11 shows the real circuit of the proposed induction heating. Here, we have designed a single board for the circuit and the capacitor part, which reduces the assembling work and its cost. The gate voltage of the MOSFETs in the oscilloscope is shown in Fig. 12. Fig. 12 (a), (b), and (c) shows the gate voltage of the MOSFETs (M_{11} and M_{12}), (M_{21} and M_{22}), and both voltages, respectively. Also, Fig. 13 shows an example of the drain voltage signals (V_{d1} and V_{d2}) of the MOSFETs in the oscilloscope. Fig. 13 (a) shows the sample of the drain voltage signal of the MOSFETs M_{11} and M_{12} the middle figure (Fig. 13 (b)) shows the sample of the drain voltage signal of the MOSFETs M_{21} and M_{22}, and both voltage of the drains of the MOSFETs (M_{11} and M_{12}, yellow diagram) and (M_{21} and M_{22} , blue diagram) in the oscilloscope are shown in Fig. 13 (c). The horizontal axis is in terms of time (second) and the horizontal axis is in terms of voltage (V). We can see the order of turning off and turning on the MOSFETs in these diagrams. The gate of the MOSFETs was switched alternately at a frequency of 34 kHz. Fig. 14 shows an example of the signal produced at the output (two ends of the induction coil) by the oscilloscope. As can be seen, this waveform is completely sinusoidal. Here, the peak-to-peak output voltage is approximately equal to 85v and the oscillation frequency is approximately equal to 31kHz. The amplitude and frequency of the output are quite suitable for inducing a magnetic field in the induction coil. Changing the number of turns of the L_3 coil is one of the most important ways to scalability the proposed work. In this case, the capacity of C_o and the number of capacitors must also be changed to achieve the desired output frequency. Therefore, by changing the number of turns of the coil, increasing (or decreasing) the diameter of the Litz wire, and increasing the power supply's current and the output capacitor's capacity, the circuit can be adapted for different applications. In addition, for high-volume production environments, as the circuit is constantly under load, cooling of the output coil should be considered. In this case, a water or oil cooling system should be used to cool the output coil.

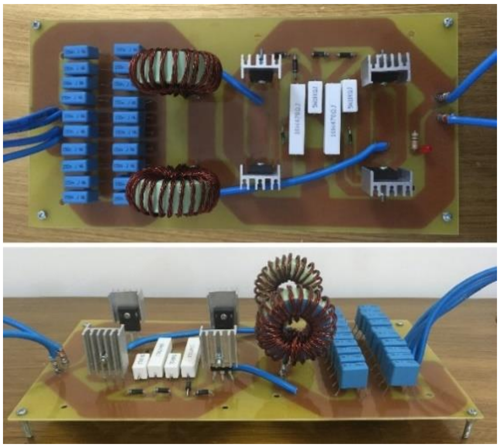

Fig. 11. The implemented practical circuit of induction sealing.

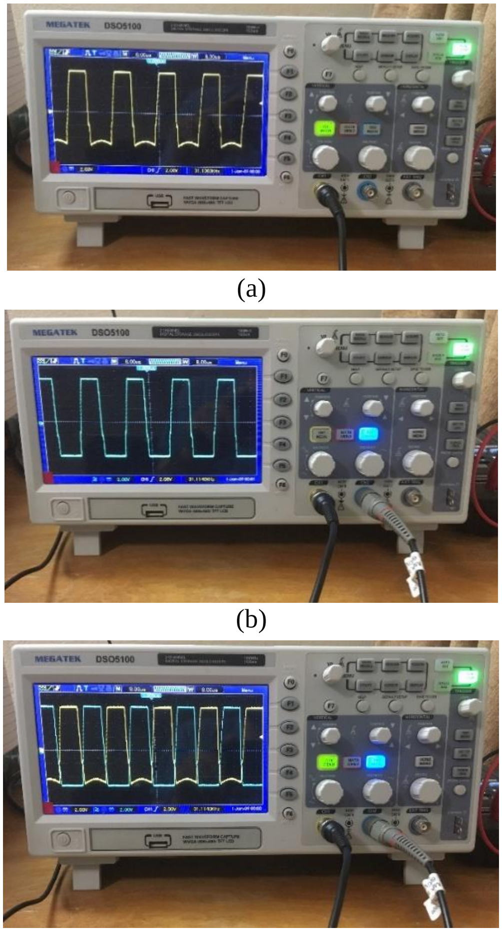

(a)

(b)

(c)

Fig. 12. The sample of the gate voltage signal of the MOSFETs M_{11} and M_{12} (a), the sample of the gate voltage signal of the MOSFETs M_{21} and M_{22} (b), and both voltage of the gates of the MOSFETs (M_{11} and M_{12}, yellow diagram) and (M_{21} and M_{22}, blue diagram) in the oscilloscope (c).

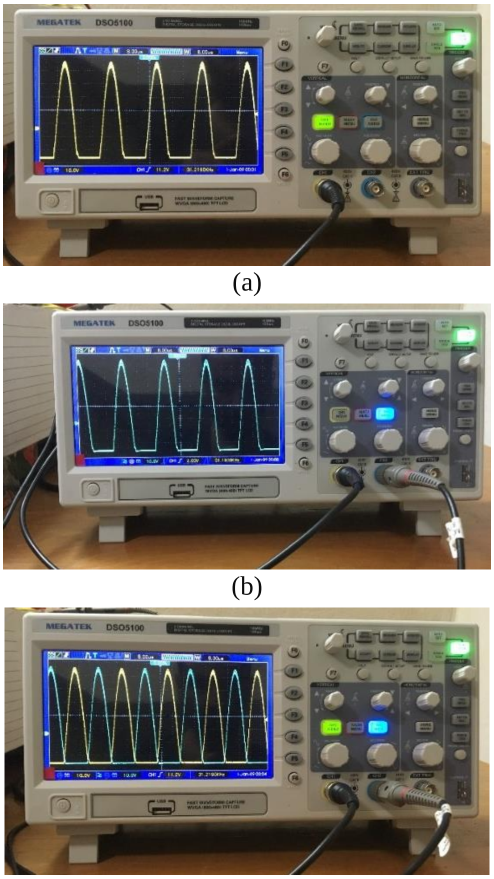

(a)

(b)

(c)

Fig. 13. The sample of the drain voltage signal of the MOSFETs M_{11} and M_{12} (a), the sample of the drain voltage signal of the MOSFETs M_{21} and M_{22} (b), and both voltage of the drains of the MOSFETs (M_{11} and M_{12}, yellow diagram) and (M_{21} and M_{22}, blue diagram) in the oscilloscope (c).

Fig. 14. An example of the output signal (two ends of the induction coil) produced in the oscilloscope.

In the presented work, the diameter range of the bottles that can be sealed is equal to 1cm to 13cm. This range is completely required by the food and pharmaceutical industries. In Fig. 15, two examples of bottles used in the pharmaceutical industry are sealed with the implemented circuit. The diameter of the bottle in Fig. 15 (a) is 4 cm and the diameter of the bottle in Fig. 15 (b) is 13 cm. This bottle (Fig. 15 (b)) is one of the largest bottles used in the pharmaceutical industry. As seen from the figure, the sealing has an acceptable result.

(a) (b)

Fig. 15. Two examples of bottles used in the pharmaceutical industry are sealed with the implemented circuit.

VII. Conclusions

Induction heating enables the conversion of electrical energy into thermal energy with fast and high conversion efficiency in a wide range of industries. In this paper, an optimized hardware design and implementation of an effective and optimal induction heating circuit for induction sealing has been investigated. The implemented induction sealing circuit works based on zero voltage switching technology to generate the output signal. In this work, the focus is on the implementation process and practical tips for implementing this circuit. In this structure, by using inductors, transistors, and capacitors with suitable tolerable current and voltage, it can supply the power and frequency of the output signal applied to the induction coil for various applications. Also, the induction coil has an elliptical structure with a uniform magnetic field along the length of the coil, which makes it suitable for sealing a wide range of bottles. In the presented structure, the frequency of the signal created at both ends of the induction coil is around 31kHz, which is suitable for generating the eddy current in the aluminum foil in the bottle caps. The proposed circuit has been tested and investigated. It has acceptable induction sealing for various industries. Future research that can be done on the circuit includes using a power supply with variable voltage to control the output power according to different applications (different bottle sizes) can be effective in designing a flexible circuit. In addition, providing an oil-based cooling system for coil cooling is another work that improves circuit performance in industrial applications.

REFERENCES

[1] Ibrahim, I.D., Hamam, Y., Sadiku, E.R., Ndambuki, J.M., Kupolati, W.K., Jamiru, T., Eze, A.A, and Snyman, J., Need for Sustainable Packaging: An Overview, *polymers*, Vol. 14, 2022, pp. 1-16.

[2] Lucia, O., Maussion, P., Dede, E., Burdio, J., Induction Heating Technology and Its Applications: Past Developments, Current Technology, and Future Challenges, *IEEE Transactions on Industrial Electronics*, Vol. 61, No. 5, 2014, pp. 2509-2520.

[3] Kumar Paul, A., Structured Protection Measures for Better Use of Nanocrystalline Cores in Air-Cooled Medium-Frequency Transformer for Induction Heating, *IEEE Transactions on Industrial Electronics*, Vol. 68, No. 5, 2021, pp. 3898-3905.

[4] Kumar Paul, A., ZVZCS SRI Guides Optimal Use of Copper and Core for Air-Cooled Nanocrystalline Transformer for Induction Heating, *IEEE Trans. Ind. Appl.*, Vol. 56, No. 2, 2020, pp. 970-978.

[5] Goldstein, R., Stuehr, W., Black, M., Design and Fabrication of Inductors for Induction Heat Treating, *Journal of Neural Engineering, 2014, Book chapter, ASM Handbook,* Vol. 4, 16, 2014, pp. 589-606.

[6] https://www.dynaplasgroup.com/induction-cap-sealing/

[7] Kumar Paul, A., Current Density Characterization of Litz Wires used in Induction Heating Coils: A Practical Approach, *Proceedings of the IEEE International Conference on Power Electronics, Drives and Energy Systems (PEDES)*, Chennai, India, 2018, pp. 1-6.

[8] Sherwali, A., Dunford, W., Experimental Evaluation of Heating Water by Electromagnetic Induction, *Pro. of the IEEE Canadian Conf. of Electrical and Computer Engineering*, Edmonton, AB, Canada, 2019, pp. 1-4.

[9] Kumar Paul, A., Robust Features of SOSMC Guides in Quality Characterization of Tank Circuit in Air-Cooled Induction Cap Sealing, *IEEE Trans. Ind. Appl.,* Vol. 54, No. 1, 2018, pp. 755-763.

[10] Kumar Paul, A., Inverter Topology for Zero-Ventilated High Frequency Induction Heating Systems, *Pro. of the IEEE Inter. Conf. on Power Electronics, Drives and Energy Systems*, Jaipur, India, 2020, pp. 1-6.

[11] Lope, I., Acero, J., Burdio, J., Carretero, C., Alonso, R., Design and Implementation of PCB Inductors With Litz-Wire Structure for Conventional-Size Large-Signal Domestic Induction Heating Applications, *IEEE Trans. Ind. Appl.*, Vol. 51, No. 3, 2014, pp. 2434-2442.

[12] Ngo-Phi, T., Nguyen-Quang, N., Variable Pulse Density Modulation for Induction Heating, *International Symposium on Electrical and Electronics Engineering (ISEE)*, Ho Chi Minh, Vietnam, 2012, pp. 1-6.

[13] Kumar Paul, A., Chinoy, S., Air Cooled Induction Heater for Efficient Sealing of Containers using Wide Range Foils, *IEEE Trans. Ind. Appl.*, Vol. 52, No. 4, 2016, pp. 3398-3407.

[14] Knauf, B., Webb, D.P., Liu, C., Conway, P.P., Low frequency induction heating for the sealing of plastic microfluidic systems, *Journal of Microfluid Nanofluid*, Vol. 9, 2010, pp. 243-252.

[15] Dimitrov, B., Hayatleh, K., Barker, S., Collier, G., Design, Analysis and Experimental Verification of the Self-Resonant Inverter for Induction Heating Crucible Melting Furnace Based on IGBTs Connected in Parallel, *Electricity*, Vol. 2, 2021, pp. 439-458.

[16] Hussain, I., Woo, D.K., Inductance Calculation of Single-Layer Planar Spiral Coil, *Electronics,* Vol. 11, 2022, pp. 1-10.

[17] Plumed, E., Acero, J., Lope, L., Burdio, J., Design methodology of high performance domestic induction heating systems under worktop, *IET Power Electronics,* Vol. 13, Iss. 2, 2020, pp. 300-306.

[18] Abdulbaqi, I.M., A. Kadhim, A.H., Abdul-Jabbar, A.H., Abood, F.A., Hasan, T.K., Design and Implementation of an Induction Furnace, *Diyala Journal of Engineering Sciences,* Vol. 08, No. 01, 2015, pp. 64-82.

[19] Serrano, J., Acero, J., Lope, I., et al., A flexible cooking zone composed of partially overlapped inductors, *IEEE Trans. Ind. Electron.,* 2023, Vol. 65, No. 10, 2018, pp. 7762-7771.

[20] Wang, H., Blaabjerg, F., Reliability of capacitors for DC-link applications in power electronics converters-A review, *IEEE Trans. Ind. Appl.,* Vol. 50, No. 5, pp. 1117-1125.

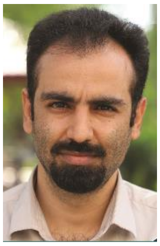

Bahram Rashidi was born in Boroujerd, Iran, in 1986. He received his B.S. degree in electrical engineering from Lorestan University, Iran, in 2009 and he received his M.S. from Tabriz University, Iran in 2011 also he obtained his Ph.D degree from Isfahan University of Technology (IUT), in 2016, where he is currently an associate professor in the department of electrical engineering at University of Ayatollah Boroujerdi. His research interests include hardware implementation for the arithmetic of finite fields, cryptographic hardware, Block ciphers and VLSI circuits for elliptic curve cryptosystems.

IECO
International Journal Of
Industrial Electronics Control and Optimization
Print ISSN: 3517-2645
Online ISSN: 3568-2645
Homepage: https://ieco.usb.ac.ir/

Novel Sliding Mode Control Approach for Quasi-Z-Source Converters with Improved Performance

Gholamreza Shahabadi[1] | Majidreza Naseh[2]

Department of Electrical Engineering, University of Applied Science and Technology, South Khorasan Branch, Iran[1]
Department of Electrical engineering, Birjand Branch, Islamic Azad University, Birjand, Iran[2]
Corresponding author's email: naseh@iaubir.ac.ir

Article Info

Article type:
Research Article

Article history:
Received: 27-January-2024
Received in revised form:
15-May-2024
Accepted: 21-May-2024
Published online: 22-Sep-2024

Keywords:
Z-Source,
Quasi-Z-Source,
Sliding mode Control,
Robust control.

ABSTRACT

Quasi-Z-source converters (QZSC) are gaining popularity because they operate in a single stage, use smaller components, and maintain continuous input current with a common ground. This converter is widely used in various applications that require a DC-DC converter. The small-signal analysis and linearization methods are often employed for controlling the Quasi-Z-source converters. The linear model of QZSC does not provide sufficient stability control over a wide range. Sliding Mode Control (SMC) is widely used in electronic power converters due to its variable structure. This paper presents a SMC for a QZSC with three objectives:1) to achieve stability across a wide range of QZSC; 2) to systematically select the proposed controller coefficients; and 3) to enable tracking of the reference voltage in spite of changes in input voltage, reference voltage, and output load. The simulations have been done with the help of MATLAB/Simulink and show the effectiveness of the proposed method.

I. Introduction

As the demand for energy grows, humanity is seeking for new ways to produce electricity on a large scale to satisfy the demands of industrial projects. Due to the limitations and risks associated with electricity generation with fossil resources and nuclear fuel, these approaches are not suitable solutions for supplying electrical power. One of the most effective methods for generating electricity is the use of renewable sources, like solar and wind energy [1, 2]. A DC-DC converter is essential because of the low voltage level and DC output from these sources [3]. Today, the use of DC-DC converters in medical equipment, power factor correction (PFC), electric vehicles, uninterruptible power supply (UPS), green energy systems, portable electrical equipment, photovoltaic systems, wind turbines, fuel cell systems, x-ray systems, auxiliary power supplies, and discharge lamps is commonplace [4, 5].

The Z-source converter (ZSC) is one of the widely used non-isolated converters. It is capable of converting power across AC-DC, AC-AC, DC-AC, and DC-DC configurations [6]. The Quasi-Z-Source converter (QZSC) is a variant of the ZSC and

Publisher: University of Sistan and Baluchestan

shares its characteristics. QZSC has all the same characteristics as ZSC. This converter is notable for its broad voltage range, great protection from electromagnetic interference, and immunity to short-circuiting [7]. QZSCs have lower voltage and current stresses, and a higher voltage gain than ZSCs. Recently, various configurations based on the traditional QZSC have emerged [8]. Each configuration is designed for particular applications [9, 10]. Considering the changes in various model parameters in electronic power converters across a wide operating range, the closed-loop control of these converters is a field of research. To effectively design the controller, it is essential to utilize the state-space model of the converter. To derive the system's state-space model, the averaged state space method has been employed. [11]. The adapted state space model is a non-linear model because of the presence of various non-linear components in the structure of converters. Different nonlinear control techniques, such as passivity-based control [12], feedback linearization [13], sliding mode control [14], and adaptive control [15], can be utilized to adjust the output voltage, providing an appropriate response to this issue. Considering the variable structure of power electronic systems and the simplicity of their design, the sliding mode control method can be an appropriate choice for controller design. The initial step in the development of the controller is choosing the sliding surface. The sliding surface can be defined from the combination of system state variables [16]. The goal here is to use a zero-sliding surface to find the control input that will place the system response on the sliding surface. To prevent chattering and limit switching frequency, an adjustable range of bandwidths around the sliding surface is chosen to determine the switching frequency [17].

The most important defect of this method is the change of switching frequency, which has been used to solve this defect by the design method of equivalent control and soft switching [18]. In the equivalent control method, it is necessary to select the derivative of the sliding surface as zero, in addition to the sliding surface itself. Consequently, the controller design assumes that the derivative of the sliding surface is zero. The equivalent control method in controller design involves experimenting with different parameters of the model until the desired output is achieved. In [19], an adaptive sliding model-based equivalent control method is employed to design the controller for the ZSC. During the controller's design, the influence of the output filter within the circuit was not considered. The design process that employs the aforementioned method is highly complex and involves a substantial amount of calculations. In [20], control is conducted by utilizing the definition of hysteresis band based on the feedback linearization control method. In this article, the hysteresis band is not clearly defined, resulting in disruption of the control operation. In [21], the controller for the converter was designed using the sliding step-back control method. By utilizing a trial-and-error approach, the control parameters for this article have been determined. The design procedure in the mentioned method is complex and requires a high number of calculations. In [22], the linearization method is employed to design the controller; however, this does not guarantee stability in a wide range. In [23], the sliding mode controller design method is employed for controller design. In the design of the controller in this method, the effect of the output filter, which is used to eliminate electromagnetic noise, has not been considered. In [24], the sliding mode control technique is employed to design the controller. This study does not examine the impact of variations in the reference voltage on the output. Also, the time required to reach the steady state in tracking the reference voltage is long. In [25], a predictive controller is employed to design the controller. The advantage of these controllers is that they can track sinusoidal currents with near-zero error. This controller has been engineered to function at a specific point within the set, which precludes it from exerting control across a wider range. Based on the presence of a right-sided zero in the voltage transfer function of the capacitor to the duty cycle, it can be inferred that the system is a nonminimum-phase system. Utilizing the duty cycle for directly adjusting the capacitor voltage leads to instability within the closed loop [26]. In order to address this problem, a forward feedback strategy has been suggested in [27]. In this reference, the adjustment of the duty cycle value is based on the steady-state error. The primary limitation of this approach is the substantial error that exists throughout a wide range of converter performance. In [28], a sliding mode controller has been designed. This controller has three drawbacks. Firstly, in order to calculate the reference current of the inverter, it requires access to the load value, which adds the need for incorporating a sensor into the structure. Secondly, the designed controller is of hysteresis type, which leads to variable frequency. Thirdly, the sliding mode controller is designed based on ideal equations, which may not hold valid in persistent state situations. In [29], the design and simulation of a neural sliding mode controller for the electric vehicle's braking system are detailed. This controller exhibits superior performance relative to that of the conventional PI controller. In [30], proposes a solution to overcome the aforementioned three issues. In this reference, an ultra-surface is introduced to regulate the DC voltage and mitigate the nonminimum-phase behavior of the capacitor voltage on the DC side. Additionally, there is no need to separately calculate the reference current of the inductor. This controller, being designed based on a nonlinear model of the converter, offers the capability to operate over a wide range. However, the effects of input voltage variations and load changes on the output voltage of the converter are not addressed in this reference. Additionally, the adjustment of seven parameters is necessary to attain zero steady-state error in the reference output voltage. Consequently, this issue leads to an amplification of computational complexity and a deceleration in the tracking operations. This research presents a novel step-by-step design method for a robust sliding mode controller in a DC-DC QZSC. The parameters of this controller are systematically determined, and then stability analysis is conducted. The design process for controlling the DC-DC flyback converter is discussed in [31]. In [32, 33], new structures of converters are presented with the aim of increasing voltage efficiency. From a control perspective, these converters, with increased voltage gain and a higher number of components, introduce more complexity in the control operation. Apart from the introduction, this article is comprised of the following sections: In the second section, the topology and averaged state-space model of the QZSC are discussed. The third section focuses on the small-signal model of the targeted converter. The fourth section describes the transfer functions of the QZSC using the small-signal model. In the fifth and sixth sections, linear and nonlinear controllers are proposed for the QZSC. The seventh section presents simulations and examines the system's response to variations in reference voltage, load changes, and input voltage variations. Finally, in the eighth section, a summary and conclusion are provided.

II. Topology and state-space model of QZSC

The QZSC has a topology as shown in Figure (1). This circuit consists of capacitors C_1 and C_2, as well as inductors L_1 and L_2. Additionally, this circuit includes a diode and a power switch, denoted as D_1 and S, respectively. In order to reduce noise in the output of this circuit, a capacitor-inductor filter is utilized, with L_f and C_f representing the respective components. The output load is denoted by R_L. In this circuit, V_{in} represents the input voltage, while V_o represents the output voltage of the converter. i_L represents the current flowing through the impedance network inductor, while i_{Lf} denotes the current flowing through the output filter. Moreover, v_{C1} denotes the voltage across the capacitors associated with the QZSC, while v_{Cf} represents the voltage across the capacitor of the output filter. To analyze this converter, it is crucial to consider the following key points:

All components are assumed to be ideal, including the control switch, which is of the MOSFET type.

The converter operates in continuous conduction mode, and its performance is analyzed during steady-state operation.

The capacitance of the capacitors is high enough to disregard the ripple voltage across them.

The state equations of the converter are derived from both the ON and OFF states of the switch. By examining these two states, we can obtain the final state equations of the converter using the method of averaging the state equations.

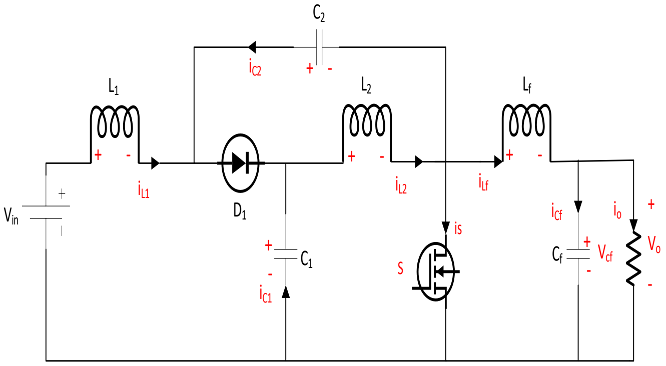

Fig. 1. Configuration of QZSC

III. Analysis of the QZSC in the ON switch state

Figure (2) illustrates the state associated with the switch being in the ON position. In this state, the diode in the converter is OFF. During this state, the capacitors associated with the impedance network in the converter start charging the inductors of the impedance network. In this case, by composing suitable equations, the state equations can be represented as equation (1).

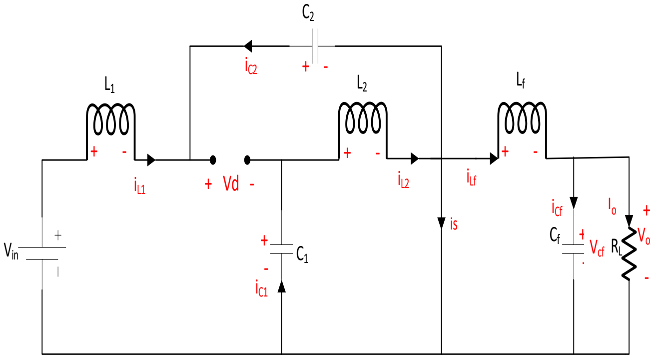

Fig. 2. Configuration of QZSC in ON switch state

$$\begin{cases} L_1\dfrac{di_{L1}}{dt}=V_{in}+v_{C2} \\ L_2\dfrac{di_{L2}}{dt}=v_{C1} \\ L_f\dfrac{di_{Lf}}{dt}=-v_{Cf} \\ C_1\dfrac{dv_{C1}}{dt}=-i_{L2} \\ C_2\dfrac{dv_{C2}}{dt}=-i_{L1} \\ C_f\dfrac{dv_{Cf}}{dt}=i_{Lf}-\dfrac{v_{Cf}}{R_L} \end{cases} \quad (1)$$

IV. Analysis of the QZSC in the OFF-switch state

The state depicted in Figure (3) corresponds to the OFF state of the switch. In this state, the energy stored in the inductors of the impedance network is transferred to the capacitors. The diode is in a forward-biased state during this condition. As a result, by formulating suitable equations, the state equations can be expressed as equation (2).

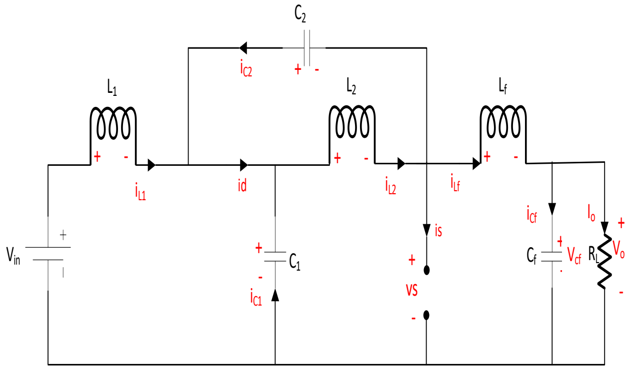

Fig. 3. Configuration of QZSC in OFF switch

$$\begin{cases} L_1\dfrac{di_{L1}}{dt} = V_{in} - v_{C1} \\ L_2\dfrac{di_{L2}}{dt} = -v_{C2} \\ L_f\dfrac{di_{Lf}}{dt} = v_{C1} + v_{C2} - v_{Cf} \\ C_1\dfrac{dv_{C1}}{dt} = i_{L1} - i_{Lf} \\ C_2\dfrac{dv_{C2}}{dt} = i_{L2} - i_{Lf} \\ C_f\dfrac{dv_{Cf}}{dt} = i_{Lf} - \dfrac{v_{Cf}}{R_L} \end{cases} \tag{2}$$

By applying the principle of the second voltage balance to the inductors, we can obtain the following equations (3):

$$\int_0^{DT_s} i_{L1}dt + \int_{DT_s}^{T_s} i_{L1}dt = 0$$
$$\int_0^{DT_s} i_{L2}dt + \int_{DT_s}^{T_s} i_{L2}dt = 0$$
$$\int_0^{DT_s} i_{Lf}dt + \int_{DT_s}^{T_s} i_{Lf}dt = 0 \tag{3}$$

In equation (3), the coefficient D represents the duty cycle, which is the ratio of the switch-on time or the duration of the short connection period to the total time of one switching cycle. By applying the principle of the second voltage balance to the inductors, the gain of the converter in the steady state can be calculated as equation (4).

$$\frac{v_{Cf}}{V_{in}} = \frac{1-D}{1-2D} \tag{4}$$

V. Averaged state-space model of QZSC

The final state equations of the system are derived by multiplying the state equations corresponding to the switch-on state by the coefficient D, and multiplying the state equations corresponding to the switch-off state by the coefficient 1-D. It should be noted that the following assumption has been made:

$$x = [i_{L1} = x_1, i_{L2} = x_2, i_{Lf} = x_3,$$
$$v_{C1} = x_4, v_{C2} = x_5, v_{Cf} = x_6] \tag{5}$$

We express the system state equations in affine form.

$$\dot{x} = f(x) + g(x)D \tag{6}$$

$$f(x) = \begin{pmatrix} \frac{V_{in}-x_4}{L_1} \\ \frac{-x_5}{L_2} \\ \frac{x_4+x_5-x_6}{L_f} \\ \frac{x_1-x_3}{C_1} \\ \frac{x_2-x_3}{C_2} \\ \frac{R_L x_3-x_6}{C_f} \end{pmatrix}, \quad g(x) = \begin{pmatrix} \frac{x_4+x_5}{L_1} \\ \frac{x_4+x_5}{L_2} \\ \frac{-x_4-x_5}{L_f} \\ \frac{x_3-x_1-x_2}{C_1} \\ \frac{x_3-x_1-x_2}{C_1} \\ 0 \end{pmatrix} \tag{7}$$

VI. Dynamic analysis and controller Design

To design a linear controller for the QZSC, it is necessary to perform linearization around a specific operating point. To achieve linearization in equation (7), we replace the state variables and the duty cycle with the relations (8).

$$x_i = X_i + \tilde{x}_i \; (i = 1 \; to \; 6)$$
$$D = d + \tilde{d} \tag{8}$$

In equation (8), $\boldsymbol{X_i}$ represents the system's operating point, while $\boldsymbol{\tilde{x}_i}$ represents the disturbances around the operating point. Using the volt-second balance law for inductors, we can express the value of the state variables in steady state as equation (9).

$$\begin{cases} X_6 = V_{ref}, D = \frac{V_{ref}-V_{in}}{2V_{ref}-V_{in}} \\ X_5 = \frac{DV_{in}}{1-2D}, X_4 = \frac{(1-D)V_{in}}{1-2D} \\ X_1 = X_2 = \frac{(1-D)V_{ref}}{(1-2D)R_{LOAD}}, X_3 = \frac{V_{ref}}{R_{LOAD}} \end{cases} \tag{9}$$

By separating the different components and neglecting the product of small signal components (small signal approximation), we can obtain the linearized state-space model of the converter. It is important to note that when simplifying the derivative related to the system's operating point, it simplifies to zero. By utilizing this property, one can calculate the operating point of the system. By separating the matrix related to the states from the matrix related to the inputs, we can also derive the matrix of this converter. It should be noted that the product of two small signal values has been disregarded. The matrix of this converter can be expressed by equation (10).

$$\dot{\tilde{x}} = A\tilde{x} + B\tilde{d}$$

$$A = \begin{bmatrix} 0 & 0 & 0 & \dfrac{d-1}{L_1} & \dfrac{d}{L_1} & 0 \\ 0 & 0 & 0 & \dfrac{d}{L_2} & \dfrac{d-1}{L_2} & 0 \\ 0 & 0 & 0 & \dfrac{1-d}{L_f} & \dfrac{1-d}{L_f} & \dfrac{-1}{L_f} \\ \dfrac{1-d}{C_1} & \dfrac{d}{C_1} & \dfrac{d-1}{C_1} & 0 & 0 & 0 \\ \dfrac{-d}{C_2} & \dfrac{1-d}{C_2} & \dfrac{d-1}{C_2} & 0 & 0 & 0 \\ 0 & 0 & \dfrac{1}{C_f} & 0 & 0 & \dfrac{-1}{R_L C_f} \end{bmatrix}$$

$$B = \begin{bmatrix} \frac{x_4+x_5}{L_1} \\ \frac{x_4+x_5}{L_2} \\ \frac{-x_4-x_5}{L_f} \\ \frac{x_3-x_2-x_1}{C_1} \\ \frac{x_3-x_2-x_1}{C_2} \\ 0 \end{bmatrix} \quad (10)$$

In the representation of state space equations, C corresponds to the output vector of the system. In two situations, the transfer function of the system will be computed. When considering the inductor current and the output capacitor voltage, vector C in the standard state equations is represented as equation (11).

$$C_1 = [1\ 0\ 0\ 0\ 0\ 0]$$

$$C_6 = [0\ 0\ 0\ 0\ 0\ 1] \quad (11)$$

VII. Transfer functions of QZSC

The voltage transfer functions of the output filter capacitor and the inductor current with respect to the QZSC during the short circuit cycle will be calculated in the following calculations. These functions are denoted as H1 and H6, respectively. The following equation is utilized to calculate the aforementioned transfer functions. By applying the Laplace transform to equation (10) and utilizing the defined matrices C, we obtain:

$$H(s) = C(SI - A)^{-1}B + E \quad (12)$$

S is the Laplace variable. In equation (12), the variable I represents the 6x6 identity matrix, and E is the feedforward matrix of the system and its value is assumed to be zero.

The transfer functions of H1 and H6 are calculated based on the values given in Table 1. These transfer functions are represented by equation (13).

$$\begin{cases} H_1(s) = \frac{n_1(s)}{d_1(s)} \\ H_6(s) = \frac{n_6(6)}{d_1(s)} \\ n_1(s) = 1.5e6s^5 + 9.438e7s^4 + 3.416e13s^3 + 1.67e15s^2 \\ \quad +1.88e20s + 5.57e21 \\ n_6(s) = -4.412e9s^4 + 1.673e12s^3 - 5.49e16s^2 - \\ \quad 2.231e19s + 5.22e22 \\ d_1(s) = s^6 + 39.22s^5 + 2.307e7s^4 + 6.739e8s^3 + \\ \quad 1.301e14s^2 + 2.014e15s + 4.68e18 \end{cases}$$

$$(13)$$

TABLE.1. NOMINAL PARAMETERS OF QZSC

Parameters	Symbol	Value
Input voltage	V_{in}	50V
Network impedance inductors	L_1, L_2	0.5mH
Output filter inductor	L_f	1mH
Network impedance capacitors	C_1, C_2	150µF
Output filter capacitor	C_f	170µF
Output resistor	R_L	150Ω
Reference voltage	V_{ref}	500V
Switching frequency	f_s	50kHz

Upon calculating the zeros and poles of the H6 transfer function, it becomes evident that this function possesses zeros situated to the right of the imaginary axis. The positions of both the zeros and poles for the H1 and H6 transfer functions are depicted in Figure 4. Hence, it is not feasible to directly regulate the capacitor voltage as an output. The H1 transfer function is a minimum-phase transfer function, allowing for indirect control of the output voltage by manipulating the inductor current. Next, we will describe the process of creating a control loop to indirectly regulate the converter's output voltage.

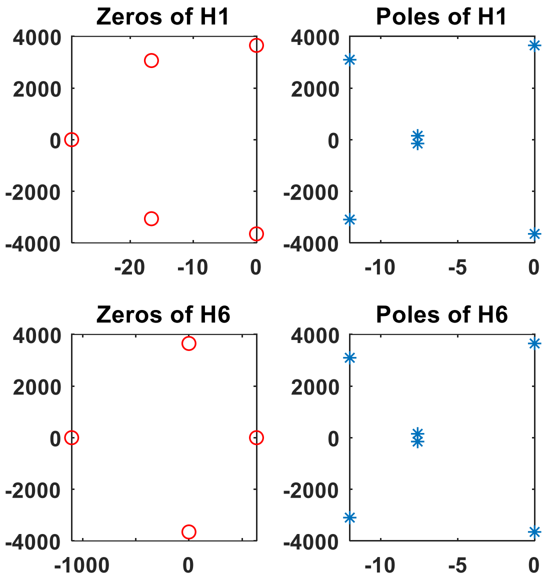

Fig. 4. Location of poles and zeros of QZSC transfer function

VIII. Indirectly controlling the output voltage of QZSC

Because the output capacitor voltage exhibits a non-minimum phase behavior and direct control is not possible, the voltage of the capacitor is indirectly regulated by manipulating the inductor current. Furthermore, considering the minimum-phase characteristic of the transfer function the inductor current to the duty cycle, the inductor current can be directly regulated by adjusting the duty cycle. The block diagram of the closed-loop system with the inclusion of the PI controller is depicted in Figure 5. The presented block diagram includes a pair of PI controllers.

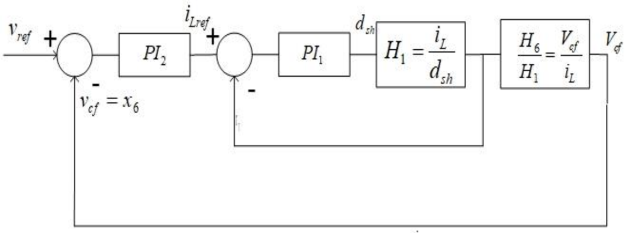

Fig. 5. Block diagram of the indirect control of the output voltage of the QZSC

The PI$_1$ controller receives the signal that is the difference between the impedance network's inductor current and its reference value. The output of the PI$_1$ controller represents the value of the duty cycle. The PI$_2$ controller selects the reference current value of the inductor according to the error between the reference voltage and the output voltage. The selection of these coefficients in this section has been done through a process of trial and error. The specific values of these coefficients are listed in Table 2. Smart algorithms can be employed to select coefficients that enable the control system to achieve desired values for evaluated parameters such as settling time, overshoot, undershoot, and steady-state error. Figure 6 illustrates the response of the block diagram when a reference voltage of 500V is chosen. The output reaches 500V after one undershoot and several overshoots. The controller design using the linearization method is relatively simple, but it does not ensure stability in a wide range. By changing the operating point, the linearized model is not valid and the output does not converge to the reference value. Hence, employing non-linear control methods is appropriate for the aforementioned system. Mr. Yutkin introduced the sliding mode control method for systems with variable structure. This method is widely used in power electronic systems because of their variable structure. The first step of the sliding mode control method is to define the sliding surface. The sliding mode control brings the system states to the sliding surface. When the system reaches the sliding surface, the sliding mode control maintains the system state close to and along the sliding surface. Usually, the sliding surface is defined as the output error of the system. After placing the answer on the surface, the system switches to the sliding mode. With proper switching, the response slides on the surface until it stabilizes.

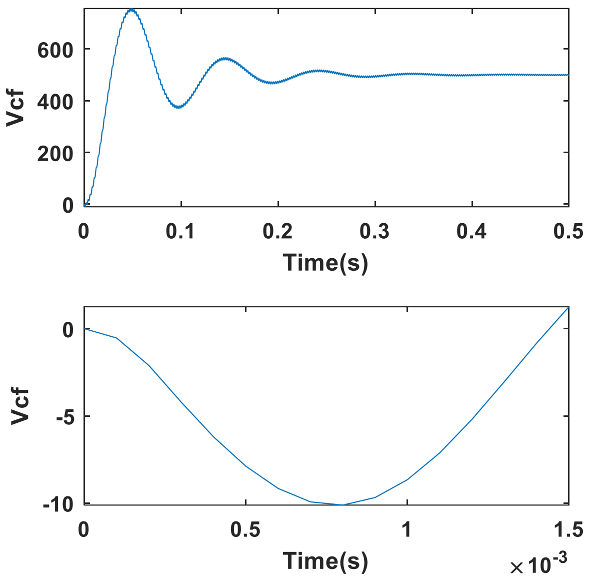

Fig.6. Step response of QZSC

TABLE. 2. SELECTED VALUES OF CONTROLLER COEFFICIENTS

controller coefficients	PI$_1$	PI$_2$
P	0.01	100
I	0.01	20

IX. Design of sliding mode controller in nominal condition

The sliding surface is defined by the current of the inductor in the impedance network. Equation (14) defines the sliding surface.

$$S = x_1^* - x_1 \tag{14}$$

The following definition is used to enter the output voltage in Equation (14).

$$x_1^* = K_I \int (x_6^* - x_6)dt \tag{15}$$

The output error is reduced to zero by including the integral factor. By substituting equation 15 into equation 14, we obtain the following result:

$$S = x_1^* - x_1 = K_I \int (x_6^* - x_6)dt - x_1 \tag{16}$$

Assuming that the sliding surface's derivative is zero, we can derive the equivalent controller.

$$\dot{S} = 0 \rightarrow \dot{x}_1^* - \dot{x}_1 = 0 \tag{17}$$

Using the state equations in equation (17), we can express the converter's short circuit cycle as equation (18).

$$D = \frac{K_I L_1 (x_6^* - x_6) + (x_4 - V_{in})}{x_4 + x_5} \tag{18}$$

Figure 7 presents the block diagram associated with the proposed control method.

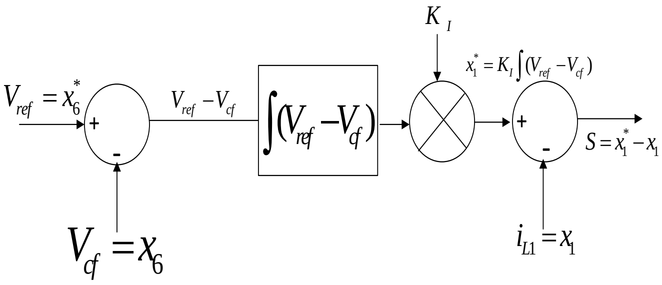

Fig.7. Block diagram of the proposed control method

By choosing the reference voltage and computing the duty cycle, the other state variables will be in the steady-state as equation (19).

$$\begin{cases} X_6 = V_{ref}, D = \frac{V_{ref} - V_{in}}{2V_{ref} - V_{in}} \\ X_5 = \frac{DV_{in}}{1-2D}, X_4 = \frac{(1-D)V_{in}}{1-2D} \\ X_1 = X_2 = \frac{(1-D)V_{ref}}{(1-2D)R_{LOAD}} \\ X_3 = \frac{V_{ref}}{R_{LOAD}} \end{cases} \quad (19)$$

X. Systematic selection of the integral coefficient on the sliding surface

By substituting equation (18) for the duty cycle into equations (6) and (7), we obtain the state equations in the form of equation (20):

$$\begin{cases} \dot{x}_1 = K_I(x_6^* - x_6),\ \dot{x}_2 = K_I(x_6^* - x_6) + \frac{x_4 - V_{in} - x_5}{L_2} \\ \dot{x}_3 = \frac{-K_I L_1(x_6^* - x_6) + V_{in} + x_5 - x_6}{L_f} \\ \dot{x}_4 = \frac{K_I L_1(x_6^* - x_6) + (x_4 - V_{in})}{x_4 + x_5}\left(\frac{x_3 - x_1 - x_2}{C_1}\right) + \\ \left(\frac{x_1 - x_3}{C_1}\right) \\ \dot{x}_5 = \frac{K_I L_1(x_6^* - x_6) + (x_4 - V_{in})}{x_4 + x_5}\left(\frac{x_3 - x_1 - x_2}{C_2}\right) + \\ \left(\frac{x_2 - x_3}{C_2}\right),\ \dot{x}_6 = x_3 - \frac{x_6}{R_L} \end{cases} \quad (20)$$

Assuming that the changes around the operating point are small, we can linearize equation (20) around a specific operating point. We use the Jacobian method to linearize the system. The system under investigation has a 6x6 Jacobian matrix, and we can calculate its terms using equation (21).

$$\begin{cases} a_{ij} = \frac{\delta f_i}{\delta x_j}\ \ (i,j = 1,2,3,4,5,6) \\ \dot{x}_1 = f_1(x_1, x_2, x_3, x_4, x_5, x_6) \\ \dot{x}_2 = f_2(x_1, x_2, x_3, x_4, x_5, x_6) \\ \dot{x}_3 = f_3(x_1, x_2, x_3, x_4, x_5, x_6) \\ \dot{x}_4 = f_4(x_1, x_2, x_3, x_4, x_5, x_6) \\ \dot{x}_5 = f_5(x_1, x_2, x_3, x_4, x_5, x_6) \\ \dot{x}_6 = f_6(x_1, x_2, x_3, x_4, x_5, x_6) \end{cases} \quad (21)$$

The components of the Jacobian matrix are calculated according to equation (22). By substituting the system parameters and the desired operating point into equation (22), we obtain the Jacobian matrix as shown in equation (23). We note that the rest of the elements in the Jacobian matrix are zero. Using the Jacobian matrix that we computed, which depends on the integral gain, we can verify the system stability near the chosen operating point. We derive the system's characteristic equation from equation $|SI - A| = 0$. According to the Routh-Hurwitz stability criterion, the systems with $0 < K_I < 200$ are stable. The system's characteristic equation is given by equation (24). Within the given range, the system has all its poles on the left of the imaginary axis. S represents the Laplace variable in this context.

$$\begin{cases} a_{16} = a_{26} = -K_I, a_{25} = \frac{-1}{L_2}, a_{24} = \frac{1}{L_2} \\ a_{35} = \frac{1}{L_f}, a_{36} = \frac{K_I L_1 - 1}{L_f} \\ a_{41} = \frac{1}{C_1} - \frac{x_4 - V_{in} + K_I L_1(x_6^* - x_6)}{C_1(x_4 + x_5)} \\ a_{42} = \frac{-(x_4 - V_{in} + K_I L_1(x_6^* - x_6))}{C_1(x_4 + x_5)} \\ a_{43} = \frac{x_4 - V_{in} + K_I L_1(x_6^* - x_6)}{C_1(x_4 + x_5)} - \frac{1}{C_1} \\ a_{44} = \frac{(x_4 - V_{in} + K_I L_1(x_6^* - x_6))(x_1 + x_2 - x_3)}{C_1(x_4 + x_5)^2} - \\ \frac{x_1 + x_2 - x_3}{C_1(x_4 + x_5)} \\ a_{45} = \frac{(x_4 - V_{in} + K_I L_1(x_6^* - x_6))(x_1 + x_2 - x_3)}{C_1(x_4 + x_5)^2} \\ a_{46} = \frac{K_I L_1(x_1 + x_2 - x_3)}{C_1(x_4 + x_5)} \\ a_{51} = -\frac{x_4 - V_{in} + K_I L_1(x_6^* - x_6)}{C_2(x_4 + x_5)} \\ a_{52} = \frac{1}{C_2} - \frac{x_4 - V_{in} + K_I L_1(x_6^* - x_6)}{C_2(x_4 + x_5)} \\ a_{53} = \frac{x_4 - V_{in} + K_I L_1(x_6^* - x_6)}{C_2(x_4 + x_5)} - \frac{1}{C_2} \\ a_{54} = \frac{(x_4 - V_{in} + K_I L_1(x_6^* - x_6))(x_1 + x_2 - x_3)}{C_2(x_4 + x_5)^2} \\ - \frac{x_1 + x_2 - x_3}{C_2(x_4 + x_5)} \\ a_{55} = \frac{(x_4 - V_{in} + K_I L_1(x_6^* - x_6))(x_1 + x_2 - x_3)}{C_2(x_4 + x_5)^2} \\ a_{56} = \frac{K_I L_1(x_1 + x_2 - x_3)}{C_2(x_4 + x_5)} \\ a_{63} = 1,\ a_{66} = \frac{-1}{R_L} \end{cases} \quad (22)$$

$$A = \begin{pmatrix} 0 & 0 & 0 & 0 & 0 & -K_I \\ 0 & 0 & 0 & 2000 & -2000 & -K_I \\ 0 & 0 & 0 & 0 & 1000 & \frac{K_I}{2} - 1000 \\ 3.5 \times 10^3 & -3.2 \times 10^3 & -3.5 \times 10^3 & -233 & 211 & 0.22K_I \\ -3.2 \times 10^3 & 3.5 \times 10^3 & -3.5 \times 10^3 & -233 & 211 & 0.22K_I \\ 0 & 0 & 1 & 0 & 0 & -6.7 \times 10^3 \end{pmatrix} \quad (23)$$

$$S^6 + 23.4S^5 + (1.684 \times 10^7 - 0.5K_I)S^4 + (3.12 \times 10^8 - 233.9K_I)S^3 + (4.68 \times 10^{13} - 6.316 \times 10^6 K_I)S^2$$

$$(6.238 \times 10^{11} - 3.119 \times 10^{9} K_I)S + 4.678 \times 10^{12} K_I = 0 \qquad (24)$$

XI. Correction of Sliding Model Controller and Proof of Stability

The relation derived for the sliding mode controller in equation (18) is based on the nominal parameters of the model. To cope with model uncertainties, $K\ sgn(S)$ can be incorporated into the equivalent controller. To ensure that the sliding surface is absorbing, we define a Lyapunov function and verify the Lyapunov stability condition. We use equation (25) to define the Lyapunov function:

$$V(S) = \frac{1}{2} S^2 \qquad (25)$$

The defined Lyapunov function has the initial condition of being positive definite. In order for the sliding surface to be absorbing, the derivative of the Lyapunov function must be negative definite.

$$\dot{V}(S) = S\dot{S} \leq -\eta |S| \qquad (26)$$

We chooseη as a positive parameter for controlling the system.

$$\dot{S} = K_I (x_6^* - x_6) - D \frac{x_4 + x_5}{L_1} - \frac{V_{in} - x_4}{L_1} \qquad (27)$$

We substitute the duty cycle with the following expression in equation (27):

$$D = \frac{K_I L_1 (x_6^* - x_6) + (x_4 - V_{in})}{x_4 + x_5} + K sgn(S) \qquad (28)$$

$$S(-K sgn(S)) \frac{x_4 + x_5}{L_1} \leq -\eta |S| \qquad (29)$$

Considering that the value of $sgn(S) = |S|/S$ is the equation (29) is simplified as follows:

$$K \geq \frac{\eta L_1}{x_4 + x_5}, \eta > 0 \qquad (30)$$

To summarize, the stability of the designed controller is ensured in a broad range of operating point and model uncertainties by selecting the control gain from equation (30). The designed controller has robustness to changes in load, input voltage and reference voltage. For instance, by choosing $\eta = 10$ and selecting the nominal operating points of the system using equation (19), we obtain a value of $K \geq 6 \times 10^{-6}$. However, in the simulations, we have opted for a value of $K = 10^{-5}$. According to equation (24), the coefficient $K_I = 100$ is considered.

TABLES.3. SETTLING TIME AND OVERSHOOT IN DIFFERENT MODES

Situation	Settling-time (s)		%O. V	
	increase	decrease	increase	decrease
Test 1	0.01	0.03	8	16
Test 2	0.006	0.02	3.98	1.52
Test 3	0.009	0.01	1.6	0.8

Figure 11 shows the block diagram where the control signal is applied to the converter. Within this diagram, the duty cycle derived from equation (28) regulates the converter's switch. This particular converter employs a unipolar switching technique.

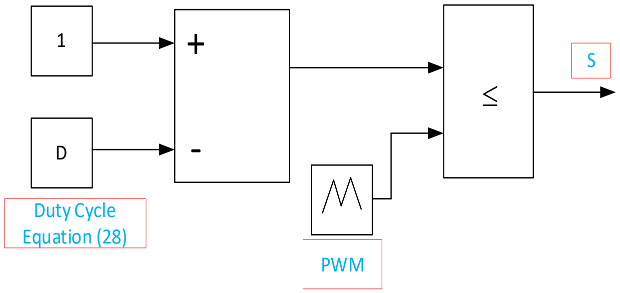

Fig.8. Shoot-through unipolar PWM technique

XII. Simulation results

This section presents simulations in MATLAB/Simulink software version 2018 that were performed to assess the performance of the suggested control technique. The system parameters of the QZSC are given in Table 1. The sampling time step for all the simulations is $1\mu s$. The following section examines how the designed controller responds to the variations of input voltage, load, and reference voltage. In Table 3, the control parameters, including settling time and overshoot, are calculated when changing the reference voltage, input voltage, and load.

Test1: This test considers the nominal values given in Table 1 and studies the step change in the output reference voltage. The output reference voltage increases from $V_{ref} = 500V$ to $V_{ref} = 550V$att $= 0.5s$and then decreases to $V_{ref} = 450V$at $t = 1s$. Figure 9 shows that the output voltage, V_o, can follow its reference value,V_{ref}. In this case output voltage error, defined by (31), tends zero in a finite time as shown in Figure 9.

$$V_{error} = V_{Cf} - V_{ref} \qquad (31)$$

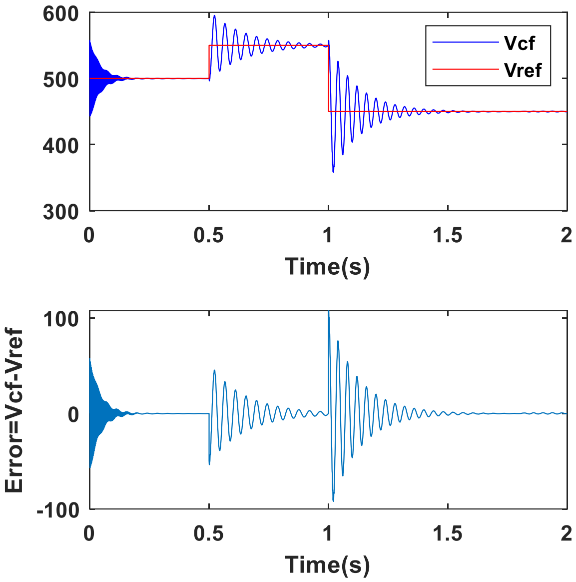

Fig.9. output reference voltage variation in test 1

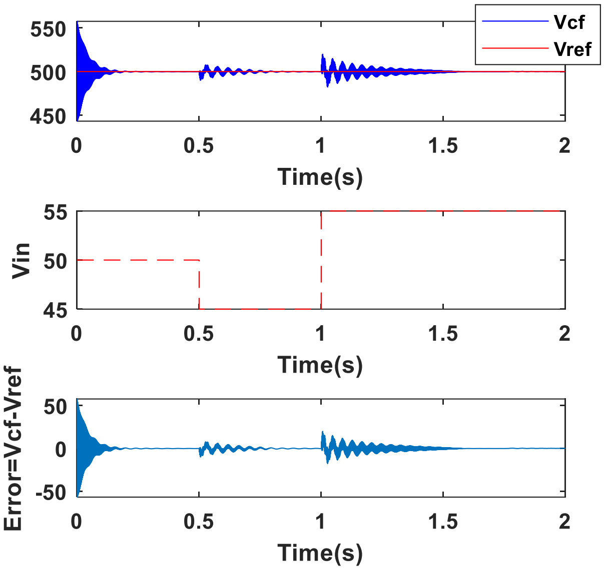

Fig.10. output reference voltage variation in test 2

Test2: To demonstrate the proposed controller's performance under input voltage disturbance, a step change in input voltage is applied. In this simulation, the input voltage is decreased to 45V in steps after 0.5s. As Figure 8 shows, the output voltage follows the reference voltage after a brief oscillation, and the steady state error is zero in this case. To enhance the impact of the input voltage on the output, this value is raised to 55V. Figure 10 shows that the output voltage reaches the reference value after a brief fluctuation. Figure 10 displays the variations in steady state error and input voltage. The results demonstrate the stability of the proposed control system under varying input voltage. Table 3 displays the results obtained by varying the input voltage. Specifically, during the increase and decrease phases, the overshoot values are 3.98 and 1.52, respectively. These findings demonstrate that the presented control system exhibits robustness to fluctuations in the input voltage.

Test3: This simulation verifies the robustness of the proposed controller under varying load conditions. The output resistance is decreased from 150Ω to 135Ω after 0.5s. Figure 11 shows the result of this change. Figure 11 shows that the output voltage reaches the initial reference voltage within 0.5s of the simulation. To examine the effect of higher output resistance on the output voltage, this value is raised to 165Ω. This change occurs 1s into the simulation. Figure 11 also presents the result of this change. Figure 11 illustrates that the output voltage matches the reference voltage quickly after the resistance increases. Hence, the proposed controller can track the reference voltage despite variations in the output resistance. Based on Table 3, the settling time and overshoot values during both the increase and decrease phases of the output load fall within an acceptable range. As a result, the provided controller exhibits robustness in load variations.

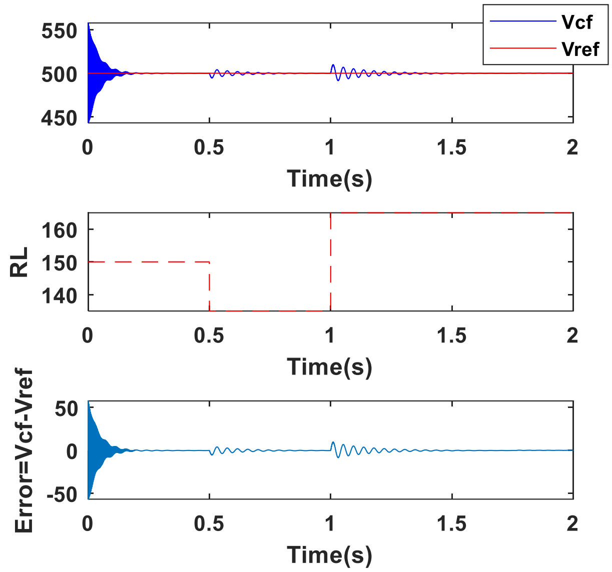

Fig .11. output reference voltage variation in test 3

Test4: This simulation explores the effect of changing the reference voltage, input voltage, and output resistance at the same time. After 0.5s from the beginning of the simulation, the reference voltage was lowered to 450V, the input voltage to 45V, and the output resistance to 135Ω. Figure12 demonstrate the results of these changes. The output could track the reference voltage and reached 450V quickly. One second after the simulation begins, the reference voltage rises to 550V, the input voltage goes up to 55V, and the output resistance grows to 165Ω. The output followed the reference voltage as the parameters increased at the same time, and it attained 550V in a brief period.

XIII. Conclusion

In this study, we investigated the equivalent sliding mode control of a DC-DC QZSC with an output filter. The principles of step-by-step design for the sliding mode controller and the selection criteria for the control coefficients in the sliding mode method are presented in detail. In the studied system, the output capacitor voltage to the duty cycle of the converter is nonminimum phase. This means we cannot control the output voltage directly by changing the duty cycle. To address this issue, we used a sliding surface defined as the proportion of the difference between the QZSC's inductor current and its reference value. Based on simulations conducted in both transient and permanent modes, the designed sliding mode controller exhibits robustness in response to changes in load and input voltage. The percentage of response overshoot in reference voltage change exceeds that of both load and input voltage changes. Furthermore, in accordance with the system's reference voltage definition, the output error remains zero throughout all tests. The proposed controller ensures local asymptotic stability. The potential for a universal asymptotic controller for the desired system can be explored in further research.

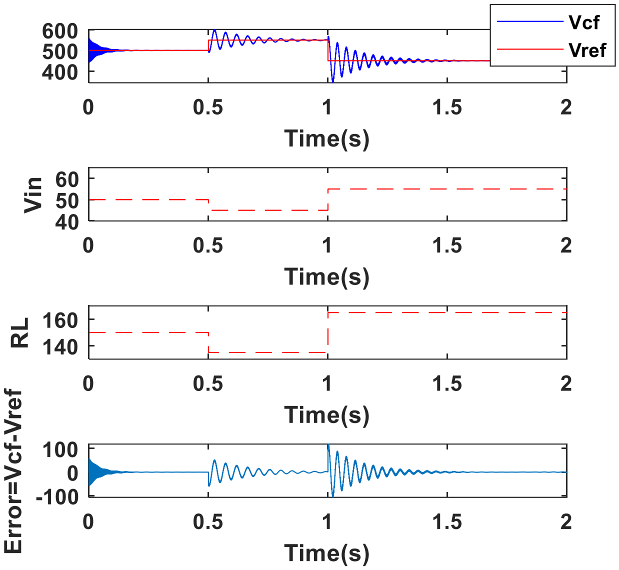

Fig. 12. output reference voltage variation in test 4

References:

[1] N. Javaid *et al.*, "An intelligent load management system with renewable energy integration for smart homes," *IEEE access*, vol. 5, pp. 13587-13600, 2017.

[2] W. Tushar, J. A. Zhang, C. Yuen, D. B. Smith, and N. U. Hassan, "Management of renewable energy for a shared facility controller in smart grid," *IEEE Access*, vol. 4, pp. 4269-4281, 2016.

[3] X. Zhu and B. Zhang, "High step-up quasi-Z-source DC-DC converters with single switched capacitor branch," *Journal of Modern Power Systems and Clean Energy*, vol. 5, no. 4, pp. 537-547, 2017.

[4] S. Padmanaban, P. K. Maroti, J. B. Holm-Nielsen, F. Blaabjerg, Z. Leonowicz, and V. Yaramasu, "Quazi Z-source single stage high step-up DC-DC converter for grid-connected PV application," in *2019 IEEE International Conference on Environment and Electrical Engineering and 2019 IEEE Industrial and Commercial Power Systems Europe (EEEIC/I&CPS Europe)*, 2019, pp. 1-6: IEEE.

[5] P. Padmavathi and S. Natarajan, "Single switch quasi Z-source based high voltage gain DC-DC converter," *International Transactions on Electrical Energy Systems*, vol. 30, no. 7, p. e12399, 2020.

[6] F. Z. Peng, "Z-source inverter," *IEEE Transactions on industry applications*, vol. 39, no. 2, pp. 504-510, 2003.

[7] J. Anderson and F. Z. Peng, "Four quasi-Z-source inverters," in *2008 IEEE Power Electronics Specialists Conference*, 2008, pp. 2743-2749: IEEE.

[8] G. R. Shahabadi, M. R. Naseh, and S. Es' haghi, "Analysis and design of switched capacitor-based Quasi-Z-Source DC-DC converter with improved operation factors," *International Journal of Electronics*, pp. 1-20, 2023.

[9] S. Laali and E. Babaei, "Developed Quasi Z-Source Inverters Based on Diode-Cells: Analysis and

Implementation," *International Journal of Industrial Electronics Control and Optimization*, vol. 5, no. 1, pp. 51-62, 2022.

[10] A. Karbalaei, M. Mardaneh, and M. Shasadeghi, "A new topology of the switched-inductor/capacitor quasi Z-source inverter with ability of uplifted-boost," *International Journal of Industrial Electronics Control and Optimization*, vol. 3, no. 1, pp. 35-46, 2020.

[11] M. K. Kazimierczuk, "Small-signal modeling of open-loop PWM Z-source converter by circuit-averaging technique," *IEEE Transactions on Power Electronics*, vol. 28, no. 3, pp. 1286-1296, 2012.

[12] S. Samanta, S. Barman, J. P. Mishra, P. Roy, and B. K. Roy, "Design of an interconnection and damping assignment-passivity based control technique for energy management and damping improvement of a DC microgrid," *IET Generation, Transmission & Distribution*, vol. 14, no. 11, pp. 2082-2091, 2020.

[13] M. Salimi and S. Siami, "Cascade nonlinear control of DC-DC buck/boost converter using exact feedback linearization," in *2015 4th International Conference on Electric Power and Energy Conversion Systems (EPECS)*, 2015, pp. 1-5: IEEE.

[14] A. A. Chlaihawi, A. M. Al-Modaffer, and Z. Alhadrawi, "Performance analysis of different methods for optimal sliding mode control of DC/DC buck converter," *Bulletin of Electrical Engineering and Informatics*, vol. 13, no. 1, pp. 117-124, 2024.

[15] N. Mukherjee and D. Strickland, "Control of cascaded DC–DC converter-based hybrid battery energy storage systems—Part II: Lyapunov approach," *IEEE Transactions on Industrial Electronics*, vol. 63, no. 5, pp. 3050-3059, 2015.

[16] F. Bagheri, H. Komurcugil, O. Kukrer, N. Guler, and S. Bayhan, "Multi-input multi-output-based sliding-mode controller for single-phase quasi-Z-source inverters," *IEEE Transactions on Industrial Electronics*, vol. 67, no. 8, pp. 6439-6449, 2019.

[17] M. Bensaada and A. B. Stambouli, "A practical design sliding mode controller for DC–DC converter based on control parameters optimization using assigned poles associate to genetic algorithm," *International Journal of Electrical Power & Energy Systems*, vol. 53, pp. 761-773, 2013.

[18] S. H. Chincholkar and C.-Y. Chan, "Design of fixed-frequency pulsewidth-modulation-based sliding-mode controllers for the quadratic boost converter," *IEEE Transactions on Circuits and Systems II: Express Briefs*, vol. 64, no. 1, pp. 51-55, 2016.

[19] S. Ahmadzadeh, G. A. Markadeh, and N. Abiadi, "Adaptive sliding mode control of step-up/step-down Z-source DC-DC converter," in *2019 27th Iranian Conference on Electrical Engineering (ICEE)*, 2019, pp. 841-845: IEEE.

[20] H. Zaman, X. Zheng, S. Khan, H. Ali, and X. Wu, "Hysteresis modulation-based sliding mode current control of Z-source DC-DC converter," in *2016 IEEE 8th International Power Electronics and Motion Control Conference (IPEMC-ECCE Asia)*, 2016, pp. 321-324: IEEE.

[21] S. Ahmadzadeh, G. A. Markadeh, and N. Abjadi, "Back-stepping sliding mode control of a Z-source DC-DC converter," in *2018 9th Annual Power Electronics, Drives Systems and Technologies Conference (PEDSTC)*, 2018, pp. 414-418: IEEE.

[22] Y. Zhang, Q. Liu, J. Li, and M. Sumner, "A Common Ground Switched-Quasi-$ Z $-Source Bidirectional DC–DC Converter With Wide-Voltage-Gain Range for EVs With Hybrid Energy Sources," *IEEE Transactions on Industrial Electronics*, vol. 65, no. 6, pp. 5188-5200, 2017.

[23] S. Ahmadzadeh, G. A. Markadeh, and N. Abjadi, "Sliding mode control of the four quadrant quasi-Z-Source DC-DC Converter," in *2017 8th Power Electronics, Drive Systems & Technologies Conference (PEDSTC)*, 2017, pp. 496-501: IEEE.

[24] A. H. Rajaei, S. Kaboli, and A. Emadi, "Sliding-mode control of Z-source inverter," in *2008 34th Annual Conference of IEEE Industrial Electronics*, 2008, pp. 947-952: IEEE.

[25] J. R. Gazoli, M. G. Villalva, and E. Ruppert, "Micro-inverter for integrated grid-tie photovoltaic module using resonant controller," *International Transactions on Electrical Energy Systems*, vol. 24, no. 5, pp. 713-722, 2014.

[26] Y. P. Siwakoti, F. Z. Peng, F. Blaabjerg, P. C. Loh, G. E. Town, and S. Yang, "Impedance-source networks for electric power conversion part II: Review of control and modulation techniques," *IEEE Transactions on Power Electronics*, vol. 30, no. 4, pp. 1887-1906, 2014.

[27] Y. Tang and S. Xie, "System design of series Z-source inverter with feedforward and space vector pulse-width modulation control strategy," *IET Power Electronics*, vol. 7, no. 3, pp. 736-744, 2014.

[28] S. Rostami, V. Abbasi, and F. Blaabjerg, "Implementation of a common grounded Z-source DC–DC converter with improved operation factors," *IET Power Electronics*, vol. 12, no. 9, pp. 2245-2255, 2019.

[29] J. A. Ruz-Hernandez, R. Garcia-Hernandez, M. A. Ruz Canul, J. F. Guerra, J.-L. Rullan-Lara, and J. R. Vior-Franco, "Neural Sliding Mode Control of a Buck-Boost Converter Applied to a Regenerative Braking System for Electric Vehicles," *World Electric Vehicle Journal*, vol. 15, no. 2, p. 48, 2024.

[30] A. Zakipour, S. Shokri-Kojori, and M. Tavakoli Bina, "Sliding mode control of the nonminimum phase grid-connected Z-source inverter," *International Transactions on Electrical Energy Systems*, vol. 27, no. 11, p. e2398, 2017.

[31] M. Salimi, "A novel approach for sliding mode controller design and parameters selection in flyback switching power supplies," Journal of Iranian Association of Electrical and Electronics Engineers, 1 vol. 16, no. 3, pp. 1-12, 2019.[In Pesian]

[32] H. B. Nouzadan, M. Babaei, and A. Ibrahim, "A novel multilevel structure for impedance source inverters," Journal of Iranian Association of Electrical and Electronics Engineers, vol. 15, no. 1, pp. 75-87, 2018. [In Persian].

[33] S. Eslami, A. Siadat, and M. Javani, "Design and simulation of an interleaved parallel boost DC-DC converter with soft switching for application in renewable energy sources," Journal of Iranian Association of Electrical and Electronics Engineers, vol. 19, no. 2, pp. 149-158, 2022. [In Persian].

Gholamreza Shahabadi was born in Birjand in 1983. He obtained his MS degree from the Faculty of Engineering at Islamic Azad University, Gonabad branch, Iran, in 2008. Later, he pursued his PhD degree in Electrical Engineering at the Islamic Azad University, Birjand branch, Iran, in 2024. Since 2013, he has been working at the University of Applied Science and Technology, South Khorasan Branch, Iran, where his research field focuses on DC-DC converters.

Majid Reza Naseh was born in Mashhad, Iran, in 1970. He earned his M.S. degree from the Faculty of Engineering at Islamic Azad University, South Tehran branch, Iran, in 1995. Later, he pursued his Ph.D. degrees in Electrical Engineering at the Islamic Azad University, Science and Research branch, Tehran, Iran, completing them in 2008. In 1998, he joined the Islamic Azad University, Birjand branch, where he began his academic career as an Instructor in the Department of Electrical Engineering. Since 2008, he has held the position of Assistant Professor. His research interests encompass a wide range of topics, including power electronic converters, power system operation and control, and hybrid renewable energy systems.

IECO
International Journal Of
Industrial Electronics Control and Optimization
Print ISSN: 3517-2645
Online ISSN: 3568-2645
Homepage: https://ieco.usb.ac.ir/

Impedance-Based Approach for Locating Short-Circuit Faults in Inverter-Based Active Distribution Networks

Morteza Behbahanipour[1] | Seyed Fariborz Zarei[1] | Mohammadhadi Shateri[2]

Department of Electrical and Computer Engineering, Qom University of Technology, Qom, Iran.[1]
Département de génie des systèmes, École de technologie supérieure, Université du Québec, Montréal, Canada.[2]
Corresponding author's email: zarei@qut.ac.ir

Article Info

Article type:
Research Article

Article history:
Received: 17-May-2024
Received in revised form: 27-June-2024
Accepted: 30-June-2024
Published online: 02-July-2024

Keywords:
Active distribution network,
Fault location,
Impedance-based approach,
Inverter-based distributed generation resources.

ABSTRACT

This paper proposes an impedance-based approach for locating short-circuit faults in active distribution networks (DNs). This topic is a crucial task for operators, especially in grids with inverter-based distributed generators (IBDGs). Various methods have been proposed in this research area, including traveling waves, impedance-based methods, and artificial intelligence (AI) techniques. Among them, the impedance-based scheme offers a straightforward and efficient feature suitable for integration with AI-based techniques. This paper introduces an enhanced fault localization method based on impedance estimation, consisting of two main components: (i) fault distance determination and (ii) faulty section identification. This method accounts for the modeling of inverter-based resources under both symmetrical and asymmetrical faults, incorporating the impact and behavior of such sources. Unlike conventional impedance-based methods, our approach does not require network information such as structure, lines, load data, or voltage and current measurements along the feeder at multiple points. It can serve as a feature in AI-based techniques, significantly enhancing accuracy and reducing the complexity of such techniques. To validate the efficacy of the proposed approach, we conducted a series of time-domain case studies and provided mathematical proofs. The results demonstrate the effectiveness of our scheme in accurately locating faults with varying resistances at different positions in the presence of IBDGs.

I. Introduction

Accurate fault location is crucial for the efficient operation of power distribution systems as it speeds up the restoration of the affected section and the resumption of faulty line operation. Fault locators are specialized devices designed to detect and pinpoint faults in power distribution systems [1]. Advanced fault locators offer a more reliable and efficient solution for identifying and resolving faults in DNs [2]. In these devices, the core processor, including the fault location scheme, is the key component. The scheme should determine the faulted section and the location of the fault within the section. The several connected feeders of the distribution network, with multiple laterals, complicate the process of fault location. Additionally, the prevalent fault resistance in the distribution network is another influencing factor. Moreover, by connecting inverter-based distributed generations (IBDGs) to the distribution network, the network becomes active with multiple feeding locations. This transformation turns the distribution systems into multi-source systems with dispersed production resources, making fault location more intricate and necessitating further investigation. During short-circuit fault conditions, the control of inverters is crucial in generating output currents. This further complicates the behavior of IBDGs, consequently affecting the fault location to the same degree.

Generally, the existing fault location schemes are divided into three categories of "impedance-based methods", "traveling waves-based schemes" and "artificial-intelligence-based techniques" [3]. Among these, impedance-based methods are preferred due to their simplicity and effectiveness, allowing for straightforward implementation using a simple thresholding model and potential integration as inputs for AI-based techniques. Consequently, this paper focuses on impedance-based schemes, with a detailed literature review provided subsequently.

Zhu et al. [4] pioneered the impedance iterative method, presenting an iterative approach for single-phase fault analysis and addressing multi-response challenges through current patterns. Lee et al. [5] later enhanced this technique by effectively resolving multi-response issues using flow patterns. Yang et al. [6] utilized the distributed line model to develop an iterative algorithm for single-phase faults, whereas Nouri et al. [7] extended this model to include single-phase and 2-phase fault localization. Works by Salim et al. [8] and Bretas et al. [9] introduced an iterative algorithm to mitigate load change issues, focusing on single-phase fault detection in the presence of DGs, and later incorporated a neural network to tackle multi-response problems [10]. Nunes et al. [11] further refined the algorithm by integrating DGs into fault analysis for single-phase and 3-phase faults. In addition, an iterative method was proposed in [12] & [13] for comprehensive fault location using an equation and addressed multi-response challenges through the current error index. Other works such as [14] & [15] contributed an iterative algorithm for all fault types, considering DGs and employing a 2nd degree equation. In 2021, Dashti et al. [16] introduced an iterative algorithm for all fault scenarios using a 5th degree equation, incorporating DG presence and leveraging artificial intelligence for load estimation, along with pattern matching to resolve multi-response issues. Despite their evolution, these methods vary in their ability to detect specific faults and in their capacity to accommodate DG units or address multi-response issues, especially in scenarios with high fault current patterns. The effectiveness of these methods is influenced by network equipment like reclosers and breakers.

Building upon the foundations established in [17], this work proposes an extended impedance-based fault location method to address the correct performance under all types of faults, support inverter-based distributed generators (DGs), and solve multi-response problems with minimal information. The key contributions and novelties of the proposed method, compared to the existing approaches and the study [17], are as follows:

- A generalized inverter control scheme under both symmetrical and asymmetrical short-circuit faults is modeled in developing the proposed scheme.
- Grid codes for inverter-based resources are considered in the proposed approach.
- Different short-circuit fault conditions are taken into account in the proposed scheme.
- The proposed approach does not rely on network information, and communication infrastructure is not required.
- The proposed scheme effectively identifies the faulted section in a multi-line, multi-lateral distribution network by considering the multi-response problems.

The paper is organized as follows: Section II covers the preliminaries of impedance-based methods, while Section III delves into the behavior of IBDGs under short-circuit fault conditions. The fundamentals of the proposed fault location approach are presented in Section IV, followed by the proposed scheme for identifying the faulty section in Section V. The paper concludes with case studies, simulation results, and conclusions in Sections VI, VII, and VIII, respectively.

II. Preliminaries of the Impedance-Based Methods

Similar to the distance relay logic, impedance-based methods utilize voltage and current phasors to estimate fault impedance. These methods are typically categorized as ‘single head’ or ‘double head’ methods. The ‘single head’ method relies on substation voltage and current data to pinpoint the fault location, while the ‘double head’ method analyzes voltage and current data from both ends of the distribution system to determine the fault location. A visual representation of the impedance-based method is depicted in Fig. 1 using a basic circuit model. Within this model, V_m denotes the voltage at the measurement node, Z_l represents fault impedance per unit length, l indicates the distance of the fault from the measurement node, V_s stands for source voltage, and Z_s signifies source impedance. Equation (1) outlines the interrelation among these parameters, facilitating the calculation of fault distance from the relay point [3] and [18].

$$l = \frac{V_m}{I_f . Z_l} \tag{1}$$

III. Modeling of Inverter-Based Distributed Generations

A. Control Loops

The schematic diagram of Fig. 2 illustrates a grid-connected inverter [19] with its two control loops of an inner current control loop and an outer DC link voltage control loop. This section will focus on the current control scheme under a short-circuit fault condition [20]. The Double Synchronous Reference Frame (DSRF) scheme has been extensively utilized in the literature to discuss the control scheme under fault condition. The DSRF method involves transforming the currents into the “dq” frame using two clockwise and counter-clockwise synchronous reference frames (SRF), as shown in Fig. 3 [21]. In the DSRF scheme, the “dq” components consist of DC and double-frequency pulsating components. As an example, when utilizing the clockwise-SRF, the positive-sequence component of $iabc$ appears as DC-components and pulsating components with a frequency of double the line frequency (2ω0). Filtering out the pulsating terms results in two independent variables, $Id+$ and $Iq+$, which can be controlled separately. Consequently, Fig. 4 displays the commonly used structure for controlling these variables. The output filter model is represented by $\frac{1}{L_f . s + R_f}$, and $\mathrm{G_i}$ is the current controller, as given in equation (2), where BW is the current control loop bandwidth.

$$\begin{gathered} \mathrm{G_i(s) = K_p + \frac{K_i}{s}} \\ \mathrm{K_p = BW. L_f} \\ \mathrm{K_i = BW. R_f} \end{gathered} \tag{2}$$

Due to space constraints, this paper focuses exclusively on the current reference generation under fault condition, and it does not delve into the specifics of the power inverter control system. However, interested readers are encouraged to refer to the related references for further information on topics such as feed-forward compensation and the current control loop decoupling, phase-locked-loop implementation, and DC-link voltage controller [22, 23, 24].

B. Behavior Under Fault Condition

According to the grid codes, the grid-connected inverters are expected to deliver reactive current during short-circuit faults to assist the power grid [25]. This requirement is incorporated in this paper, as depicted in Fig. 5 and detailed in (3).

$$I_{q0-GC} = \begin{cases} -2.5I_n(V_1 - 0.9) & 0.5 < V_1 < 0.9 \\ I_n & V < 0.5_1 \end{cases} \tag{3}$$

In a general form, assume that the grid voltages and the output currents are expressed as shown in (4) and (5), respectively.

$$V = V_1 e^{\,j\omega t} \tag{4}$$

$$I = I_{d0} e^{\,j\omega t} + I_{q0} e^{\,j(\omega t - \frac{\pi}{2})} \tag{5}$$

, where $V1$ is the grid voltage positive sequence component. Also, $Id0$ and $Iq0$ are positive sequence currents aligned with “d” and “q” axes of SRF, respectively.

Substituting (4) and (5) into (6) gives the injected active power flowing into the grid as shown in (7).

$$p(t) = \Re(1.5I^*V) \tag{6}$$

$$\bar{p}(t) = 1.5V_1 I_{d0} \tag{7}$$

Substituting equation (7) into equation (5) and calculating the amplitude of the three-phase currents yields the following equation for three-phase current values.

$$|I_{abc}| = \sqrt{\bar{p}^2 A^2 + I_{q0}^2}, \text{ where } A = \frac{2}{3V_1} \tag{8}$$

This equation specifies the current injected by IBDGs in terms of the bus voltage. The obtained current references are utilized in developing the proposed fault location scheme, which ensures the correct operation in presence of IBDGs.

IV. Fundamentals of the Proposed Fault Location Method

In this section, we will first outline the process for determining the distance of various types of faults along a power line. Subsequently, we will elaborate on how this approach can be adapted to effectively manage networks with IBDGs.

A. Calculation of Fault Distance in a Sample Line

Fig. 6 shows a sample line, which is used for developing the fault distance calculation equations. In this figure, d is fault distance in per unit; m and n are phases “a”, “b” or “c”; r , i are real and imaginary parts of variables; V_{sa} is phase “a” terminal “S” voltage; V_{Fm} is phase “m” fault point voltage; I_{Fm} is phase “m” fault current; I_{Lm} is phase “m” load current; I_{sa} is phase “a” sending-end current; I_{sm} is phase “m” sending-end current; R_{Fm} is phase “m” Fault resistance; Z_{aa} is phase “a” self-impedance; Z_{th} is terminal “R” equivalent impedance; V_{th} is terminal “R” equivalent voltage.

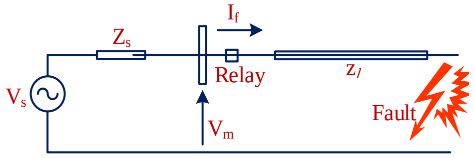

Fig. 1. The concept of impedance-based methods

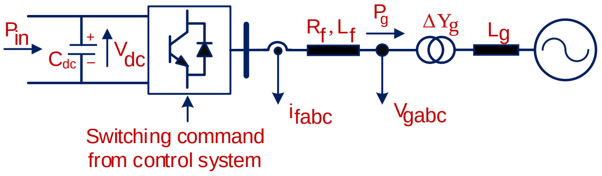

Fig. 2. Schematic diagram and power circuit of a grid-connected inverter

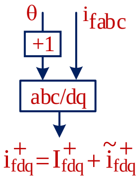

Fig. 3. Obtaining “dq” component using clockwise and counter-clockwise synchronous reference frames (SRFs), namely double-SRF (DSRF)

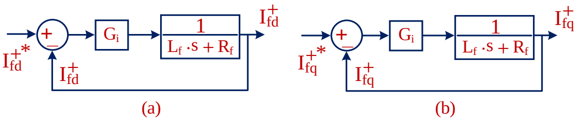

Fig. 4. Control of positive/negative sequence current components of Id +, Iq + in DSRF (a) positive-sequence current control in “d” axis of clockwise SRF, (b) positive-sequence current control in “q” axis of clockwise SRF.

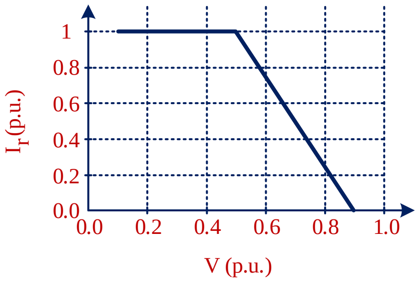

Fig. 5. Reactive current requirement under short circuit fault condition according to the Danish grid code.

With refer to Fig. 6, the steps for calculating the single-phase fault distance in a line are as follows [5], [8]:

1. As an initial assumption, the load current during the fault equals to the load current before the fault.

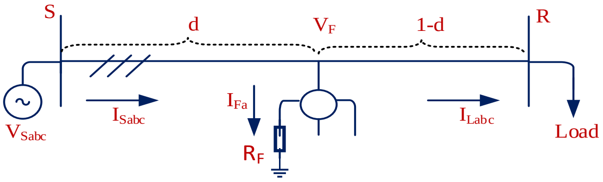

Fig. 6. LG short-circuit fault in a line

2. Calculate the fault current:

$$I_{sm} = I_{Fm} + I_{Lm} \tag{9}$$

3. Calculate the fault distance:

$$\begin{bmatrix} d \\ R_F \end{bmatrix} = \frac{\begin{bmatrix} I_{Fmi} & -I_{Fmr} \\ -M_{2m} & M_{1m} \end{bmatrix}}{M_{1m} I_{Fmi} - M_{2m} I_{Fmr}} . \begin{bmatrix} V_{Smr} \\ V_{Smi} \end{bmatrix} \tag{10}$$

where,

$$\begin{aligned} M_{1m} &= \sum_k (Z_{mkr} I_{Skr} - Z_{mki} I_{Ski}) \\ M_{2m} &= \sum_k (Z_{mkr} I_{Ski} + Z_{mki} I_{Skr}) \end{aligned} \tag{11}$$

4. Calculate the fault point voltage:

$$\begin{bmatrix} V_{Fa} \\ V_{Fb} \\ V_{Fc} \end{bmatrix} = \begin{bmatrix} V_{Sa} \\ V_{Sb} \\ V_{Sc} \end{bmatrix} - d. \begin{bmatrix} Z_{aa} & Z_{ab} & Z_{ac} \\ Z_{ba} & Z_{bb} & Z_{bc} \\ Z_{ca} & Z_{cb} & Z_{cc} \end{bmatrix} . \begin{bmatrix} I_{Sa} \\ I_{Sb} \\ I_{Sc} \end{bmatrix} \tag{12}$$

5. Update the load current at the moment of the fault, assuming a constant impedance load.

a- If the estimated fault is downstream of IBDG:

Calculate the paralleling capacity of the loads and lines, and obtain the load current from the opposite equation (refer to Fig. 7). The presence of IBDG affects the voltage and current at the beginning of the line [9][26].

$$I_{Lm} = \frac{V_{Fm}}{Z_{th\,m}} \tag{13}$$

b- If the estimated fault is above IBDG:

Calculate the load current from the opposite equation (refer to Fig. 8). The presence of IBDG affects the load current at the end of the line [11][27].

$$I_{Lm} = \frac{V_{Fm} - V_{th\,m}}{Z_{th\,m}} \tag{14}$$

6. Return to step 2, update the fault current, and repeat the steps until convergence .

$$|d_n - d_{n-1}| < \delta \tag{15}$$

B. Assessing the Different Types of Faults

Referring to Fig. 9, Fig. *10*, and Fig. 11, if a two-phase to ground, two-phase, or three-phase fault occurs, the third stage of section A is obtained from the following equations [8]:

a- If a two-phase fault occurs between phases "m" and "n" and the ground

In this case, the following equation is applied.

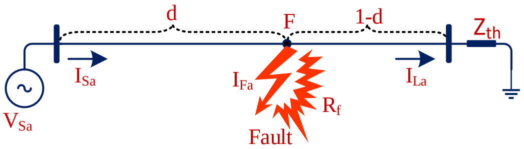

Fig. 7. The fault is downstream of IBDG

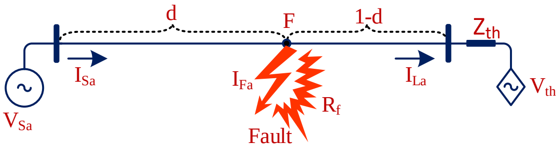

Fig. 8. The fault is upstream of IBDG

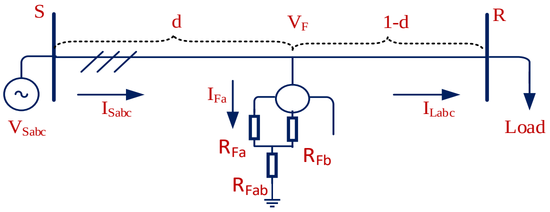

Fig. 9. LLG short-circuit fault in a line

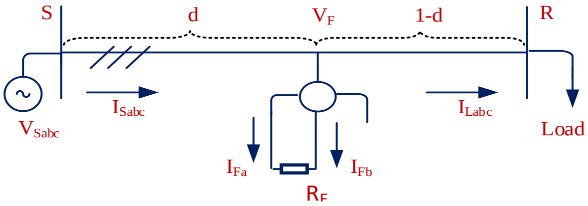

Fig. 10. LL short-circuit fault in a line

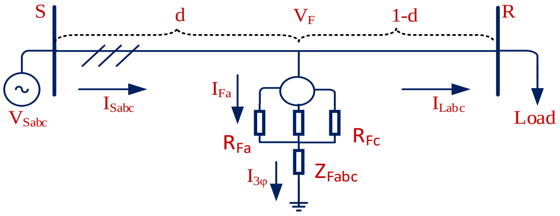

Fig. 11. LLL short-circuit fault in a line

$$\begin{bmatrix} d \\ R_{Fm} \\ R_{Fn} \\ R_{Fmn} \end{bmatrix} = T_1 . \begin{bmatrix} V_{Smr} \\ V_{Smi} \\ V_{Snr} \\ V_{Sni} \end{bmatrix}$$

where, (16)

$$T_1 = \begin{bmatrix} M_{1m} & I_{Fmr} & 0 & I_{Fmr} + I_{Fnr} \\ M_{2m} & I_{Fmi} & 0 & I_{Fmi} + I_{Fni} \\ M_{1n} & 0 & I_{Fnr} & I_{Fmr} + I_{Fnr} \\ M_{2n} & 0 & I_{Fni} & I_{Fmi} + I_{Fni} \end{bmatrix}^{-1}$$

b- If a two-phase fault occurs between phases "m" and "n",

In this case, the following equation is applied.

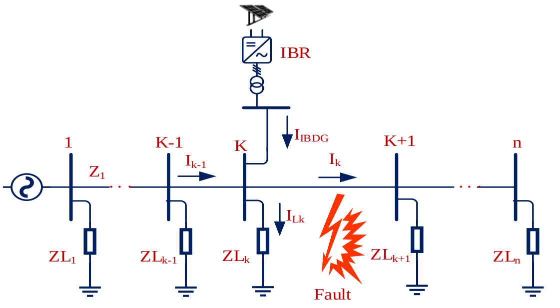

Fig. 12. The distribution network with a fault in downstream of IBDG.

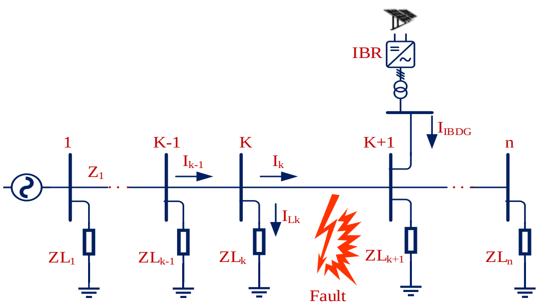

Fig. 13. The distribution network with a fault in upstream of IBDG.

$$\begin{bmatrix} d \\ R_F \end{bmatrix} = \begin{bmatrix} M_3 & I_{Fmr} \\ M_4 & I_{Fmi} \end{bmatrix}^{-1} . \begin{bmatrix} V_{Smr} - V_{Snr} \\ V_{Smi} - V_{Sni} \end{bmatrix} \qquad (17)$$

where,

$$\begin{aligned} M_3 = \sum_k \big(&(Z_{mkr} - Z_{nki}).I_{Skr} \\ &- (Z_{mki} - Z_{nki}).I_{Ski} \big) \\ M_4 = \sum_k \big(&(Z_{mkr} - Z_{nki}).I_{Ski} \\ &- (Z_{mki} - Z_{nki}).I_{Skr} \big) \end{aligned} \qquad (18)$$

where k is phases “a”, “b” or “c”.

c- If a three-phase fault occurs between phases “a” and “b” and c

In this case, the following equation is applied.

$$\begin{bmatrix} d \\ R_{Fa} \\ R_{Fb} \\ R_{Fc} \\ R_{Fabc} \\ X_{Fabc} \end{bmatrix} = T_2 . \begin{bmatrix} V_{Sar} \\ V_{Sai} \\ V_{Sbr} \\ V_{Sbi} \\ V_{Scr} \\ V_{Sci} \end{bmatrix}$$

where,

$$T_2 = \begin{bmatrix} M_{1a} & I_{Far} & 0 & 0 & I_{3\phi r} & -I_{3\phi i} \\ M_{2a} & I_{Fai} & 0 & 0 & I_{3\phi i} & I_{3\phi r} \\ M_{1b} & 0 & I_{Fbr} & 0 & I_{3\phi r} & -I_{3\phi i} \\ M_{2b} & 0 & I_{Fbi} & 0 & I_{3\phi i} & I_{3\phi r} \\ M_{1c} & 0 & 0 & I_{Fcr} & I_{3\phi r} & -I_{3\phi i} \\ M_{2c} & 0 & 0 & I_{Fci} & I_{3\phi i} & I_{3\phi r} \end{bmatrix}^{-1} \qquad (19)$$

$$\begin{aligned} I_{3\phi} &= I_{Fa} + I_{Fb} + I_{Fc} \\ Z_{Fabc} &= R_{Fabc} + JX_{Fabc} \end{aligned} \qquad (20)$$

$$\begin{aligned} I_k &= I_{k-1} - I_{Lk} + I_{IBDG} \\ I_{Lk} &= \frac{V_k}{Z_{Lk}} \\ V_k &= V_{k-1} - L.Z_{k-1}.I_{k-1} \\ |I_{IBDG}| &= \sqrt{\bar{p}^2 A^2 + I_{q0}^2} \\ A &= \frac{2}{3V_k} \end{aligned} \qquad (21)$$

C. Extending the Equations to the Network

In cases where the calculated distance "d" along a line exceeds 1.0, it becomes necessary to apply the distance algorithm for the subsequent line. This iterative process is continued until a "d" value less than one is obtained for at least one line. In this specific scenario, faults occurring in sections A or B are assumed to arise within a network incorporating distributed generation resources. As outlined in section A, determining the distance along each line necessitates knowledge of the voltage and current at the line's origin, as well as the load specifications at the line's terminus.

a- If the estimated fault is downstream of IBDG

The voltage and current at the beginning of the faulted line are derived from the equations presented below:

where,

V_k	voltage vector at kth node
Z_k	impedance matrix of kth line section
Z_{Lk}	impedance of kth load
I_k	current vector of kth line section
I_{Lk}	current vector of kth load
L	line length

The equations given in (21) consist of the equation (8) which was obtained in section III . Also, I_{IBDG} is the current injected by IBDG. The voltage vector at k-th node can be obtained through a power flow program [28], as shown in Fig. 12.

b- If the estimated fault is above IBDG,

The voltage and current at the beginning of the faulted line are obtained from the following equations, knowing the structure of Fig. 13:

$$\begin{aligned} I_k &= I_{k-1} - I_{Lk} \\ I_{Lk} &= \frac{V_k}{Z_{Lk}} \\ V_k &= V_{k-1} - L.Z_{k-1}.I_{k-1} \end{aligned} \qquad (22)$$

V. The Proposed Method to Identify the Faulty Section

In distribution networks, impedance-based techniques can encounter challenges due to multiple potential solutions arising from various sub-branches. To address this issue, this section adopts an approach in which each solution identified in Section IV is treated as a potential fault location. Subsequently, a fault index is computed for each potential location. The fault location with the lowest index value is then determined as the most accurate fault location. This methodology aids in pinpointing the precise fault location amidst the complexities of distribution networks [12].

A. Single Phase Fault

According to Fig. 6, if a fault occurs in phase “a”, the values of healthy phases “b” and “c” are incorporated into the equation presented below.

$$E_{index} = |I_{Fb}|^2 + |I_{Fc}|^2 \tag{23}$$

B. Double Phase Line-to-Line Fault

According to Fig. 9 and Fig. 10, if a two-phase fault occurs between phases “b” and “c”, the values from the healthy phase “a” are incorporated into the equation presented below.

$$E_{index} = |I_{Fa}|^2 \tag{24}$$

C. Three Phase Fault

According to Fig. 11, in the event of a three-phase fault occurring between phases “a”, “b” and “c”, the equation presented below is employed [13]:

$$\begin{aligned} E_{index} = |I_{Fa,act} - I_{Fa}|^2 + |I_{Fb,act} - I_{Fb}|^2 \\ + |I_{Fc,act} - I_{Fc}|^2 \end{aligned} \tag{25}$$

From the calculated value of I_F in (1), the actual fault currents in all of the phases are computed by steady-state fault analysis. Let the actual fault currents be $I_{Fa,act}$, $I_{Fb,act}$, $I_{Fc,act}$. The error index is then defined as in equation (25).

The flowchart depicted in Fig. 14 illustrates the fault location process outlined in this study. Initially, relays detect the fault, followed by the sampling of voltage and current signals. The fault type is then determined based on these signals, which leads to the implementation of a fault location algorithm. Further details of this process are elaborated upon below.

- *Pre-Fault Analysis*

The pre-fault analysis involves calculating the voltage and current of subsequent buses step-by-step from one bus to another, using the initial feeder's pre-fault voltage and current. By considering the power consumption of loads (S_{LK}) and applying specific equations, the load impedance prior to the fault is determined. It is assumed that this load impedance remains constant both pre and post-fault.

$$I_{LK} = \left(\frac{S_{LK}}{V_k}\right)^* \qquad Z_{LK} = \frac{V_k}{I_{Lk}} \tag{26}$$

- *Post-Fault Analysis*

In the post-fault analysis, the impedance of loads from the previous step is utilized along with voltage and current measurements after the fault to calculate the values at the start of each line. Kirchhoff's laws and ladder power flow analysis are employed for this calculation. Subsequently, the distance algorithm for each line, illustrated in Fig. 14, is executed based on the obtained voltage and current values.

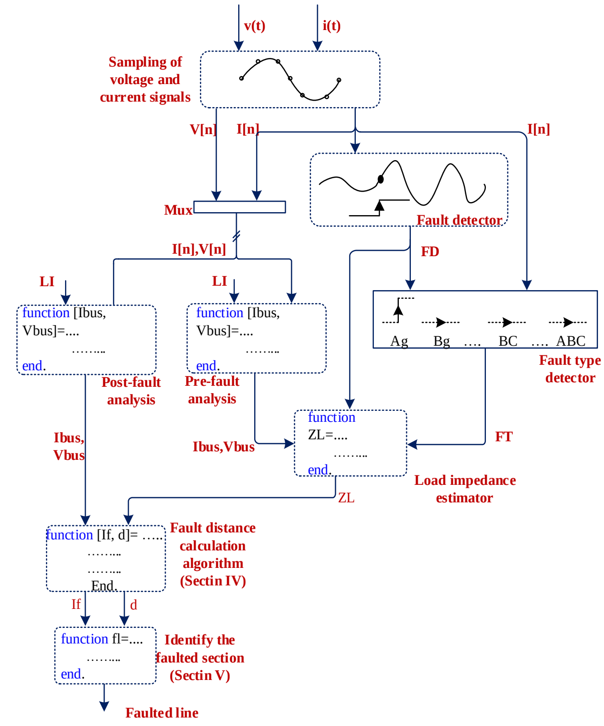

Fig. 14. Flowchart of the proposed method

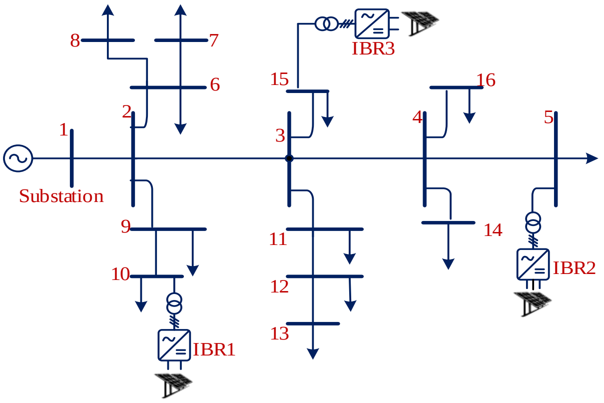

Fig. 15. Single line diagram of test system

VI. Case Study

Fig. 15 presents the single-line-diagram of a three-phase, 11 kV, 50 Hz modified IEEE 15-bus radial distribution system [29]. The line parameters and load data for the 15-bus radial distribution system are sourced from [30]. In this model, three inverter-based distributed generators (IBDGs), which are photovoltaic inverters, are integrated at bus-5, bus-10, and bus-15.

To evaluate the performance of the proposed fault location method, the modified 15-bus distribution feeder was simulated using detailed time-domain simulation in the MATLAB/Simulink environment. The system includes 14 line sections, 16 buses, 12 load buses, and three inverter based generators. The system has a total three-phase power of 7.5 MVA, with each of the inverter based distributed generators

TABLE I. LOAD DATA OF TEST SYSTEM

node	active power (kW)	reactive power (kVar)
1	0	0
2	44.1	44.99
3	70.1	71.44
4	40	142.82
5	44.1	44.99
6	140	142.82
7	140	142.82
8	70	71.414
9	70	71.44
10	44.1	44.99
11	140	142.82
12	70	71.414
13	44.1	44.99
14	70	71.414
15	44.1	44.99

TABLE II. LINE DATA OF TEST SYSTEM

Line No.	from	to	*r* (ohm)	*x* (ohm)
1	1	2	1.35309	1.32349
2	2	3	1.17024	1.14464
3	3	4	0.84111	0.82271
4	4	5	1.52348	1.0276
5	2	9	2.01317	1.3279
6	9	10	1.68671	1.1377
7	2	6	2.55727	1.7249
8	6	7	1.0882	0.734
9	6	8	1.25143	0.8441
10	3	11	1.79553	1.2111
11	11	12	2.44845	1.6515
12	12	13	2.01317	1.3579
13	3	15	1.52348	1.0276
14	4	14	2.23081	1.5047
15	4	16	1.9702	0.8074

TABLE III. THE ACCURACY OF THE FAULT DISTANCE CALCULATION METHOD

R_F (Ω)	Error [%]		
	LG	*LL*	*3PH*
0	0.01	0.00	0.01
10	0.01	0.02	0.01
20	0.03	0.03	0.04
50	0.08	0.09	0.06
100	0.20	0.22	0.24

TABLE IV. THE ACCURACY OF IDENTIFYING THE FAULTY SECTION

Actual value of d and faulty section	feeder 1-2		feeder 2-3		feeder 2-6	
	d	*EI* *	*d*	*EI*	*d*	*EI*
0.2 feeder 2-3	1.37	----	0.200	8.96* e-9	0.127	1.23
0.5 feeder 2-6	1.26	----	0.775	2.59	0.500	6.88* e-8
0.8 feeder 2-9	1.54	----	۰٫961	1.95	0.635	2.75

* EI: Error Index

contributing 250 KVA. The IBDGs operates at an output voltage of 250 V, and are connected to the network via a transformer.

To validate the methodology, a four-wire grounded neutral RL model was employed. The feeder configuration exhibits unequal distances between phases and non-transposed lines, resulting in an unbalanced line impedance matrix. The line impedance matrix was generated using Carson's equations [31]. Load and line information is detailed in the table I and II.

VII. Simulation Results

In this section, we present the outcomes of tests conducted on fault conditions at various distances from the feeder's origin. These faults encompass single-phase, two-phase, and three-phase scenarios. The findings are detailed in Tables III and IV. Table III showcases the fault distance calculations in the distribution grid with the inclusion of IBDG. The table illustrates that as the fault's phase count and resistance increase, the method's precision diminishes. Nonetheless, even under the most challenging circumstances, the proposed approach maintains high accuracy. Table IV presents the results of fault section determination. When the fault distance ‘d’ is smaller than faults detected in multiple lines, there are several potential fault locations. According to this table, the faulty section is accurately identified from the potential fault sites, effectively resolving the issue of multiple possible answers.

The percentage errors were calculated by (27):

$$\text{error (\%)} = \left|\frac{d_{actual} - d_{estimated}}{L_T}\right| \times 100 \qquad (27)$$

where $d_{estimated}$ is the estimated fault distance in km, d_{actual} is the real fault distance in km, and L_T is the total line length in km.

VIII. CONCLUSION

This paper examines various existing fault location methods, highlighting their principles and fundamentals. To address the limitations of these methods, an enhanced feature based on impedance-based methodology is proposed, requiring only local terminal data. This approach overcomes the challenges of traditional impedance-based methods, which include the necessity for extensive system and load data, voltage and current measurements, and knowledge of the distribution system structure. To evaluate the performance of the proposed scheme, a series of equations and mathematical proofs are developed for SLG, LL, LLG, and LLL short-circuit faults. These proofs demonstrate the accuracy and effectiveness of the new method. To further validate its performance, extensive time-domain simulations are conducted using a modified 15-bus IEEE network with multiple branches and inverter-based DGs, including photovoltaic systems and type IV wind generators.

The accuracy of the fault distance calculation method is assessed for LG, LL, LLG, and LLL faults at various distances from the network's substation and across different feeders. The results show that the distance calculation error is minimal, with a worst-case scenario error of 0.24% for different fault resistances ranging from 0 to 100 Ohms.

In addition, the accuracy of the faulty section detection method is evaluated for all identified faults. A specific error index is proposed and computed for each potential fault, ensuring that the faulty section is identified without any errors.

In conclusion, the proposed methodology is suitable for distribution systems with multiple laterals and both balanced and unbalanced loads, even in the presence of inverter-based DGs under faults with different resistances at various locations. This method offers high accuracy compared to traditional techniques for fault location. Additionally, the proposed feature can be integrated into AI-based techniques, significantly improving accuracy and simplifying complexity.

REFERENCES

[1] Yadegar, M., Zarei, S. F., Meskin, N., & Blaabjerg, F. (2023). A Distributed High-Impedance Fault Detection and Protection Scheme in DC Microgrids. IEEE Transactions on Power Delivery.

[2] Stefanidou-Voziki, P., Sapountzoglou, N., Raison, B., Dominguez Garcia, J.L.: A review of fault location and classification methods in distribution grids. Electr. Power Syst. Res. 209, 108031 (2022).

[3] S. Gururajapathy, H. Mokhlis, and H. Illias, "Fault location and detection techniques in power distribution systems with distributed generation: A review," Renewable and Sustainable Energy Reviews, vol. 74, pp. 949-958, 2017.

[4] Jun Zhu, D. L. Lubkeman and A. A. Girgis, "Automated fault location and diagnosis on electric power distribution feeders," in IEEE Transactions on Power Delivery, vol. 12, no. 2, pp. 801-809, April 1997, doi: 10.1109/61.584379.

[5] Seung-Jae Lee et al., "An intelligent and efficient fault location and diagnosis scheme for radial distribution systems," in IEEE Transactions on Power Delivery, vol. 19, no. 2, pp. 524-532, April 2004, doi: 10.1109/TPWRD.2003.820431.

[6] X. Yang, M. Choi, S. Lee, C. Ten and S. Lim, "Fault Location for Underground Power Cable Using Distributed Parameter Approach," in IEEE Transactions on Power Systems, vol. 23, no. 4, pp. 1809-1816, Nov. 2008, doi: 10.1109/TPWRS.2008.2002289.

[7] H. Nouri and M. M. Alamuti, "Comprehensive Distribution Network Fault Location Using the Distributed Parameter Model," in IEEE Transactions on Power Delivery, vol. 26, no. 4, pp. 2154-2162, Oct. 2011, doi: 10.1109/TPWRD.2011.2161620.

[8] R. H. Salim, M. Resener, A. D. Filomena, K. R. C. De Oliveira, and A. S. Bretas, "Extended fault-location formulation for power distribution systems," *IEEE Transactions on Power Delivery,* vol. 24, no. 2, pp. 508-516, 2009.

[9] A. S. Bretas and R. H. Salim, "Fault Location in Unbalanced DG Systems using the Positive Sequence Apparent Impedance," 2006 IEEE/PES Transmission & Distribution Conference and Exposition: Latin America, 2006, pp. 1-6, doi: 10.1109/TDCLA.2006.311611.

[10] R. H. Salim, K. R. C. de Oliveira, A. D. Filomena, M. Resener and A. S. Bretas, "Hybrid Fault Diagnosis Scheme Implementation for Power Distribution Systems Automation," in IEEE Transactions on Power Delivery, vol. 23, no. 4, pp. 1846-1856, Oct. 2008, doi: 10.1109/TPWRD.2008.917919.

[11] J. U. N. Nunes and A. S. Bretas, "Impedance-based fault location formulation for unbalanced primary distribution systems with distributed generation," 2010 International Conference on Power System Technology, 2010, pp. 1-7, doi: 10.1109/POWERCON.2010.5666589.

[12] K. Ramar and E. E. Ngu, "A new impedance-based fault location method for radial distribution systems," IEEE PES General Meeting, Minneapolis, MN, USA, 2010, pp. 1-9, doi: 10.1109/PES.2010.5588189.

[13] R. Krishnathevar and E. E. Ngu, "Generalized Impedance-Based Fault Location for Distribution Systems," in IEEE Transactions on Power Delivery, vol. 27, no. 1, pp. 449-451, Jan. 2012, doi: 10.1109/TPWRD.2011.2170773.

[14] S. F. Alwash, V. K. Ramachandaramurthy and N. Mithulananthan, "Fault-Location Scheme for Power Distribution System with Distributed Generation," in IEEE Transactions on Power Delivery, vol. 30, no. 3, pp. 1187-1195, June 2015, doi: 10.1109/TPWRD.2014.2372045

[15] F.M. Aboshady, D.W.P. Thomas, Mark Sumner, A new single end wideband impedance based fault location scheme for distribution systems, Electric Power Systems Research, Volume 173, 2019, Pages 263-270, ISSN 0378-7796, https://doi.org/10.1016/j.epsr.2019.04.034

[16] H. Mirshekali, R. Dashti, A. Keshavarz, A. J. Torabi and H. R. Shaker, "A Novel Fault Location Methodology for Smart Distribution Networks," in IEEE Transactions on Smart Grid, vol. 12, no. 2, pp. 1277-1288, March 2021, doi: 10.1109/TSG.2020.3031400.

[17] Morteza Behbahani poor, and Seyed Fariborz Zarei, “A Fault Location Scheme for Distribution Networks with Inverter-Based Resources,” presented at the POWER ELECTRONICS AND DRIVES: SYSTEMS AND TECHNOLOGIES CONFERENCE PEDSTC. 2024, [Online]. Available: https://sid.ir/paper/1132495/en

[18] Zarei, Seyed Fariborz, Hossein Mokhtari, and Frede Blaabjerg. "Fault detection and protection strategy for islanded inverter-based microgrids." IEEE Journal of Emerging and Selected Topics in Power Electronics 9.1 (2019): 472-484.

[19] Zarei, Seyed Fariborz, Mohamad Amin Ghasemi, and Saeed Khankalantary. "Current limiting strategy for grid-connected inverters under asymmetrical short circuit faults." International Journal of Electrical Power & Energy Systems 131 (2021): 107020.

[20] D. Tzelepis, A. O. Rousis, A. Dyśko, C. Booth, and G. Strbac, "A new fault-ride-through strategy for MTDC networks incorporating wind farms and modular multi-level converters," International Journal of Electrical Power & Energy Systems, vol. 92, pp. 104- 113, 2017.

[21] Du, Y. Liu, G. Wang, P. Sun, H.-M. Tai, and L. Zhou, "Three?phase grid voltage synchronization using sinusoidal amplitude integrator in synchronous reference frame," International Journal of Electrical Power & Energy Systems, vol. 64, pp. 861-872, 2015.

[22] A. Yazdani and R. Iravani, Voltage-sourced converters in power systems: modeling, control, and applications: John Wiley & Sons, 2010.

[23] F. Blaabjerg, R. Teodorescu, M. Liserre, and A. V. Timbus, "Overview of control and grid synchronization for distributed power generation systems," IEEE Transactions on industrial electronics, vol. 53, no. 5, pp. 1398-1409, 2006.

[24] R. Teodorescu, M. Liserre, and P. Rodriguez, Grid converters for photovoltaic and wind power systems vol. 29: John Wiley & Sons, 2011.

[25] J. Jia, G. Yang, and A. H. Nielsen, "A review on grid-connected converter control for short-circuit power provision under grid unbalanced faults," IEEE Transactions on Power Delivery, vol. 33, no. 2, pp. 649-661, 2017.

[26] Zarei, Seyed Fariborz, et al. "A Fault Detection Scheme for Islanded-Microgrid with Grid-Forming Inverters." 2021 6th IEEE Workshop on the Electronic Grid (eGRID). IEEE, 2021.

[27] Zarei, Seyed Fariborz, and Mostafa Parniani. "A comprehensive digital protection scheme for low-voltage microgrids with inverter-based and conventional distributed generations." IEEE Transactions on Power Delivery 32.1 (2016): 441-452.

[28] W. H. Kersting, Distribution System Modeling and Analysis, Boca Raton, FL: CRC, 2002.

[29] A. Gopi and P. A. D. V. Raj, ”Distributed generation for line loss reduction in radial distribution system” proc.- ICETEEEM 2012, Int. Conf.Emerg. Trends Electr.Eng. Energy Manag., pp. 29-32,2012.

[30] Kawambwa, S., Mwifunyi, R., Mnyanghwalo, D. et al. An improved backward/forward sweep power flow method based on network tree depth for radial distribution systems. Journal of Electrical Systems and Inf Technol 8, 7 (2021). https://doi.org/10.1186/s43067-021-00031-0

[31] Mathworks Matlab. Natick, MA, 2009. [Online]. Available: http://www.mathworks.com

Morteza Behbahanipour received his BSc degree from Qom University of Technology, Qom, Iran, in 2017. He is currently pursuing his M.S. degree at the same university. His research interests focus on the application of power electronics in power distribution systems. His thesis is centered on fault location in active distribution networks with high penetration of inverter-based distributed generators.

Seyed Fariborz Zarei received his B.Sc. degree in Electrical Engineering from the Department of Electrical Engineering at Amirkabir University of Technology (Tehran Polytechnic), Tehran, Iran, in 2012. He continued his academic pursuits by achieving both his M.Sc. and Ph.D. degrees in Electrical Engineering from the Department of Electrical Engineering at Sharif University of Technology, Tehran, Iran, in 2014 and 2019, respectively. From February to August 2018, he served as a Visiting Ph.D. Scholar at the Department of Energy, Aalborg University, Aalborg, Denmark. In January 2021, Dr. Zarei joined Qom University of Technology, Qom, Iran, as an Assistant Professor in the Department of Electrical and Computer Engineering. Dr. Zarei has authored over 30 conference and journal papers in the field of power electronics and electrical power engineering. His research is centered on the application of power electronics systems in power grids, with a focus on modeling, control, protection, and stability aspects. Additionally, Dr. Zarei established the Power Electronic and Grid Laboratory at Qom University of Technology in January 2022. This laboratory conducts studies on DC/AC converters and their interaction with the AC power grid. The experimental platform of the laboratory offers a flexible environment for implementing diverse control methodologies on three-phase converters, facilitating investigations into control, protection, and stability aspects.

Mohammadhadi Shateri (Member, IEEE) received the B.Sc. degree (Hons.) in electrical engineering from the Amirkabir University of Technology (Tehran Polytechnic), Tehran, Iran, in 2012, the M.Sc. degree (Hons.) in electrical engineering from the University of Manitoba, Winnipeg, MB, Canada, in 2017, and the Ph.D. degree in electrical engineering from McGill University, Montreal, QC, Canada, in 2021. He is currently an Assistant Professor at École de technologie supérieure and a member of the Laboratoire d’imagerie, de vision et d’intelligence artificielle (LIVIA). His research interests include machine learning, data privacy, and security in machine learning models with a focus on deep generative models.

IECO

This page intentionally left blank.

IECO International Journal Of
Industrial Electronics Control and Optimization
Print ISSN: 3517-2645
Online ISSN: 3568-2645
Homepage: https://ieco.usb.ac.ir/

LMI-Based Approach for Regulating Microgrids Using Sliding Mode Control

Mohammed Y. Yakoob[1] | Mina Salim[2] | Amir A. Ghavifekr[3]

Faculty of Electrical and Computer Engineering, University of Tabriz, Tabriz, Iran.[1,2,3]
Corresponding author's email: m.salim@tabrizu.ac.ir

Article Info

Article type:
Research Article

Article history:
Received: 11-February 2024
Received in revised form:
31-May-2024
Accepted: 15-June-2024
Published online: 22-Sep-2024

Keywords:
Islanded Microgrid (IMG),
Slide Mode Control (SMC),
Linear Matrix Inequality (LMI),
Voltage Source Inverter (VSI),
Distributed Generation (DG).

ABSTRACT

Regulating voltage and current signals in microgrids (MG) is essential to ensure stability, optimize power quality, support grid integration, enhance operational efficiency, and promote safety within the system. This paper introduces a novel Linear Matrix Inequalities (LMI)-based approach aimed at regulating voltage and current signals within microgrids through the utilization of sliding mode control. The MG under examination in this paper is composed of a voltage source inverter (VSI) for DC to AC voltage conversion, a filter to ensure sinusoidal signal quality, and an array of loads, including those with uncertain characteristics. The objective of this study is to regulate the output voltage and current in a short period of time in the presence of diverse loads. By promptly adjusting voltage and current levels, the microgrid can effectively accommodate fluctuations in demand and maintain optimal performance under changing conditions. The presented controller consists of two parts: a state feedback gain calculated from the LMI and a sliding mode-based controller to maintain system stability. This controller is intended to reject disturbances, track reference signals, and minimize steady-state errors in a limited time. The satisfactory performance of the microgrid will have a significant impact on various parameters, such as frequency, active power, reactive power, and power factor. Simulating the voltage source inventor and presenting numerical results demonstrate the effectiveness of the proposed controller to provide high robustness against uncertainty and nonlinear loads while maintaining system stability.

I. Introduction

In recent years, distributed generation systems have gained the attention of numerous researchers. This is due to the increasing global demand for energy, the high costs associated with traditional energy sources, and the adverse environmental effects stemming from conventional operations. Consequently, numerous countries have initiated a transition from traditional methods to renewable energy sources such as photovoltaic, wind turbines, and solar thermal systems [1]. Distributed generation and microgrids are closely related concepts in the field of decentralized energy systems. Distributed generation refers to small-scale power generation facilities that are located close to the point of consumption. Microgrids, on the other hand, are localized energy systems that can operate independently or in connection with the main power grid [2]. Distributed generators form the foundation for enhancing the performance of the power grid and enabling efficient power management within smart networks [3]. In recent years, developers are increasingly focusing on enhancing microgrid functionality to attain superior efficiency and performance [4]. There are numerous benefits to apply a microgrid in a distribution power system (DPS). For instance, it can reduce losses, facilitate the utilization of renewable energy, and enhance system reliability. Furthermore, several factors, such as the remote location of the main grid from urban areas, its high cost, and the complexity of connecting to it, have contributed to the adoption of microgrids in standalone mode[5]. Fig. 1 depicts the basic diagram of the islanded microgrid (IMG) and its architecture. The MG constitutes a single, controllable, independent power system comprising distributed generation (DG), load, energy storage (ES), and control devices, with DG and ES directly connected to the user

Publisher: University of Sistan and Baluchestan

side in parallel. On the microgrid side, it can be considered a controlled cell, while on the user side, it can fulfill unique demands, such as reduced feeder loss and increased local reliability. With capabilities for autonomous control, protection, and management, a microgrid can operate either in parallel with the main grid or in islanded mode [6].

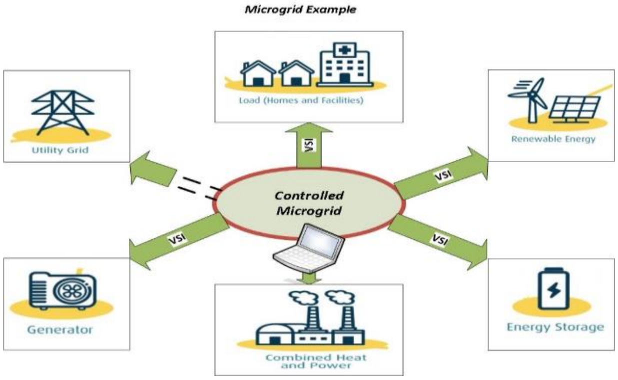

Fig. 1. Microgrid Architecture

Voltage and current signals regulation play a critical role in the reliable and efficient operation of microgrid systems. It is essential for ensuring stability, maintaining power quality, supporting grid integration, optimizing system operation, and promoting safety. Stable voltage and current levels are crucial for the reliable operation of connected loads and equipment, while proper regulation helps prevent issues such as harmonic distortions, which can affect the performance of sensitive electronic devices [7]. Additionally, regulated voltage and current facilitate the smother integration of microgrids with the main utility grid or other distributed energy resources, ensuring efficient power exchange and grid stability. Precise control of these signals enables operators to optimize the utilization of distributed energy resources, enhance system efficiency, and reduce operating costs[8]. Thus, a significant challenge lies in obtaining high-quality voltage and current waveforms from microgrids. The Voltage Source Inverter (VSI) plays a critical role in microgrids, and effectively controlling it poses a substantial endeavor.

It is important to use control strategies with MG's in order to control the voltage and current signals' shape and frequency, as well as correct the active and reactive powers [9]. The most commonly used technique is the PID controller, which enables fast response times and minimizes overshoot. In [10], it is noted that PI controllers do not perform well in unbalanced systems. In cases with varying loads, the system's characteristics do not exhibit a consistent transfer function. To overcome this issue, hysteresis controllers have been developed. These controllers are utilized in grid-connected mode, where it ensures that the grid current tracks a reference signal. The key attributes of these controllers include simplicity, robustness, and a favorable transient response. However, a drawback of them is the switching frequency's dependence on load parameters. Another extension is drop controller which has been utilized to stabilize the grid voltage and frequency. The selection of a controller gain depends on the balancing power criteria. Usually, it is used with more than one inverter in parallel. In [11], by using this controller, the MG can achieve active and reactive power balancing. It controls the active and reactive power on the basis of frequency and voltage droop control methods. [12] introduces an adaptive cooperative energy management scheme based on droop control for an autonomous DC microgrid powered by photovoltaic (PV) batteries. Additional emphasis is placed on achieving optimal voltage regulation to enhance robustness against time-delay, as opposed to conventional voltage observers that often result in significant observation errors. Also, Evolutionary algorithms techniques have been applied for the optimal tuning of parameters of these controllers[13]. In [14], an improved state feedback control approach is proposed for the distributed secondary voltage and frequency control within an islanded microgrid. The innovative controllers synchronize the output voltages and frequencies of distributed generators with their reference values. A scheme based on the adaptive input-output feedback linearization control has been proposed in [15]. Implementing the devised control scheme ensures that the output voltage of distributed generation (DG) sources exhibits negligible harmonics. Moreover, it effectively tracks the references for generated voltage, active power, and reactive power.

Sliding mode control (SMC) has emerged as a promising technique for enhancing the performance and stability of microgrids, offering robust and adaptive control capabilities. [16] introduces a novel power control strategy for microgrids based on sliding mode techniques. Compared to the PI controller, the proposed control strategy exhibits a fast response and the capability to closely follow a reference signal with minimal steady-state error. A novel method based on LMI, has been proposed in [17] for designing decentralized control, specifically targeting large-scale systems. The efficacy of this approach is demonstrated through its application to interconnected clusters of microgrids. To enhance energy extraction from the PV system, [18] introduces a novel controller design strategy aimed at tracking the Maximum Power Point (MPP) utilizing a sliding mode control method for self-optimization. The proposed controller design ensures rapid and precise convergence to the MPP under steady-state conditions and during fluctuations in environmental parameters. A centralized robust sliding mode controller is proposed in [19] aiming to minimize frequency deviation while optimizing power distribution among distributed generations within an isolated microgrid. [20] introduces distributed predictive control implemented at the secondary level of microgrids. The controller proposed takes into account the objectives of frequency and voltage regulation, as well as achieving consensus on the real and reactive power contributions from each power unit within the microgrid. [21] presents a novel approach to decentralized and communication-free control strategies for regulating frequency and voltage in (PV)-Storage islanded Microgrids.

In [22], an adaptive sliding mode controller has been designed with a single-phase MG to stabilize the voltage, frequency, and power of the output. Also, in [23], a recursive fast terminal sliding mode controller is presented to regulate a single-phase IMG, where the test is done with a low-voltage grid and is used to stabilize the voltage output by tracking the reference and reducing the error rate between the output and the reference signals. Furthermore, [24] presents an advanced exponential sliding mode controller for microgrids in autonomous and grid-connected modes that outperforms other controllers in terms of fixing a voltage and frequency at the distributed-generated system's common coupling point (CCP).

The desired controller for the MG system, should be cheap and easily implementable. It should guarantee the closed loop's stability and have robustness against a wide range of uncertainties and disturbances. In addition, it would be usable to regulate both of the single-phase MG and the three phase MG, to give the pure shape of the voltage and current signals, to provide a high-power factor, get a stable frequency over time, and correct the active and reactive powers. The purpose of this paper is satisfying these conditions by presenting an LMI approach to regulate microgrid voltage and current signals by utilizing sliding mode controller. The proposed controller collects all the properties of the aforementioned scheme and utilizes the compound techniques of SMC and LMI, to provide high robustness against the load variant and uncertainties. The system is asymptotically stable, and the tracking errors converge to zero in finite time. Our study contributes significantly to the existing literature by proposing a novel approach that combines Linear Matrix Inequalities with sliding mode control techniques for regulating microgrids. This integration of LMI methods with sliding mode control offers a systematic and robust framework for addressing the challenges of microgrid regulation, providing advantages over traditional approaches.

In a summary, this paper is organized as follows: In section 2, the modeling of a single and three-phase autonomous mode MG is presented, the controller design and its stability proof is provided in section 3. In sections 4, and 5, the simulation and tests of a single and three-phase MG are shown, respectively. And finally, section 6 is presented the conclusion and related feature work.

II. Islanded Microgrid and Modelling System

For a microgrid to ensure satisfactory performance and stability, it must be equipped with a proper configuration and structure. The parameters of the proposed MG are mentioned in table (1). For modeling purposes, the system can be divided into two categories: single phase IMG and three phase IMG.

A. Single Phase Islanded Microgrid

Single phase MG is modeled based on the inductor current (i_L) in the L-C filter as shown in Fig. 2.

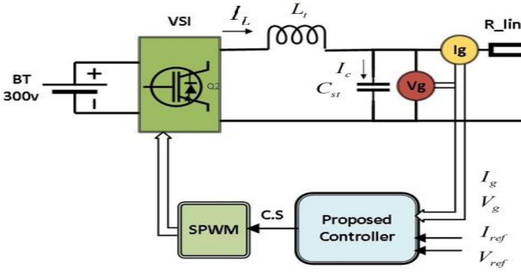

Fig. 2. Single Phase Microgrid Structure

The inductor current is divided into (i_c) and (i_g), and the controller design is based on:

$$L_t \frac{di_L}{dt} = v_{s\omega} - v_g \tag{1}$$

Where the v_{sw} is implementation of the switching voltage over the sine-wave pulse width modulation (SPWM), and v_g is the grid voltage.

Also, the capacitance current can be written as:

$$i_c = C_{st} \frac{dv_g}{dt} \tag{2}$$

From equations (1) and (2), the state space model can be written as in equation (3).

$$\begin{gathered}\frac{dx}{dt} = Ax + Bu + d\omega \\ y = Cx + Du\end{gathered} \tag{3}$$

Where x is the state vector, u is the input vector, and ω is the exogenous input vector of the MG. d is defined as the disturbance vector. This disturbance is considered due to the unknown configuration of the MG and is associated with the grid current. Any change of the MG parameters can happen, which causes the unknown MG configuration and also the unknown grid current and voltage. The state vector, input vector, and disturbance vector of the MG are shown below:

$$x = \begin{bmatrix} i_L \\ v_g \end{bmatrix}; \quad u = [v_{sw}]; \quad d = [i_g] \tag{4}$$

The state space form is shown in equation (5) as:

$$\frac{d}{dt}\begin{bmatrix} i_L \\ v_g \end{bmatrix} = \begin{bmatrix} 0 & \frac{-1}{L_t} \\ \frac{1}{C_{st}} & 0 \end{bmatrix}\begin{bmatrix} i_L \\ v_g \end{bmatrix} + \begin{bmatrix} \frac{1}{L_t} \\ 0 \end{bmatrix}[v_{s\omega}] + \begin{bmatrix} 0 \\ \frac{-1}{C_{st}} \end{bmatrix}[i_g] \tag{5}$$

And the output of the system is defined in equation (6) as:

$$y = [v_g] = \begin{bmatrix} 0 & 1 \end{bmatrix}\begin{bmatrix} i_L \\ v_g \end{bmatrix} \tag{6}$$

B. Three Phase Islanded Microgrid

The modeling of three phase MG in Fig.3. can be derived as:

$$\begin{gathered} v_{t,abc} = L_t \frac{di_{t,abc}}{dt} + R_t i_{t,abc} + v_{abc} \\ i_{t,abc} = C_{st} \frac{dv_{abc}}{dt} \end{gathered} \tag{7}$$

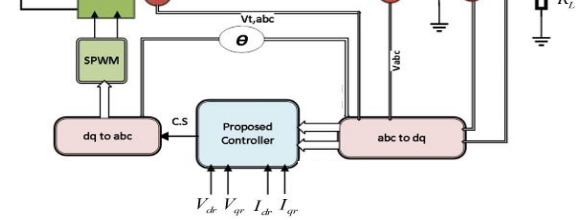

Fig. 3. Three Phase Microgrid Structure

The modeling system in (7) can transfer from abc-frame to *αβ*-reference frame as:

$$\frac{d(i_{t,\alpha\beta})}{dt} = -\frac{R_t}{L_t} i_{t,\alpha\beta} - \frac{v_{\alpha\beta}}{L_t} + \frac{v_{t,\alpha\beta}}{L_t}$$
$$\frac{d(v_{\alpha\beta})}{dt} = \frac{i_{t,\alpha\beta}}{C_{st}} \qquad (8)$$

And finally, the equation in (8) is converted to a dq-rotating frame and the result in:

$$\frac{d(I_{t,dq})}{dt} + sI_{t,dq} = -\frac{R_t}{L_t} I_{t,dq} + \frac{V_{t,dq}}{L_t} - \frac{V_{dq}}{L_t} \qquad (9)$$

$$\frac{d(V_{dq})}{dt} + sV_{dq} = \frac{i_{t,dq}}{C_{st}} \qquad (10)$$

where: $s = jw_o$.

The state-space model of the open-loop three-phase MG is represented in (9) and (10) is written as the state-space model in (3) and (4). The state space matrices are written as:

$$A = \begin{bmatrix} 0 & W_0 & \frac{1}{C_t} & 0 \\ -W_0 & 0 & 0 & \frac{1}{C_t} \\ -\frac{1}{4} & 0 & -\frac{R_t}{L_t} & W_c \\ 0 & -\frac{1}{L_t} & W_0 & -\frac{R_t}{L_t} \end{bmatrix};$$

$$B = \begin{bmatrix} 0 & 0 & -\frac{1}{C_t} & 0 \\ 0 & 0 & 0 & -\frac{1}{C_t} \\ \frac{1}{4} & 0 & 0 & 0 \\ 0 & \frac{1}{4} & 0 & 0 \end{bmatrix}; \quad C = \begin{bmatrix} 1 & 0 & 0 & 0 \\ 0 & 1 & 0 & 0 \\ 0 & 0 & 1 & 0 \\ 0 & 0 & 0 & 1 \end{bmatrix}; \qquad (11)$$

x is the state vector, u is the input vector, and d is the disturbance vector, of the MG that are shown below:

$$x = \begin{bmatrix} V_d \\ V_q \\ I_{td} \\ I_{tq} \end{bmatrix} \quad u = \begin{bmatrix} V_{td} \\ V_{tq} \\ I_{Ld} \\ I_{Lq} \end{bmatrix} \quad d = \begin{bmatrix} V_{gd} \\ V_{gq} \\ I_{gd} \\ I_{gq} \end{bmatrix} \qquad (12)$$

III. Controller Design Based on LMI Approach

The proposed controller is guaranteed to be asymptotically stable and the tracking errors will lead to zero. Firstly, depending on the state space model as written in (3) and (10) for single and three-phase MG models, the stability of the sliding mode controller based on LMI is proven by using Lyapunov theory.

The tracking error is defined as:

$$z = x - x_r \qquad (13)$$

Where xr is the desired value.

By assuming the Lyapunov equation as

$$v = z^T P z \qquad (14)$$

The controller signal is $u = u_{ARE} + u_r + u_s$.

u_{ARE}: The state feedback gain ($u = kx$), that calculating by solving the Algebraic Ricatii Equation (ARE) by using LMIs.

u_r: The desired control gain. u_s: The switching control signal.

$$u_{ARE} = kx = R^{-1}B^T P x \qquad (15)$$

$$u_r = -R^{-1}B^T P x_r - B^{-1}Ax_r + B^{-1}\frac{dx_r}{dt} \qquad (16)$$

$$u_s = -B^{-1}\eta sign(z) \qquad (17)$$

where η is the amplitude value of the *sign* function.

In proposed simulation, the *Sign*(.) function is replaced by *Sat*(.) to reduce the chattering effect and some errors that are caused by using *Sign*(.) function. The *Sat*(.) will be implemented as shown in Fig. (4).

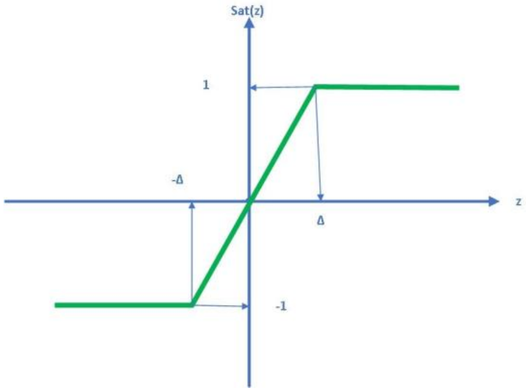

Fig 4. Saturation function implementation

We can obtain a close loop equation by substituting the controller signal in the state space equation:

$$\frac{dx}{dt} = Ax + B(u_{ARE} + u_r + u_s) + d \qquad (18)$$

Then, the closed loop system equation will be:

$$\frac{dx}{dt} = Ax + B(R^{-1}B^T Px - R^{-1}B^T Px_r -$$
$$B^{-1}Ax_r + B^{-1}\frac{dx_r}{dt} - B^{-1}\eta sign(z)) + d$$

The derivative of the Lyaponuv equation in (14) is

$$\frac{dv}{dt} = \frac{dz^T}{dt} Pz + z^T P \frac{dz}{dt} \qquad (19)$$

And the derivative of the tracking error equation in (13) gets the equation below in (20):

$$\frac{dz}{dt} = \frac{dx}{dt} - \frac{dx_r}{dt} \qquad (20)$$

By substantiation (18) into equation (20):

$$\frac{dz}{dt} = Ax + B(u_{ARE} + u_r + u_s) + d - \frac{dx_r}{dt} \qquad (21)$$

The next equation has two parts that are obtained from substitutes in the derivative of the Lyaponuv equation. The first part will be equal to:

$$-\eta sign(z) + d \qquad (22)$$

and that part will be guaranteed to be equal or less than zero by putting the $\eta >= |d|$ where $|d|$ is the absolute value of the disturbance vector.

The second part will be as follows:

$$(Az + BR^{-1}B^{T}Pz)^{T}Pz + z^{T}P(Az + BR^{-1}B^{T}Pz) \tag{23}$$

However, the Lyapunov equation guarantees that any system will be asymptotically stable if and only if:

$$A^{T}P + PA <= -Q \tag{24}$$

From [25], the algebraic ricatii equation in (23) guarantees the stability of the MG system if and only if

$$(A^{T}P + PA + Q)/2 + PBR^{-1}B^{T}P <= 0 \tag{25}$$

Now, by applying the Shur lemma[26], we will get the inequality below:

$$\begin{bmatrix} (A^{T}P + PA + Q)/2 & PB \\ B^{T}P & -R \end{bmatrix} <= 0 \tag{26}$$

By using LMI in MATLAB, the equation (26) is solved to get the state feedback gain ($k = R^{-1}B^{T}P$), and the parameters ($P = P^{T} > 0$), ($R > 0$), and ($Q >= 0$).

IV. Performance and Simulation Results for the Single-Phase MG

In general, the design of the proposed controller is explained in some steps:

Step 1: We use LMI in MATLAB (YALMIP toolbox) to solve the inequality equation in (26) as a single-phase or three-phase model.

Step 2: In single-phase MG, we chose a sinusoidal as the voltage and current reference signal. But with three-phase MG, the references are 0.6 and 0.8 for voltage and current as dq-frame.

Step 3: The controller component will be implemented using equations (15), (16), and (17).

Step 4: We implement the MG plant and add the disturbances that come from the grid's voltage and current as shown in Figs. (2) and (3).

Step 5: In this step, the VSI is programmed to rely on Figs. (2) and (3) by tacking the control signal to supply the Sinusoidal Pulse Width Modulation (SPWM), which will activate the VSI.

Step 6: Finally, draw the plant's outputs, which should be similar to the references. Also, the voltage and current output signals should be plotted to show the performance of the controller with the MG.

The single-phase IMG in Fig.2. is designed and the parameters are taken from the table (1). However, the first implementation is presented with 40 Ω as the resistive load. Where the reference signals are implemented in a sinusoidal wave with 1 as amplitude and $50H_z$. The state feedback gain (k) in (27) is determined by using the LMI technique where Q is chosen to be (2×10^{-6}). The parameters of the switching function *Sign*(.) or *Sat*(.) are chosen as $\eta = [10;300]$. The simulation results are shown in figures (5-A, B, C, and D), which act as the current control signal, the voltage control signal of the presented controller, the current reference and current output, and the voltage reference and voltage output of the plant, respectively.

TABLE 1 PARAMETERS OF THE SINGLE-PHASE AND THREE PHASE IMG

Parameter	1Phase MG	3Phase MG
DC Battery (v_{dc})	$300v$	$2000v$
Inductor Filter (L_t)	$2mH$	$100mH$
Shunt Capacitance C_{st}	$15\mu F$	$100\mu F$
Resistance of the Line (R_{Line})	0.45Ω	
Consumer Load (R_L)	40Ω	40Ω
Frequency (f)	$50H_z$	$50H_z$
MG terminal Voltage (Line to Line)	$300v$	$400v$
Transformer Voltage Ratio (Y/Δ)		12.4/3.4
SPWM Carrier Frequency (f_{sw})	6000 kH_z	6000 kH_z
Distributed Generation Rated Power		$3MVA$

Figures (7-A and B) represent the voltage output and current output of the MG, respectively. From the results, we can show that the presented controller against the resistive load with the MG model has a high performance where the outputs of the plant track the reference signals and the output of the MG is admissible. While the MG's performances against the different loads are shown below:

$$k = \begin{bmatrix} -4.1924 \times 10^{4} & 344.1670 \\ -4.0027 \times 10^{3} & 4.1702 \times 10^{3} \end{bmatrix} \tag{27}$$

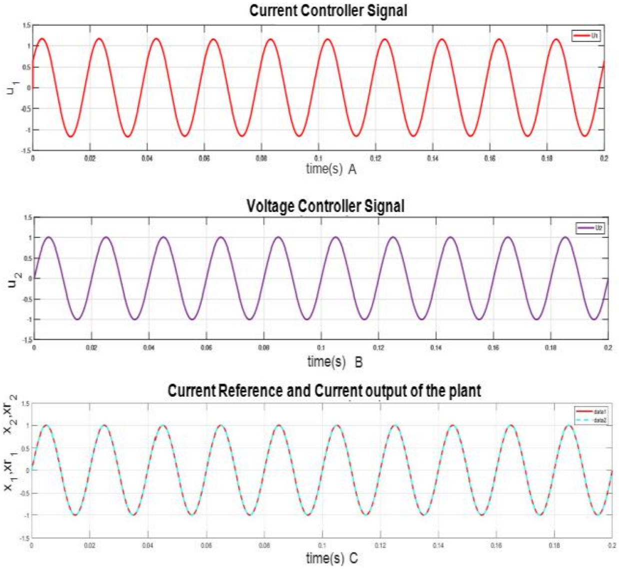

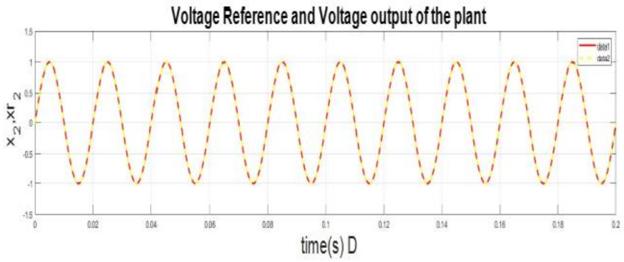

Fig. 5. Controller signals and output of the plant, (A) Current control signal (B)Voltage control signal, (C) Current reference and current output signals, (D)Voltage reference and voltage output signals

A. Performance Against the Unknown Loads

In Fig.6.A, the unknown loads are connected to the single-phase IMG system, and the proposed controller is simulated in the presence of them. The simulation is completed within 0.2 seconds, with the load changing within 0.1 seconds upon closing the switch. The state feedback gain (k) in (28) is evaluated by using the LMI technique where Q is chosen to be (2×10^{-6}). The switching function *Sign*(.) or *Sat*(.) are chosen as $\eta = [10;300]$. All the results for this test are shown in figures (5-A, B, C, and D) implement the current control signal, the voltage control signal of the proposed controller, the output current, and the output voltage of the plant, respectively. Also, the figures (8-C and D) are the voltage output and current output of the IMG.

$$k = \begin{bmatrix} -4.1924 \times 10^4 & 344.1670 \\ -4.0027 \times 10^3 & 4.1702 \times 10^3 \end{bmatrix} \tag{28}$$

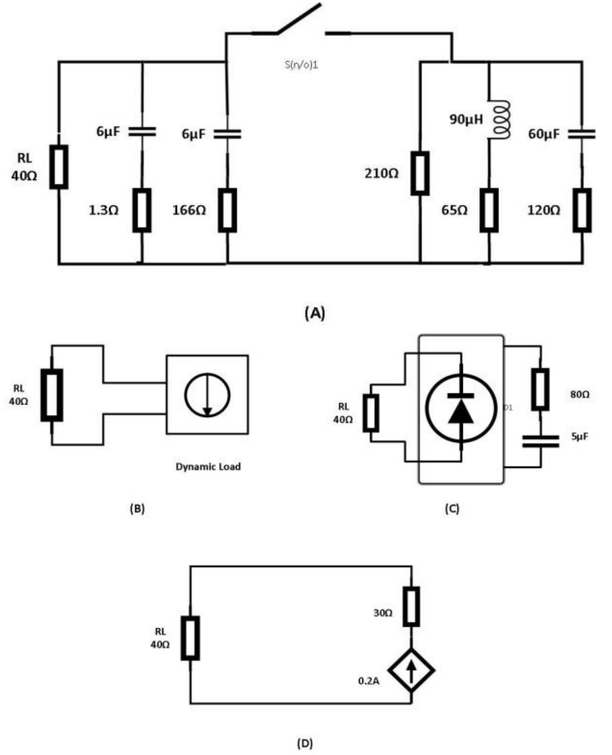

Fig. 6. Types of Different Loads in MG, (A) Unknown Loads, (B) Dynamic Load, (C) Harmonic Load (D)Nonlinear Load

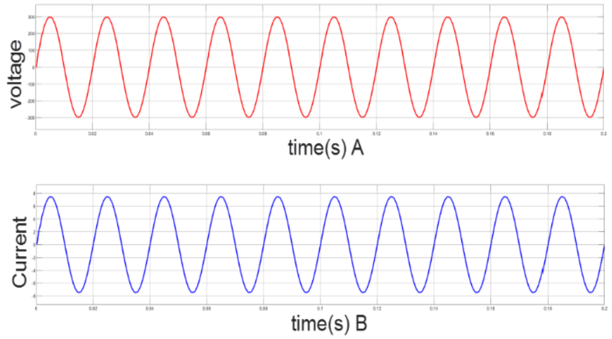

Fig. 7. The output of MG with R_L=40Ω, the dynamic load, the non-linear load, and the harmonic load (A)Voltage Output and (B) Current Output.

B. Performance Against the Dynamic Load

In this part, the single-phase IMG is simulated against a dynamic load as shown in Fig.6.B with parameters being taken as ($V_{rms} = 300v$, $F = 50H_z$, $P = 50w$, and $Q = 2var$). The state feedback gain (k) in (29) is determined by using the LMI technique. Q is chosen to be (2×10^{-6}). The parameters of the switching functions *Sign*(.) or *Sat*(.) are chosen as $\eta = [10;300]$. The results are shown in figures (5-A, B, C, and D) for the current control signal, the voltage control signal of the proposed controller, the output current, and the output voltage of the plant, respectively. The dynamic load is added to the MG, and the test happens in 0.2 seconds. We can demonstrate that the proposed controller performs well against dynamic loads, where the plant's output current and voltage track the reference signals, and the MG provides admissible waveforms.

$$k = \begin{bmatrix} -4.1924 \times 10^4 & 344.1670 \\ -4.0027 \times 10^3 & 4.1702 \times 10^3 \end{bmatrix} \tag{29}$$

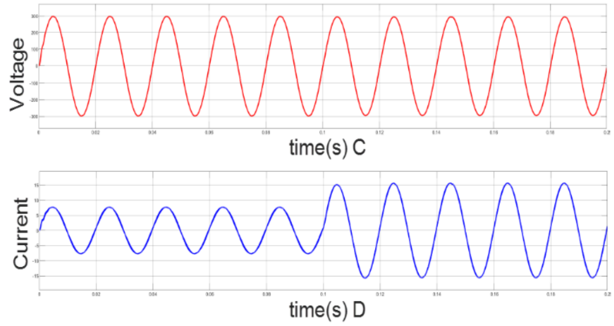

Fig. 8. The output of MG against the unknown loads (C)Voltage Output and (D) Current Output.

C. Performance Against the Non-Linear Load

The nonlinear load in Fig. 5.C is simulated with the single-phase IMG. The time of the simulation is 0.2 seconds, and the nonlinear load is connected to the MG from the beginning. Where the state feedback gain (k) in (30) is calculated by using the LMI technique. Q is chosen to be (2×10^{-6}). The parameters of the switching functions *Sign*(.) or *Sat*(.) are chosen as $\eta = [10;300]$. As shown in the results, the proposed controller works well with the MG model, where the current and voltage outputs track the reference signals. As shown in the results, the proposed controller works well with the MG model, where the current and voltage outputs track the reference signals. In addition, the output voltage and current of the MG have admissible waveforms.

$$k = \begin{bmatrix} -4.1924 \times 10^4 & 344.1670 \\ -4.0027 \times 10^3 & 4.1702 \times 10^3 \end{bmatrix} \quad (30)$$

D. Performance Against the Harmonic Load

The single-phase MG is simulated against the harmonic load as shown in figure(6-D), where the current source with 0.2A and F = 150H_z is added to R = 30Ω. The state feedback gain (k) in (31) is determined by using the LMI technique where Q is chosen to be (10^{-5}). The parameters of the switching functions *Sign*(.) or *Sat*(.) are chosen as η = [10;300]. All the tests were completed in 0.2 seconds, and the harmonic load was connected for the first time. It was shown that the presented controller has high performance with the MG, where the outputs of the model track the reference signals and the outputs of the MG have admissible waveforms.

$$k = \begin{bmatrix} -1.4795 \times 10^5 & 1.877 \times 10^3 \\ -1.3039 \times 10^4 & 3.1641 \times 10^4 \end{bmatrix} \quad (31)$$

E. Performance Against the Compound Loads

In this section, the test with a single-phase MG is simulated against the compound loads with the same specifications as in the above tests. In figures (6-C, A, and D) the proposed controller, for the resistive load R_L = 40 is connected from the first time. At time 0.01 seconds, the nonlinear load is added; at time 0.03 seconds, the unknown loads are connected; the switch is closed at time 0.07 seconds, and the harmonic load is added at time 0.1 seconds. Where the state feedback gain (k) in (32) is evaluated by using the LMI technique where Q is chosen to be (10^{-5}). The parameters of the switching function *Sign*(.) or *Sat*(.) are chosen as η = [16;305]. Reference signal and voltage output of the MG model, shown in Fig. 9, where the output voltage is shown in (K) and (L) is presented as the output current of the MG. From the results, the outputs of the MG model with the proposed controller track the reference signals, and the outputs of the MG give admissible waveforms.

$$k = \begin{bmatrix} -1.4795 \times 10^5 & 1.877 \times 10^3 \\ -1.3039 \times 10^4 & 3.1641 \times 10^4 \end{bmatrix} \quad (32)$$

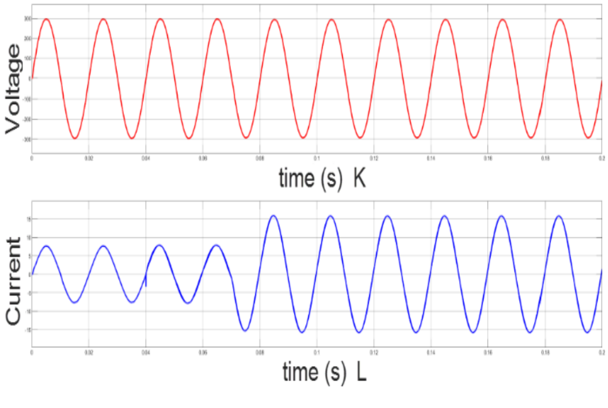

Fig. 9. The output of MG against the compound load (K) Output voltage and (L) Output current.

V. Performance and Simulation Results for the Three Phase MG

Three-phase IMG is simulated with the proposed controller, as shown in Fig. 3. The references for the voltage and current are chosen to be 0.6*DC* for a V_d and I_d and 0.8*DC* for a V_q and I_q in the *dq – frame* to be similar to the three phase signals in *abc – frame*. The angle Θ is calculated in the second step by integrating W_o, where W_o equals to ($2\pi f$). Where the state feedback gain (k) in (33) is calculated by using the LMI technique. The parameters of the switching function *Sign*(.) or *Sat*(.) are chosen as η = [350;200;6;0.5]. However, all of the tests performed in this section are compared to papers such as [27-29], and [30] to demonstrate that the performance of the proposed controller is better. So, we start the simulation with R_L = 40 connected as the first terminal to the lines of the MG and the other terminal to the ground. The test is applied for 0.2 seconds, and the resistive load is connected for the first time. Figures (12-A, B, C, and D) show the controller's input as a reference, the output voltage and current of the MG plant in a *dq – frame*, the voltage control signal, and the current control signal of the proposed controller, in that order. Also, what shown in the figures (13-E, F, G, and H) are the outputs of the three-phase MG: voltage, current, active power, and reactive power, respectively. There are some tests that are performed with the three-phase MG and the proposed controller, as shown below.

$$k = \begin{bmatrix} -1.1 \times 10^4 & 1.15 \times 10^4 & -1.96 \times 10^7 & 8.2 \times 10^4 \\ -3.66 \times 10^4 & -2.5 \times 10^4 & 1.04 \times 10^5 & -1.9 \times 10^7 \\ 1.8 \times 10^7 & 1.6 \times 10^4 & -3.9 \times 10^4 & 9.6 \times 10^4 \\ 1.6 \times 10^4 & 1.8 \times 10^7 & -1.7 \times 10^4 & 3.14 \times 10^4 \end{bmatrix} \quad (33)$$

A. Performance Against the Unknown Loads

The second test is done by connecting the three phase unknown loads as shown in figure (6-A), where the first part is from the R_L = 40Ω side. The first terminal is connected to the first phase line of the MG, and the second terminal is connected to the ground. Then it is repeated with every phase. Also, the second part is added in the same way after a three-phase switch, with a three-phase MG and the proposed controller, where the simulation happens for 0.2 seconds and the switch is closed at 0.1 second. The state feedback gain (k) in (34) is determined by using the LMI technique. The parameters of the switching function *Sign*(.) or *Sat*(.) are chosen as η = [300;200;11;1]. The results are shown in figures (12-A and B) which represent the plant output voltage and current. In addition, figures (12-C and D) represent the controller voltage and current signals. Moreover, the figures (13-E, F, G, and H) are the voltage, current, active power, and reactive power output of the three-phase MG, respectively.

$$k = \begin{bmatrix} -1.1 \times 10^4 & 1.15 \times 10^4 & -1.96 \times 10^7 & 8.2 \times 10^4 \\ -3.66 \times 10^4 & -2.5 \times 10^4 & 1.04 \times 10^5 & -1.9 \times 10^7 \\ 1.8 \times 10^7 & 1.6 \times 10^4 & -3.9 \times 10^4 & 9.6 \times 10^4 \\ 1.6 \times 10^4 & 1.8 \times 10^7 & -1.7 \times 10^4 & 3.14 \times 10^4 \end{bmatrix} \quad (34)$$

B. Performance Against the Dynamic Load

This section is testing a three-phase IMG against a three-phase dynamic load, where the specifications of the dynamic load as shown in figure (5-B) are $v_{rms} = 400 volts$, $F = 50 H_z$, $P = 1000 watts$, $and Q = 20 var$, with the proposed controller. The simulation is presented in real time for 0.2 seconds, and the dynamic load is connected from the beginning. Where the Q is chosen to be 0.65×10^{-7}. The state feedback gain (k) in (35) is evaluated by using the LMI technique.

$$k = \begin{bmatrix} 215.89 & -74.56 & -4.7\times10^{3} & 1.149\times10^{3} \\ -186.48 & 265.57 & 1.17\times10^{3} & -4.68\times10^{3} \\ 1.28\times10^{4} & 2.27\times10^{3} & -2.6\times10^{3} & 467.387 \\ 2.12\times10^{3} & 1.8\times10^{4} & -77.436 & -3.04\times10^{3} \end{bmatrix} \quad (35)$$

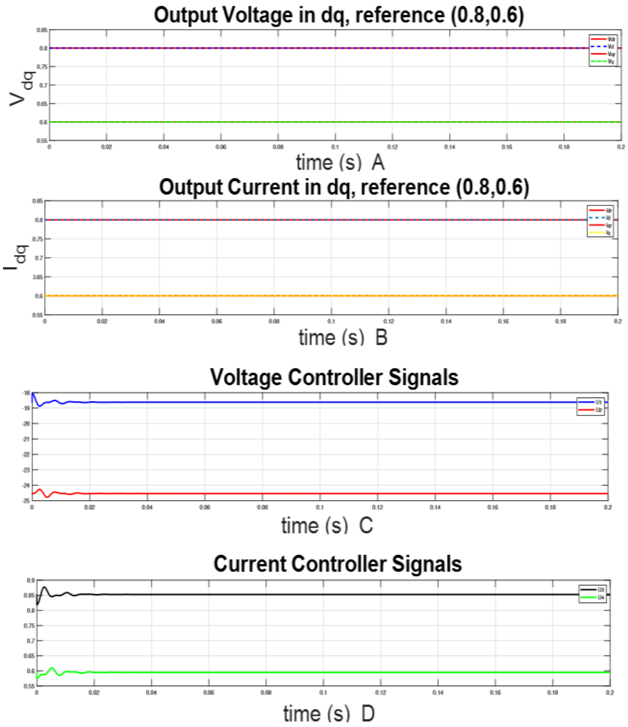

Output Voltage in dq, reference (0.8,0.6)

Output Current in dq, reference (0.8,0.6)

Voltage Controller Signals

Current Controller Signals

Fig. 10. The input and output of the controller with a MG plant against the resistive load (A-B)Voltage and Current in dq-frame (C-D) Control signals in dq-frame.

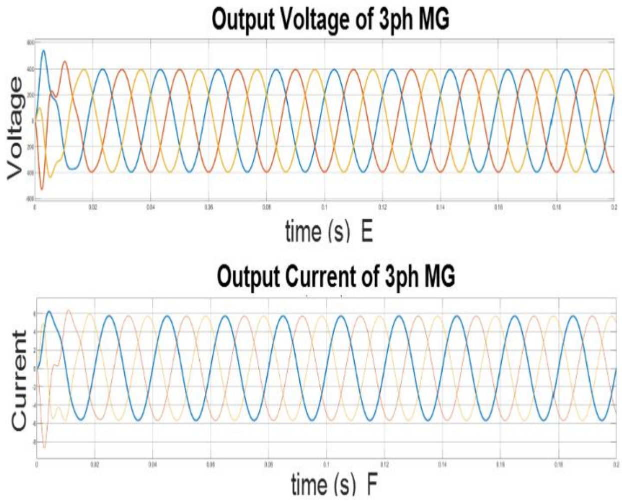

Output Voltage of 3ph MG

Output Current of 3ph MG

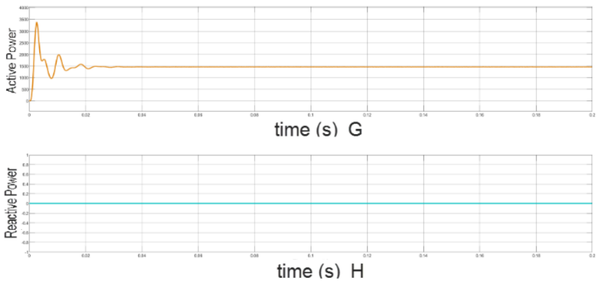

Fig. 11. The output of a three phase MG against the resistive load (E)Voltage Output of the MG (F) Current Output of the MG (G) Active Power Output of the MG, (H) Reactive Power Output of the MG.

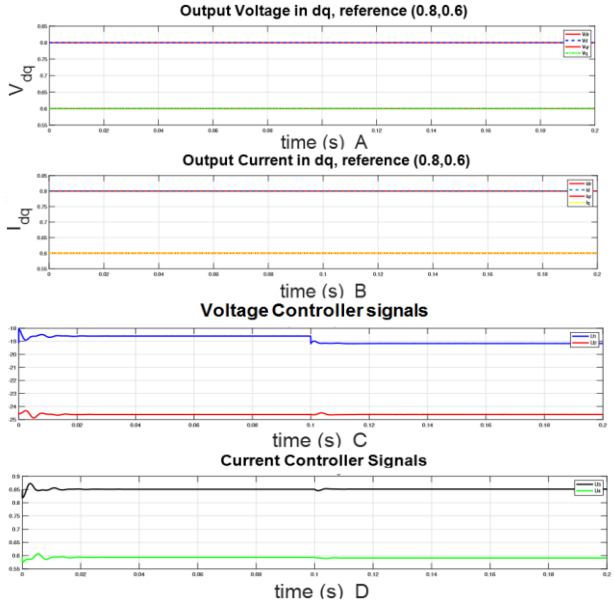

Output Voltage in dq, reference (0.8,0.6)

Output Current in dq, reference (0.8,0.6)

Voltage Controller signals

Current Controller Signals

Fig. 12. The input and output of the controller with a MG plant against the unknown loads (A-B) Voltage and Current in dq-frame (C-D) Control signals in dq-frame.

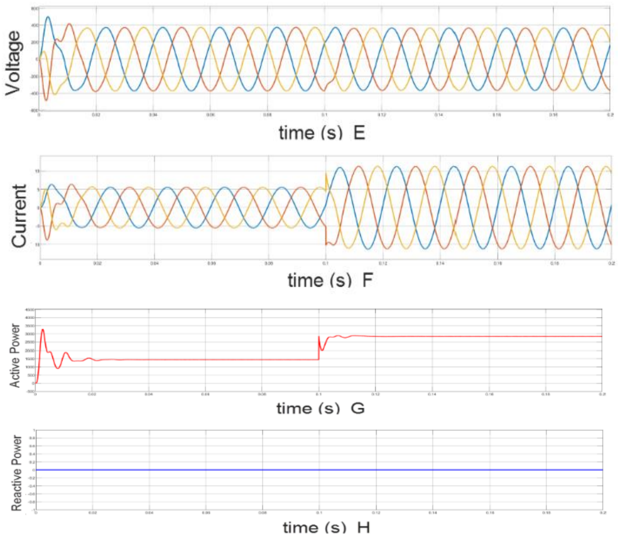

Fig. 13. The output of a three phase MG against the unknown loads (E)Voltage Output of the MG (F) Current Output of the MG (G) Active Power Output of the MG (H) Reactive Power Output of the MG

The parameters of the switching function *Sign*(.) or *Sat*(.) are chosen as η = [600;500;5;12]. However, the results of the test are shown in figures (14-A and B), The voltage and current outputs of the three-phase MG plant in $dq - frame$ and (C, D) are the voltage and current signals of the controller. Moreover, the figures (15-E, F, G, and H) are the output voltage, current, active power, and reactive power of the three-phase MG, respectively. From the above results, we can conclude that the proposed controller is performing well because it has outputs from the MG model that track the reference signals.

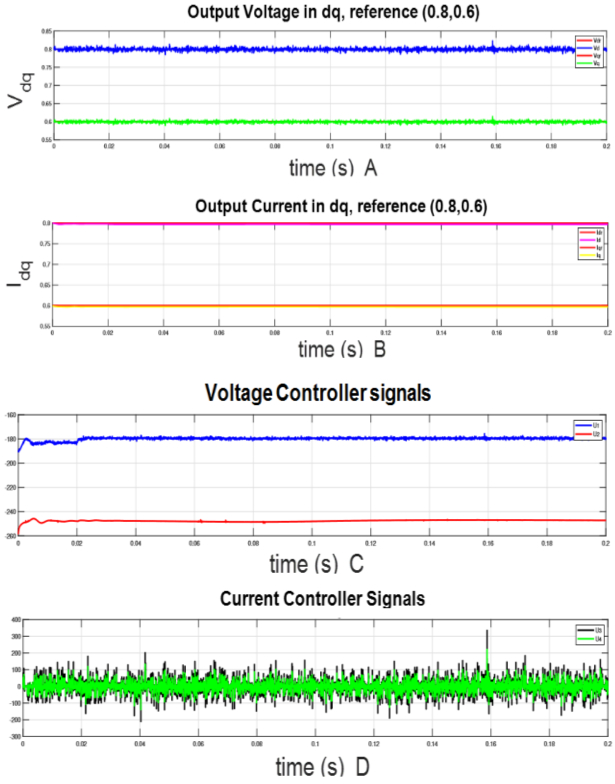

Fig. 14. The input and output of the controller with a MG plant against the dynamic load (A-B) Voltage and Current in dq-frame (C-D) Control signals in dq-frame.

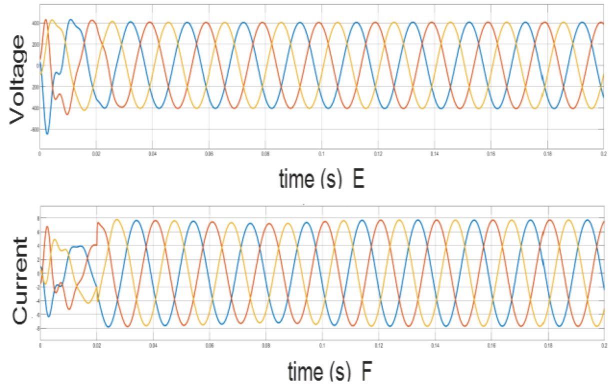

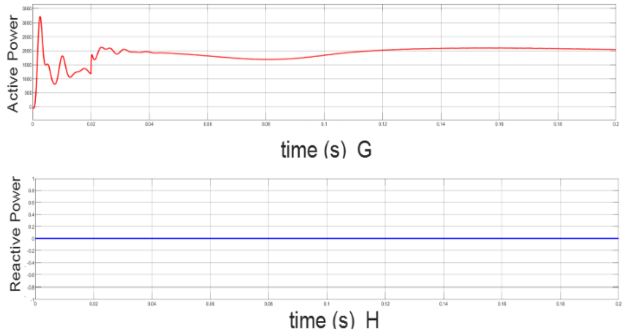

Fig. 15. The output of a three phase MG against the dynamic load (E)Voltage Output of the MG (F) Current Output of the MG (G) Active Power Output of the MG, (H) Reactive Power Output of the MG

C. Performance Against the Non-linear Load

For this test, the three-phase nonlinear load is connected to a three-phase IMG. The simulation was done with R_L = 40Ω during a time of 0.2 seconds, and the nonlinear load was added at 0.1 second. Where the Q is chosen to be 10^{-5}. The state feedback gain (k) in (36) is calculated by using the LMI technique. The parameters of the switching function *Sign*(.) or *Sat*(.) are chosen as η = [300;350;5;10]. The results are shown in figures (16-A, B, C,and D), the input as reference in the $dq - frame$, the output voltage, current in the $dq - frame$ of the three phase MG plant, the voltage control signal, and the current control signal output of the proposed controller, respectively. In addition, the figures (17-E and F) are the output voltage and current of the three-phase MG, and (G and H) are the active and reactive power of the MG.

$$k = \begin{bmatrix} -580.2 & -283.2 & -6.1\times10^{4} & 2.7\times10^{3} \\ -344.2 & -697.0 & 2.7\times10^{3} & -1.1\times10^{4} \\ 6.5\times10^{4} & -3.7\times10^{3} & 412.69 & 776.89 \\ -3.6\times10^{3} & 6.6\times10^{4} & 933.75 & 703.23 \end{bmatrix} \quad (36)$$

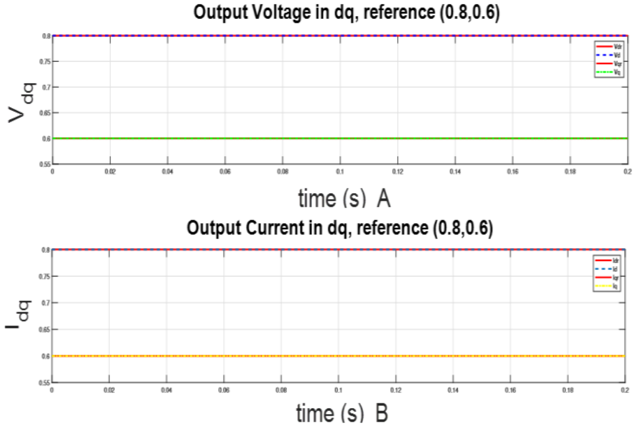

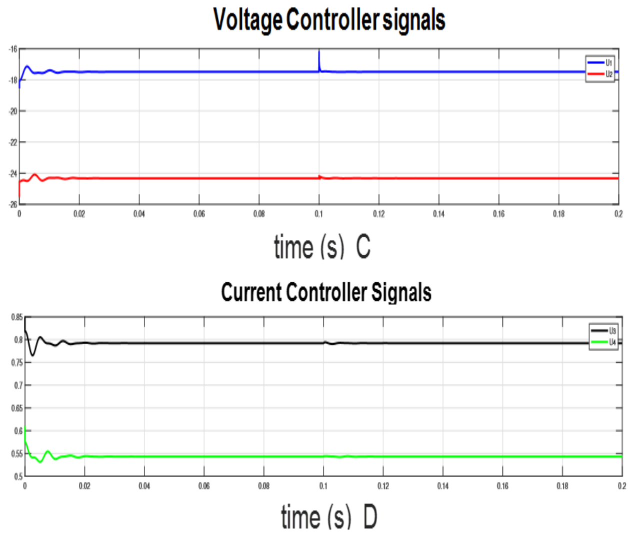

Fig. 16. The input and output of the controller with a MG plant against the nonlinear load (A-B) Voltage and Current in dq-frame, (C-D) Control signals in dq-frame.

D. Performance Against the Compound Loads

The final test is a three-phase IMG, and the proposed controller is against the compound loads. This means all the loads are connected to the MG, where the first $R_L = 40\Omega$ and the dynamic loads are connected at the beginning. The unknown loads are added at 0.03 seconds and the switch is closed at 0.06 seconds. In the third case, the harmonic load is added at 0.1 second, and in the end, the nonlinear load is added at 0.15 second. Where the Q is chosen to be 0.65×10^{-5}. The state feedback gain (k) in (37) is calculated by using the LMI technique. The parameters of the switching function *Sign*(.) or *Sat*(.) are chosen as $\eta = [600;500;5;20]$.

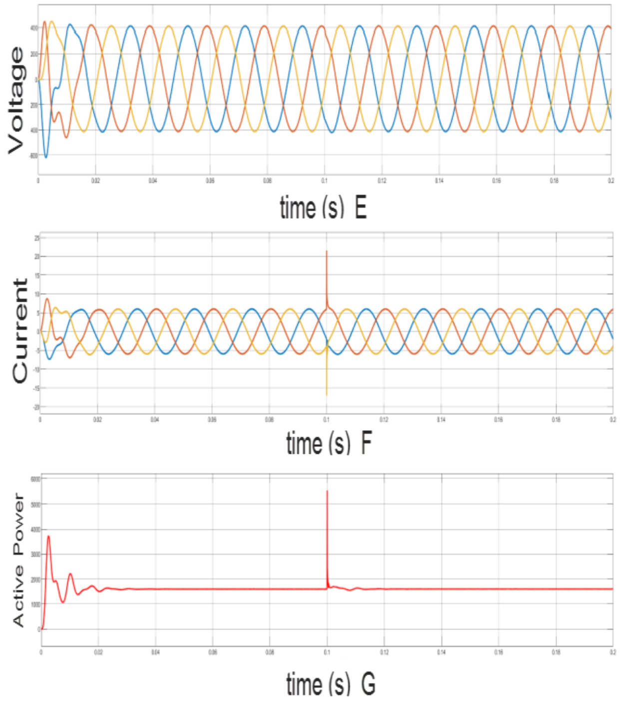

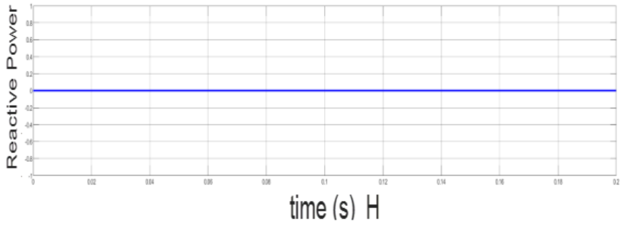

Fig. 17. The output of a three phase MG against the nonlinear load (E)Voltage Output of the MG (F) Current Output of the MG (G) Active Power Output of the MG (H) Reactive Power Output of the MG.

However, the results for 0.2 seconds are shown in figures (18-A, B, C, and D), which are the reference signals in a $dq - frame$, output voltage, current of the MG plant, voltage, and current control signal of the proposed controller, respectively.

$$k = \begin{bmatrix} 215.89 & -74.56 & -4.7 \times 10^3 & 1.149 \times 10^3 \\ -186.48 & 265.57 & 1.17 \times 10^3 & -4.68 \times 10^3 \\ 1.28 \times 10^4 & 2.27 \times 10^3 & -2.6 \times 10^3 & 467.387 \\ 2.12 \times 10^3 & 1.8 \times 10^4 & -77.436 & -3.04 \times 10^3 \end{bmatrix} \quad (37)$$

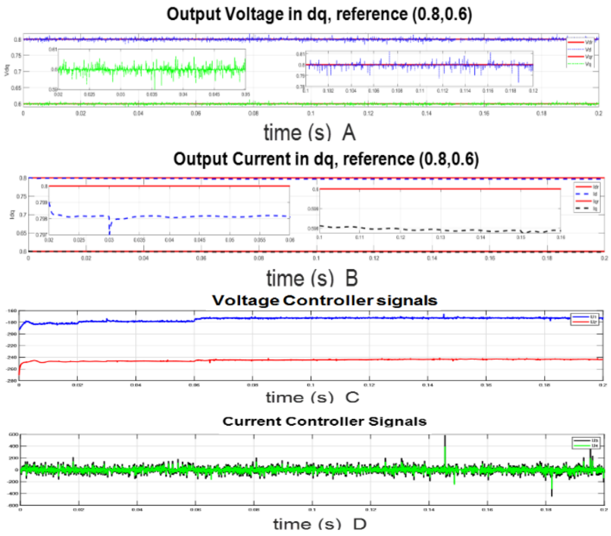

Fig. 18. The input and output of the controller with a MG plant against the compound loads (A-B)Voltage and Current in dq-frame (C-D) Control signal in dq-frame.

As demonstrated in the results, the performance of the proposed controller is deemed acceptable, particularly considering the challenge of managing various loads within the same test scenario. Utilizing the voltage control signal for microgrid regulation proves advantageous due to the dynamic load's impact on the entire system. Consequently, the output waveforms of the microgrid exhibit satisfactory characteristics.

VI. Conclusion

This paper introduces a sliding mode controller utilizing the LMI approach, designed to regulate and optimize both the voltage and current signals in single-phase and three-phase microgrids. The application of the presented controller results in the MG model's output precisely tracking the reference signals, demonstrating the effectiveness and precision of the control strategy in maintaining desired performance levels. Additionally, the output voltage and current signals of the microgrid display acceptable waveforms, while the correction time is notably shorter compared to similar studies. Simulated results demonstrate that the proposed controller can enhance various aspects of the MG's outputs, including active power, reactive power, and power factor. Moreover, the proposed controller is not a complex composite structure when compared to similar counterparts. Future developments of the proposed controller will focus on the LC filter, which will be modified adaptively along with the loads to ensure compatibility with the controller's operation and deliver admissible output waveforms for the MG. Furthermore, because the structure of the proposed controller is not complex and its outputs are voltage and current signals, it can simultaneously regulate two Voltage Source Inverters using a single regulator, which makes the proposed controller more cost-effective. Future work should aim to develop a controller capable of simultaneously regulating multiple VSIs in a single MG. This advancement would facilitate more efficient utilization of renewable energy sources and enhance the overall performance of the microgrid system.

REFERENCES

[1] Z. Yang, F. Yang, H. Min, H. Tian, W. Hu, and J. Liu, "Review on optimal planning of new power systems with distributed generations and electric vehicles," *Energy Reports,* vol. 9, pp. 501-509, 2023.

[2] S. Ahmad, M. Shafiullah, C. B. Ahmed, and M. Alowaifeer, "A review of microgrid energy management and control strategies," *IEEE Access,* vol. 11, pp. 21729-21757, 2023.

[3] S. Vuddanti and S. R. Salkuti, "Review of energy management system approaches in microgrids," *Energies,* vol. 14, no. 17, p. 5459, 2021.

[4] S. Mizani and A. Yazdani, "Optimal design and operation of a grid-connected microgrid," in *2009 IEEE Electrical Power & Energy Conference (EPEC),* 2009: IEEE, pp. 1-6.

[5] R. Bayindir, E. Hossain, E. Kabalci, and R. Perez, "A comprehensive study on microgrid technology," *International Journal of Renewable Energy Research,* vol. 4, no. 4, pp. 1094-1107, 2014.

[6] F. Li, R. Li, and F. Zhou, *Microgrid technology and engineering application*. Elsevier, 2015.

[7] M. J. Ghadi, A. Rajabi, S. Ghavidel, A. Azizivahed, L. Li, and J. Zhang, "From active distribution systems to decentralized microgrids: A review on regulations and planning approaches based on operational factors," *Applied Energy,* vol. 253, p. 113543, 2019.

[8] A. Iovine, M. J. Carrizosa, E. De Santis, M. D. Di Benedetto, P. Pepe, and A. Sangiovanni-Vincentelli, "Voltage regulation and current sharing in DC microgrids with different information scenarios," *IEEE Transactions on Control Systems Technology,* vol. 30, no. 5, pp. 1905-1919, 2021.

[9] M. H. Andishgar, E. Gholipour, and R.-a. Hooshmand, "An overview of control approaches of inverter-based microgrids in islanding mode of operation," *Renewable and Sustainable Energy Reviews,* vol. 80, pp. 1043-1060, 2017.

[10] A. M. Bouzid, J. M. Guerrero, A. Cheriti, M. Bouhamida, P. Sicard, and M. Benghanem, "A survey on control of electric power distributed generation systems for microgrid applications," *Renewable and Sustainable Energy Reviews,* vol. 44, pp. 751-766, 2015.

[11] Y. Sun *et al.*, "An fP/Q droop control in cascaded-type microgrid," *IEEE Transactions on Power Systems,* vol. 33, no. 1, pp. 1136-1138, 2017.

[12] S. Sahoo, S. Mishra, S. Jha, and B. Singh, "A cooperative adaptive droop based energy management and optimal voltage regulation scheme for DC microgrids," *IEEE Transactions on Industrial Electronics,* vol. 67, no. 4, pp. 2894-2904, 2019.

[13] M. Ahmadi Kamarposhti, "Optimal control of islanded micro grid using particle swarm optimization algorithm," *International Journal of Industrial Electronics Control and Optimization,* vol. 1, no. 1, pp. 53-60, 2018.

[14] M. Alizadeh, H. Askarian Abyaneh, A. Bakhshai, and N. Khodabakhshi Javinani, "An Enhanced Distributed State Feedback for Secondary Control in an Islanded Microgrid," *International Journal of Industrial Electronics Control and Optimization,* vol. 5, no. 2, pp. 123-132, 2022.

[15] N. R. Abjadi, "Adaptive input-output feedback linearization control for islanded inverter-based microgrids," *International Journal of Industrial Electronics Control and Optimization,* vol. 6, no. 3, pp. 183-192, 2023.

[16] R. Sedaghati and M. R. Shakarami, "A new sliding mode-based power sharing control method for multiple energy sources in the microgrid under different conditions," *International Journal of Industrial Electronics Control and Optimization,* vol. 2, no. 1, pp. 25-38, 2019.

[17] M. Khanbaghi and A. Zečević, "An LMI-based control strategy for large-scale systems with applications to interconnected microgrid clusters," *IEEE Access,* vol. 10, pp. 111554-111563, 2022.

[18] Y. M. Alsmadi *et al.*, "Sliding mode control of photovoltaic based power generation systems for microgrid applications," *International Journal of Control,* vol. 94, no. 6, pp. 1704-1715, 2021.

[19] S. Prasad, "Robust sliding mode controller for frequency regulation in a microgrid," *Transactions of the Institute of Measurement and Control,* vol. 45, no. 10, pp. 1947-1964, 2023.

[20] J. S. Gomez, D. Saez, J. W. Simpson-Porco, and R. Cárdenas, "Distributed predictive control for frequency and voltage regulation in microgrids," *IEEE Transactions on Smart Grid,* vol. 11, no. 2, pp. 1319-1329, 2019.

[21] A. Rosini, D. Mestriner, A. Labella, A. Bonfiglio, and R. Procopio, "A decentralized approach for frequency and voltage regulation in islanded PV-Storage microgrids," *Electric Power Systems Research,* vol. 193, p. 106974, 2021.

[22] U. K. Kalla, B. Singh, S. S. Murthy, C. Jain, and K. Kant, "Adaptive sliding mode control of standalone single-phase microgrid using hydro, wind, and solar PV array-based generation," *IEEE transactions on smart grid,* vol.

9, no. 6, pp. 6806-6814, 2017.

[23] S. K. Gudey and R. Gupta, "Recursive fast terminal sliding mode control in voltage source inverter for a low - voltage microgrid system," *IET Generation, Transmission & Distribution,* vol. 10, no. 7, pp. 1536-1543, 2016.

[24] A. Elnady and M. AlShabi, "Advanced exponential sliding mode control for microgrid at autonomous and grid-connected modes," *Bulletin of Electrical Engineering and Informatics,* vol. 10, no. 1, pp. 474-486, 2021.

[25] B. Carvalho and L. Rodrigues, "Multivariable PID synthesis via a static output feedback LMI," in *2019 IEEE 58th Conference on Decision and Control (CDC),* 2019: IEEE, pp. 8398-8403.

[26] C. Olalla, R. Leyva, A. El Aroudi, and I. Queinnec, "Robust LQR control for PWM converters: An LMI approach," *IEEE Transactions on industrial electronics,* vol. 56, no. 7, pp. 2548-2558, 2009.

[27] M. Armin *et al.*, "Robust extended $H\infty$ control strategy using linear matrix inequality approach for islanded microgrid," *IEEE access,* vol. 8, pp. 135883-135896, 2020.

[28] F. R. Badal, P. Das, S. K. Sarker, and S. K. Das, "A survey on control issues in renewable energy integration and microgrid," *Protection and Control of Modern Power Systems,* vol. 4, no. 1, pp. 1-27, 2019.

[29] M. Y.-Y. U. Haque, M. R. Islam, J. Hasan, and M. R. I. Sheikh, "Negative imaginary theory-based proportional resonant controller for voltage control of three-phase islanded microgrid," *Journal of Control, Automation and Electrical Systems,* vol. 32, pp. 214-226, 2021.

[30] M. Y.-Y. U. Haque, M. R. Islam, T. Ahmed, and M. R. I. Sheikh, "Improved voltage tracking of autonomous microgrid technology using a combined resonant controller with lead-lag compensator adopting negative imaginary theorem," *Protection and Control of Modern Power Systems,* vol. 7, no. 1, p. 10, 2022.

Mohammed Yousif Yakoob was born in Iraq, in 1983, he received his Bcs from Basra University and Master degree from University of Tabriz, and he is working in Iraqi ministry of electrical, Nasiriyah Thermal Power Station.

Mina Salim was born in Mahabad, Iran in 1983. She received her B.sc in Electrical Engineering from Sahand University of Technology in 2005, Sahand, Iran, and her M.Sc. degree in Electrical Engineering from University of Tabriz, Iran in 2009. She received her Ph. D degree in Electrical Engineering from Sahand University of Technology in 2016. She is currently an Assistant professor in Department od Control Engineering, Faculty of Electrical and Computer Engineering at University of Tabriz, Iran. Her currently interest area are Data Driven Fault Detection and Control Methods and their Application for industrial processes, Robust Control, and Intelligent Algorithms.

Amir.A. Ghavifekr is currently an assistant professor of control engineering at university of Tabriz-Iran. He was studying at University of Tabriz in Electrical –Control Engineering and received his B.Sc. and M.Sc. degrees in Control Engineering in 2009 and 2012. He received his Ph.D. degree in control engineering in the field of Teleoperation systems from university of Tabriz with cooperation of university of Verona in Italy in 2018. His thesis was about “Multi-rate control of Teleoperation systems with Networked Structures”. His research interests are focused on: Teleoperation and Telesurgery, Robotic manipulators, Network Control Systems (NCS), Multi-rate Control, Digital Control, Nonlinear Control, Virtual reality, and also, he has worked on intelligent systems. He has actively engaged with the professional community. Amir is an active Senior member of the IEEE and the member of development committee of IEEE Iran section. Recently he has been selected as the chair of the IEEE young professional committee of Iran section. He has also served several reputable IEEE indexed conferences such as PEDSTC, ICCIA, ICEE and SGC as the executive chair and international relation chair.

International Journal Of
Industrial Electronics Control and Optimization
Print ISSN: 3517-2645
Online ISSN: 3568-2645
Homepage: https://ieco.usb.ac.ir/

Control of a shunt Active Power Filter with Voltage Source Model to Improve the Power Quality Performance

Mohammad Ali Heydari | Mahdi Hassanniakheibari | Gholamreza Sadeghi

Department of Electrical and Computer Engineering, University of Sistan and Baluchestan, Zahedan, Iran[1]
Department of Electrical Engineering, Zahedan Branch, Islamic Azad University, Zahedan, Iran[2]
Department of Electrical and Computer Engineering, Arak University of technology, Arak, Iran[3]
Corresponding author's email: mahdi.hassannia@iau.ac.ir

Article Info

Article type:
Research Article

Article history:
Received: 21-March-2024
Received in revised form:
03-July-2024
Accepted: 15-July-2024
Published online: 22-Sep-2024

Keywords:
Active Power Filter (APF),
Voltage Source Converter,
Error Dynamic,
Grid Harmonics,
Power Quality.

ABSTRACT

Active power filters (APFs) play a vital role in reducing the current harmonics and improving power quality. This work studies a shunt APF (SAPF) based on the three-phase voltage source converter (VSC). This paper investigates the new robust control approach using error dynamics. Stable first-order error dynamics are considered when designing the control inputs. Three control inputs are obtained to control the currents at any phase by choosing and optimizing the appropriate parameters. This strategy is also simple to implement in practical applications because it is the same as the proportional-derivative controller design. In addition, the new control method can be utilized for any system with low dynamic information so that the destructive effects of lumped uncertainties in the output channels of the SAPF can be alleviated. The minimum voltage and current measurements are used to control the SAPF, and the grid current harmonics will be reduced by achieving the stabilization of tracking error dynamics. Some numerical simulations are performed by MATLAB software to confirm the proposed method.

I. Introduction

Electric energy loss is one of the most challenging issues in the power grid, and it can significantly impact its stability. The power grid losses are influenced by the impedance of transmission lines, which occur with the flow of current through them. If the load connected to the grid consumes reactive power, it causes an increase in losses and a decrease in the power transmission capacity of the lines. The proposed solution for these loads uses reactive power compensators, which large consumers usually utilize capacitors for compensation. The distribution grid uses compensators for small consumers at the beginning of feeder lines to solve this problem in the distribution lines and prevent them from reaching the transmission lines [1]-[3].

Technological advancements have led to the connection of loads to the grid that inject harmonic currents into it. Increasing these loads can significantly reduce the power transmission capacity and cause power plants to generate harmonic losses. In other words, power plants are built only for their outputs to be wasted and their costs to become irrecoverable. In this area, the harmonic compensator is an effective solution that can resolve the power grid's many crises [4]-[6].

Harmonics are also a critical problem in discussing power quality in distribution and transmission systems. Electricity companies must control the level of harmonic distortions in the grid and provide limitations to prevent damage to the equipment of residential and industrial customers. In most cases, voltage distortion is less than one percent in transmission systems, and as we get closer to the customers, the level of these distortions increases [7]-[10].

Distorted waveforms can be decomposed into a sum of the fundamental frequency and its harmonics. It is also common to use an index known as the total harmonic distortion (THD) to determine any waveform's distortion level. A higher value of the THD can lead to harmonic losses greater than the losses of the fundamental component. This failure can be solved by

Publisher: University of Sistan and Baluchestan

designing and implementing filters [11], [12].

Active Power Filters (APFs) are converters that generate compensating voltage and current as needed by using reactive instantaneous power and preventing harmonics from nonlinear loads from entering the grid. The main issue in this topic is how to control the converter for better and more accurate performance in compensating the grid's harmonic content. The APFs are classified into various categories, including their connection to the grid, type of converter, number of phases, modulation, and control methods [13]-[16].

Gyugyi and Strycula introduced shunt APFs (SAPFs) in 1976 [1]. These filters are an effective method for neutralizing harmonic currents from nonlinear loads. SAPFs are connected to the load and source in shunt. They monitor the current flow from the source to the load and generate a compensating current to neutralize harmonic content. SAPFs are typically used for low-power applications and filtering low-frequency harmonics. The advantage of SAPFs is their ease of implementation and their ability to have a fast response time [17].

The voltage source converter (VSC)s are generally used for low power levels, and the most important reason is the lower switching power loss compared to current source converters. Different models of VSC have been described in the literature. From this point of view, the VSC will be associated with unstructured uncertainties in the model. Therefore, dealing with uncertainties and the control of SAPF will become a controversial challenge. For this reason, a robust control method is required to deal with the lumped uncertainties in SAPF. Various control strategies for APFs have been reported in articles and research, including finite-set model predictive control [18], nonlinear control [19], adaptive sliding-mode backstepping control [20], neural network approach [21], [22], adaptive fuzzy control [23], [24], model-based control [25], and proportional-integral (PI) vector control [26]. In addition, the incorporation of robust control techniques that have been introduced in recent years can be considered for having the desired outputs in nonlinear systems. In other words, they can improve the design aspects and reduce the influence of destructive factors in the responses [27]-[31].

In [18], a finite-set model predictive control with coupling capacitor voltage observer scheme was proposed for thyristor-controlled LC-coupling hybrid APF. It ensures a fast transient response, low steady-state error, and good robustness under both inductive and capacitive load situations.

Research [19] introduces a nonlinear control technique for a three-phase APF. The control strategy includes a cascade structure of two loops. The inner-loop regulator is designed using the sliding mode control technique, and Lyapunov approaches to ensure the power factor correction objective by forcing the grid current to follow a given reference signal. The outer loop consists mainly of a PI regulator to regulate the output voltage. This scheme is implemented based on three control objectives:

- forcing the photovoltaic output voltage to track a reference signal provided by the maximum power point tracking block to produce their maximum power
- regulating the DC link voltage to satisfy the correct operation mode of the three-phase APF
- satisfying power factor correction objective at the point of common coupling

Recently, a novel hybrid two-loop nonlinear controller was designed for stabilization and robust control of the LCL-type SAPF in reference [20]. Backstepping, sliding mode, and adaptive controllers were combined to solve the closed-loop system's instability problem and the LCL coupling's inherent resonance in this work. The main objective of this strategy is to directly make the grid current in phase with the grid voltage.

In [21], an adaptive sliding mode reference model is proposed using a radial basis function neural network to control a single-phase APF. The neural network approximates the nonlinear function and eliminates modelling errors in the active power filter system. Moreover, a sliding mode voltage controller based on an exponential approach law is designed in reference [21] to improve the performance of AC side voltage tracking.

Research [22] proposes a new intelligent sliding-mode control approach to achieve harmonic suppression of an APF effectively. This work uses an intelligent complementary terminal sliding-mode controller to improve the control accuracy of the current loop and deal with the lumped disturbances in the system that are so attractive. In addition, a multiloop neural network, whose parameter learning laws are derived based on the Lyapunov laws, is proposed to approximate the unknown nonlinear function term in the APF dynamic model to reduce chattering.

In research [23], an adaptive fuzzy model reference control was studied to improve the dynamic performance of power, such as current tracking and THD for SAPFs. The fuzzy method was utilized to approximate the nonlinear model of the APF, which arises from nonlinear characteristics, variable parameters, and external disturbances. This study presents an adaptive fuzzy control system for the APF consisting of a Takagi-Sugeno fuzzy control part and a sliding mode control part, which can enhance the system's robust performance.

An adaptive fuzzy sliding mode control system is proposed in [24] to enhance the dynamic performance of a three-phase APF. Adaptive fuzzy systems are employed to approximate both the equivalent control term and the switching control term in the sliding mode controller. Thus, an online adaptive tuning algorithm for the subsequent parameters in the fuzzy rules is designed in [24]. Continuous switching control can somewhat reduce the phenomenon of chattering, and simulations conducted in [24] demonstrate that the proposed control method exhibits excellent dynamic performance, including minor current tracking errors, reduction in THD, high robustness in the presence of parameter variations, and nonlinear loads.

Resilient model-based control for a three-phase SAPF is discussed in [25]. In the proposed control method in this study, a linear converter model is utilized, which is incorporated into the Kalman filter structure to estimate the system's state variables. Even though the estimated states in this method do not precisely match the real system variables, resulting in some error in their estimation, designing three sliding mode controllers is still feasible.

A PI vector control for controlling a hybrid LC APF system with ideal steady-state error, optimal transient response, and good robustness is presented in [26]. A transfer function for the proposed PI vector current controller is introduced in this research, and the parameter design for achieving an optimal transient response is discussed. Detailed analysis of the robustness of the PI vector current controller against system parameter variations, distorted grid voltages, and grid frequency variations is conducted.

This paper studies an SAPF based on the three-phase VSC and investigates the new robust control approach using error dynamics. When designing the control inputs, stable first-order error dynamics are considered. Three control inputs are obtained to control the currents at any phase by choosing and optimizing the appropriate parameters. This strategy is also simple to implement in practical applications because it is the same as the proportional-derivative controller design. In addition, the new control method can be utilized for any system with low dynamic information so that the destructive effects of lumped uncertainties in the output channels of the SAPF can be alleviated.

The rest of this paper is organized as follows: In Section II, the mathematical model of a SAPF is introduced. Discretization of the dynamic system is investigated in Section III. Section IV is dedicated to proposing the new robust control method. To verify the new proposed control scheme and investigation of the performance, a number of simulation results are provided in Section V. Finally, Section VI draws the conclusions.

II. Model of the three-phase APF system

According to [25], an appropriate model of the three-phase APF was introduced, and this model is considered for the design of the proposed control scheme. Figure 1 shows the electrical circuit of the three-phase APF. The differential equations of this model are as follows:

$$
\begin{aligned}
\frac{di_{F_a}(t)}{dt} &= -\frac{v_{dc}(t)}{2L_F}u_a(t)+\frac{v_{dc}(t)}{6L_F}(u_a(t)+u_b(t)+u_c(t))+\frac{v_a(t)}{L_F}\\
\frac{di_{F_b}(t)}{dt} &= -\frac{v_{dc}(t)}{2L_F}u_b(t)+\frac{v_{dc}(t)}{6L_F}(u_a(t)+u_b(t)+u_c(t))+\frac{v_b(t)}{L_F}\\
\frac{di_{F_c}(t)}{dt} &= -\frac{v_{dc}(t)}{2L_F}u_c(t)+\frac{v_{dc}(t)}{6L_F}(u_a(t)+u_b(t)+u_c(t))+\frac{v_c(t)}{L_F}\\
\frac{dv_{dc}(t)}{dt} &= \frac{i_{F_a}(t)u_a(t)}{2C}+\frac{i_{F_b}(t)u_b(t)}{2C}+\frac{i_{F_c}(t)u_c(t)}{2C}
\end{aligned}
\tag{1}
$$

where $i_{F_a}(t), i_{F_b}(t), i_{F_c}(t), v_{dc}(t)$ are the state variables, $u_a(t), u_b(t), u_c(t)$ are the control input commands which must be designed appropriately, and $v_a(t), v_b(t), v_c(t)$ are the voltages at the point of common coupling. In this paper, the main goal is the control of the system states to follow the references or $i^*_{F_a}(t), i^*_{F_b}(t), i^*_{F_c}(t), v^*_{dc}(t)$. In [25], by neglecting the effect of neutral-point voltage or

$$
v_n(t)=\frac{v_{dc}(t)}{6}(u_a(t)+u_b(t)+u_c(t)) \tag{2}
$$

a simple model has been achieved from (1). In other words, the voltage $v_n(t)$ is a high-frequency signal. This model is given by (3):

$$
\begin{aligned}
\frac{di_{F_a}(t)}{dt} &= -\frac{v_{dc}(t)}{2L_F}u_a(t)+\frac{v_a(t)}{L_F}\\
\frac{di_{F_b}(t)}{dt} &= -\frac{v_{dc}(t)}{2L_F}u_b(t)+\frac{v_b(t)}{L_F}\\
\frac{di_{F_c}(t)}{dt} &= -\frac{v_{dc}(t)}{2L_F}u_c(t)+\frac{v_c(t)}{L_F}\\
\frac{dv_{dc}(t)}{dt} &= \frac{i_{F_a}(t)u_a(t)}{2C}+\frac{i_{F_b}(t)u_b(t)}{2C}+\frac{i_{F_c}(t)u_c(t)}{2C}
\end{aligned}
\tag{3}
$$

where $v_i(t), i=a,b,c$ are determined by (4):

$$
\begin{aligned}
\frac{dv_i(t)}{dt} &= \omega_0 v_{iq}(t)\\
\frac{dv_{iq}(t)}{dt} &= -\omega_0 v_i(t)
\end{aligned}
\tag{4}
$$

and ω_0 is the grid frequency.

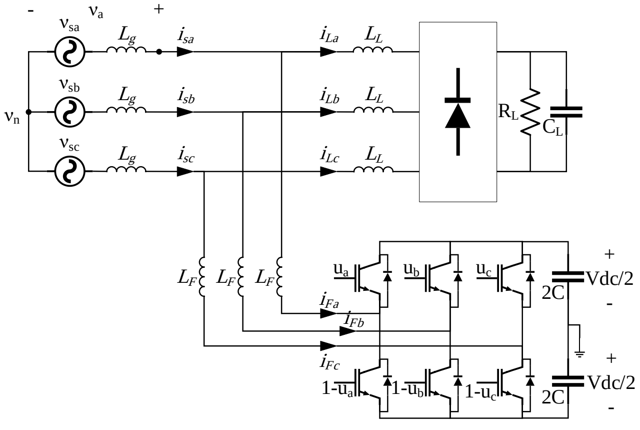

Fig. 1. The three-phase SAPF circuit connected to grid

III. Discretization of the dynamic system

Consider the following approximation for the derivation of $f(x)$ related to x:

$$\frac{df(x)}{dx} \cong \frac{f(x+\Delta x)-f(x)}{\Delta x} \tag{5}$$

The step Δx must be chosen very small. Nevertheless, the derivation computation process is long, and calculations in the microcontroller are done slowly.

Based on (5), a set of state equations described by (6) can be discretized.

$$\frac{dX(t)}{dt} = F(X(t),U(t),D(t)) \tag{6}$$

In (6), $X(t)=\left[x_1(t)\ \ x_2(t)\ \ \cdots\ \ x_n(t)\right]^T$ is the system state vector, $x_i(t), i=1,2,\cdots,n$ are the state variables, $F(\cdot)$ is the nonlinear function vector, $U(t)=\left[u_1(t)\ \ u_2(t)\ \ \cdots\ \ u_m(t)\right]^T$ is the control input vector, and $D(t)=\left[d_1(t)\ \ d_2(t)\ \ \cdots\ \ d_l(t)\right]^T$ is the disturbance vector.

Now, according to (5), the following expression is obtained for (6):

$$\begin{aligned} &\frac{dX(t)}{dt} \cong \frac{X(t+\Delta t)-X(t)}{\Delta t} = F(X(t),U(t),D(t)) \\ &X(t+\Delta t) = F(X(t),U(t),D(t))\Delta t + X(t) \end{aligned} \tag{7}$$

Therefore, by assigning the step k and sampling time $T_s = 1/f_s$, the following result is concluded:

$$X(k+1) = F(X(k),U(k),D(k))T_s + X(k) \tag{8}$$

Based on (8), the dynamic model (3) or three-phase APF is discretized to model (9).

$$\begin{aligned} i_{F_a}(k+1) &= \left(-\frac{v_{dc}(k)}{2L_F}u_a(k)+\frac{v_a(k)}{L_F}\right)T_s + i_{F_a}(k) \\ i_{F_b}(k+1) &= \left(-\frac{v_{dc}(k)}{2L_F}u_b(k)+\frac{v_b(k)}{L_F}\right)T_s + i_{F_b}(k) \\ i_{F_c}(k+1) &= \left(-\frac{v_{dc}(k)}{2L_F}u_c(k)+\frac{v_c(k)}{L_F}\right)T_s + i_{F_c}(k) \\ v_{dc}(k+1) &= \left(\frac{i_{F_a}(k)u_a(k)+i_{F_b}(k)u_b(k)+i_{F_c}(k)u_c(k)}{2C}\right)T_s \\ &+v_{dc}(k) \end{aligned} \tag{9}$$

where

$$\begin{aligned} v_i(k+1) &= \omega_0 v_{iq}(k)T_s + v_i(k) \\ v_{iq}(k+1) &= -\omega_0 v_i(k)T_s + v_{iq}(k) \end{aligned} \tag{10}$$

for $i=a,b,c$.

IV. New robust controller design

Based on Fig. 1, by defining the tracking error as (11), the expressions (12) for error dynamics are obtained.

$$\begin{aligned} e_1(k) &= i_{S_a}(k)-i^*_{S_a}(k) = i_{F_a}(k)+i_{L_a}(k)-i^*_{S_a}(k) \\ e_2(k) &= i_{S_b}(k)-i^*_{S_b}(k) = i_{F_b}(k)+i_{L_b}(k)-i^*_{S_b}(k) \\ e_3(k) &= i_{S_c}(k)-i^*_{S_c}(k) = i_{F_c}(k)+i_{L_c}(k)-i^*_{S_c}(k) \\ e_4(k) &= v_{dc}(k)-v^*_{dc}(k) \end{aligned} \tag{11}$$

$$\begin{aligned} &e_1(k+1) = \\ &\left(-\frac{v_{dc}(k)}{2L_F}u_a(k)+\frac{v_a(k)}{L_F}\right)T_s + i_{F_a}(k)+i_{L_a}(k+1)-i^*_{S_a}(k+1) \\ &e_2(k+1) = \\ &\left(-\frac{v_{dc}(k)}{2L_F}u_b(k)+\frac{v_b(k)}{L_F}\right)T_s + i_{F_b}(k)+i_{L_b}(k+1)-i^*_{S_b}(k+1) \\ &e_3(k+1) = \\ &\left(-\frac{v_{dc}(k)}{2L_F}u_c(k)+\frac{v_c(k)}{L_F}\right)T_s + i_{F_c}(k)+i_{L_c}(k+1)-i^*_{S_c}(k+1) \\ &e_4(k+1) = \\ &\left(\frac{i_{F_a}(k)u_a(k)}{2C}+\frac{i_{F_b}(k)u_b(k)}{2C}+\frac{i_{F_c}(k)u_c(k)}{2C}\right)T_s + v_{dc}(k)-v^*_{dc} \end{aligned} \tag{12}$$

where $i^*_{S_a}(k), i^*_{S_b}(k), i^*_{S_c}(k)$ are grid currents references, $i_{L_a}(k), i_{L_b}(k), i_{L_c}(k)$ are load currents or disturbances and $v^*_{dc}(k)$ is constant or $v^*_{dc}(k)=v^*_{dc}$.

The error dynamic equations can be assumed as follows:

$$e_i(k+n)+\sum_{j=0}^{n-1}\gamma_{ji}e_i(k+j)=0 \tag{13}$$

In (13), γ_{ji} are the design parameters, and they are dependent on the number of steps. Due to the control inputs $u_a(k), u_b(k), u_c(k)$ are appreciated in the first step of the three-phase APF system equations; hence based on (13), the following relations can be written:

$$\begin{aligned} e_1(k+1)+\gamma_{01}e_1(k) &= 0 \\ e_2(k+1)+\gamma_{02}e_2(k) &= 0 \\ e_3(k+1)+\gamma_{03}e_3(k) &= 0 \\ e_4(k+1)+\gamma_{04}e_4(k) &= 0 \end{aligned} \tag{14}$$

Therefore, according to (12) and (14), a set of equations or (15) for designing the control inputs are the result. There are three control commands in (15), and no input exists for controlling the $v_{dc}(k)$. This failure can be resolved by adding three parameters as $K_{s1}(k), K_{s2}(k), K_{s3}(k)$, and assigning auxiliary input $u_{dc}(k)$ into $u_a(k), u_b(k), u_c(k)$.

$$\begin{aligned} \gamma_{01}e_1(k) &= -\left(-\frac{v_{dc}(k)}{2L_F}u_a(k)+\frac{v_a(k)}{L_F}\right)T_s - i_{F_a}(k) \\ &-i_{L_a}(k+1)+i^*_{S_a}(k+1) \\ \gamma_{02}e_2(k) &= -\left(-\frac{v_{dc}(k)}{2L_F}u_b(k)+\frac{v_b(k)}{L_F}\right)T_s - i_{F_b}(k) \\ &-i_{L_b}(k+1)+i^*_{S_b}(k+1) \\ \gamma_{03}e_3(k) &= -\left(-\frac{v_{dc}(k)}{2L_F}u_c(k)+\frac{v_c(k)}{L_F}\right)T_s - i_{F_c}(k) \\ &-i_{L_c}(k+1)+i^*_{S_c}(k+1) \\ \gamma_{04}e_4(k) &= -\left(\frac{i_{F_a}(k)u_a(k)+i_{F_b}(k)u_b(k)+i_{F_c}(k)u_c(k)}{2C}\right)T_s \\ &-v_{dc}(k)+v^*_{dc} \end{aligned} \tag{15}$$

In the following, firstly, control of the variables $i_{S_a}(k), i_{S_b}(k), i_{S_c}(k)$ is studied, and then the control of $v_{dc}(k)$ is investigated. Regarding (15), by dividing the first, second, and third equations by $\gamma_{01}, \gamma_{02}, \gamma_{03}$, (16) is obtained:

$$
\begin{aligned}
e_1(k) &= -\left(-\frac{v_{dc}(k)}{2\gamma_{01}L_F}u_a(k)+\frac{v_a(k)}{\gamma_{01}L_F}\right)T_s-\frac{i_{F_a}(k)}{\gamma_{01}} \\
&\quad -\frac{i_{L_a}(k+1)}{\gamma_{01}}+\frac{i^*_{S_a}(k+1)}{\gamma_{01}} \\
e_2(k) &= -\left(-\frac{v_{dc}(k)}{2\gamma_{02}L_F}u_b(k)+\frac{v_b(k)}{\gamma_{02}L_F}\right)T_s-\frac{i_{F_b}(k)}{\gamma_{02}} \\
&\quad -\frac{i_{L_b}(k+1)}{\gamma_{02}}+\frac{i^*_{S_b}(k+1)}{\gamma_{02}} \\
e_3(k) &= -\left(-\frac{v_{dc}(k)}{2\gamma_{03}L_F}u_c(k)+\frac{v_c(k)}{\gamma_{03}L_F}\right)T_s-\frac{i_{F_c}(k)}{\gamma_{03}} \\
&\quad -\frac{i_{L_c}(k+1)}{\gamma_{03}}+\frac{i^*_{S_c}(k+1)}{\gamma_{03}}
\end{aligned}
\tag{16}
$$

Consider the following control inputs:

$$
\begin{aligned}
u_a(k) &= \frac{2\gamma_{01}L_F}{T_s v_{dc}(k)}\Big(K_{d1}e_1(k+1)+\big(K_{p1}+1\big)e_1(k)+T_sK_{s1}(k)u_{dc}(k)\Big) \\
u_b(k) &= \frac{2\gamma_{02}L_F}{T_s v_{dc}(k)}\Big(K_{d2}e_2(k+1)+\big(K_{p2}+1\big)e_2(k)+T_sK_{s2}(k)u_{dc}(k)\Big) \\
u_c(k) &= \frac{2\gamma_{03}L_F}{T_s v_{dc}(k)}\Big(K_{d3}e_3(k+1)+\big(K_{p3}+1\big)e_3(k)+T_sK_{s3}(k)u_{dc}(k)\Big)
\end{aligned}
\tag{17}
$$

where $K_{di},K_{pi},i=1,2,3$ are the design parameters. Also, $u_{dc}(k)$ is an input for controlling the $v_{dc}(k)$. By substituting these relations into (16), (18) can be obtained:

$$
\begin{aligned}
e_1(k) &= K_{d1}e_1(k+1)+\big(K_{p1}+1\big)e_1(k)+T_sK_{s1}(k)u_{dc}(k) \\
&\quad -\frac{v_a(k)}{\gamma_{01}L_F}T_s-\frac{i_{F_a}(k)}{\gamma_{01}}-\frac{i_{L_a}(k+1)}{\gamma_{01}}+\frac{i^*_{S_a}(k+1)}{\gamma_{01}} \\
e_2(k) &= K_{d2}e_2(k+1)+\big(K_{p2}+1\big)e_2(k)+T_sK_{s2}(k)u_{dc}(k) \\
&\quad -\frac{v_b(k)}{\gamma_{02}L_F}T_s-\frac{i_{F_b}(k)}{\gamma_{02}}-\frac{i_{L_b}(k+1)}{\gamma_{02}}+\frac{i^*_{S_b}(k+1)}{\gamma_{02}} \\
e_3(k) &= K_{d3}e_3(k+1)+\big(K_{p3}+1\big)e_3(k)+T_sK_{s3}(k)u_{dc}(k) \\
&\quad -\frac{v_c(k)}{\gamma_{03}L_F}T_s-\frac{i_{F_c}(k)}{\gamma_{03}}-\frac{i_{L_c}(k+1)}{\gamma_{03}}+\frac{i^*_{S_c}(k+1)}{\gamma_{03}}
\end{aligned}
\tag{18}
$$

Remark 1 *To achieve the desirable control of the three-phase APF, it is important the control of $v_{dc}(k)$. In other words, this issue affects the control procedure of the other state variables. For this reason, the weighted coefficients $K_{s1}(k),K_{s2}(k),K_{s3}(k)$ are considered to decrease the destructive effects of the $u_{dc}(k)$. This strategy can lead to satisfactory tracking and less ripple in the state variables and system outputs.*

Rearranging the (18) and dividing the error dynamics by K_{d1},K_{d2},K_{d3}, (19) one gets:

$$
\begin{aligned}
e_1(k+1) &= -\frac{K_{p1}}{K_{d1}}e_1(k)+\varepsilon_1(k) \\
e_2(k+1) &= -\frac{K_{p2}}{K_{d2}}e_2(k)+\varepsilon_2(k) \\
e_3(k+1) &= -\frac{K_{p3}}{K_{d3}}e_3(k)+\varepsilon_3(k)
\end{aligned}
\tag{19}
$$

where

$$
\begin{aligned}
\varepsilon_1(k) &= \frac{v_a(k)}{\gamma_{01}K_{d1}L_F}T_s+\frac{i_{F_a}(k)+i_{L_a}(k+1)-i^*_{S_a}(k+1)}{\gamma_{01}K_{d1}} \\
&\quad -\frac{T_sK_{s1}(k)}{K_{d1}}u_{dc}(k) \\
\varepsilon_2(k) &= \frac{v_b(k)}{\gamma_{02}K_{d2}L_F}T_s+\frac{i_{F_b}(k)+i_{L_b}(k+1)-i^*_{S_b}(k+1)}{\gamma_{02}K_{d2}} \\
&\quad -\frac{T_sK_{s2}(k)}{K_{d2}}u_{dc}(k) \\
\varepsilon_3(k) &= \frac{v_c(k)}{\gamma_{03}K_{d3}L_F}T_s+\frac{i_{F_c}(k)+i_{L_c}(k+1)-i^*_{S_c}(k+1)}{\gamma_{03}K_{d3}} \\
&\quad -\frac{T_sK_{s3}(k)}{K_{d3}}u_{dc}(k)
\end{aligned}
\tag{20}
$$

We consider the $\varepsilon_1(k),\varepsilon_2(k),\varepsilon_3(k)$ are lumped uncertainties in the error dynamics. According to (20), if the parameters $\gamma_{01},\gamma_{02},\gamma_{03}$ and K_{d1},K_{d2},K_{d3} be the large numbers, then the destructive effects of $v_i(k)$, $i_{Fi}(k)$, $i_{Li}(k+1)$, $i^*_{si}(k+1)$, $u_{dc}(k)$, $i=a,b,c$ in $\varepsilon_1(k),\varepsilon_2(k),\varepsilon_3(k)$ can be attenuated. Hence, $\varepsilon_1(k),\varepsilon_2(k),\varepsilon_3(k)$ in (20) can be considered weak perturbations. Finally, by tuning the parameters K_{p1},K_{p2},K_{p3}, the stability of the error dynamics is guaranteed, and tracking errors $e_1(k),e_2(k),e_3(k)$ can be set near to zero by increasing step k. For stabilizing (19), $K_{di},K_{pi},i=1,2,3$ must be chosen as follows:

$$
\frac{K_{p1}}{K_{d1}}>0,\frac{K_{p2}}{K_{d2}}>0,\frac{K_{p3}}{K_{d3}}>0 \tag{21}
$$

Now the design of $u_{dc}(k)$ for controlling the state variable $v_{dc}(k)$ is investigated. Based on the fourth equation in (15), and according to the definition of inputs in (17), the following expression can be obtained:

$$
\begin{aligned}
e_4(k) &= -\frac{L_FT_s}{\gamma_{04}Cv_{dc}(k)}\Big(\gamma_{01}i_{F_a}(k)K_{s1}(k)+\gamma_{02}i_{F_b}(k)K_{s2}(k) \\
&\quad +\gamma_{03}i_{F_c}(k)K_{s3}(k)\Big)u_{dc}(k)-\varepsilon_4(k)
\end{aligned}
\tag{22}
$$

where

$$
\begin{aligned}
\varepsilon_4(k) &= \frac{\gamma_{01}L_Fi_{F_a}(k)}{\gamma_{04}Cv_{dc}(k)}\Big(K_{d1}e_1(k+1)+\big(K_{p1}+1\big)e_1(k)\Big) \\
&\quad +\frac{\gamma_{02}L_Fi_{F_b}(k)}{\gamma_{04}Cv_{dc}(k)}\Big(K_{d2}e_2(k+1)+\big(K_{p2}+1\big)e_2(k)\Big) \\
&\quad +\frac{\gamma_{03}L_Fi_{F_c}(k)}{\gamma_{04}Cv_{dc}(k)}\Big(K_{d3}e_3(k+1)+\big(K_{p3}+1\big)e_3(k)\Big) \\
&\quad +\frac{v_{dc}(k)}{\gamma_{04}}-\frac{v^*_{dc}}{\gamma_{04}}
\end{aligned}
\tag{23}
$$

If the parameter γ_{04} be a large number enough, then it is clear that the destructive effect of $\varepsilon_4(k)$ can be neglected in (22), or alternatively $\varepsilon_4(k)$ is a weak perturbation. Consequently, by supposing the $u_{dc}(k)$ as proposed in (24), the new error dynamic (25) will be constructed:

$$
\begin{aligned}
u_{dc}(k) &= -\frac{\gamma_{04}Cv_{dc}(k)}{L_FT_s}\times \\
&\frac{\Big(K_{d4}e_4(k+1)+\big(K_{p4}+1\big)e_4(k)\Big)}{\Big(\gamma_{01}i_{F_a}(k)K_{s1}(k)+\gamma_{02}i_{F_b}(k)K_{s2}(k)+\gamma_{03}i_{F_c}(k)K_{s3}(k)\Big)}
\end{aligned}
\tag{24}
$$

$$e_4(k+1) = -\frac{K_{p4}}{K_{d4}} e_4(k) + \varepsilon_4(k) \qquad (25)$$

Finally, by choosing the K_{p4} appropriately, the tracking error $e_4(k)$ is set near to zero, and $v_{dc}(k)$ follows the reference signal v^*_{dc}. Accordingly, the stabilization of the error dynamic (25) is guaranteed by considering the following inequality:

$$\frac{K_{p4}}{K_{d4}} > 0 \qquad (26)$$

V. Simulation results

The new controller is simulated by MATLAB software to confirm the performance of the three-phase APF and analyze the electrical circuit outputs. For simulating the nonlinear load, a three-phase diode rectifier connected with a resistor load has been employed, and the grid current references are constructed as $i^*_{S_i}(k)=u_{dc}(k)v_i(k)$. The APF switches are IGBT type in the shunt form with inverse diode. In addition, the power circuit has some voltage and current measurements.

Generally, the distribution grid load is defined in an interval between minimum and maximum modes or cases. It is clear that minimum and maximum intervals are also considered for linear loads, and the performance of the APF is studied at this interval—moreover, the diode bridge resistor load changes between two currents, 8A and 16A.

The parameter values for simulation are $\gamma_{01} = \gamma_{02} = \gamma_{03} = \gamma_{04} = 100$, $K_{p1}=K_{p2}=K_{p3} = 100$, $K_{d1}=K_{d2}=K_{d3} = 10$, and $K_{s1}(k)=K_{s2}(k)=K_{s3}(k) = 1$. The circuit parameter values are $v_s = 220V$, $v_{dc} = 400V$, $L_F = 5mH$, $C = 1500\mu F$, $f_{switching} = 10KHz$, $f_s = 20KHz$.

A. *The maximum current case*

In this case, the diode bridge resistor load is considered 24Ω with a grid current of 16A and a THD of 26.69%. Fig. 2 illustrates the current harmonic frequency spectrum for the nonlinear load.

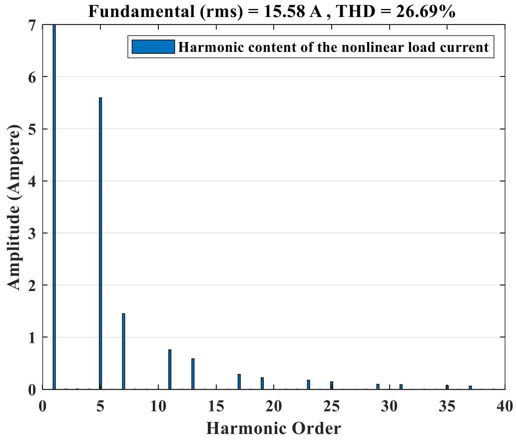

Fig. 2. The harmonic frequency spectrum for the nonlinear load current in the maximum case

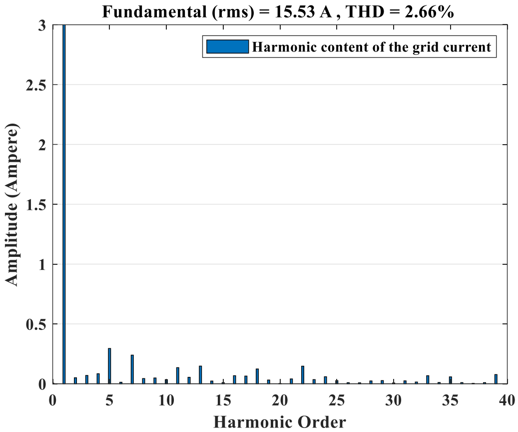

Fig. 3. The harmonic frequency spectrum for the nonlinear load current in the maximum case with existing the SAPF

After connecting the SAPF to the grid, the grid harmonic content is decreased based on Fig. 3. In this case, the amount of THD is reduced to 2.66%, an admissible value.

Fig. 4-a shows the waveform of the nonlinear current load constructed by the bridge diode. By connecting the SAPF to the grid, the grid current is as Fig. 4-b. To remove the nonlinear current harmonics from the grid current, the filter current should be as Fig. 4-c. In this simulation, the DC link capacitor's reference voltage is 400V, shown in Fig. 4-d.

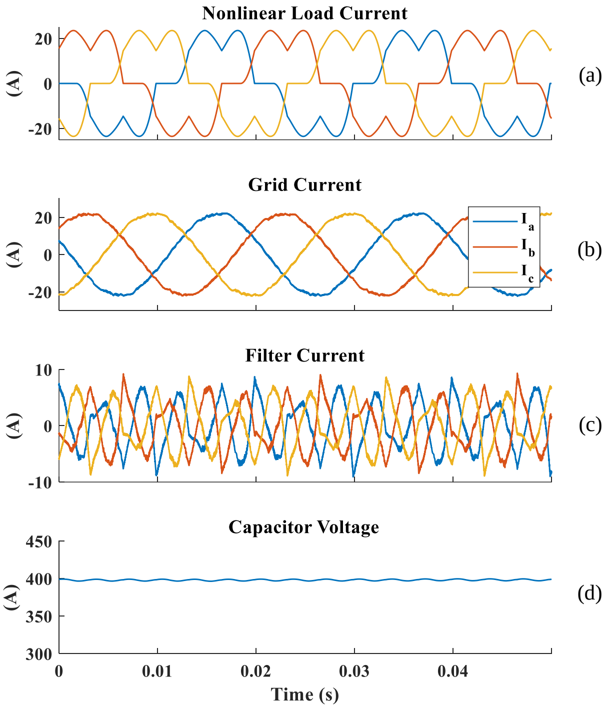

Fig. 4. The simulation results of the SAPF with nonlinear load constructed by diode bridge. (a) The waveform of the nonlinear load current (b) The waveform of the grid current after connecting the SAPF (c) The waveform of the SAPF (d) The waveform of the DC link capacitor voltage

B. *The minimum current case*

The minimum current for a nonlinear load can be obtained by considering a 48Ω resistor instead of 24Ω in the output of the bridge diode. The harmonic frequency spectrum is depicted in Fig. 5.

TABLE I
THE COMPARISON AMONG DIFFERENT CONTROLLERS FOR APF

Controller	[18]	[19]	[20]	[21]	[22]	[23]	[24]	[25]	[26]	Proposed
Year	2023	2022	2023	2015	2023	2015	2013	2016	2021	This work
Design complexity	Low	Low	Medium	High	High	Medium	low	Low	Medium	Low
Practical implementation	Medium	Medium	Hard	Hard	Medium	Hard	Medium	Simple	Medium	Simple
Dynamic model information	Yes	Yes	Yes	No	Yes	Yes	Yes	Yes	Yes	No
Robustness	Medium	Weak	Weak	Medium	Medium	Medium	Medium	Medium	Weak	High
Confrontation with uncertainty	Indirect	Indirect	Indirect	Indirect	Indirect	Indirect	Indirect	Indirect	Indirect	Direct
Steady-state accuracy	High	High	Medium	Medium	High	Medium	Medium	High	High	Medium
Transient response speed	Fast	Slow	Fast	Medium	Medium	Fast	Fast	Fast	Fast	Fast

In the case of minimum current, the amount of current is $8A$, and THD is 36.52%. Naturally, this THD is greater than that from the maximum current case. Based on Fig. 6, employing the SAPF reduces the amount of THD for grid current to 3.73%.

In Fig. 7, the waveforms of the nonlinear load at minimum current mode, the grid current with the SAPF already in the grid, the SAPF current, and the DC link capacitor voltage have been demonstrated to be similar to the maximum mode.

These results are confirmed in the minimum case, and the performance of the control approach is verified.

Finally, the comparison among different controllers designed in references [18]-[26] for APF has been tabulated in Table I. According to Table I, several aspects of the controllers introduced in previous works are investigated. A number of factors are explained in this table, for example, the design complexity, practical implementation, the amount of dynamic model information for design, robustness, and confrontation with uncertainty of the controllers. Also, the steady-state accuracy and the transient response speed for methods are compared.

Based on Table I and the comparison between the other methods provided in [18]-[26], it is clear that the proposed approach has a simple design. In other words, the tuning of parameters $K_{pi}, K_{di}, \gamma_{0i}$ is necessary, according to the level of uncertainties and control objects. The robustness ratio can be regulated using γ_{0i}. In addition, unlike the other methods, we can deal with lumped uncertainties directly. Also, in the design of the proposed method, the dynamic model information is not necessary. These issues are the advantages of the proposed method over the other approaches.

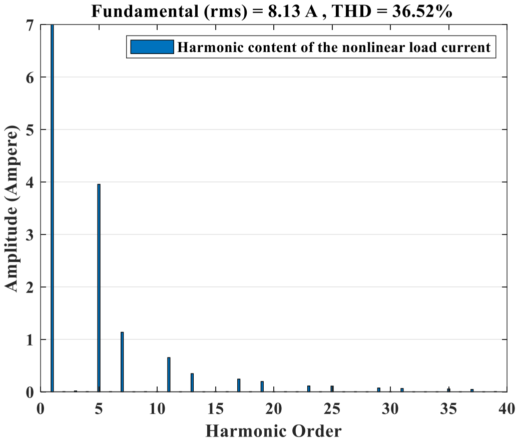

Fig. 5. The harmonic frequency spectrum for the nonlinear load current in the minimum case

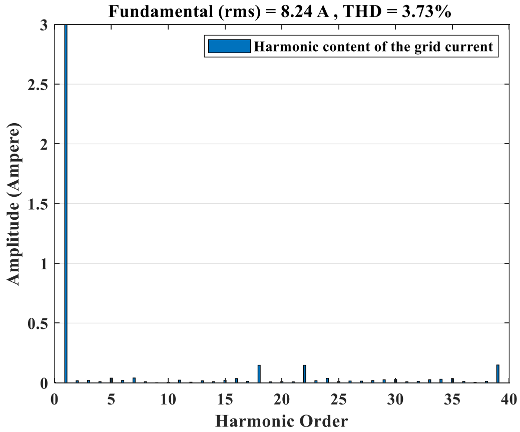

Fig. 6. The harmonic frequency spectrum for the nonlinear load current in the minimum case with existing the SAPF

VI. Conclusion

This paper takes into account the SAPF based on the three-phase current source converter. According to error dynamics, a new robust control method was introduced in this paper, and numerical simulation with experimental results were provided. The robust control approach is simple to implement in practical situations. This control method is fast, in contrast to other methods. Also, this approach is highly robust compared to the variation of the parameters and unmolded dynamics. The simulation results explicated the satisfactory performance of the SAPF in compensating the harmonics.

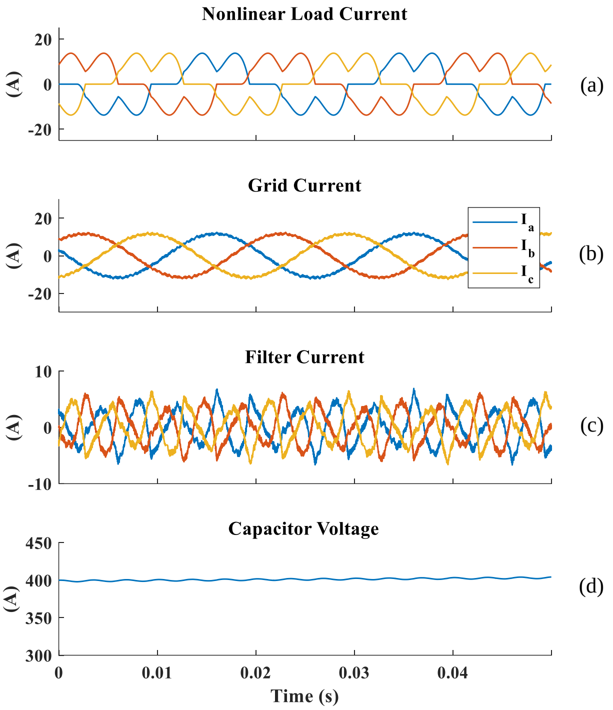

Fig. 7. The simulation results of the SAPF with nonlinear load constructed by diode bridge. (a) The waveform of the nonlinear load current (b) The waveform of the grid current after connecting the SAPF (c) The waveform of the SAPF (d) The waveform of the DC link capacitor voltage.

REFERENCES

[1] F. Blaabjerg, Control of Power Electronic Converters and Systems: Volume 2, 1st edit. Elsevier, 2018.

[2] A. Terciyanli et al., “A Current Source Converter-Based Active Power Filter for Mitigation of Harmonics at the Interface of Distribution and Transmission Systems,” IEEE Trans. Ind. Appl., vol. 48, no. 4, pp. 1374–1386, Jul. 2012, doi: 10.1109/TIA.2012.2200009.

[3] N. Bagheri, H. Alipour, L. Mohammadian, J. Beiza, and M. Ebadpour, “A Multiport isolated resonant LLC converter for grid-tied renewable energy powered bidirectional EV charger,” International Journal of Industrial Electronics Control and Optimization (IECO), vol. 6, no. 1, pp.37-48, 2023.

[4] B. Singh, K. Al-Haddad, and A. Chandra, “A review of active filters for power quality improvement,” IEEE Trans. Ind. Electron., vol. 46, no. 5, pp. 960–971, 1999, doi: 10.1109/41.793345.

[5] A. Govind, V. Kumar Tayal, and R. K. Kumawat, “Comparison of Current Controlling Methods for Shunt Active Power Filters to Improve Power Quality,” in 2022 10th International Conference on Reliability, Infocom Technologies and Optimization (Trends and Future Directions) (ICRITO), Oct. 2022, no. Lc, pp. 1–5, doi: 10.1109/ICRITO56286.2022.9965182.

[6] M. Sabarimuthu, N. Senthilnathan, N. Priyadharshini, M. A. Kumar, N. Telagam, and S. K. Sree, “Comparison of Current Control Methods for a Three Phase Shunt Active Filter,” in 2021 7th International Conference on Electrical Energy Systems (ICEES), Feb. 2021, pp. 32–37, doi: 10.1109/ICEES51510.2021.9383754.

[7] H. Akagi, “New trends in active filters for power conditioning,” IEEE Trans. Ind. Appl., vol. 32, no. 6, pp. 1312–1322, 1996, doi: 10.1109/28.556633.

[8] J. Afonso, C. Couto, and J. Martins, “Active Filters with Control Based on the p-q Theory,” IEEE Ind. Electron. Soc., vol. 47, no. May 2014, pp. 5–10, 2000, [Online]. Available: http://hdl.handle.net/1822/1921.

[9] Z. Xiao, H. Xue, T. Liu, and G. Zheng, “Research on Control Strategy of Shunt Active Power Filter,” in 2023 8th Asia Conference on Power and Electrical Engineering (ACPEE), Apr. 2023, pp. 2377–2382, doi: 10.1109/ACPEE56931.2023.10135649.

[10] C. Ranga Rao, R. Balamurugan, and R. Alla, “Synchronization control techniques for shunt active power filter: an overview,” Bull. Electr. Eng. Informatics, vol. 12, no. 1, pp. 1–9, Feb. 2023, doi: 10.11591/eei.v12i1.4300.

[11] M. Miletić, K. R. Raguž, V. Zeleničić, I. Erceg, and D. Sumina, “Development of Single-Phase Shunt Active Power Filter for Reduction of Current Harmonics in Data Center Power System,” in 2023 11th International Conference on Smart Grid (icSmartGrid), Jun. 2023, pp. 1–7, doi: 10.1109/icSmartGrid58556.2023.10170839.

[12] R. Hou, P. Wang, J. Wu, and D. Xu, “Research on Oscillation Suppression Methods in Shunt Active Power Filter System,” Energies, vol. 15, no. 9, 2022, doi: 10.3390/en15093125.

[13] L. Zhou, Z. Zhou, J. Qi, and W. Han, “Hybrid Prediction-Based Deadbeat Control for a High-Performance Shunt Active Power Filter,” IEEE Access, vol. 11, no. January, pp. 11118–11131, 2023, doi: 10.1109/ACCESS.2023.3241300.

[14] J.-H. Urrea-Quintero, N. Muñoz-Galeano, and J. M. López-Lezama, “Robust Control of Shunt Active Power Filters: A Dynamical Model-Based Approach with Verified Controllability,” Energies, vol. 13, no. 23, p. 6253, Nov. 2020, doi: 10.3390/en13236253.

[15] H. Sadeghi, and H.R. Mohammadi, “An improved fuzzy controlled back-to-back electric spring using hybrid structure of ES-1 and shunt-APF to improve power quality in microgrids,” International Journal of Industrial Electronics Control and Optimization (IECO), vol. 5, no. 1, pp.89-98, 2022.

[16] T. Toumi, A. Allali, A. Meftouhi, O. Abdelkhalek, A. Benabdelkader, and M. Denai, “Robust control of series active power filters for power quality enhancement in distribution grids: Simulation and experimental validation,” ISA Trans., vol. 107, no. xxxx, pp. 350–359, 2020, doi: 10.1016/j.isatra.2020.07.024.

[17] A. Munduate, G. Garcera, and E. Figueres, “Robust control of a Shunt Active Power Filter for the medium voltage range based on a three-level Neutral Point Clamped converter,” in IECON 2006 - 32nd Annual Conference on IEEE Industrial Electronics, Nov. 2006, pp. 2162–2167, doi: 10.1109/IECON.2006.347274.

[18] W.-K. Sou, P.-I. Chan, C. Gong, and C.-S. Lam, “Finite-Set Model Predictive Control for Hybrid Active Power Filter,” IEEE Transactions on Industrial Electronics, vol. 70, no. 1, pp. 52–64, Jan. 2023, doi: 10.1109/tie.2022.3146550.

[19] A. Elallali, A. Abouloifa, I. Lachkar, C. Taghzaoui, F. Giri, and Y. Mchaouar, “Nonlinear control of grid-connected PV

systems using active power filter with three-phase three-level NPC inverter," IFAC-PapersOnLine, vol. 55, no. 12, pp. 61–66, 2022, doi: 10.1016/j.ifacol.2022.07.289.

[20] V. Hajbani, A. Zakipour, and M. Salimi, "A novel Lyapunov-based robust controller design for LCL-type shunt active power filters using adaptive sliding-mode backstepping approach," e-Prime - Advances in Electrical Engineering, Electronics and Energy, vol. 5, p. 100200, Sep. 2023, doi: 10.1016/j.prime.2023.100200.

[21] Y. Fang, J. Fei, and K. Ma, "Model reference adaptive sliding mode control using RBF neural network for active power filter," Int. J. Electr. Power Energy Syst., vol. 73, pp. 249–258, Dec. 2015, doi: 10.1016/j.ijepes.2015.05.009.

[22] L. Zhang and J. Fei, "Intelligent Complementary Terminal Sliding Mode Using Multiloop Neural Network for Active Power Filter," IEEE Transactions on Power Electronics, vol. 38, no. 8, pp. 9367–9383, Aug. 2023, doi: 10.1109/tpel.2023.3266738.

[23] K. Ma and J. Fei, "Model reference adaptive fuzzy control of a shunt active power filter," J. Intell. Fuzzy Syst., vol. 28, no. 1, pp. 485–494, 2015, doi: 10.3233/IFS-141325.

[24] S. Hou and J. Fei, "Adaptive fuzzy sliding control with fuzzy sliding term for three-phase active power filter," in 2013 10th IEEE International Conference on Control and Automation (ICCA), Jun. 2013, no. 2612012, pp. 1318–1323, doi: 10.1109/ICCA.2013.6564895.

[25] R. Guzman, L. G. de Vicuna, J. Morales, M. Castilla, and J. Miret, "Model-Based Control for a Three-Phase Shunt Active Power Filter," IEEE Trans. Ind. Electron., vol. 63, no. 7, pp. 3998–4007, Jul. 2016, doi: 10.1109/TIE.2016.2540580.

[26] C. Gong, W.-K. Sou, and C.-S. Lam, "Design and Analysis of Vector Proportional–Integral Current Controller for LC-Coupling Hybrid Active Power Filter With Minimum DC-Link Voltage," IEEE Trans. Power Electron., vol. 36, no. 8, pp. 9041–9056, Aug. 2021, doi: 10.1109/TPEL.2021.3049834.

[27] A. Zarei, M. S. Poutari, and S. M. Barakati, "Trajectory tracking for two-degree of freedom helicopter system using a controller-disturbance observer integrated design," ISA Transactions, vol. 74, pp. 99–110, Mar. 2018, doi: 10.1016/j.isatra.2017.12.026.

[28] A. Zarei, Y. Mousavi, R. Mosalanezhad, and M. H. Atazadegan, "Robust Voltage Control in Inverter-Interfaced Microgrids Under Plug-and-Play Functionalities," IEEE Systems Journal, vol. 14, no. 2, pp. 2813–2824, Jun. 2020, doi: 10.1109/jsyst.2019.2956684.

[29] Y. Mousavi, A. Zarei, and Z. S. Jahromi, "Robust adaptive fractional-order nonsingular terminal sliding mode stabilization of three-axis gimbal platforms," ISA Transactions, vol. 123, pp. 98–109, Apr. 2022, doi: 10.1016/j.isatra.2021.05.027.

[30] A. Zarei and S. Tavakoli, "Lumped uncertainty alleviation in output channels of MIMO nonlinear systems based on robust disturbance observer-based control strategy," Asian Journal of Control, vol. 25, no. 3, pp. 2001–2011, May 2022, doi: 10.1002/asjc.2834.

[31] A. Hassannia, S. M. Barakati, and S. H. Torabi, "Robust discrete sliding mode controller design for a single-phase onboard integrated electric vehicle charger with disturbance estimation," Computers and Electrical Engineering, vol. 110, p. 108881, Sep. 2023, doi: 10.1016/j.compeleceng.2023.108881.

Mohammad Ali Heydari; received his M.Sc in Electrical engineering from Sajjad Mashhad University of Technology, Mashahd, Iran in 2015 and Ph.D degree in Electrical engineering at University of Sistan and Baluchestan, Zahedan, Iran.

Mahdi Hassanniakheibari was born in Gonabad, Iran, in 1987. He received his PhD in Power Electrical Engineering from the Islamic Azad University, Science and Research Branch, Tehran, Iran, in 2020. He is an Assistant Professor at the Islamic Azad University, Zahedan Branch. His research interests include power systems, distribution networks, demand response, and power electronic converters.

Gholamreza Sadeghi; received his B.Sc degree in Electrical engineering from Imam Ali university, Iran in 2009. Now he is pursuing M.Sc degree in power electronic at the Arak University of technology, Arak, Iran.

IECO

This page intentionally left blank.